DOE-ER-0313/47
Distribution
Categories
UC-423, -424

FUSION MATERIALS
SEMIANNUAL PROGRESS REPORT
FOR THE PERIOD ENDING

December 31, 2009

Prepared for
DOE Office of Fusion Energy Sciences
(AT 60 20 10 0)

DATE PUBLISHED: February 2010

Prepared by
OAK RIDGE NATIONAL LABORATORY
Oak Ridge, Tennessee 37831
Managed by
UT-Battelle, LLC
For the
U.S. DEPARTMENT OF ENERGY

FOREWORD

This is the forty-seventh in a series of semiannual technical progress reports on fusion materials science activity supported by the Fusion Energy Sciences Program of the U.S. Department of Energy. It covers the period ending December 31, 2009. This report focuses on research addressing the effects on materials properties and performance of exposure to the neutronic, thermal and chemical environments anticipated in the chambers of fusion experiments and energy systems. This research is a major element of the national effort to establish the materials knowledge base for an economically and environmentally attractive fusion energy source. Research activities on issues related to the interaction of materials with plasmas are reported separately.

The results reported are the product of a national effort involving a number of national laboratories and universities. A large fraction of this work, particularly in relation to fission reactor irradiations, is carried out collaboratively with partners in Japan, Russia, and the European Union. The purpose of this series of reports is to provide a working technical record for the use of program participants, and to provide a means of communicating the efforts of fusion materials scientists to the broader fusion community, both nationally and worldwide.

This report has been compiled under the guidance of F. W. (Bill) Wiffen and Renetta Godfrey, Oak Ridge National Laboratory. Their efforts, and the efforts of the many persons who made technical contributions, are gratefully acknowledged.

G. R. Nardella
Research Division
Office of Fusion Energy Sciences

A SEARCH FOR CHANNEL DEFORMATION IN IRRADIATED VANADIUM TENSILE SPECIMENS—

D. S. Gelles, M. B. Toloczko and R. J. Kurtz (Pacific Northwest National Laboratory)*

OBJECTIVE

The objective of this effort is to investigate channel deformation in deformed irradiated vanadium alloys in order to better understand deformation behavior in this class of materials.

SUMMARY

A miniature tensile specimen of V-4Cr-4Ti which had be irradiated in the 17J test at 425°C to 3.7 dpa was mechanically polished, deformed to 3.9% strain at room temperature, and examined by scanning and transmission electron microscopy in order to look for evidence of channel deformation. It was found that uniform deformation can occur without channel deformation, but evidence for channeling was found with channels appearing most prominently after the onset of necking. The channeling occurs on wavy planes with large variations in localized deformation from channel to channel.

PROGRESS AND STATUS

Introduction

Recent tensile tests on selected irradiated V-4Cr-4Ti specimens showed unstable response, possibly due to channel deformation [1-3]. Channel deformation is often found in irradiated materials and is characterized by extensive shear on specific planes such that localized deformation can be very high. An excellent example is in the recent work of Fukumoto and coworkers on V-(3-5%)Cr-(3-5%)Ti deformed after irradiation at 300ºC [4-6]. In that work, confocal microscopy was used to examine the specimen surface during tensile testing, and it was possible to stop testing at the ultimate tensile stress. Surfaces in the necked region showed surface steps and TEM revealed that deformation bands were present in the microstructure that were free of irradiation induced defects and dislocations. The deformation bands showed up to a 10º rotation with respect to adjacent undeformed regions. More recent work showed examples where these channels could not penetrate grain boundaries, with tangles of dislocations in the vicinity of the boundary. Our recent examinations of compression test specimens irradiated in the RB-17J test at 425ºC did not provide definite evidence of channel deformation [7,8]. To determine if the propensity for channel deformation is influenced by stress-state, a tensile specimen of the same composition as the compression specimens was examined.

Experimental Procedure

Miniature tensile specimens UN01 and UB36 were obtained from Oak Ridge National Laboratory for testing and examination. UN01 was an SS-J2 geometry of the Japanese NIFS-2 heat and UB36 was an SS-J1 geometry of the US heat 832665, so that UN01 was approximately twice as thick as UB36 but otherwise was very similar. Both had been irradiated in the RB-17J experiment at 425ºC to 3.7 dpa [9,10]. Both specimens were surface ground to a 0.3 μm diamond polish finish, so that UN01 was reduced to about the thickness of UB36 and then both were tested in a miniature test frame at room temperature and a low strain rate of ~0.051 mm/min. Following testing, the samples were examined by SEM in a JEOL 840 to identify surface features and failure modes, where relevant, and then the UB36 sample was prepared for transmission electron microscopy using standard ion milling procedures. This involved gluing gauge sections to 3 mm molybdenum washers, dimple grinding and polishing, and then ion milling in a Gatan PIMS using argon ions at 5 KeV. Following thinning, the edge of the gauge section was visible, so it was possible to identify the tensile axis in micrographs. Transmission microscopy was performed on a JEOL 2010F and images were recorded digitally.

*Pacific Northwest National Laboratory (PNNL) is operated for the U.S. Department of Energy by Battelle Memorial Institute under contract DE-AC06-76RLO-1830.

Results

Specimen UN01 broke at a very low applied stress, with a brittle cleavage fracture surface at approximately right angle to the tensile axis. It was presumed that extensive surface grinding might have caused embrittlement. UB36 was deformed to ~4% strain, with a yield stress of 525 MPa, fairly typical for these irradiation conditions. The tensile trace is shown in Figure 1.

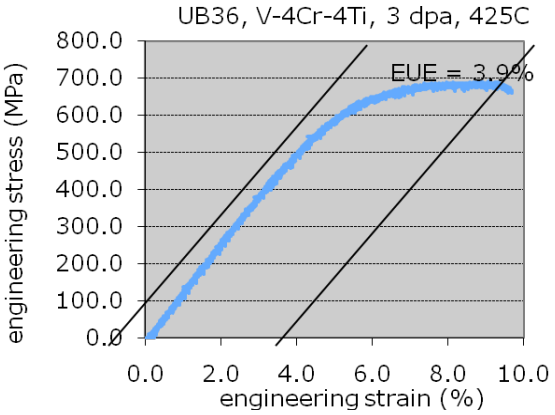

Figure 1. Tensile trace for specimen UB36 tested at room temperature following irradiation at 425ºC to 3.7 dpa.

SEM revealed that the sample was necking at one end of the gauge section, but otherwise showed no apparent effects of deformation. However, the two sides did show significant differences. Images of the more interesting side are provided in Figures 2 through 5 at increasing magnifications. Figure 2 shows the complete gauge section at low magnification with the necked region near the end on the right. Figure 3 shows the necked area at higher magnification revealing some regions with surface steps, but with adjacent regions showing no steps. Figures 4 and 5 provide examples at higher magnifications of a region containing steps; the steps are non-uniformly spaced, wavy in nature and with large variations in apparent height.

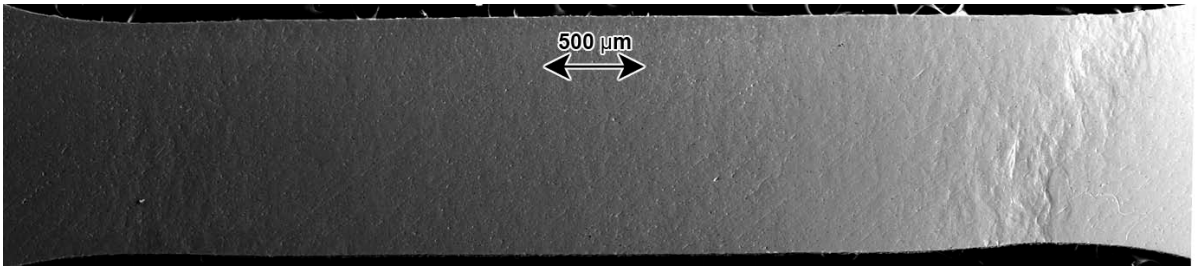

Figure 2. Surface damage at low magnification on UB36 following deformation.

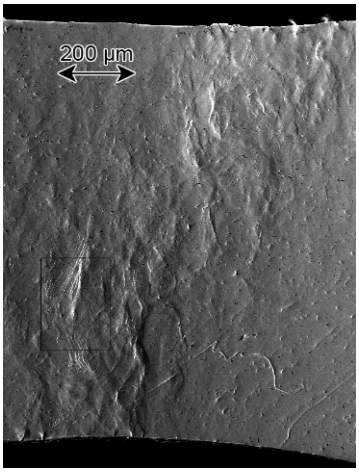

Figure 3. Necked region on UB36 following deformation.

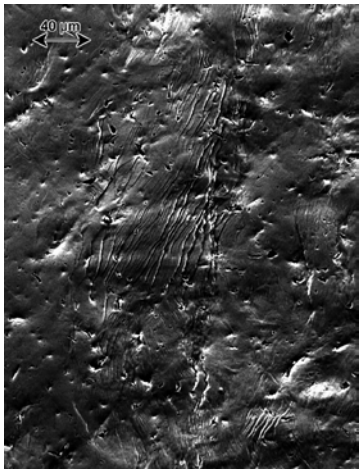

Figure 4. Surface steps in the necked region of UB36.

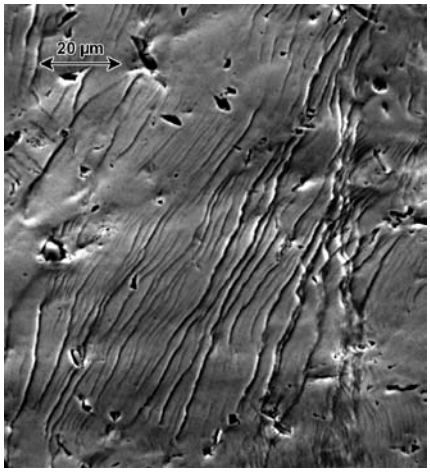

Figure 5. Surface steps at higher magnification on UB36.

The other side of specimen UB36 showed less structure resulting from deformation. Surface steps were not found; instead cavities appeared. An example is shown in Figure 6. The behavior is understood to be a result of a poor surface polish which left an oxide coating on the specimen. Deformation resulted in fractures in the oxide coating with resultant deformation restricted to regions below these fractures. Therefore, deformation induced surface steps are only created on clean surfaces.

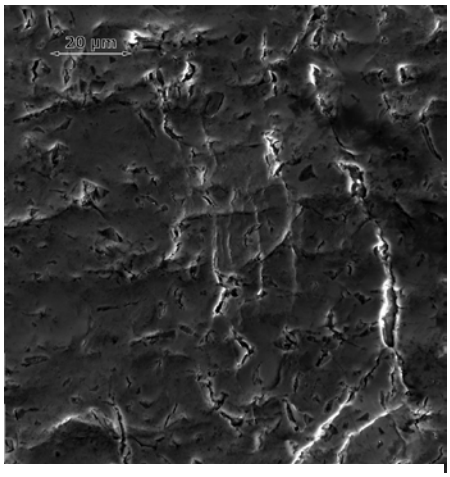

Figure 6. Surface features in the necked region on the other side of UB36.

Two samples were prepared from specimen UB36 for TEM, one centered in the necked region and a second in a region that had undergone uniform deformation. Each had been dimpled from the oxide-coated side so that thin area was closer to the well polished surface. Both had developed many perforations that had merged, giving a good deal of thin material covering an area on the order of 200 µm by 300 µm. Both samples revealed microstructures that appeared deformed, with complex bend contours throughout. However, imaging of dislocations was difficult due to the high density of precipitate particles present following irradiation. Similar precipitation response had been previously observed [11,12]. Both samples were examined during tilting experiments so that the movement of bend contours could be followed as the sample was tilted, in order to identify areas where discontinuous bend contour motion occurred, in order to reveal evidence of high local deformation. The two samples differed in that the one with uniform deformation showed no evidence of local high deformation areas whereas the necked sample contained several "steps." An example of a step is provided in Figure 7. The sample has been tilted so that one side is in strong g=110 contrast, whereas the other side is in weak contrast because the orientation is different. Corresponding convergent beam diffraction patterns are superimposed to show the tilt between these regions.

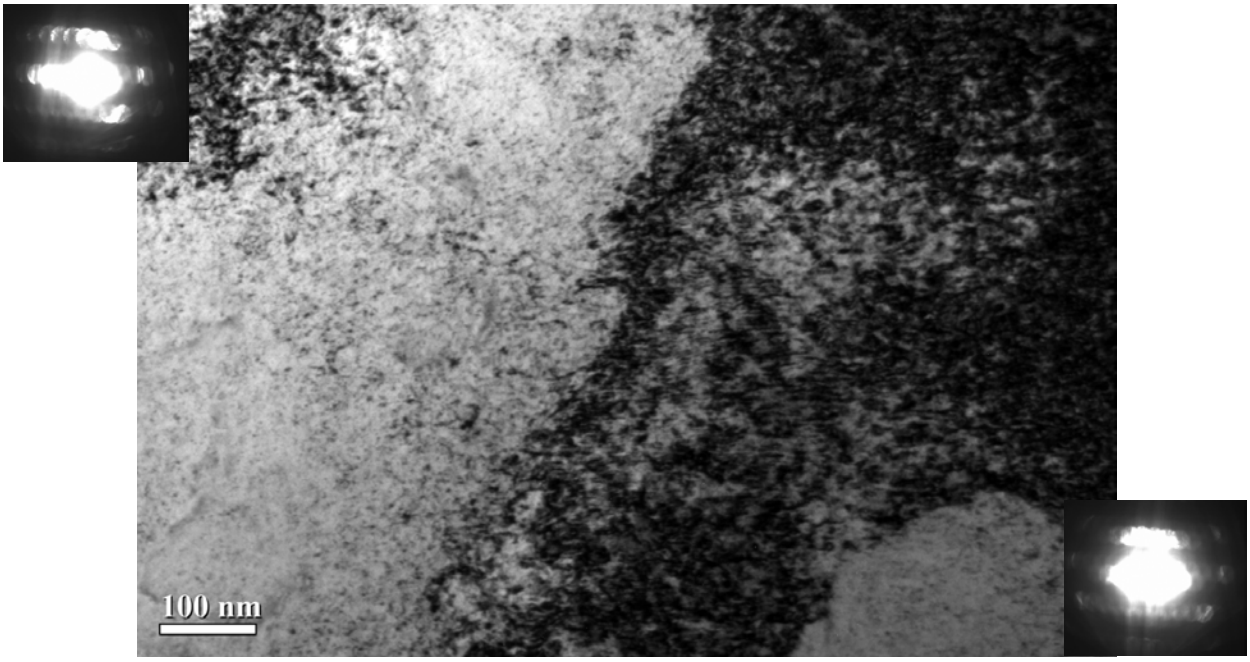

Figure 7. An area in the necked region of UB36 showing a shift in contrast between adjacent regions.

Figure 7 provides a typical example of the deformed microstructure in UB36. Dislocation images are difficult to identify. Under strong imaging conditions, they can be seen, but under weaker imaging conditions, they are hard to resolve because of the high density of precipitate strain fields. A step in contrast extends from upper right to lower left and approximately parallel to the applied stress direction. The nature of the step interface can be seen to be non-planar and complex. The closely spaced horizontal fringes in the strongly contrasted region possibly designate an inclined plane that separates the two regions.

Discussion

The phenomenology of channel deformation, if it exists in V-4Cr-4Ti following irradiation at 425ºC to 3.7 dpa in HFIR, appears to be as follows. Uniform deformation can occur without channel deformation, and channels appear most prominently after the onset of necking. Channeling occurs on wavy planes with large variations in localized deformation from channel to channel.

This is very different from that observed by Fukumoto and co-workers for V-(3-5%)Cr-(3-5%)Ti following irradiation at 300ºC and also by Garza and co-workers for V-4Cr-4Ti following ion irradiation and neutron irradiation in EBR-II to 4 dpa at 390ºC [13]. Following irradiation at the lower temperatures, the behavior follows classical response whereby dislocations are able to remove irradiation induced defects in their path and thereby reduce drag stresses. Following irradiation in our experiment at the higher temperature, the irradiation-induced obstacles are in the form of oxy-carbo-nitride precipitates [11,12] that are not easily destroyed by passing dislocations. Therefore, it appears that a different mechanism is required to create deformation channels where dislocation drag is more complex.

The nature of the mechanism required to overcome oxy-carbo-nitride precipitates at moderate strains is not yet understood. It appears to require significant cross slip as would be available in the complex stress state developed during necking. It can be argued that similar behavior was found in Fe-9Cr following irradiation and tensile deformation, where surface steps were found but dislocation free channels could not be identified [14]. Instead, evidence for channel deformation in the microstructure was limited to the observation of bands of distorted voids with adjacent regions containing undistorted voids.

CONCLUSIONS

Evidence for channel deformation is found as surface steps in a specimen of V-4Cr-4Ti irradiated at 425ºC to 3.7 dpa in the RB-17J that had been deformed at room temperature. Steps were only prominent in the necked region of the specimen after uniform strains on the order of 3.9% had been achieved. Microscopy indicated that the surface steps could be correlated with rough transgranular planes that represented complex tilt boundaries. This behavior was different from the more classical behavior found in V-(3-5%)Cr-(3-5%)Ti following irradiation at the lower temperature of 300ºC and is ascribed to the presence of oxy-carbo-nitride precipitate particles with greater obstacle strength.

References

[1] A. F. Rowcliffe, S. J. Zinkle and D. T. Hoelzer, J. Nucl. Mater., 283-287 (2000) 508.
[2] D. T. Hoelzer and A. F, Rowcliffe, J. Nucl. Mater., 307-311 (2002) 596.
[3] Private communication: RB-17J Specimen Test Results.
[4] K. Fukumoto and H. Matsui, “Dislocation channel formation process in neutron irradiated vanadium alloys using confocal laser microscopy” presented at the 6th IEA Vanadium Workshop held in Tucson, AR, USA in June 2002.
[5] K. Fukumoto, M. Sugiyama, and H. Matsui, J. Nucl. Mater. 329-333 (2004) 467.
[6] K. Fukumoto, M. Sugiyama, and H. Matsui, J. Nucl. Mater. 367-370 (2007) 829.
[7] M. B. Toloczko, R. M. Ermi, D. S. Gelles, R. J. Kurtz in DOE/ER-0313/44 (2008) 1.
[8] D. S. Gelles, in DOE/ER-0313/45 (2008) 1.

[9] D. K. Felde, A. L. Qualls, K. R. Thoms, D. W. Heatherly, R. G. Sitterson and R. L Wallace, in DOE/ER-0313/36 (2004) 120.
[10] D. K. Felde, and R. L Wallace, in DOE/ER-0313/38 (2005) 159.
[11] D. S. Gelles, P. M. Rice, S. J. Zinkle and H. M. Chung, J. Nucl. Mater. 258-263 (1998) 1380.
[12] K. Fukumoto, H. Matsui, Y. Candra, K. Takahashi, H. Sasanuma, S. Nagata, and K. Takahiro, J. Nucl. Mater. 283-287 (2000) 535.
[13] J. Garza, M. Meshii and H. M. Chung, J. Nucl. Mater. 258-263 (1998) 1437.
[14] D. S. Gelles, M. L. Hamilton and R. E. Schäublin, "Post-Irradiation Deformation Microstructures in Fe-9%Cr," in Effects of Radiation on Materials: 20th International Symposium, ASTM STP 1405, S. T. Rosinski, M. L. Grossbeck, T. R. Allen, and A. S. Kumar, Eds., American Society for Testing and Materials (2001) 523.

THE ELECTRICAL CONDUCTIVITY OF SiC_f/SiC WITH CORRECTIONS FOR CONTACT RESISTANCE—G. E. Youngblood and E. Thomsen (Pacific Northwest National Laboratory)* and R. J. Shinavski (Hyper-Therm HTC, Inc.)

OBJECTIVE

The primary objectives of this task are: (1) to assess the properties and behavior of SiC_f/SiC composites made from SiC fibers (with various SiC-type matrices, fiber coatings and architectures) before and after irradiation, and (2) to develop analytic models that describe these properties as a function of temperature and dose as well as composite architecture. Recent efforts have focused on examining the electrical conductivity properties of SiC_f/SiC composites considered for application in FCI-structures in support of the U.S. dual-coolant lead-lithium (DCLL) fusion reactor blanket concept.

SUMMARY

Electrical conductivity (EC) data for several forms of two-dimensional, silicon carbide composite made with a chemical vapor infiltration matrix (2D-SiC/SiC) were acquired from RT to 800°C and analyzed. When using a 2-probe method, measured transverse EC-values require a fairly substantial correction due to contact resistance at the sample-electrode interface. Previously reported transverse EC-values were o too low because this correction was not considered. In this report, new transverse EC-values are reported for several forms of 2D-SiC/SiC. Many of these new values exceed the limit of 20 S/m desired for the flow channel insert application, especially at higher temperatures. The analysis showed that the EC for 2D-SiC/SiC strongly depends on the net thickness of the pyrocarbon fiber coatings, the interconnectivity and alignment of the carbon fiber network, and the thickness and, depending upon temperature, the type of composite seal coat. The in-plane EC-values also depend upon the carbon network interconnectivity, and typically greatly exceed transverse values by factors of roughly x15 (high temperatures) up to x100 (high temperatures).

PROGRESS AND STATUS

Introduction

New EC data for several forms of silicon carbide composite made with chemical vapor infiltration (CVI) matrix are reported. The data was acquired in support of a DOE-sponsored SBIR contract (DE-FG02-07ER84717) with Hyper-Therm HTC, Inc. The EC measurement systems and protocol and results for similar SiC/CVI-SiC composite materials as well as for dense, monolithic CVD-SiC were described in previous Fusion Material Semiannual Progress Reports [1-4].

In the last report [4], a simple model was introduced that described the transverse EC(T) of a 2D-SiC/CVI-SiC plate in terms of the EC of the interior, carbon net-worked SiC fabric-layered region in series with outer “seal coat” layers of densely adherent, single phase CVD-SiC (in our case). The transverse EC(T) for such a three-layered composite can be expressed by:

$$EC(T) = EC_{int}[1 - 2f(1 - R)]^{-1} \quad (1)$$

In Eq. (1), T is temperature, f = t/L where t is the average seal coat thickness, L is the composite plate thickness and EC_{int} is the transverse EC across only the interior region of a 2D-SiC/CVI-SiC. Presumably EC_{int} can be measured by grinding the seal coat off the surfaces of the sample leaving only the interior region. Also, R is the ratio EC_{int}/EC_{sc}, where EC_{sc} is the electrical conductivity of the seal coat. Equation (1) is useful because it expresses the overall EC(T) in terms of material properties that are temperature dependent and an easily controllable fabrication design parameter “f” that is temperature independent.

*Battelle Memorial Institute operates Pacific Northwest National Laboratory for the U.S. Department of Energy under contract DE-AC06-76RLO-1830.

The EC of carbon (~10^4–10^6 S/m) exhibits only slightly increasing EC-values with increasing temperature while the EC of SiC, a semi-conductor, is relatively low at lower temperatures (~0.1 S/m at RT) but increases rapidly with increasing temperature (i.e., ~ 100 S/m at 800°C). As a result, electrical conduction in the interior region of a high quality composite is controlled by the amount of high conductivity carbon, even though the amount is only a few percent. More importantly, the amount or lack of interconnectivity of a carbon network through touching fiber coatings dominates the overall conduction. Also, if the seal coat is relatively thin "2f" is small (~ 0.033 in our case), and the seal coat will only mildly affect the overall transverse EC(T) at moderate temperatures and above. In Eq. (1), at sufficiently high temperatures, $R \approx 1$, and $EC(T) \sim EC_{int}$; whereas at lower temperatures, $R > 1$, and $EC(T) < EC_{int}$, more so for larger values of "f."

Several model cases using Eq. (1) were considered and compared to measured EC(T)-values for a 2D-SiC/CVI-SiC with a CVD-SiC seal coat. EC(T) curves were predicted for a range of seal coat thicknesses from 10 to 500 μm and also for a range of EC_{sc}-values for CVD-SiC. For our particular case with t = 50 μm, as expected the predicted EC(T)-curve for a 2D-SiC/SiC with intact seal coat was only slightly lower than the measured $EC_{int}(T)$-curve (see Fig. 3 in [4]). However, our measured EC(T)-curves were dramatically less than any of the Eq. (1) model predictions even for a seal coat thickness of 500 μm. Furthermore, the 1000/T temperature dependence of the model predictions was entirely different than observed, especially at lower temperatures where the contributions of the SiC seal coat compared to the interior region should gradually become more important.

Apparently, when using a 2-probe method, as in our experimental procedure, contact resistance is larger than initially thought and cannot be ignored. What this means is measured EC(T)- and $EC_{int}(T)$-values must be corrected for contact resistance before comparison to the model predictions. In fact, we believe that all transverse EC(T)-values for 2D-SiC/SiC quoted in the literature, if measured by a 2-probe method, should be considered suspect. It is likely that these EC-values are actually less than "true" values for this material. Most transverse EC(T)-values reported for 2D-SiC/CVI-SiC have been less than the ~20 S/m limit desired for the FCI-application; so transverse EC through a SiC/SiC wall has not been considered a problem. Based on this new analysis of transverse EC-data this issue should be reconsidered.

In this report the contact resistance will be estimated, and our 2-probe EC-data will be corrected to obtain more reliable estimates of the transverse EC(T) for 2D-SiC/CVI-SiC. In addition, the effects of fabric architecture and orientation on EC(T) will be examined for several forms of this composite type.

Experimental Procedure and Results

Several bar and disc samples of 2D-SiC/SiC, produced from Hi-Nicalon™ type S fabric or braided preforms, were obtained from Hyper-Therm, HTC. This composite exhibits highly anisotropic properties in the two principal directions, normal and in-plane, and possibly some property dependence on in-plane weave orientation as well. Therefore, EC(T) was measured for the transverse direction and for two in-plane directions with weave orientations 0/90° or 45/45° with respect to the in-plane current direction.

These samples were made with three types of weave pattern, five-harness satin (5HS), eight-harness satin (8HS), and 60°-biaxial braid oriented in the hoop direction. Bar samples (40 x 5.3 x 3.1 mm) were used for 4-probe in-plane EC measurements; disc samples (10 mm od x ~3 mm tk.) were used for measurements normal to the plane of the woven or braided SiC fabric layers. About 0.1 mm was ground from each face of a few disc samples to acquire EC_{int}-values. Sample codes, batch designation, weave-type and orientations as well as the individual sample bulk density values are listed in Tables 1 and 2 for the bar and disc samples, respectively. Also listed are the descriptions for a bar and a disc reference sample of 2D-SiC/SiC made by General Electric. Complete characterization of this material was given in reference [5].

Table 1. Bar Samples (4-probe in-plane EC)

Code	Type	Orientation	Bulk Density (g/cc)
B1	Batch 1, 5HS weave	0/90°	2.77
B2	Batch 1, 5HS weave	0/90	2.78
B4	Batch 1, 5HS weave	45/45	2.74
B5	Batch 1, 5HS weave	45/45	2.71
B7	Batch 2, 8HS weave	0/90	2.75
B9	Batch 2, 8HS weave	0/90	2.85
B10	Batch 2, 8HS weave	45/45	2.76
B11	Batch 2, 8HS weave	45/45	2.65
B12	Batch 2, 60° braid	Hoop	2.65
B13	Batch 2, 60° braid	Hoop	2.75
B15	Batch 2, 60° braid	15°	2.80
B16	Batch 2, 60° braid	15°	2.79
2D-GE	Reference, 5HS weave	0/90	2.69

Table 2. Disc Samples (2-probe transverse EC)

Code	Type	Orientation	Bulk Density (g/cc)
D1	Batch 1, 5HS weave	0/90°	2.71
D4	Batch 1, 5HS weave	0/90	2.82
D8	Batch 2, 8HS weave	0/90	2.79
D9	Batch 2, 8HS weave	0/90	2.81
D10	Batch 2, 30° braid	normal to braid	2.73
D11	Batch 2, 30° braid	normal to braid	2.69
2D-GE	Reference, 5HS weave	0/90	2.69

All the preforms were produced with Hi-Nicalon™ type S fiber yarns containing 500 SiC filaments (~12 μm diameter). Hyper-Therm HTC fabricated three composite plates in a similar manner from these preforms, first by applying multilayer pyrocarbon PyC)/CVI-SiC fiber coatings by CVI (nominally 150 nm PyC + 4 x (100 nm SiC + 20 nm PyC layers)), and then by depositing the CVI-SiC matrix. A final ~50 μm thick CVD-SiC seal coat was applied at the completion of the matrix densification. The multilayer PyC/SiC fiber coating and CVD-SiC seal coat constituents represented ~8.0% and ~3.3% of the total sample volume, respectively. The reference 2D-GE samples were fabricated in a similar manner with 5HS type S fabrics except the fiber coating consisted of a single ~150-nm thick layer of PyC. In Figures 1(a-d), micrographs of ground and polished surfaces for the Hyper-Therm HTC 5HS composite show typical views of the macroscopic fiber architecture (optical) and the microscopic fiber and fiber coating structures (SEM).

The generally high range of SiC/SiC composite bulk density values from 2.65 to 2.85 g/cc, determined for the individual samples by dimensioning and weighing, indicated that the overall infiltration was consistent and of high quality. The 5HS and 8HS fabrics had 18 and 22 yarns/inch, respectively. To achieve the same fractional fiber volumes in each batch (38.4% and 37.6%, respectively), the 5HS plates contained 11 plies and the 8HS plates contained 9 plies for approximately the same plate thicknesses. Composite porosity was estimated to be about 12% and consisted primarily as a few rather large (~mm), laminar-shaped pores between the fabric layer planes (Fig. 1b) or numerous needle-shaped pores aligned parallel between the individual filaments within a fiber bundle (Fig. 1c). The braided composite was produced with 11 layers and had a slightly lower fiber volume (33.3%) due to a lower areal weight of the braid architecture.

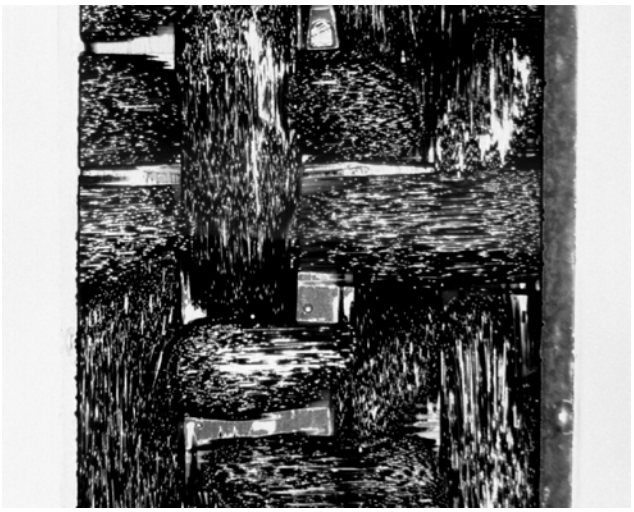

1(a) ---------- 1 mm

1(b) ---------- 1 mm

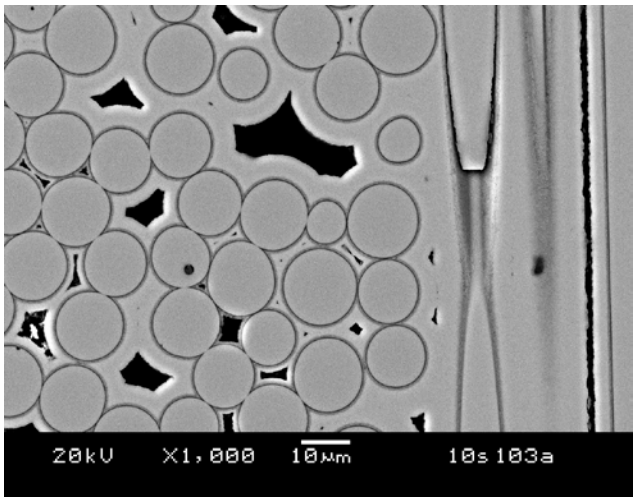

1(c)

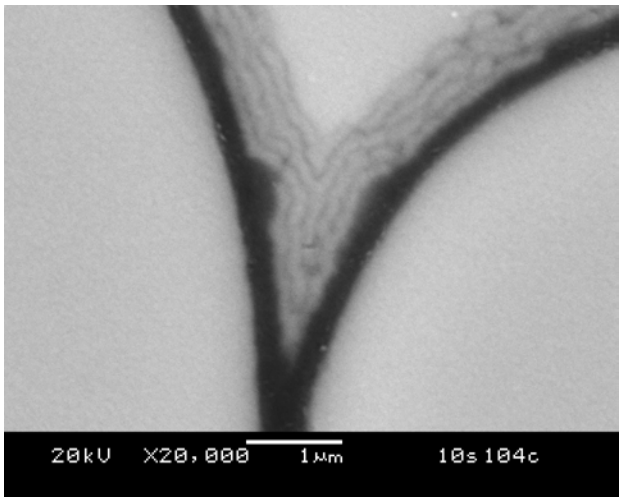

1(d)

Figures 1(a-d). Optical micrographs of in-plane and transverse cross-sections of 2D-SiC/SiC composite showing the general weave spacing and alignment for a 5HS weave sample (1a and 1b, respectively), and SEM views showing details of continuous PyC interconnectivity along individual fibers or an intermittent PyC interconnectivity between neighboring fibers within the yarn bundles (1c). As well, note the multilayer fiber coating structure for the Hyper-Therm HTC composites in (1d). In the SEM views using backscatter electrons the carbon layers are dark and the SiC matrix and fiber components are light grey.

The effects of fabric weave orientation on the in-plane EC was examined for bar samples cut with either 0/90° or ±45° fiber orientation with respect to the bar length (the electrical current direction). Likewise, in-plane EC was measured in the braiding direction resulting in 15° fiber orientation with respect to the bar length. Most importantly, EC-values for bar samples with axial current were compared to those for disc samples with transverse current normal to either the satin weave or braided weave layers.

The details of the two types of measurement assemblies used (4-probe for bar samples and 2-probe for disc samples) and the protocol for determining composite in-plane and transverse EC-values as a function of temperature up to ~800°C were given in previous reports [2,3]. In general, the sample electrical resistance was determined at each measurement temperature (heating and cooling in 40–50°

steps) from the slopes of applied dc voltage (0 to ± 0.1 volts) and measured current voltamagrams. EC-values were then determined from sample resistances (slopes of the voltamagrams) and the appropriate sample geometry factor when assuming uniform linear current flow. However, such 2D-SiC/SiC composites are far from homogeneous, so actual microscopic current densities were not uniform through the composite matrix, fiber and fiber coating constituents.

In Figure 2, the in-plane EC(T)-values for the bar samples listed in Table 1 (except for samples B15 and B16) are given from RT to ~800°C. In Figure 3, the corresponding transverse EC(T)-values for discs D1, D8 and reference 2D-GE samples listed in Table 2 are given. For the latter case, discs D1 and D8 are representative of the 5HS- and 8HS-weave composite batches, respectively. Measurements on the other disc samples listed in Table 2 are in progress. Usually the cooling legs of each 800°C temperature cycle were reproducible for all of the samples, so for clarity only the values determined for the decreasing temperature leg are presented.

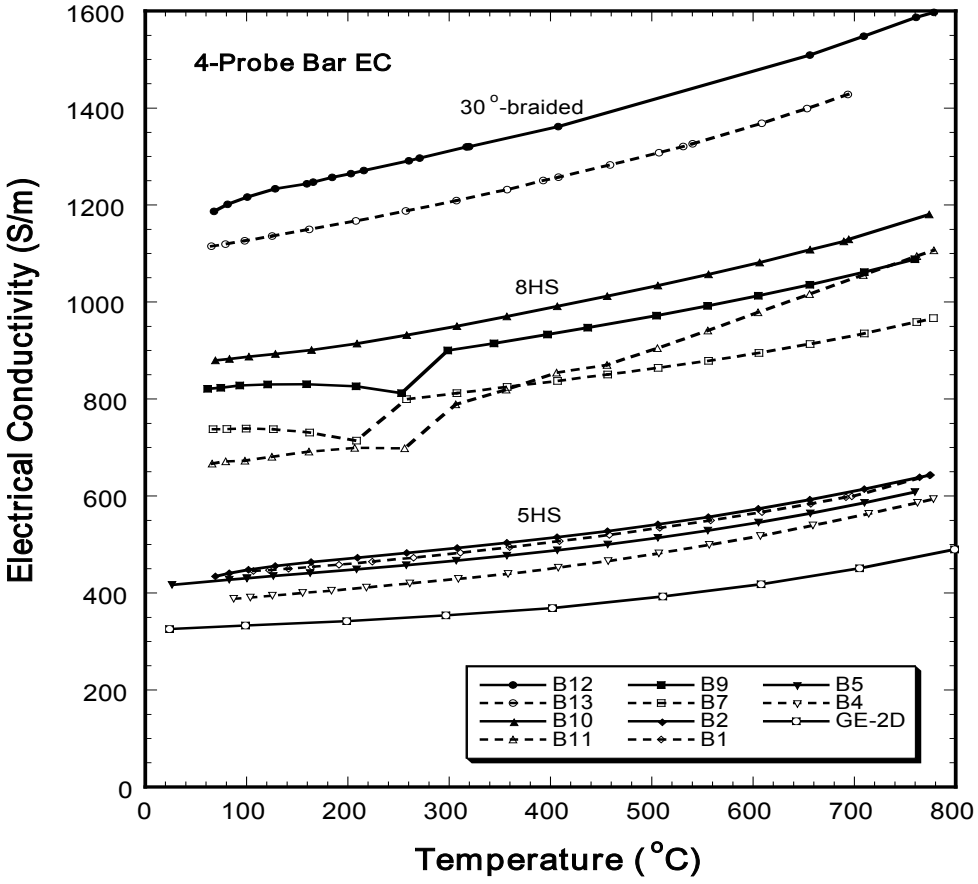

Figure 2. In-plane EC(T) for the bar samples with 60° braided (B12 and B13), 8HS weave (B10, B11, B9, and B7), and 5HS weave (B2, B1, B5 and B4), see Table 1. These samples had a multilayer PyC/SiC fiber coating (total PyC thickness 230 nm). For comparison, the EC-values also are plotted for a bar sample of 2D-5HS SiC/SiC (GE-2D) with a single 150-nm layer PyC fiber coating. All measurements on bars used a 4-probe dc method.

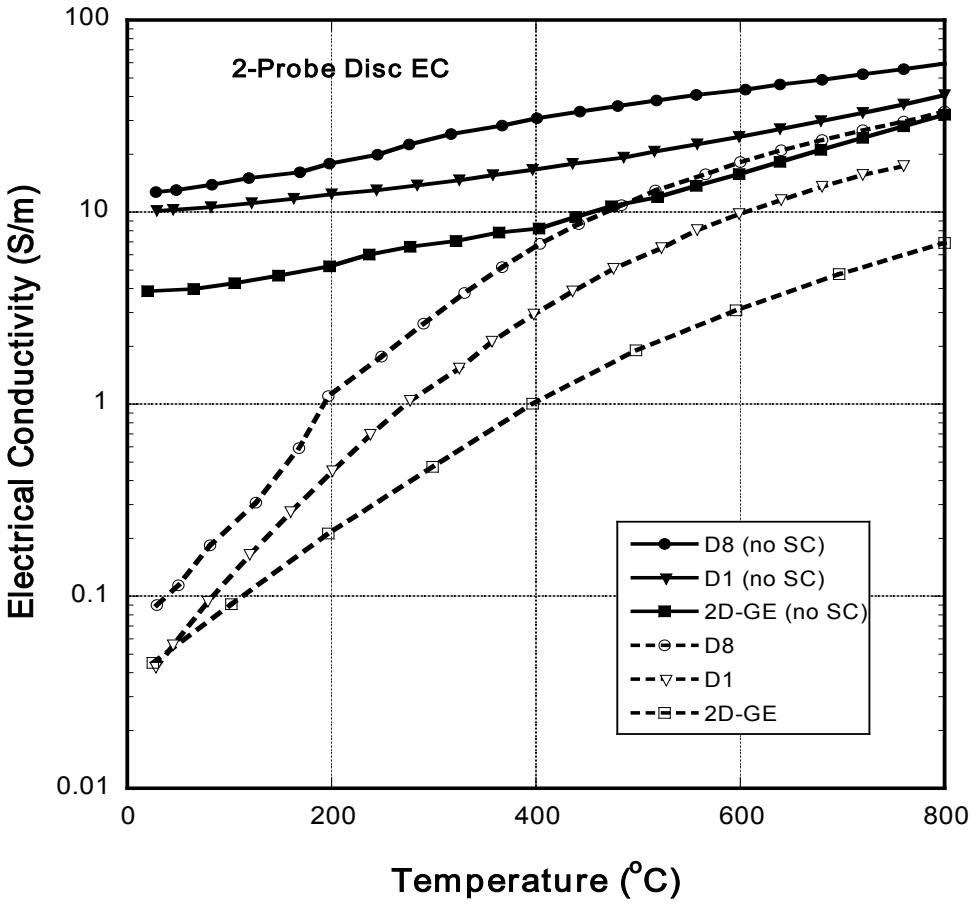

Figure 3. Transverse EC(T) for three of the disc samples listed in Table 2. Samples D8 (8HS) and D1 (5HS) contained multilayer PyC/SiC fiber coatings (~230-nm total PyC layer thickness) and the 2D-GE reference sample (5HS) contained a single layer PyC fiber coating ~150-nm thick. Measurements were repeated after the dense, SiC seal coat had been removed by grinding to expose only the carbon networked interior regions of these three representative composite discs. A 2-probe dc method was used.

Analysis and Discussion

The in-plane EC(T)-data in Fig. 2 appear to exhibit three general features. First, all the EC-values (400-1600 S/m) are high compared to EC-values for pure SiC (~0.1-100 S/m), as expected when EC through the numerous continuous PyC fiber coatings dominates EC through the SiC fiber/matrix components. Also, the observed relatively shallow and linearly increasing temperature dependence is characteristic of metallic-like carbon conductivity, not semi-conductor SiC conductivity. Second, it appears that these EC(T)-data can be sub-divided into three sub-groups according to the ranges of their values: the Batch 2 samples with braided weave fall in the highest range (~1200–1600 S/m), the Batch 2 samples with 8HS weave are in an intermediate range (~700-1100 S/m), and the Batch 1 samples with 5HS weave are in the lowest range (~400–600 S/m). Third, for samples with the same orientation and weave pattern, the spread of the EC-curves varies at most ~10%. Thus, within this limit, dependence of in-plane EC-values on weave orientation with respect to the current direction (either 0/90° or ±45°) will not be discernible. The small dips in the EC-values observed in the 200-300°C temperature range for bar samples B7, B9 and B11 likely are artifacts as such departures from a smooth temperature dependence are not observed for any other bar samples.

The in-plane EC-values for the GE-2D reference composite (~300-500 S/m) with the single ~150-nm thick layer PyC fiber coating are roughly parallel to the EC-values for any of the Hyper-Therm composites with multilayer coatings (~230 nm total thickness of PyC), but lie somewhat below those values. The lower EC-values for the GE-2D composite likely reflect the lower total amount of carbon fiber coating present in this material (~2.0%) compared to the Hyper-Therm multilayer materials (~2.9%).

The fairly large difference (~x2) between the ranges of EC(T)-values for the composites with the 5HS and 8HS weave patterns, nominally the same type and with similar orientations, was unexpected. One possible explanation for this occurrence is that the 5HS weave is more "open" than the 8HS weave, i.e., more fabric layers (11 vs. 9) but fewer yarns per inch (18 vs. 22) to achieve the same fiber volume. Ultimately the differences in fabric stacking and yarn shape for the 5HS and 8HS weaves must affect the pyrolytic carbon infiltration process within the composite structure. The overall interconnectivity of the carbon network and the net number of effective carbon conduction pathways in the 8HS composites must be greater than in the 5HS composites.

This carbon network interconnectivity effect appears to be quite important in determining the in-plane EC for 2D-SiC/SiC. It certainly is more important than orientation of the weave patterns as no discernible difference between EC-values for the 0/90 and 45/45 orientations is apparent. Finally, the Batch 2 composites with 2D-braided weave patterns must have even more effective carbon network interconnectivity than either of the two 2D-woven fabric composites, because their EC(T)-values are another ~50% greater than those for the 8HS weave material.

In Figure 3, the transverse EC(T)-values for the carbon networked interior portions of these selected 2D-SiC/SiC materials range from ~10 S/m at RT up to ~50 S/m at 800°C (solid lines). In contrast, the as measured transverse EC(T)-values for the same disc samples with their SiC seal coats intact are lower, ranging from ~0.1 S/m up to ~10 S/m at 800°C (dashed lines).

By far the most important feature observed in Fig. 3 is the large discrepancy between the EC(T)-values for samples with seal coat intact or ground off. This difference is attributed to a large contact resistance inherent when using a 2-probe measuring method. In our case, use of a 2-probe method is dictated by the small size of the disc samples used (~1 cm dia.) and the inhomogeneous nature of 2D-SiC/SiC made with stacked layers of woven fabric. A 4-probe method could not possibly be connected to measure uniform potential drops across such a thin, inhomogeneous disc-shaped sample.

Apparently, grinding off the dense SiC seal coat considerably reduces the contact resistance by exposing the carbon networked interior regions of the composite. Then the applied metallic electrodes make good electrical contact and a 2-probe method may provide acceptable data. Previously, for a similar 2-probe set-up, the specific contact resistance for disc samples with seal coat ground off was estimated to be relatively small, continuously decreasing from ~6 to 0.8 Ωcm^2 for temperatures increasing from RT to ~800°C, respectively (see Fig. 1 in [4]). Furthermore, in the reference [4] work little difference was observed for three different electrode types (porous Ni, and evaporated C or Au).

In Figure 3, at RT the large separation of the EC(T)-values between seal coat intact and seal coat removed (no SC) cases likely was due to the observed electrical resistance difference of from ~400 up to 900 ohms, quantities much larger than the total resistance values measured for any of the "no SC" cases. Although the thin SiC seal coat itself contributes a small amount to this difference in resistance, most of the separation is due to contact resistance at the electrode-SiC interface. Then, if the small contact resistance for the no SC case is ignored (<6 to 0.8 Ωcm^2), the specific contact resistance (R_c) can be estimated for resistances in series as

$$R_c \sim R_{tot} - R_{int} - 2r \qquad \text{Eq. (2)}$$

where R_{tot} and R_{int} are the measured resistances across a disc sample with seal coat intact or ground off, respectively; and r is the calculated resistance for the thin SiC seal coat layer on each as-received disc.

We calculated r for a seal coat layer 50 microns thick and using EC(T)-values measured in our lab for high-purity CVD-SiC [3]. The R_c(T)-values estimated by using Eq. (2) are shown in Fig. 4 for the three cases: samples 2D-GE, D1 and D8, the only samples at this time for which we have EC-data measured sequentially on the same samples with and without seal coat.

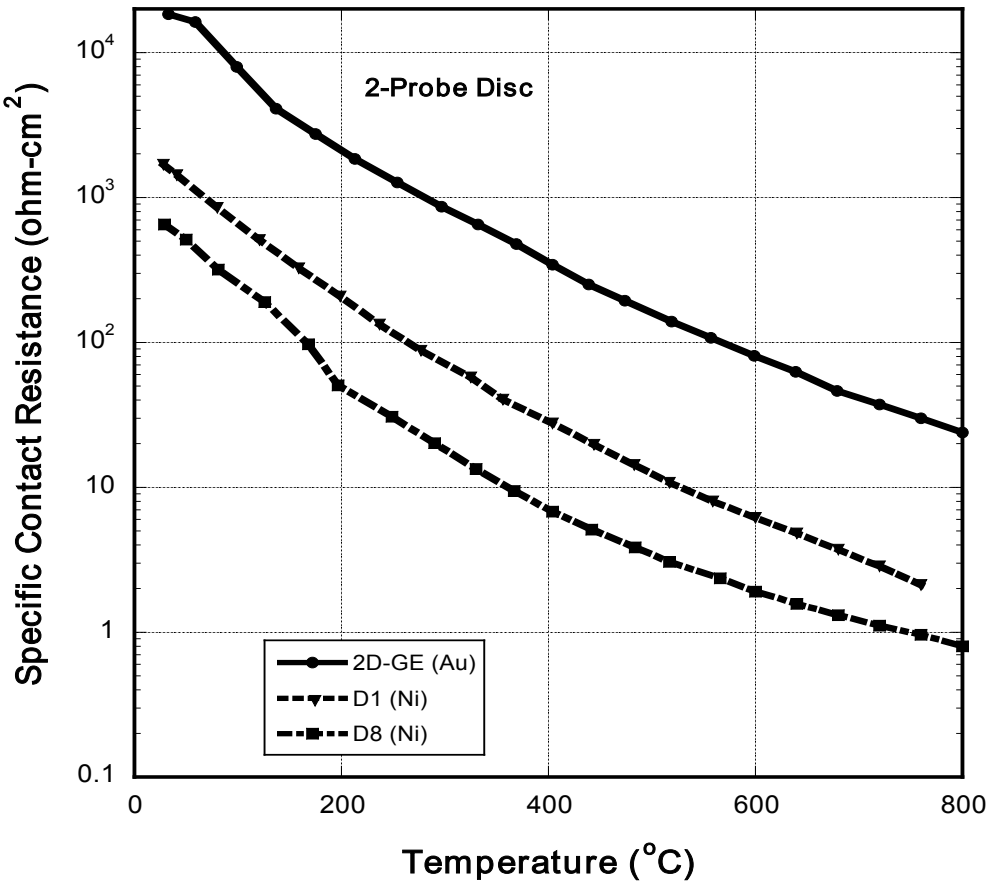

Figure 4. Estimated R_c(T) from Eq. (2) for SiC/SiC disc samples 2D-GE (evaporated Au electrodes), and D1 and D8 (porous Ni electrodes), when using a 2-probe dc method.

In Figure 4, R_c(T) decreases rapidly with increasing temperature from > 500 Ωcm^2 at RT to ~1-10 Ωcm^2 at 800°C. Also, R_c-values for evaporated Au electrodes are significantly larger than those for porous Ni electrodes. The porous Ni electrodes were achieved by applying a thin layer of NiO "ink" to each disc face using a screen-printing technique. Then the organics were driven off and the NiO reduced to porous Ni by heating to 800°C in a 3% H_2-atmosphere. This method of applying porous Ni electrodes has effectively been used in our fuel cell program. The NiO layer applied to sample D8 was thicker than that applied to D1, so the thicker layer likely is responsible for obtaining lower R_c-values. Nevertheless, the contact resistance is large for samples with metal electrode-pure SiC interfaces, especially at low temperatures, and will seriously affect EC(T)-values when using a 2-probe method.

The estimated R_c(T)-values depicted in Fig. 4 are themselves subject to error. First, because the contact resistance in the 2-probe measurement of R_{int} was ignored, although this error is thought to be relatively small; and second (and more importantly), because the actual EC(T)-values for the seal coat CVD-SiC are unknown. EC(T) for CVD-SiC may vary over two or more orders of magnitude depending on impurity levels and type [2]. Without knowing the actual impurity contents of the SiC seal coat, we assumed

EC(T)-values measured previously for a particular high purity CVD-SiC (see Fig. 5). Again, for a thin seal coat this correction is relatively small, except possibly at low temperatures.

Then, the most reliable way to obtain transverse EC(T)-values is to measure $EC_{int}(T)$ with a minimum influence of contact resistance and use Eq. (1). In Figure 5, the corrected transverse EC(T)-values from Eq. (1) are compared to the measured $EC_{int}(T)$-values for the three samples D1, D8 and 2D-GE. These corrected EC(T)-values should replace the uncorrected transverse EC(T)-values presented in Fig. 3 for samples with seal coat intact (dashed lines), and reported previously in reference [2]. For comparison, the measured EC(T)-values for the high-purity CVD-SiC used to estimate the effects of the SiC seal coat also are included in Fig. 5.

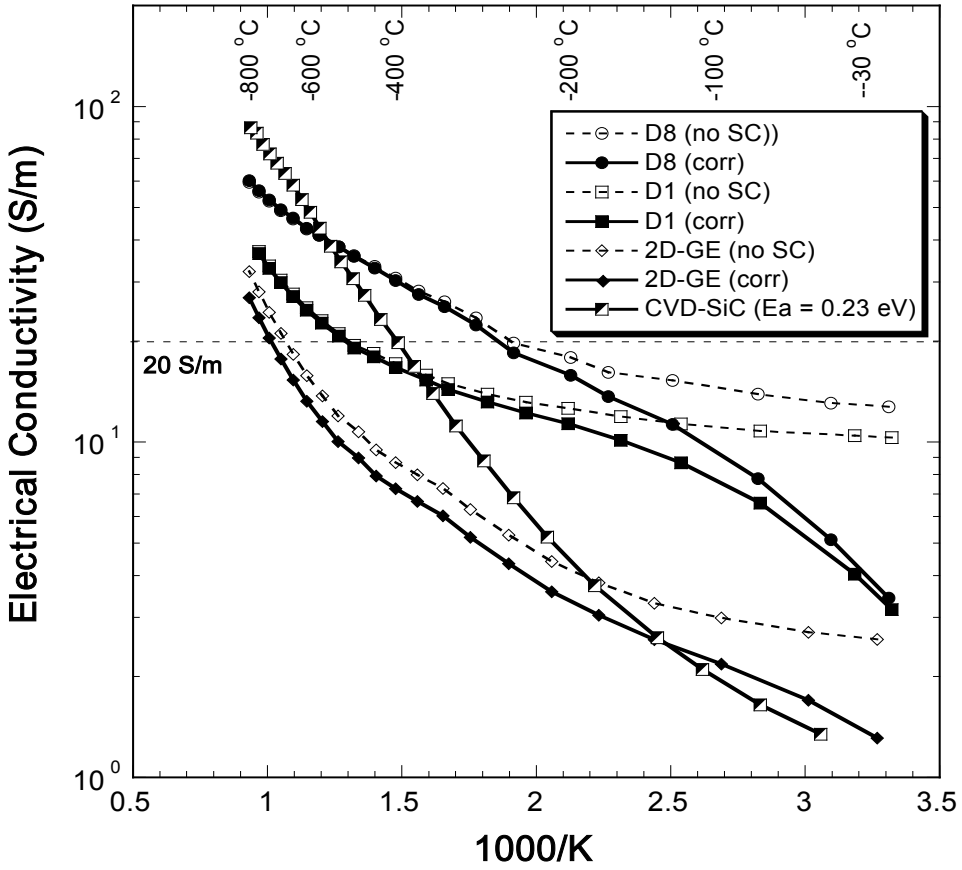

Figure 5. Transverse EC(T) from Eq. (1) (solid lines) and measured $EC_{int}(T)$ with minimum contact resistance (dashed lines) for three types of 2D-SiC/SiC. Samples D8 (8HS weave) and D1 (5HS weave) had multilayer PyC/SiC fiber coatings (~230-nm total PyC thickness), and 2D-GE (5HS weave) had single layer PyC fiber coatings (~150-nm PyC thickness). EC(T)-values measured for a high-purity CVD-SiC also are given.

In Figure 5, for T>~300°C the corrected EC(T)-values are approximately the same as the measured $EC_{int}(T)$-values for each corresponding sample. For T<~300°C, corrected EC(T)-values begin to deviate more and more below the corresponding sample $EC_{int}(T)$-values as the temperature decreases. Also, at high temperatures the temperature dependence (slopes of the EC(T)-curves) approaches but remains somewhat less than that of CVD-SiC, at moderate temperatures the slopes are less and deviate more from those of CVD-SiC, and at low temperatures the temperature dependence again approaches that of CVD-SiC. These observations are interpreted: at high temperatures electrical conduction through the SiC matrix and fiber components dominates, at moderate temperatures conduction through the

interconnected PyC fiber coating network dominates, and at sufficiently low temperatures conduction becomes limited by the SiC seal coat.

Interestingly, the corrected and measured EC(T)-values appear to rank in the same order as the in-plane EC(T)-values; i.e., values for multilayer 8HS weave (D8) > multilayer 5HS weave (D1) > monolayer 5HS weave (2D-GE). This ranking order suggests that in the transverse direction, as in the in-plane directions, the PyC fiber coating network interconnectivity for the 8HS material is more effective than in the 5HS material. Likewise, lower amounts of PyC decrease EC(T) as well, as suggested by the monolayer 2D-GE sample having the lowest EC(T)-values of all samples. Of course, the extent and arrangement of the porosity, especially for the larger laminar-shaped pores with their mid-planes normal to the current direction, also plays a major role in reducing the transverse EC for these composites as suggested by the fact that their EC(T)-values are less than values observed for dense CVD-SiC at sufficiently high temperatures.

Also from Fig. 5, the newly corrected transverse EC-values for these 2D-SiC/SiC composites exceeds the FCI-application limit of 20 S/m for temperatures greater than ~300°C, ~500°C and ~700°C for the multilayer 8HS, multilayer 5HS, and monolayer 5HS types, respectively.

By examining Eq. (1), several methods for reducing transverse EC(T) are suggested. Reducing the total thickness of the PyC fiber coatings, which reduces EC_{int}, would be effective over the entire temperature range. Increasing the seal coat thickness, which increases "f" in Eq. (1), would only be effective at lower temperatures where R (=EC_{int}/EC_{sc}) >1. The most effective way to reduce EC(T) would be to make R>1 for all temperatures. Replacing the SiC seal coat with some other compatible material that is electrically insulating over the entire temperature range could do this.

CONCLUSIONS

1. The contact resistance is large when using a 2-probe method to measure transverse EC(T) through a 2D-SiC/SiC plate with a SiC seal coat. The simplest and most reliable way to estimate these EC(T)-values is to use the 2-probe method to measure EC_{int}(T) of disc samples with seal coat ground off and then calculate EC(T) using Eq. (1). The effect of contact resistance will be minimized when measuring EC_{int}(T) because now the metallic electrodes make good electrical contact with the highly conductive PyC fiber-coating network with numerous intersections at the ground surfaces.

2. Newly estimated transverse EC-values for several types of 2D-SiC/SiC composite exceeded the FCI-application limit of 20 S/m for temperatures greater than ~300°C to 700°C.

3. The in-plane EC-values for these same types of 2D-SiC/SiC ranged from ~300 to 1600 S/m over the RT to 800°C temperature range, values much larger than EC-values observed for pure SiC (~0.1-100 S/m). This occurs when the EC through along the numerous, continuous PyC fiber coatings dominates EC through the SiC fiber/matrix components. Also, the in-plane EC-values were approximately 15-100 times larger than transverse EC-values as expected for these 2D materials.

4. The EC in both the in-plane and transverse directions for 2D-SiC/SiC with PyC fiber coatings also is strongly controlled by conduction through the interconnections of the carbon network within and between fiber bundles, especially at moderate temperatures (~300°C to 700°C).

5. The EC(T)-value ranges, determined for 2D-SiC/SiC with various SiC fabric weave patterns, rank in order: braided weave > 8HS weave > 5HS weave. This can be explained by the existence of a greater degree of electrical pathway interconnectivity through the carbon fiber coating network for the materials in the order of their ranked weave patterns.

6. The in-plane EC, within the limits of sample-to-sample variations, did not depend upon orientation of the various 2D-weave patterns examined.

References

[1] G.E. Youngblood, R.J. Kurtz and R.H. Jones, “Development of SiC/SiC for application as a flow channel insert,” pp 3-8 in Fusion Materials Semiannual Progress Report (FMSPR) for period ending Dec. 31, 2004 (DOE/ER-0313/37).

[2] G.E. Youngblood, E. Thomsen and G. Coffey, “Electrical conductivity of SiC/SiC,” pp 46-51 in FMSPR for period ending Dec. 31, 2005 (DOE/ER-0313/39).

[3] G.E. Youngblood, E. Thomsen and G. Coffey, “Electrical conductivity measurements of SiC-based materials,” pp 17-23 in FMSPR for period ending December 31, 2006 (DOE/ER-0313/41).

[4] G.E. Youngblood and E. Thomsen, “Modeling the electrical conductivity of SiC/SiC for FCI-application,” pp 35-42 in FMSPR for period ending December 31, 2008 (DOE/ER-0313/45).

[5] G.E. Youngblood and R.H. Jones, “Characterization of a 2D-SiC/SiC composite made by ICVI with Hi-Nicalon™ type S fabric,” pp 34-40 in FMSPR for period ending June 30, 2003 (DOE-ER-0313/34).

MECHANICAL PROPERTIES OF ADVANCED SIC FIBER COMPOSITES IRRADIATED AT VERY HIGH TEMPERATURES – Y. Katoh, K. Ozawa, L.L. Snead (Oak Ridge National Laboratory), T. Hinoki (Kyoto University), Y.B. Choi (Hiroshima University), A. Hasegawa (Tohoku University)

OBJECTIVE

This work addresses several important aspects of the effect of neutron irradiation on mechanical properties of advanced SiC/SiC composites produced through chemical vapor infiltration (CVI). First, the effect of irradiation at temperatures exceeding 1000ºC is determined. Second, the influences of different SiC fibers and interphase thicknesses on post-irradiation mechanical properties are addressed. Finally, the effect of neutron irradiation on the matrix cracking stress is addressed.

SUMMARY

Six different composite materials with various near-stoichiometric silicon carbide (SiC) fiber reinforcements and pyrolytic carbon or SiC/pyrolytic carbon multilayer interphases were neutron-irradiated to ~$6x10^{25}$ n/m2 (E > 0.1 MeV) at nominal temperatures of 800ºC and 1300ºC, and tested for tensile properties at room temperature. Only insignificant or very minor modifications to the tensile strength were admitted in all materials. However, two-parameter Weibull statistical analysis on relatively large specimen populations revealed minor but significant strength degradation for some composites. 50 – 150 nm appeared to be within the optimum PyC interphase thickness range for both fiber types in terms of tensile properties. The misfit stresses present in the unirradiated samples were significantly reduced after irradiation. The change in misfit stress was attributed to the irradiation-induced modification of coefficient of thermal expansion. True matrix cracking stress estimated from the proportional limit stress and misfit stress did not appear to degrade by neutron irradiation.

PROGRESS AND STATUS

Introduction

Silicon carbide (SiC) continuous fiber-reinforced SiC matrix (SiC/SiC) composites are promising, commercially available materials for fusion applications. The advantage of SiC/SiC composites as fusion reactor materials comes mainly from the exceptional radiation stability, high temperature performance, and low activation properties inherent to SiC.[1, 2] Moreover, recent research and development of SiC/SiC composites for advanced fission energy systems accelerate the design and application technology development toward the deployment of these materials for nuclear services.[3] An extensive neutron irradiation campaign designated RB-18J was carried out in US/Japan fusion blanket/materials collaboration program for the purposes of 1) gaining fundamental understanding of irradiation effects in SiC composites and their constituents in aggressive, fusion-relevant conditions, 2) determining the effects of neutron irradiation on various properties of new generation materials, 3) advancing constitutive modeling of irradiation effects in composites, and 4) determining irradiated engineering properties in support of blanket systems research and development. In this experiment, a variety of composite materials fabricated with different near-stoichiometric SiC fibers, fiber/matrix interphases, and matrix materials were evaluated for mechanical and physical properties following neutron irradiation up to ~7 dpa at temperatures nominally in an 800-1300ºC range.

This paper addresses several important aspects of the effect of neutron irradiation on mechanical properties of advanced SiC/SiC composites produced through chemical vapor infiltration (CV). First, the effect of irradiation at temperatures exceeding 1000ºC is determined. The previous reports indicates relatively minor but potential degradation of mechanical properties, in particular the matrix cracking stress, after low dose irradiation at very high temperatures for materials which had been proven to be radiation-stable up to ~10 dpa at below ~800ºC.[4] Second, the influences of different SiC fibers and interphase thicknesses on post-irradiation mechanical properties are addressed. Majority of the published data on irradiation effect on advanced SiC/SiC composites are those for Hi-Nicalon™ Type-S

(HNLS) fiber composites.[5-8] Irradiation performance of the composites with different type commercial SiC fiber is comparatively determined. The optimum pyrocarbon interphase thickness range for use in high radiation environment of composites in these classes is discussed. Moreover, the effect of neutron irradiation on the matrix cracking stress is addressed. The potential irradiation-induced degradation of proportional limit stress (PLS), roughly corresponding to the matrix cracking stress, of advanced SiC/SiC composites has been pointed out; however, previously reported effect of irradiation on PLS has been inconsistent. In this paper, this issue is clarified based on the misfit stress analysis.

Experimental

Materials irradiated and examined are CVI SiC matrix composites reinforced with two-dimensional (2D) woven fabrics of either Hi-Nicalon™ Type-S (Nippon Carbon Co., Tokyo, Japan) or Tyranno™-SA3 (Ube Industries, Ltd., Ube, Japan), as summarized in Table 1. Fiber coatings with pyrocarbon (PyC) or PyC/SiC multilayer were applied to form the adequately weak interphase between the fibers and matrices. The PyC coating thickness was nominally 50 nm or 150 nm. In the multilayer interphase, details of which are found elsewhere,[8] incorporates a nominally 20 nm-thick PyC innermost layer which serves as the sliding interphase. The interphase coating and matrix densification were provided by Hypertherm High-Temperature Composites, Inc. (Huntington Beach, CA)

Table 1: Summary of composite materials studied.

Designator	Reinforcement	Interphase	Matrix
SA3/ PyC150	Tyranno-SA3 7.5 micron (SA3-S1I16PX), 2D Plain Weave (PSA-S17I16PX), 17x17 tpi, 0º/90º	PyC(150nm)	CVI-SiC
SA3/ PyC50	Tyranno™-SA Grade-3 7.5 micron (SA3-S1I16PX), 2D Plain Weave (PSA-S17I16PX), 17x17 tpi, 0º/90º	PyC(50nm)	CVI-SiC
SA3T/ PyC150	Tyranno™-SA Grade-3 10 micron (SA3-S1F08PX), 2D Plain Weave (PSA-S17F08PX), 17x17 tpi, 0º/90º	PyC(150nm)	CVI-SiC
HNLS/ PyC150	Hi-Nicalon™ Type-S 900 denier (#383213), 2D Plain Weave (HNS9P2424), 24x24 tpi, 0º/90º	PyC(150nm)	CVI-SiC
HNLS/ PyC50	Hi-Nicalon™ Type-S 900 denier (#383213), 2D Plain Weave (HNS9P2424), 24x24 tpi, 0º/90º	PyC(50nm)	CVI-SiC
HNLS/ ML	Hi-Nicalon™ Type-S 1800 denier, 2D-Satin Weave, 16x16 tpi, 0º/90º	5x[PyC(20nm)/ SiC(100nm)]	CVI-SiC

It is worth noting that non-standard fabrics or fibers were used for some of the composites studied. For the PyC interphase HNLS composites, 24x24 thread-per-inch (TPI) fabrics with 250 filament yarns were used instead of the standard 16x16 TPI fabric with 500 filament yarns. The use of finer weave fabrics increased the interlaminar porosity resulting in substantially reduced interlaminar strength.[9] For the SA3 composites, fabrics of 800 filament yarns of thick fibers (nominally 10 micron diameter) were used in addition to the fabrics of the standard 1600 filament yarns of 7.5 micron diameter fibers.

Irradiation was performed in the RB* facility located in the reflector beryllium position of High Flux Isotope Reactor (HFIR), Oak Ridge National Laboratory (ORNL). The nominal irradiation temperatures are 800ºC and 1300ºC. There is evidence that some of the samples in the 800ºC zone had received irradiation at significantly lower temperatures; however, most of the composite samples are believed to have been irradiated at the vicinity of 800ºC based on the thermocouple reading . The 1300ºC zone lost thermocouples at the early irradiation and was operated to maintain the highest design temperature after then; therefore, the actual irradiation temperature may likely be higher than 1300ºC. The average fast (E

> 0.1 MeV) neutron fluence for the 800ºC and 1300ºC zones are estimated to be ~5.9 and ~5.8 x 1025 n/m2 , respectively.

Tensile properties were examined at room temperature using straight beam specimens which measure 40 mm x 4 mm x 2 mm per general standard test practice in ASTM C1275-00. Strain was determined by averaging the readings from a pair of strain gauges attached to both faces within the gauge section. The intermittent unloading/reloading sequences were incorporated for extracting information related with the residual thermal stress and interfacial sliding stress. All the tensile specimens were measured for elastic modulus by impulse excitation and vibration method according to ASTM C1259-01. Fracture surfaces were examined by scanning electron microscopy following the tensile test.

Results

The tensile stress-strain properties before and after irradiation are shown in Fig. 1. All six materials exhibited pseudo-ductile tensile fracture behavior before irradiation, and such behavior was not altered after irradiation at either 800ºC or 1300ºC. The Hi-Nicalon HNLS composites exhibited an extensive non-linear strain with an exception of the multilayer interphase composite. The strain to failure exceeding 0.5% is exceptionally large for these composites and may be attributed to the poor matrix densification. The multilayer interphase can be considered a PyC interphase of ~20 nm thickness as far as fast fracture properties are concerned. Therefore, the relatively low strength and the premature failure observed for the multilayer interphase composite may be attributed to the excess interfacial friction due to insufficient interphase thickness to accommodate adequate interfacial sliding.[6, 10] It is noted that the non-linear strain is slightly enlarged in the irradiated HNLS, multilayer interphase composite. The SA3 composites exhibited similar tensile behavior regardless of interphase thickness (50 or 150 nm), fiber diameter, and irradiation condition. The strain to failure for these composites appeared to be in a 0.2 – 0.3% range, typical to SA3 fiber, CVI SiC matrix composites.

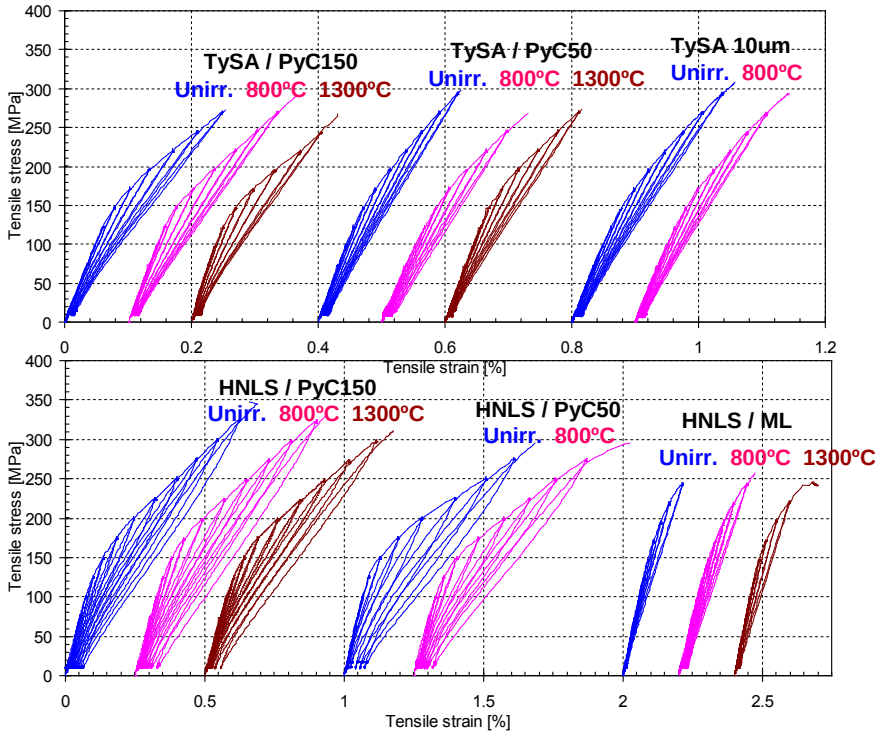

Fig. 1: Representative stress-strain curves recorded during tensile tests of six different SiC/SiC composites in unirradiated and irradiated conditions.

The results of sonic modulus and tensile properties determination are graphically summarized in Fig. 2. The decrease in elastic modulus, which is expected to occur to a very slight extent at these irradiation temperatures, either by vibration or tensile test appeared to be within the range of data scatter. Either PLS or ultimate tensile stress (UTS) did not undergo obvious change. However, the UTS of the HNLS and the 10 micron diameter SA3 composites may have degraded slightly.

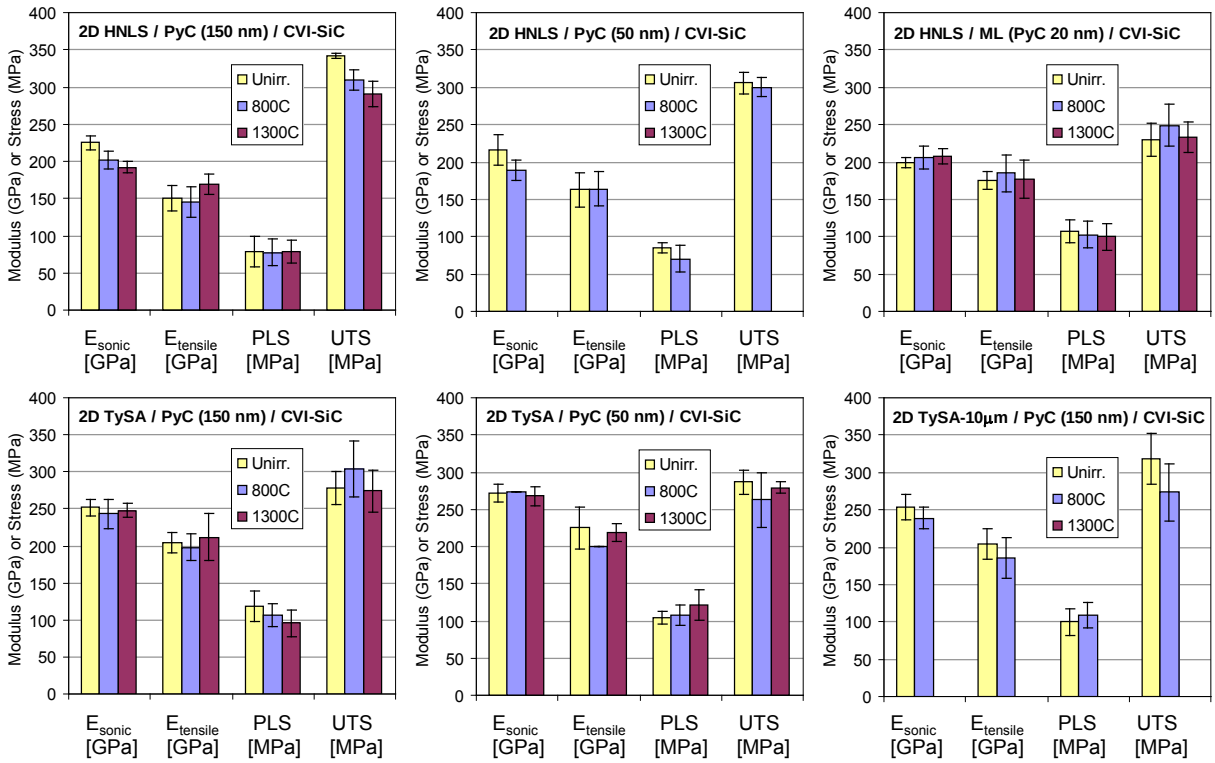

Fig. 2: Summary of the tensile properties and sonic modulus values in unirradiated and irradiated conditions. E_{sonic} and $E_{tensile}$ denote Young's moduli determined by sonic resonance and tensile tangential fit, respectively. Error bars represent one standard deviations.

Fracture surfaces of the 150 nm PyC interphase composites with HNLS and SA3 fibers are compared in Fig. 3 before and after irradiation. The fractographs reveal relatively long fiber pull-outs for the HNLS composites and much shorter fiber pull-outs for the SA3 composites, both of which do not noticeably change after irradiation at either temperature. Moreover, fracture surfaces of the individual fibers, typically consisting of rather indistinctive fracture mirror and a river pattern, did not show any sign of fiber strength change due to irradiation.

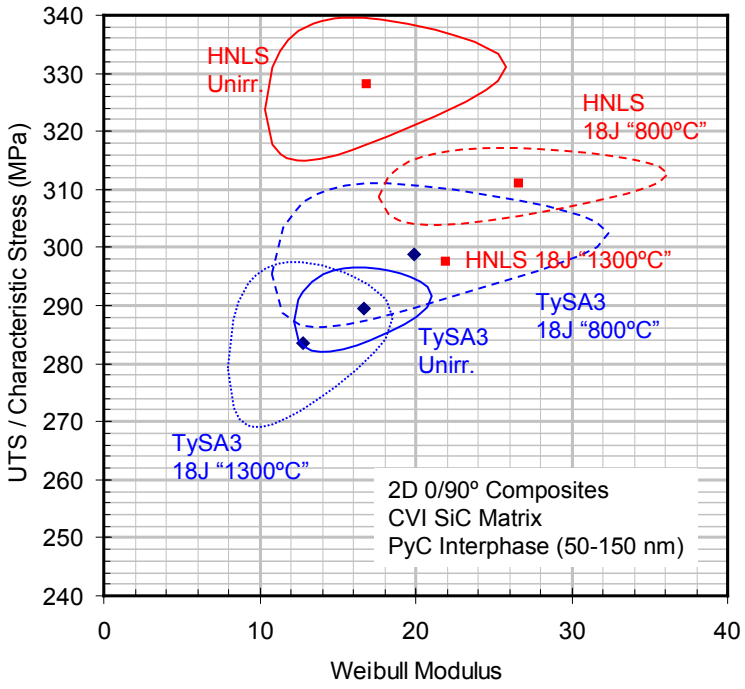

Fig. 3: Fracture surfaces of the 150 nm-thick PyC interphase composites with Hi-Nicalon™ Type-S and Tyranno™-SA3 reinforcements.

Discussion

The present result appeared to be consistent with the general perception that the stoichiometric SiC fiber, CVI SiC matrix composites do not significantly degrade their mechanical properties by irradiation to the intermediate fluence levels (e.g., ~10 dpa) at temperatures below ~800ºC. It also suggested that such trend retains true to irradiation temperature largely exceeding 1000ºC. However, in the previous studies, potential strength modification could not be much discussed because of the very limited statistics in contrast to the inherent scatter of strength of ceramic composites. Here, two-parameter Weibull statistics are examined for the UTS of both HNLS and SA3 composites. Because the tensile properties appeared very similar for the nominally 150 nm and 50 nm PyC interphases, UTS data for both interphases were combined for greater number of data. The plot, shown in Fig. 4 as the 95% confidence parameter bound rings, indicates fairly high Weibull shape parameters of 16 – 17 for the unirradiated condition. Both Weibull parameters were about the same for the two different PyC interphases in either fiber composite, indicating that the combining the different interphase thicknesses did not disturb the statistics. The result indicates that the UTS change of HNLS composites after irradiation at 800ºC may be statistically significant, although the decrease in average characteristic UTS value is only ~5%. On the other hand, the changes in UTS of SA3 composites appear insignificant at both irradiation temperatures. Because the UTS is determined primarily by fiber strength, the result implies that the SA3 fiber is more radiation resistant.

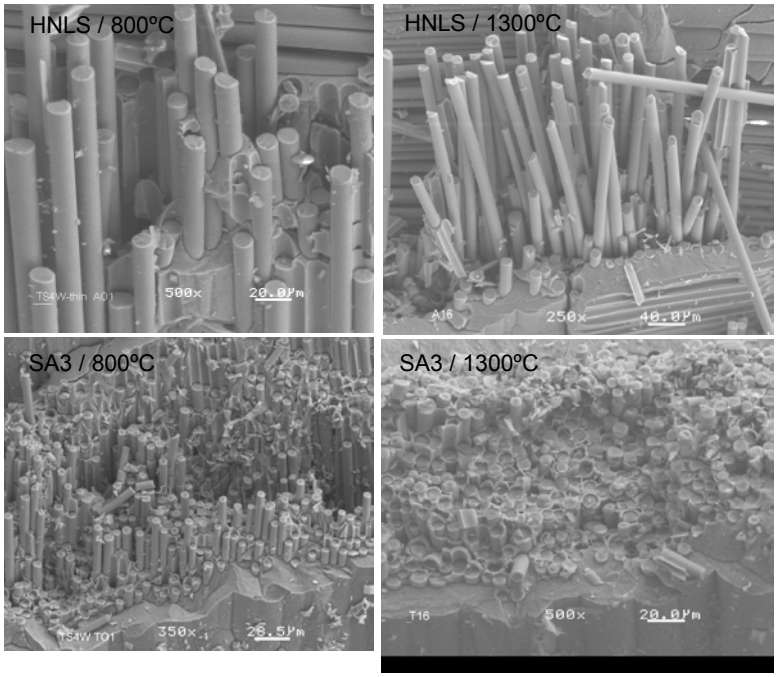

Fig. 4: Weibull statistic parameters for the UTS of 50-150 nm-thick PyC interphase composites in unirradiated and irradiated conditions. The parameters were determined by the maximum likelihood analysis. The rings indicate 95% confidence bounds.

Among six different materials examined in this work, only the HNLS composite with multilayer interphase exhibited the significant premature failure behavior, or the composite fracture far before the matrix crack saturation is achieved. Such erratic behavior has been reported for SiC/SiC composites with very thin interphases, in a more pronounced way in a uni-direction architecture, and is believed to be caused by the excess frictional stress for interfacial sliding.[6, 10] A closer examination of the stress-strain behavior of the HNLS multilayer composite, Fig. 1, reveals the greater extent of non-linear elongation after irradiation. Similar trend has been reported in previous work for a uni-directional composite with nominally the same fiber and interphase.[6] Thus, although the macroscopic modification of tensile properties by neutron irradiation did not appear substantial, there is rather a clear indication that the interfacial sliding property has been altered. Carbon materials are known to degrade mechanical properties by accumulation of displacement damage in excess of certain so-called “turn around” fluence levels and the degradation gets noticeably accelerated at higher irradiation temperatures. Therefore, in order to have the optimum interfacial properties retained during high fluence irradiation, the preferred interphase thickness may be smaller for composites for radiation services than for other applications so that stronger post-irradiation interfacial sliding stress may be achieved.

The PLS approximately correspond to the matrix cracking stress, or the composite stress at which at least one transverse matrix crack is developed and starts to open. Therefore, the PLS will likely give design stress guidelines for applications involving prolonged service durations. Interestingly, there have been conflicting reports with regard to the effect of neutron irradiation on the PLS; slight but significant reduction in the PLS has been reported in some works whereas no significant change has been reported in others.[4-6, 11, 12]

The matrix cracking stress is generally influenced by the residual thermal stress in a significant manner.[13] The near-stoichiometric SiC fibers reportedly possess the coefficient of linear thermal expansion (CTE) slightly greater than that of vapor-deposited high purity SiC. For example, the manufacturer-claimed CTE of HNLS fiber is 5.1×10^{-6} K^{-1} (RT-500ºC) as compared to 3.8×10^{-6} K^{-1} for CVD SiC in the same temperature range, giving substantial axial compressive and tensile residual stresses to matrices and fibers, respectively, upon cooling from the matrix infiltration temperature. The CTE misfit stresses, estimated from the regression analysis of the tensile reloading segments, appeared to be ~40 MPa for all the SA3 and multilayer interphase HNLS composites and ~60 MPa for PyC interphase HNLS composites in an unirradiated condition. The greater misfit stresses in the PyC interphase HNLS composites are considered to be reflecting the lesser extent of matrix infiltration. In the irradiated materials, these misfit stresses appeared to have significantly reduced, as shown if Fig. 5. Potential reasons for the reduced misfit stress include irradiation creep and modification of CTE of the constituents. With the irradiation temperature of ~1300ºC, which is close to or even higher than the matrix processing temperature, irradiation creep does not explain the misfit stress reduction. It is not clear whether the mechanism of CTE modification is structural modification of the impure fibers or radiation defect accumulation in SiC crystals.

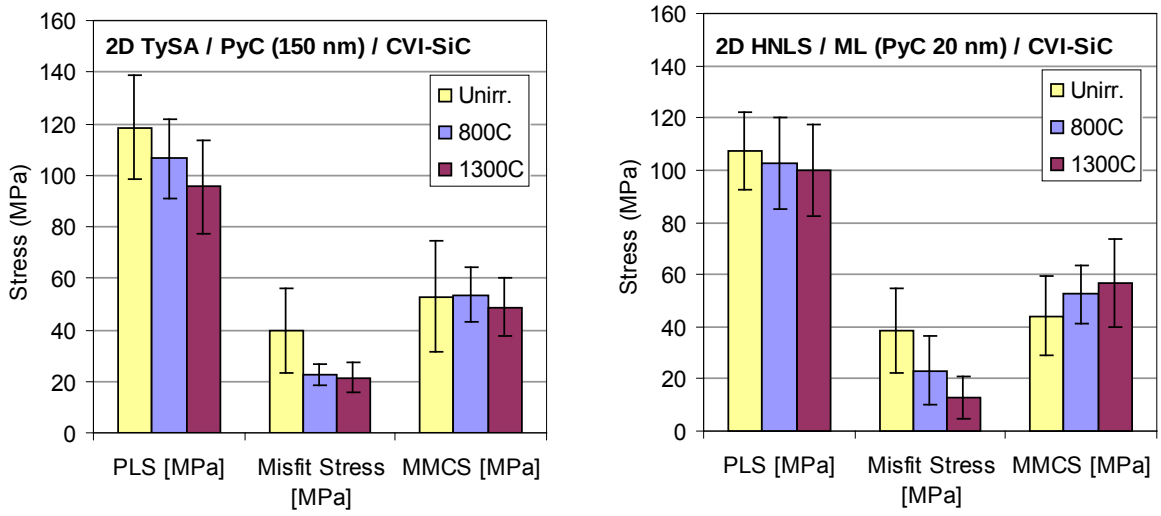

Fig. 5: Misfit stress and true “mini-matrix” cracking stress (MMCS, see text for explanation) estimated for selected composites based on the tensile reloading regression analysis.

Under an in-plane tensile loading to 0/90º 2D composites, cracks are believed to initiate typically within the matrix encapsulating the 90º fiber tows (90º “mini-matrix”). Tensile stress in such elements, σ_{mmx}, can be described by:

$$\sigma_{mmx} = \frac{\sigma_c + \sigma_{th}}{E_c}\left(\frac{E_c - f_{mc}E_{mc}}{1 - f_{mc}}\right) \qquad (1)$$

where σ_c = composite stress, σ_{th} = residual stress, E_c = composite modulus, f_{mc} and E_{mc} = volume fraction and modulus of 0º mini-composite elements, respectively.[14] The result of misfit stress and mini-matrix cracking stress analyses, provided in Fig. 5, indeed indicates that the detrimental effect of neutron irradiation on the true matrix cracking stress is inadmissible. Similar analysis on the PyC interphase HNLS composites provided only invalid result due to the poor matrix infiltration.

Conclusions

The effect of neutron irradiation on in-plane tensile properties of near-stoichiometric SiC fiber, CVI SiC matrix composites was determined. The following outstanding results were obtained.

1) Only insignificant and/or very minor modification to the tensile strength were admitted following irradiation to ~6 dpa nominally at 800ºC and 1300ºC.

2) Two-parameter Weibull statistics analysis revealed no significant irradiation effect on strength of the SA3 fiber composites, and significant yet minor strength degradation for the HNLS fiber composites.

3) 50 – 150 nm appeared to be within the optimum PyC interphase thickness range for both fiber types in terms of tensile properties. However, the optimum interphase thickness range may be altered with high fluence irradiation at high temperatures.

4) CTE misfit stresses present in the unirradiated samples were significantly reduced after irradiation. Irradiation-induced CTE modification is the likely reason.

5) True matrix cracking stress estimated from the PLS and misfit stress did not appear to degrade by neutron irradiation.

References

1. Y. Katoh, L.L. Snead, C.H. Henager, A. Hasegawa, A. Kohyama, B. Riccardi, and J.B.J. Hegeman, *Current status and critical issues for development of SiC composites for fusion applications.* Journal of Nuclear Materials, 2007. **367-370**: p. 659-671.
2. T. Nozawa, T. Hinoki, A. Hasegawa, A. Kohyama, Y. Katoh, L.L. Snead, C.H. Henager, and J.B.J. Hegeman, *Recent advances and issues in development of silicon carbide composites for fusion applications.* Journal of Nuclear Materials, 2009. **386-388**: p. 622-627.
3. L.L. Snead, Y. Katoh, W.E. Windes, R.J. Shinavski, and T.D. Burchell. *Ceramic composites for near term reactor application*. in *The 4th International Topical Meeting on High Temperature Reactor Technology (HTR-2008)*. 2008. Washington, D.C.: ASME.
4. T. Nozawa, K. Ozawa, S. Kondo, T. Hinoki, Y. Katoh, L.L. Snead, and A. Kohyama, *Tensile, Flexural, and Shear Properties of Neutron Irradiated SiC/SiC Composites with Different Fiber-Matrix Interfaces.* Journal of ASTM International, 2005. **2**(3): p. 12884-1-13.
5. T. Hinoki, L.L. Snead, Y. Katoh, A. Hasegawa, T. Nozawa, and A. Kohyama, *The effect of high dose/high temperature irradiation on high purity fibers and their silicon carbide composites.* Journal of Nuclear Materials, 2002. **307**: p. 1157-1162.
6. Y. Katoh, T. Nozawa, L.L. Snead, and T. Hinoki, *Effect of Neutron Irradiation on Tensile Properties of Unidirectional Silicon Carbide Composites.* Journal of Nuclear Materials, 2007. **367-370**: p. 774-779.
7. L.L. Snead, Y. Katoh, A. Kohyama, J.L. Bailey, N.L. Vaughn, and R.A. Lowden, *Evaluation of neutron irradiated near-stoichiometric silicon carbide fiber composites.* Journal of Nuclear Materials, 2000. **283-287**: p. 551-555.
8. G.A. Newsome, L.L. Snead, T. Hinoki, Y. Katoh, and D. Peters, *Evaluation of neutron irradiated silicon carbide and silicon carbide composites.* Journal of Nuclear Materials, 2007. **371**: p. 76-89.
9. Y. Katoh, K. Ozawa, L.L. Snead, T. Hinoki, Y.B. Choi, and A. Hasegawa, ***Mechanical characterization of silicon carbide composites for HFIR-18J experiment in unirradiated condition*** in *Fusion Materials Semi-annual Progress Report*. 2008, Oak Ridge National Laboratory.
10. C. Sauder, A. Brusson, and J. Lamon, *INFLUENCE OF INTERFACE CHARACTERISTICS ON THE MECHANICAL PROPERTIES OF Hi-NICALONS AND SA3 FIBER REINFORCED SiC/SiC*

MINICOMPOSITES. International Journal of Applied Ceramic Technology, to be published.
11. T. Nozawa, T. Hinoki, Y. Katoh, and A. Kohyama, *Effects of fibers and fabrication processes on mechanical properties of neutron irradiated SiC/SiC composites.* Journal of Nuclear Materials, 2002. **307**: p. 1173-1177.
12. T. Nozawa, T. Hinoki, L.L. Snead, Y. Katoh, and A. Kohyama, *Neutron irradiation effects on high-crystallinity and near-stoichiometry SiC fibers and their composites.* Journal of Nuclear Materials, 2004. **329-33**: p. 544-548.
13. E. Vagaggini, J.-M. Domergue, and A.G. Evans, *Relationships between hysteresis measurements and the constituent properties of ceramic matrix composites: I, theory.* Journal of the American Ceramic Society, 1995. **78**: p. 2709-2720.
14. G.N. Morscher, M. Singh, J.D. Kiser, M. Freedman, and R. Bhatt, *Modeling stress-dependent matrix cracking and stress–strain behavior in 2D woven SiC fiber reinforced CVI SiC composites.* Composites Science and Technology, 2007. **67**: p. 1009-1017.

FLEXURAL TESTS OF 3C-SIC AFTER HIGH TEMPERATURE NEUTRON IRRADIATION ——
S. Kondo, Y. Katoh, and L.L. Snead (Oak Ridge National Laboratory)

OBJECTIVES

This work is intended to the development of miniature equibiaxial flexural test for irradiated ceramics and obtain fracture strength of high purity β-SiC following neutron irradiation at 1100-1500˚C by such a technique.

SUMMARY

The flexure strength of miniature disk specimens were evaluated for both the unirradiated and irradiated CVD SiC by equibiaxial flexural tests developed in this work. The results for the unirradiated specimens indicated no stress magnification at the loading point, which is often concerned in biaxial tests for the disk specimens. The irradiation strength was retained after the irradiation at 1100 and 1300˚C, ~20% of reduction was observed for the samples irradiated at 1500˚C. It is clearly seen that the smooth cleavage of large grains were frequently observed in the sample irradiated at 1500 comparing to specimens irradiated at lower temperatures. A substantially lower population of finer defect clusters such as loops, vacancy, and vacancy clusters may be attributed to the reduction of the strength at the higher irradiation temperatures.

INTRODUCTION

Silicon carbide (SiC) based materials are considered for various applications in fusion reactors due to their high temperature performance, chemical inertness, and low activation [1]. Effect of neutron irradiation at intermediate temperatures on mechanical properties of chemically vapor deposited (CVD) silicon carbide has been extensively studied and it is now generally accepted that the irradiation-induced strengthening of SiC in a temperature range 300-800˚C is true [2]. The observed strengthening is likely attributed to the densely distributed stable point defects and/or nano-sized defect clusters, which are the dominant radiation products in the intermediate temperature regime. However, at higher temperatures where technological interest exists for applications to advanced high temperature blankets, irradiated strength data is very limited for SiC in spite of the anticipated effects of the more progressive microstructural evolution on mechanical properties.

PROGRESS AND STATUS

Experimental

2.1. Test apparatus

Although miniaturized disk specimens have been used for the post-irradiation mechanical tests, the stress concentrations associated with specific loading configurations such as ball-on-ring tests can be a significant problem for most ceramics because the fracture strength greatly depends on the effective loading area/volume and statistical distribution of the potential fracture origins. The equibiaxial flexural test in a ring-on-ring configuration, where a disk specimen on a support ring is loaded with a smaller coaxial loading ring, is often utilized to mitigate the stress concentration issues. For thin, high elastic modulus/strength (E/σ) ratio specimens, the uniform maximum stress occurs within the central region bounded by the loading ring.

In this study, the loading and supporting rings were designed to utilize miniature disk specimens in accordance with ASTM C1499-05 [3] as shown in Fig. 1. The equibiaxial stress is calculated as follows:

$$\sigma_f = \frac{3F}{2\pi h^2}\left[(1-\nu)\frac{D_S^2 - D_L^2}{2D^2} + (1+\nu)\ln\frac{D_S}{D_L}\right] \qquad (1)$$

, where F [N] is the applied load, h [mm] is the specimen thickness, D_S [mm] is the supporting ring diameter, D_L [mm] is the loading ring diameter, D [mm] is the sample diameter, and ν is Poisson's ratio (Test Method ASTM C1259). Both the outer diameters of loading and supporting fixtures are designed to be same as the specimen diameter for ease of alignment. No compliant layer, which is sometimes used to eliminate a stress concentration and frictional stress at the rings, were used for the present study. Alternatively, industrial lubricant was applied to the ring tips. The displacement rate was set at 0.1 mm/min. The crack patterns and fracture surfaces were examined following the bend tests.

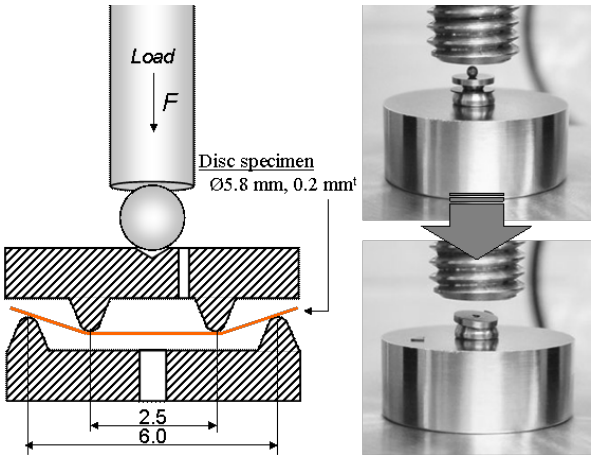

Fig. 1 Schematic and photos of concentric ring-on-ring test apparatus.

2.2. Experimental procedure

The material used for this work was poly crystalline β-SiC which was produced by chemically vapor deposition by Rohm and Haas Advanced Materials (Woburn, Massachusetts, USA) [4]. The CVD material is extremely pure, with typical total impurity concentration of less than 5 wppm. The material is typically free of micro cracks or other large flaws, but atomic layer stacking faults on the {111} planes are common. There is no porosity in CVD SiC, and the material is generally considered to be of theoretical density (approximately 3.21 g/cm^3).

For the unirradiated case, 23 specimens, which were machined and polished in the same manner as described below for the irradiated samples, were tested. In addition to the unirradiated specimens, specimens irradiated in the High Flux Isotope Reactor at Oak Ridge National Laboratory were tested. The fluence for the specimens studied here ranged from 5.1×10^{25} to 9.7×10^{25} n/m^2 (E>0.1MeV). Irradiation temperatures were 1100, 1300, and 1500, which were estimated by post -irradiation viewing of melt wires inserted in both ends of each sub-capsule. Specimens of 5.8 mm diameter with 3.2mm thickness were sliced into thin disks and lap finished for both surfaces with 3 μm diamond suspension aiming to ~200 μm thickness. A minimum of 10 specimens tested validly is, normally,

required for the purpose of estimating a mean biaxial flexural strength. For the estimation of the Weibull parameters, a minimum of 30 specimens validly tested is recommended. However, only 5 to 6 specimens were tested in the case of post-irradiation experiment. Therefore, the Weibull statistical analysis was not conducted for the irradiated specimens.

Table 1 Irradiation conditions and results of the ring on ring tests.

Sample ID	Irradiation Temperature	Irradiation Fluence	Mean Thickness	Mean Equibiaxial Stress	Std. Dev.	% Change	Weibull Modulus	Number of samples
	[degree C]	[dpa]	[mm]	[MPa]	[MPa]	[%]		
unirrad.	-	0	0.202	357	87	-	5.0	23
m14	1100	7.0	0.195	329	100	-7.8	-	6
m56	1300	5.1	0.205	345	61	-3.4	-	5
m20	1500	9.7	0.198	279	42	-22	-	5

Results and discussion

3.1. Unirradiated SiC

The equibiaxial stresses are plotted as a function of specimen thickness in Fig. 2, where the mean flexural stress is 352 MPa (Weibull mean; 357 MPa) and the standard deviation is 73 MPa. The lowest flexural stress of 254 MPa was obtained for the specimen with 204 μm in thickness and the highest of 573 MPa was obtained for the specimen with 208 μm thickness. The strength seems not to depend on the sample thickness ranging 155-246 μm. The highly scattered data points were generally found in samples showed relatively higher strength probably due to the low population of the effective surface flaws as discussed below. Although the edges of some specimens were slightly chipped, the edge chip seemed not to affect the flexural strength in the present study.

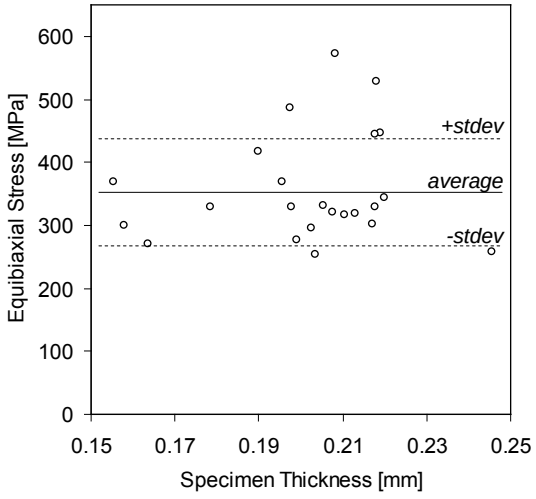

Fig. 2 Equibiaxial strength of unirradiated CVD SiC.

The failure strength of β-SiC have been well reviewed in [2], where the data points were mostly obtained by uniaxial or ring-compression tests and varied from 200 to over 3100 MPa. Such a large variation is due primarily to the specimen size effect, because the strength at the inner weakest flaw determines the overall strength of the brittle materials [5]. Byun et al., however, found that the failure strength of the tubular brittle specimens under diametrical loading can be determined by the effective

surface area rather than the volume [6]. Therefore, the strength obtained in the present work was depended on the surface conditions on the tension side.

In our preliminary finite-element (FE) analysis, stress magnification at the loading point was noted for a sample with 50 μm in thickness due to the deviation from a linear load and displacement relationship as shown in Fig. 3. On the other hand, uniform stress distribution within the loading ring was theoretically demonstrated for samples with t>100 μm. The likely thickness independent fracture strength as seen in Fig. 2 indicates that the samples (t~200 μm) are thick enough to avoid the stress magnification. Although, many factors, such as the effective flaw populations subject to stress, may influence the relation between equibiaxial and uniaxial strength of ceramics and should be considered, the simple and rapid procedure of the ring-on-ring test may be favored for the study on irradiation effects on the mechanical properties of SiC.

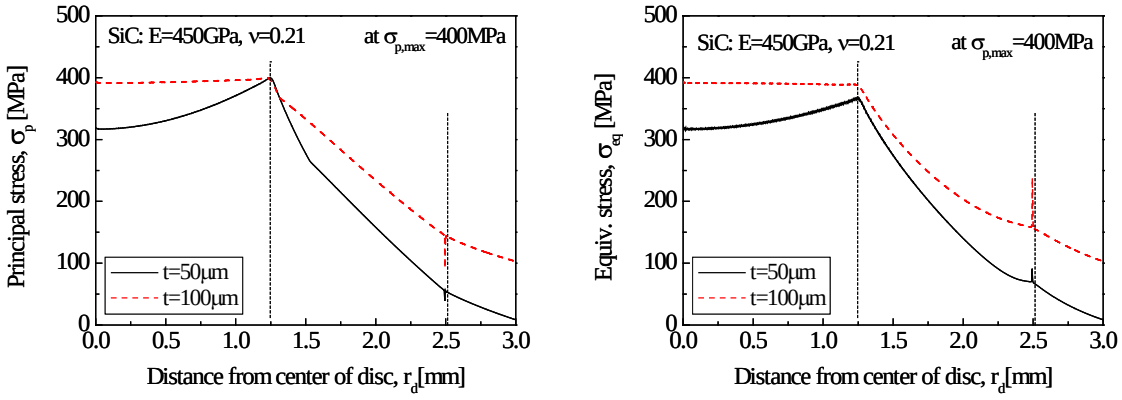

Fig. 3 Stress distributions estimated by FEM for (a) principal and (b) equivalent stresses.

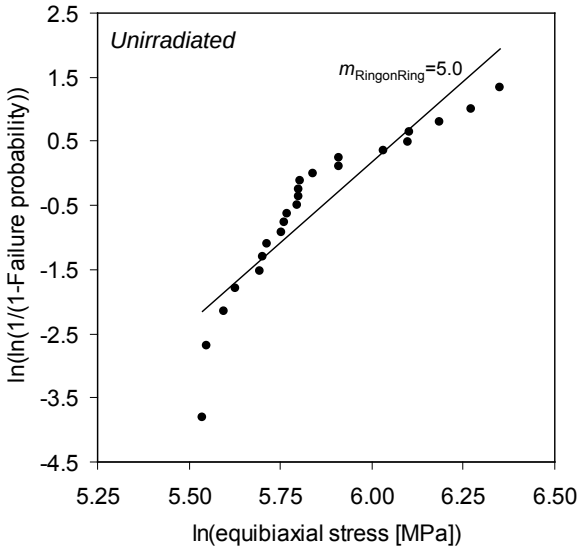

Fig. 4 Weibull plots of flexural strength of unirradiated CVD SiC.

In Fig. 4, Weibull stastical plots of the flexural strength of unirradiated samples are shown. The Weibull modulus of SiC at room-temperature is reported to be widely ranged from 2 to 12, depending on the condition of the SiC material and method of tests [2]. The high Weibull modulus (m=7–11) was often measured by the flexural and tensile tests, while the lower values (m=3–9) were obtained in the ring compression test. Cockeram [7] assumed that the flaw distributions were quite different between a flexural bar and a small tubular (ring) specimen. The lower m values obtained by the ring compression tests were therefore considered primarily as a significant surface roughness rather than some other possibility such as the irregularity of the ring shape. The obtained Weibull modulus of 5.0 for the present study is within the data band of ring compression tests and is below the data band of tensile test results.

Fractographic examination of the test specimens is recommended to determine the location of test specimen fracture [8]. Typical examples of the fracture patterns at the tensioned surface are shown in Fig. 5, where the possible contact lines of the supporting and loading rings are indicated as dotted circles. The fracture initiated likely in the area bounded by loading ring or just inside the loading ring in all samples, though the difference of the complexity of the final fracture patterns were observed depending on the strength. For high strength case as Fig. 5 (a), primary crack plane is located near center line of the circular sample and significant flaw branching were observed. For intermediate strength case as Fig. 5 (b), likely crack origin was located generally near the center. The successful avoidance of the stress magnification at the loading ring as stated above was confirmed for these cases. For low strength case as Fig. 5 (c), however, the primary crack was initiated just inside the loading ring, and samples were divided into only 4-5 pieces. This indicates that the results showing lower strength might be attributed to the stress magnification near the loading ring in addition to the being of relatively large surface flaws. The misalignment of the test fixtures and the sample may be suspected as one of the primary cause of the stress magnification.

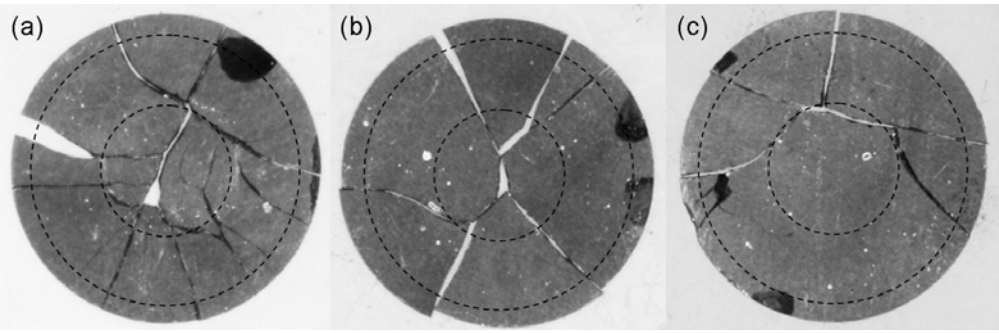

Fig. 5 Typical fracture patterns at the tensioned surface of unirradiated specimens showed a flexural strength of; (a) σ_f = 573 MPa,(b) σ_f = 321 MPa, and (c) σ_f = 270 MPa.

3.2. Irradiated SiC

The irradiated flexural strengths normalized to unirradiated values are plotted with neutron data reported previously as a function of irradiation temperature in Fig. 6. Since the strength of irradiated SiC is strongly dependent on the form of the material tested, results except for pyrolytic β-SiC are excluded from the chart. For all the cases except for the present results, the values are for Weibull's mean with error bars indicating ±1 Weibull's standard deviation [9-12]. The irradiation-induced strengthening is statistically observed at 300-800˚C. Meanwhile, the flexural strength was almost same as the unirradiated values at 1100 and 1300˚C and ~20% decreased at 1500˚C. The formation of strength peak is likely attributed to the reduction of the Young's modulus accompanied by lattice dilation due to the distribution of dense point defects and/or tiny interstitial clusters [13] which are

generally observed in irradiated SiC at 200-800˚C [14]. The increase in effective fracture energy is probably due primary to the modification of the local internal stress at the dense defect clusters [15], though the fracture energy increase may be attributable to the combined effect of a number of mechanisms operating simultaneously. On the other hand, the damage microstructure above ~1000˚C was characterized by much larger Frank faulted loops coarsely distributed [16]. Therefore, the significant reduction in the population of irradiation-induced finer defects may prohibit the strengthening at >1000˚C. The microstructural development in irradiated 3C-SiC is summarized in Fig. 7.

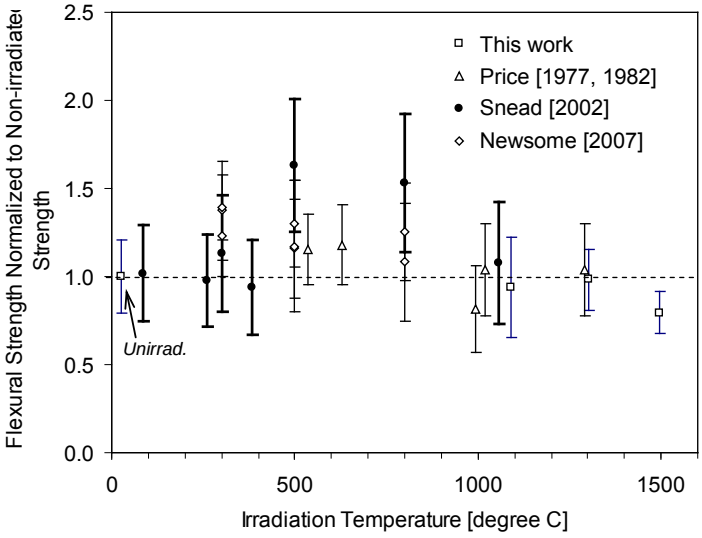

Fig. 6 Effect of irradiation temperature on normalized flexural strength of CVD SiC.

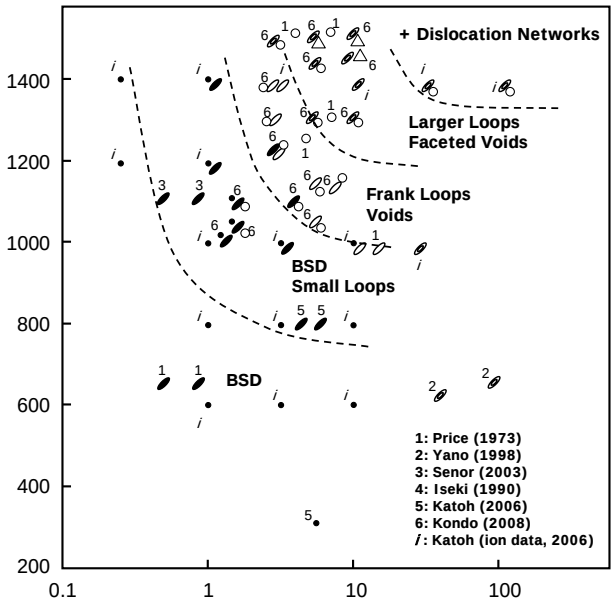

Fig. 7 Microstructural defect map in irradiated 3C SiC.

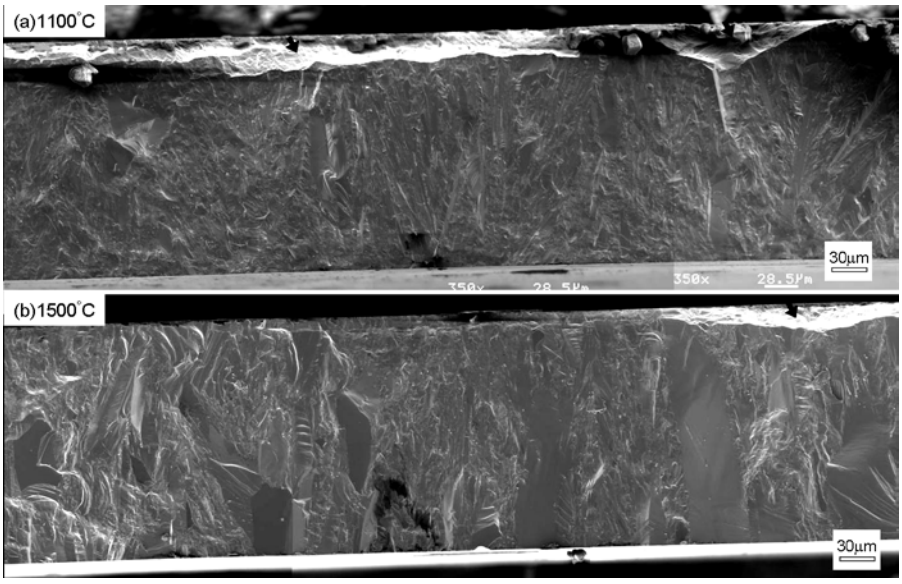

Fig. 8 Scanning electron microscope images of the fracture surface of the samples irradiated at (a) 1100°C, and (b) 1500°C.

Fracture surfaces of a couple of samples tested were examined for each irradiation condition by scanning electron microscopy as typically shown in Fig. 8; irradiation temperature of 1100°C for (a), and 1500°C for (b), where tensioned surfaces face upward of the images. In each case, fracture likely initiated at relatively large surface flaws indicated by black arrows. It is clearly seen that the transgranular smooth cleavage of large grains were frequently observed in the samples irradiated at 1500°C as shown in Fig. 8 (b). The frequency of cleavage has been reported to be reduced by neutron irradiation at 300-800°C [13]. It was stated in [13] that the irradiation might increase the cleavage energy by the irradiation toughening at the irradiation temperatures range. At °C; however, this mechanism may not be applicable because of the absence of the toughening. Retaining of the unirradiated fracture toughness and Young's modulus at >1100°C reported by micro Vickers and nano-indentation techniques, respectively, supports this. It suggests that the void-crack interaction, which has been observed by transmission electron microscope [17], also very limited in irradiated SiC. Furthermore, the array of voids with {111} facets, which is preferentially formed at stacking faults, may modify the fracture energy at the cleavage plane observed. Any significant differences of fracture patterns from unirradiated samples were not observed as shown in Fig. 9. It was confirmed that the ring-on-ring configuration may applicable to both the irradiated and unirradiated miniature SiC specimens. However, the sufficient number of samples to statistical analysis is strongly recommended for obtaining clear understanding of the irradiation effects due to the complex fracture mechanisms.

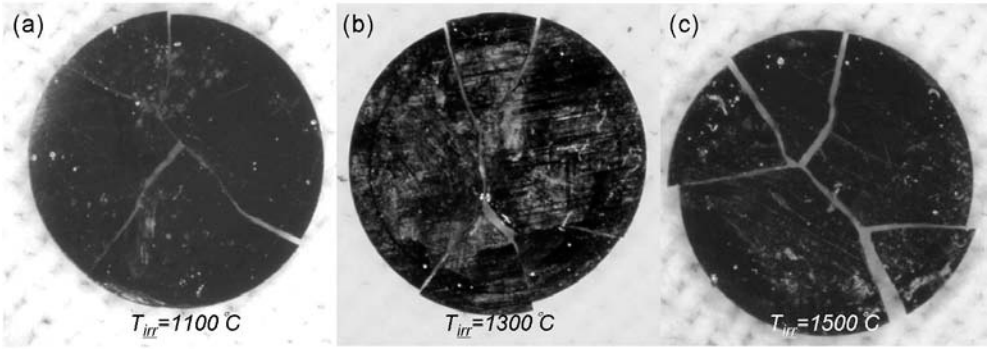

Fig. 9 Typical fracture patterns at the tensioned surface of irradiated specimen; (a) T_{irr}= 1100˚C, σ_f = 314 MPa, (b) T_{irr}= 1300˚C, σ_f = 339 MPa, and (c) T_{irr}= 1500˚C, σ_f = 313 MPa.

References

[1] Y. Katoh, L.L. Snead, Jr., C.H. Henager, A. Hasegawa, A. Kohyama, B. Riccardi, H. Hegeman. J. Nucl. Mater. 367-370 (2007) 659-671.
[2] L.L. Snead, T. Nozawa, Y. Katoh, T.S. Byun, S. Kondo, D.A. Petti, J. Nucl. Mater. 371 (2007) 329-377.
[3] ASTM C 1499-05, Standard Test Method for Monotonic Equibiaxial Flexural Strength of Advanced Ceramics at Ambient Temperature.
[4] Rohm and Haas Co. Ltd. Home page, http://www.cvdmaterials.com/.
[5] Report CEGA-002820, Rev. 1 (July 1993).
[6] T.S. Byun, E. Lara-Curzio, R.A. Lowden, L.L. Snead, Y. Katoh, J. Nucl. Mater. 367-370 (2007) 653-658.
[7] B.V. Cockeram, J. Am. Ceram. Soc. 85 (2002) 603.
[8] ASTM C 1322
[9] R. Price, Nucl. Technol. 35 (1977) 320-336.
[10] R.J. Price and G.R. Hopkins, J. Nucl. Mater. 108&109 (1982), 732-738.
[11] L.L. Snead, T. Hinoki, Y. Katoh, Report DOE/ER-0313/33 (2002).
[12] G. Newsome, L.L. Snead, T. Hinoki, Y. Katoh, D. Peters, J. Nucl. Mater. 371 (2007) 76-89.
[13] Y. Katoh, L.L. Snead, J. ASTM Intl. Paper ID JAI12377.
[14] Y. Katoh, H. Kishimoto, A. Kohyama, J. Nucl. Mater. 307-311 (2002) 1221.
[15] Y. Katoh, T. Hinoki, A. Kohyama, T. Shibayama, and H. Takahashi, Ceram. Eng. Sci. Proc. 20 (1999) 325-332.
[16] S. Kondo, *et al*., in proceedings of ICFRM-13, J. Nucl. Mater. (2008).
[17] F.W. Clinard, Jr., G.F. Hurley, R.A. Youngman, and L.W. Hobbs, J. Nucl. Mater. 133&134 (1985) 701-704.

EFFECT OF NEUTRON IRRADIATION ON FRACTURE RESISTANCE OF ADVANCED SIC/SIC COMPOSITES—K. Ozawa, Y. Katoh, L.L. Snead (Oak Ridge National Laboratory), T. Nozawa (Japan Atomic Energy Agency)

OBJECTIVE

The objective of this work is to determine the neutron irradiation effects on fracture toughness of advanced nuclear grade SiC/SiC composites reinforced with advanced silicon carbide fibers.

SUMMARY

In order to identify the neutron irradiation effects on fracture resistance of advanced SiC/SiC composites, unloading-reloading single edge notched bend tests were conducted and an analytical model based on non-linear fracture mechanics was applied. As a result of the analysis, energy release rate contributed by macro-crack initiation of 3.1 kJ/m^2 for both unirradiated and irradiated advanced SiC/SiC composites (Hi-Nicalon Type-S (0°/90° plain woven) / multilayer / chemically vapor infiltration) is estimated. This result indicates no significant degradation in fracture resistance after neutron irradiation to 5.9 $\times$ 10^{25} n/m^2 at 800°C.

PROGRESS AND STATUS

Introduction

A silicon carbide fiber reinforced silicon carbide matrix (SiC/SiC) composite is an attractive candidate material for structural and functional components in fusion energy systems due to its good radiation stability coupled with inherently low induced radioactivity and after-heat [1, 2].

The focus on irradiation study of SiC/SiC composites in the past few decades has been mainly 'material screening,' but this phase is coming to a close. In recent years, multidirectional, statistical evaluation of mechanical properties using the "reference nuclear grade" SiC/SiC composites has been studied. Nuclear grade materials are generally defined as containing stoichiometric SiC fibers infiltrated with a matrix by chemically vapor infiltration (CVI), or the class of nano-infiltration and transient eutectic-phase (NITE) ceramics.

For the new class of nuclear grade composites, determining fracture resistance is one of the most important issues to be investigated. However, this is quite difficult because composites consist of several constituents and hence the fracture toughness of composites with non-uniform properties cannot be determined by simply applying a compliance method based on linear elastic fracture mechanics (LEFM). For example, Droillard *et al.* extended LEFM for composites using a two-step approach, in which the fracture behavior was subject to the combination of two parallel ideal composite systems [3]. In the current study, we try to apply non-linear fracture mechanics, based on actual crack increment measurements. While there has been a vigorous effort to study the irradiation effects in the SiC/SiC composite system [4-8], there are no published result on the effects of irradiation on fracture toughness. It is noted that an abstract on the subject, utilizing Hi-Nicalon™ Type-S fiber reinforced SiC matrix composites after neutron irradiation to 4.3 $\times$10^{24} n/m^2 at 40ºC, was located [9].

The main objective of this study is to determine the neutron irradiation effects on fracture toughness of advanced nuclear grade SiC/SiC composites. For this purpose, unloading-reloading tests and direct observations of crack propagation were conducted. Additionally a new analysis based on energy balance for composites' fracture resistance has been applied.

Experimental Procedure

Description of the material used is listed in Table 1. In this study, Tyranno™-SA3 or Hi-Nicalon™ Type-S

2D fabric-reinforced, chemically vapor infiltration (CVI) SiC matrix composites with 50 and 150 nm-thick pyrolytic carbon (PyC) or PyC/SiC multilayer interphase were prepared. The specimens were machined to miniature pre-notched rectangular beams for in-plane mode-I fracture toughness evaluation. Figure 1 is a drawing of the single edge notched bend (SENB) specimen. These miniature notched specimens were used because of the limitation of irradiation capsule volume. Three tests can be conducted with one specimen. The size effects on fracture resistance of advanced SiC/SiC composites are discussed elsewhere [10, 11], and notch insensitivity was demonstrated. Test coupons including an artificial notch were machined from the composite plate using a diamond saw. The radius of the notch root was approximately 150 μm. It is noted that the notch depth to width ratio was fixed for all specimens (a/W= 0.50). One side of the specimen surface was polished with 1 μm diamond film to aid in crack extension observation. Detailed information about the material fabrication and characterization before/after neutron irradiation is given elsewhere [12, 13].

Neutron irradiation was in the high flux isotope reactor (HFIR) at the Oak Ridge National Laboratory. The peak neutron fluence was ~5.9×10^{25} n/m^2 (E>0.1MeV), while the nominal irradiation temperature was ~800°C (HFIR-18J). An equivalence of one displacement per atom (dpa) = 1×10^{25} n/m^2 (E > 0.1 MeV) is assumed for these irradiations.

The SENB tests were conducted at room-temperature using an electromechanical testing machine (Insight 10, MTS Systems Co.) with a load capacity of 10 kN with ±0.26 % precision. Test specimens were loaded using a three-point bend fixture with a support span of 16 mm under a constant crosshead displacement rate of 0.05 mm/min. Crack opening displacement (COD) was measured by a clip-on gauge attached to a pair of aluminum tabs. The unloading-reloading sequences were applied to evaluate the damage accumulation behavior during testing. After each loading-unloading cycle, the test specimen was removed from the test machine in order to make replica images. Acetobutyrate (Tacphan) replicating sheets with a thickness of 100μm were used. Replicas at each damage level were observed by conventional optical microscopy.

Results and Discussion

Typical load-COD curves of advanced SiC/SiC composites before/after neutron irradiation are reproduced in Fig. 2. As shown in Fig. 2 (b), (c) and (d), the composites reinforced with Hi-Nicalon Type-S (A, E and M) exhibited typical quasi-ductility. In Fig. 2 (c) and (d), the change in crack length is also plotted from the microscopic measurements on the replica films. As an example, the optical micrographs of the replica images for the M7C specimen were shown in Fig. 3. According to this result, the fracture behavior consists of three stages as follows: [i] deformation induced not by macro-crack but micro-crack, [ii] linear increase of macro-crack, and [iii] crack branching and load transfer by friction at the fiber/matrix interface and fiber fracture (Fig. 2 (c) and (d)). In contrast to the Hi-Nicalon Type-S behavior, the composites reinforced with Tyranno-SA3 fiber (samples T, X and F) exhibited relatively low quasi-ductility. This is primarily attributed to very high interfacial strength caused by the thin interphase and large fiber roughness, which results in rapid crack extension. No significant change in the load-COD curves following neutron irradiation are observed for either composite type. This is in agreement with the result of tensile property evaluations [13].

The test results apparently show quasi-ductility of composites with F/M interphase, i.e., energy consumption during irreversible damage accumulation beyond matrix cracking. Therefore, considering separately the contributions from irreversible energies such as interfacial friction, thermal-residual strain energy, and fiber fracture becomes a key issue. Because of this quasi-ductility, using an analytical model based on non-linear fracture mechanics [14, 15] is reasonable. Hence, the analytical method developed by Nozawa *et al.* [10, 11] has been applied. In this model, the total work during the notched specimen test (w) is defined in Fig. 4 as:

$$w = U_e + U_{fr} + U_r + \Gamma_{total} \quad (1)$$

, where U_e is elastic energy, U_{fr} friction energy at the interface, U_r the residual strain energy, and Γ_{total} the crack surface formation energy. It is noted that the crack surface formation energy includes both micro- and macro-crack-forming energies. Then, the fracture resistance (G_{total}) can be written as:

$$G_{total} = \frac{\partial \Gamma_{total}}{t \partial a} = \frac{1}{t} \frac{\partial \Gamma_{total}}{\partial x} \frac{\partial x}{\partial a} \tag{2}$$

with a being the crack length, t the specimen thickness, and x the crack opening displacement.

Following the definition in Fig. 4, the crack surface formation energy of the M composite before/after irradiation was plotted as a function of crack opening displacement in Fig. 5. From Fig. 5, it is apparent that the crack surface formation energy rapidly increases with damage accumulation. Of particular note is that the crack surface formation energy seems proportional to the crack opening displacement in the stage [ii]. Combining the stage [ii] data of the crack length change in Fig. 2 (c), (d) and the crack surface formation energy change in Fig. 5, apparent fracture resistances of ~4.22 kJ/m^2 at macro crack initiation for the unirradiated composite and ~4.37 kJ/m^2 for the irradiated composite were obtained using Eq. (2).

However, as depicted above, the fracture resistance defined in Eq. (2) cannot unambiguously distinguish between contributions from micro- and macro-crack formation. In this study, a macro-crack is defined as the main crack that can lead to failure of a composite, and it is assumed that such main crack initiates at the peak load. Micro-cracks are the cracks that do not contribute to the main crack directly and are formed just after the proportional limit, such as the matrix cracks formed along the fiber longitudinal direction. Since the fracture resistance is determined by the main crack extension, it should be evaluated as the contribution of only macro-cracks, not including any contribution of micro-crack accumulation. Figure 4 also gives a schematic illustration for determination of the energy release rate during micro-crack formation from the load-displacement curve. From the figure, micro-crack surface formation energy was empirically obtained as:

$$\Gamma_{micro} \cong \sum_{i=1}^{n} C_i \left(1 - \frac{a}{W}\right)^i \tag{3}$$

, where Γ_{micro}, C_i (i=1,2, …, n), W are the micro-crack surface formation energy, constants, and specimen width, respectively. An energy release rate for micro-crack (G_{micro}) is then defined as follows:

$$G_{micro} \equiv -\frac{\Delta \Gamma_{micro}}{t \Delta a} \cong \frac{1}{Wt} \sum_{i=1}^{n} i C_i \left(1 - \frac{a}{W}\right)^{i-1} \tag{4}$$

Simply applying a linear fit in Eq. (4), we obtained an energy release rate of ~1.25 kJ/m^2 for unirradiated and ~1.11 kJ/m^2 for irradiated tests. Eventually, the actual fracture resistance for macro-crack (G_{macro}) is simply given by $G_{macro} = G_{total} - G_{micro}$. As a result, ~3.1 kJ/m^2 was estimated for both composites, before and after irradiation, indicating no significant degradation for the neutron irradiation conditions studied.

Acknowledgement

The authors would like to thank Ms. A.M. Williams, Mr. L.T. Gibson, Ms. P.S. Tedder, Ms. A.D. Harrison, Ms. S.G. Beck and Mr. L.E. Reid for post-irradiation experiments. Irradiation was carried out in the Department of Energy High Flux Isotope Reactor User Facility. This research was sponsored by the Office of Fusion Energy Sciences, US Department of Energy under contract DE-AC05-00OR22725 with UT-Battelle, LLC. This study was also a part of 'JUPITER-II (currently TITAN)' US Department of Energy/Japanese Ministry of Education, Culture, Sports, Science and Technology (MEXT) collaboration for

fusion material system research.

References

[1] T. Nozawa, T. Hinoki, A. Hasegawa, A. Kohyama, Y. Katoh, L.L. Snead, C.H. Henager Jr, J.B.J. Hegeman, J. Nucl. Mater. 386-388 (2009) 622.
[2] Y. Katoh, L.L. Snead, C.H. Henager Jr, A. Hasegawa, A. Kohyama, B. Riccardi, H. Hegeman, J. Nucl. Mater. 367-370 (2007) 659.
[3] C. Droillard, P. Voisard, C. Heibst, J. Lamon, J. Am. Ceram. Soc. 78 (1995) 1201.
[4] T. Nozawa, Y. Katoh, L.L. Snead, J. Nucl. Mater. 384 (2009) 195.
[5] T. Nozawa, K. Ozawa, S. Kondo, T. Hinoki, Y. Katoh, L.L. Snead, A. Kohyama, J. ASTM Int. 2 (2005) 12884.
[6] K. Ozawa, T. Hinoki, T. Nozawa, Y. Katoh, Y. Maki, S. Kondo, S. Ikeda, A. Kohyama, Mater. Trans. 47 (2006) 207.
[7] K. Ozawa, T. Nozawa, Y. Katoh, T. Hinoki, A. Kohyama, J. Nucl. Mater. 367-370 (2007) 713.
[8] Y. Katoh, T. Nozawa, L.L. Snead, T. Hinoki, J. Nucl. Mater. 367-370 (2007) 774.
[9] G. Vekinis, K. Mergia, G. Xanthopoulou, Abstracts of International Symposium on New Frontier of Advanced Si-Based Ceramics and Composites (2004) 25.
[10] T. Nozawa, T. Hinoki, A. Kohyama, H. Tanigawa, Preprints of the 22nd IAEA Fusion Energy Conference FT/P2 (2008) 17.
[11] T. Nozawa, H. Tanigawa, J.S. Park, A. Kohyama, Ceram. Eng. Sci. Proc. 30 [10] (2009) 65, doi: 10.1002/9780470584002.ch6.
[12] Y. Katoh, K. Ozawa, L.L. Snead, Y.B. Choi, T. Hinoki, A. Hasegawa, Fusion Mater. DOE/ER-0313/45 (2008) 21.
[13] Y. Katoh, T. Hinoki, K. Ozawa, Y.B. Choi, A. Hasegawa, L.L. Snead, in these proceedings (2009).
[14] V. Kostopoulos, Y.P. Markopoulos, Y.Z. Pappas, S.D. Peteves, J. Eur. Ceram. Soc. 18 (1998) 69.
[15] M. Sakai, K. Urashima, M. Inagaki, J. Am. Ceram. Soc. 66 (1983) 868.

Table 1: Materials used in this study.

Name	Initial ID	Density [g/cm^3]	Fiber	Architecture	Interphase	Matrix
TySA-CVI-Ref	T	2.60	Tyranno-SA3	2D P/W [0°/90°]	150nm PyC	CVI
TySA-CVI-TI	X	2.60	Tyranno-SA3	2D P/W [0°/90°]	50nm PyC	CVI
TySA-CVI-TF	F	1.60	Tyranno-SA3	2D P/W [0°/90°]	150nm PyC	CVI
HNLS-CVI-Ref	A	2.50	Hi-Nicalon Type-S	2D P/W [0°/90°]	150nm PyC	CVI
HNLS-CVI-TI	E	2.50	Hi-Nicalon Type S	2D P/W [0°/90°]	50nm PyC	CVI
HNLS-CVI-ML	M	2.50	Hi-Nicalon Type S	2D P/W [0°/90°]	ML	CVI

Note: P/W; plain-woven, UD; uni-directional, PyC; pyrolytic carbon, ML; multi-layered, CVI; chemically vapor infiltration.

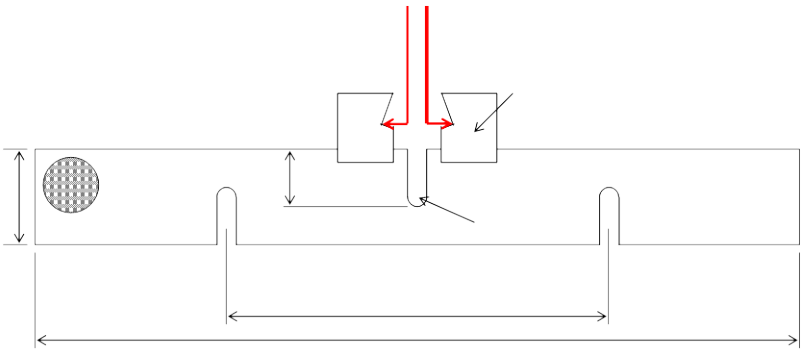

Fig. 1: Drawing of a miniaturized SENB specimen used in this study.

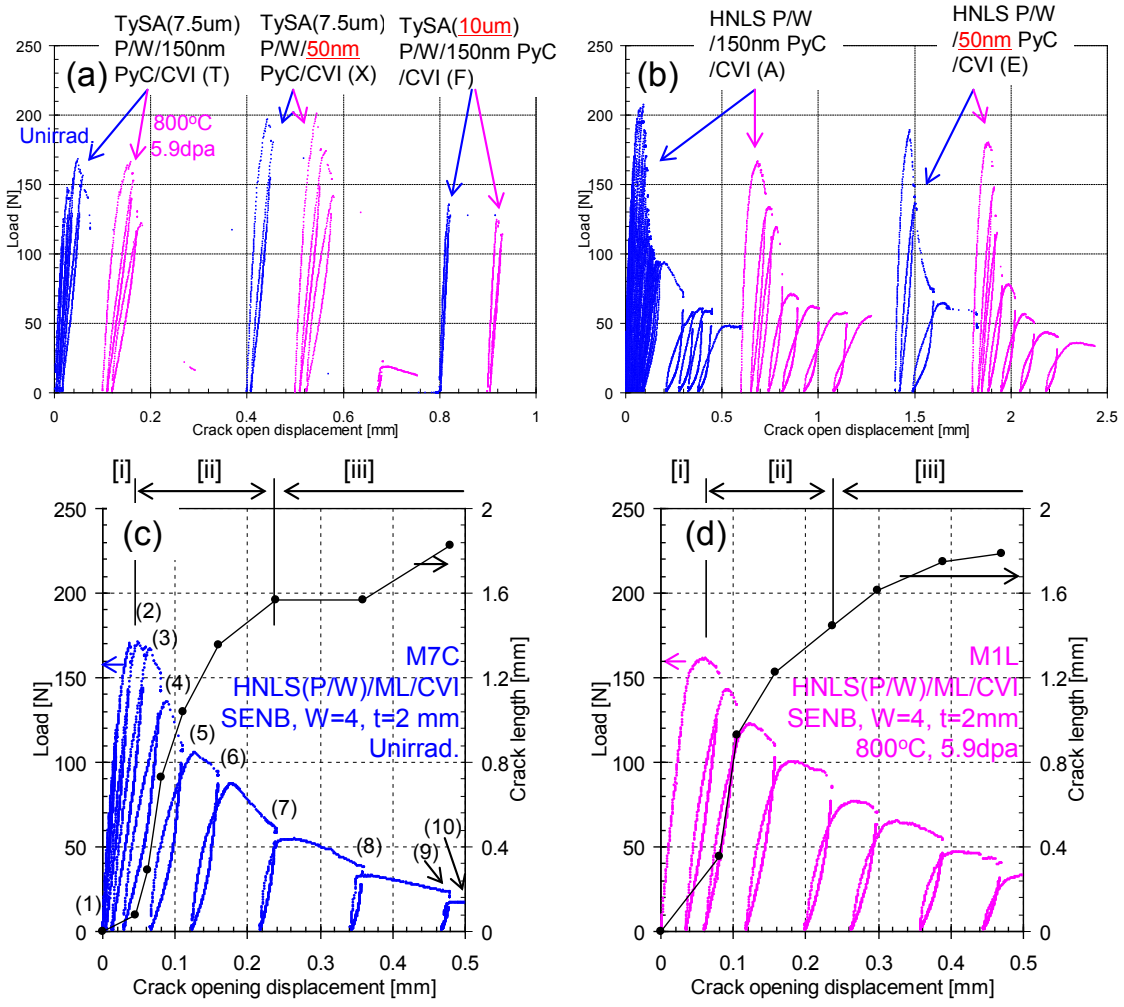

Fig. 2: Load-crack opening displacement curves. (a) TySA-CVI-Ref, -TI and -TF, (b) HNLS-CVI-Ref and -TI, (c) unirradiated HNLS-CVI-ML, and (d) irradiated HNLS-CVI-ML to 5.9dpa at 800°C.

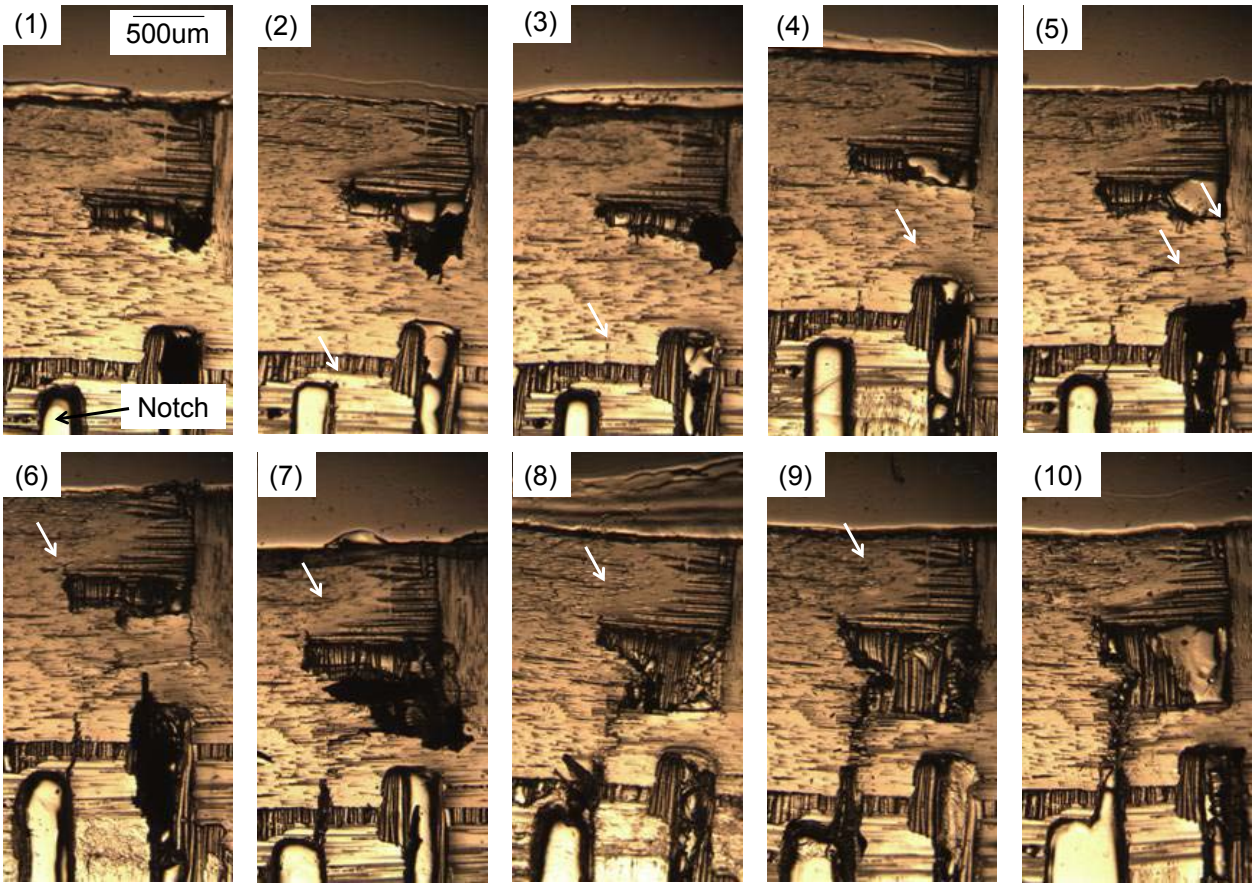

Fig. 3: Optical micrographs of crack in the unirradiated HNLS/ML/CVI composite (M7C). Arabic numbers in parenthesis correspond to each peak load in Fig. 2 (c).

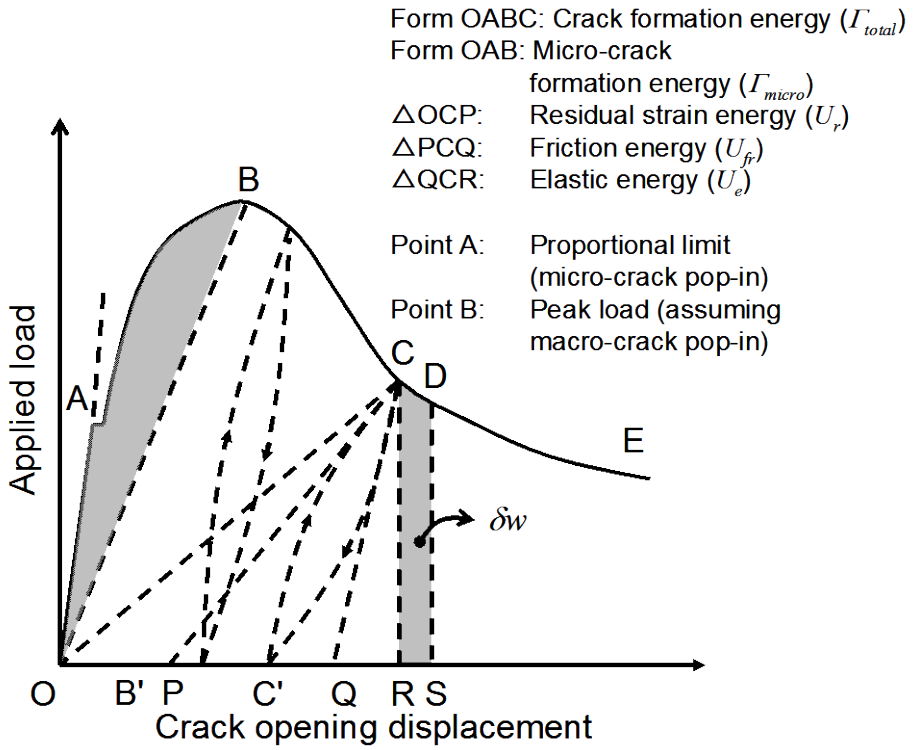

Fig. 4: Schematic illustration of load-crack opening displacement curve and definition of each energy.

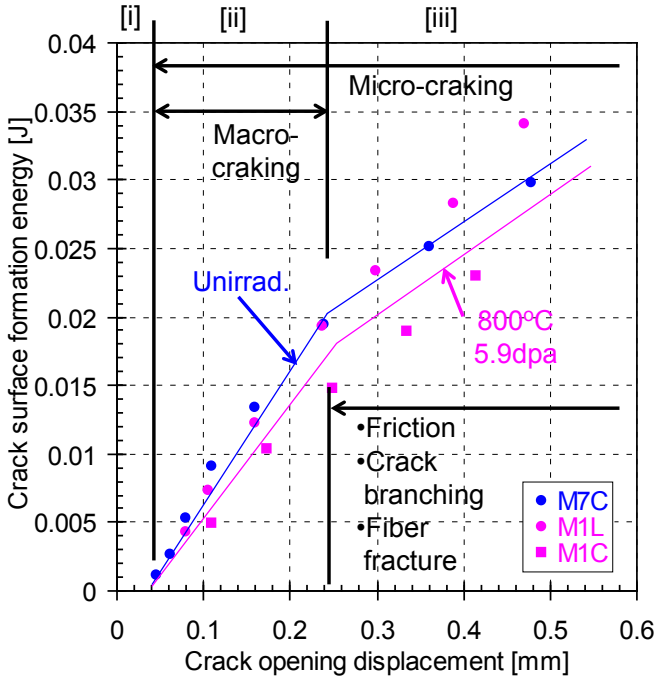

Fig. 5: Crack surface formation energy of unirradiated and irradiated HNLS (P/W)/ML/CVI (M).

LOW ACTIVATION JOINING OF SiC/SiC COMPOSITES FOR FUSION APPLICATIONS[1]—
C. H. Henager, Jr., D. J. Edwards, and A. L. Schemer-Kohrn (Pacific Northwest National Laboratory[2])

OBJECTIVE

This work discusses the latest developments in TiC + Si displacement reaction joining at PNNL based on new scanning electron microscopy and electron backscatter diffraction results.

SUMMARY

The use of SiC composites in fusion environments may require joining of plates using reactive joining or brazing. One promising reactive joining method is the use of solid-state displacement reactions between Si and TiC to produce Ti_3SiC_2 + SiC. We continue to explore the processing envelope for this type of joint for the Titan collaboration to produce the best possible joints to undergo irradiation studies in HFIR. Joining pressure appears to require almost 30 MPa at 1673K in order to produce strong and dense joints. Recently pressures of 40 MPa and temperatures of 1698K have been used to produce excellent joints with apparent optimal density and microstructure. This increased temperature and pressure appears to provide for better bonding between the SiC and joining compound due to interfacial SiC formation and growth during the joint processing. Electron backscatter diffraction was used to show that local epitaxy exists between the SiC and interfacial SiC grown in the joint region.

PROGRESS AND STATUS

Introduction

SiC is an excellent material for fusion reactor environments, including first wall plasma facing materials and breeder-blanket modules. It is low-activation, temperature-resistant, and radiation damage tolerant compared to most materials. In the form of woven or braided composites with high-strength SiC fibers it has the requisite mechanical, thermal, and electrical properties to be a useful and versatile material system for fusion applications, especially since microstructural tailoring during processing allows control over the physical properties of interest [1-7]. However, it is difficult to mechanically join large sections of such materials using conventional fasteners so the analog of welding is being pursued for these ceramic materials [2, 6, 8-15]. Such methods include metallic brazes [9, 16], glass ceramics [8, 17], preceramic polymers [15], and displacement reactions [2]. This paper reports on the current status of SiC and SiC-composite joining for fusion applications based on displacement reactions between Si and TiC. This has been used to produce bulk composite material consisting of SiC-Ti_3SiC_2, with small amounts of TiC determined by the phase equilibria conditions [18].

Experimental Procedure

Joints are made using a tape calendering process using organic binders and plasticizers together with a mixture of TiC and Si powders, with 99.99% purity, average diameters less than 45 μm, and a TiC:Si ratio of 3:2. The flexible calendered tapes were 200 μm thick and were cut to shape and applied between two Hexoloy SiC or SiC/SiC composite coupons cut to a rectangular parallelepiped shape 20mm x 4mm x 2mm in size. Joints were formed by heating the coupon sandwiches in argon to 1698K at 10K/min and holding for 2 hours at 30 to 40 MPa applied pressure. The resulting joints were dense and approximately 12 to 30 μm thick. They were prepared for optical and scanning electron microscopy using standard ceramographic cutting, grinding, and polishing methods. A final polish using colloidal silica followed by a light argon ion etch was preferred for joints taken into the SEM and characterized using electron backscatter diffraction (EBSD) methods.

[1] Partly based on Invited Oral Presentation at ICFRM-14, Sapporo, Japan, September 2009.
[2] PNNL is operated for the U.S. Department of Energy by Battelle Memorial Institute under Contract DE-AC06-76RLO 1830.

Results

Figure 1 shows scanning electron micrographs of a joint processed at 1673K for 2 hours at 30 MPa and one processed at 1698K at 30 MPa. Both joints appear dense in these images but the joint shown in Figure 1a has regions of lower density as shown in Figure 2. Figure 2 shows a less dense a region of the joint in Fig. 1(a) and processed at 1673K, 30 MPa. The joints processed at 1698K, 30 MPa or 40 MPa, did not exhibit these less dense regions, although each joint does have some porosity that may be unavoidable due to gas release during tape binder burnout. Based on these more extensive SEM examinations, the PNNL joint processing has been modified to 1698K, 40 MPa for 2 hours in argon.

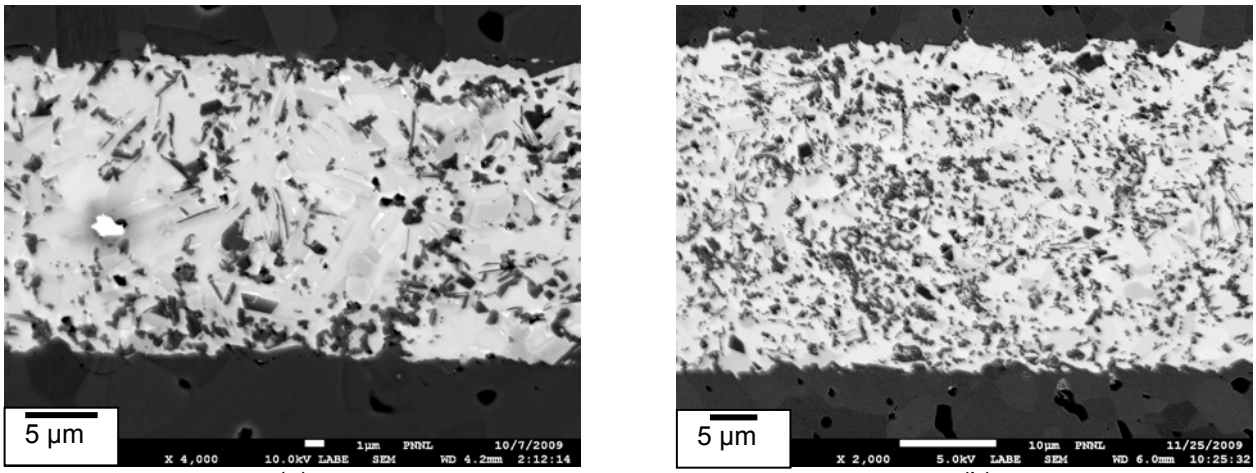

(a) (b)

Figure 1. SEM micrographs of Ti_3SiC_2+SiC joint between Hexoloy SiC coupons. Shown in (a) is a joint processed at 1673K and (b) processed at 1698K, both at 30 MPa applied pressure for 2h during joining in purified argon gas. Both joints (taken at different magnifications; note micron markers) show mixture of SiC particles in Ti_3SiC_2 with significant in-growth of SiC at the joint/Hexoloy interfaces.

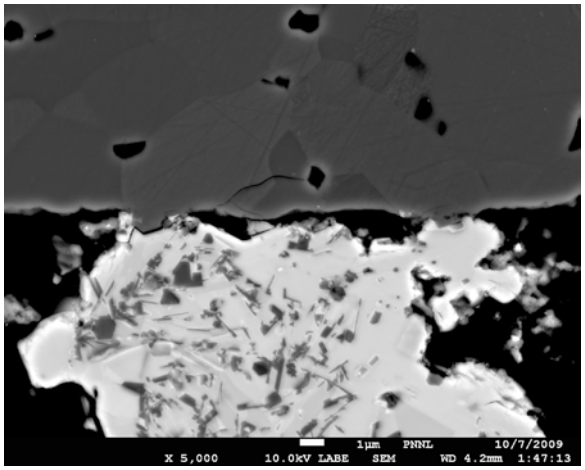

Figure 2. SEM micrograph of a region of a Ti_3SiC_2+SiC joint between Hexoloy SiC coupons showing less dense region after 1673K processing for 2h at 30 MPa. Based on this result, processing temperature was increased to 1698K for 2h.

A newly installed JEOL 7600 SEM was used for more detailed studies of the joint line interface and joint microstructure. One key parameter that appears to be controlling the joint strength is the excellent

bonding observed between the displacement reaction formed joint and the original SiC materials. For this study the original Hexoloy interfaces were polished flat and smooth using submicron diamond paste such that interface growth features formed during joining could be observed and studied. Figure 3 shows a SEM micrograph of the joint interface and clearly shows small voids at the original Hexoloy interface along with SiC that has grown in at the interface during the joining process.

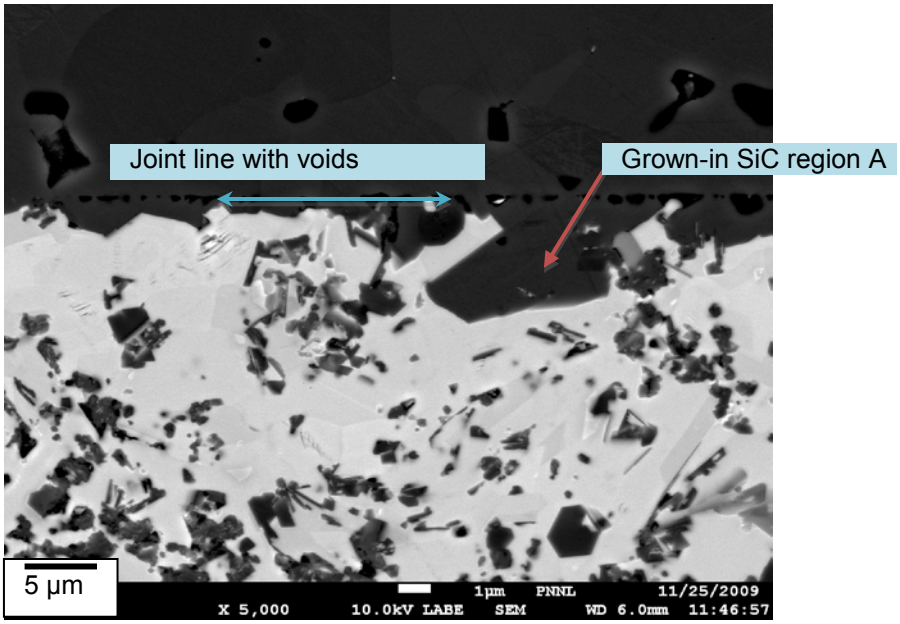

Figure 3. SEM micrograph showing joint line voids and large grown-in SiC regions (marked on micrograph). EBSD data indicates that the grown-in SiC regions have the same crystallographic orientation (epitaxy) as the grain they are attached to at the original SiC interface.

These regions, in particular, and the interior joint regions were studied using electron backscatter diffraction (EBSD) in the JEOL 7600 SEM. EBSD provides detailed crystallographic orientation information from near surface Kikuchi diffraction patterns that can be used to determine orientation relations between phases or grains present in the sample. For this work, EBSD data was acquired in the Hexoloy and joint regions with an emphasis on the joint line. This was more successful than EBSD data obtained from the joint interior because of the small grain sizes within the joint region compared to the larger SiC grains at the interface and within the Hexoloy. Briefly, this work supports our earliest findings from TEM studies that there is local epitaxy between the interface SiC grains that have grown into the joint region at the interface and the existing Hexoloy SiC grains [2]. Three interface regions were studied using EBSD and all of them indicated that grown-in SiC was epitaxial to existing SiC grains at the interface. This is shown in Figure 4 for one such region, where local epitaxy is found across the SiC/joint interface. Sample charging, thermal drifting, sub-micron grain sizes, and the complex crystallography of a-SiC all contributed to making it a difficult task to obtain high-quality EBSD patterns from these joints.

The EBSD data confirm that SiC formed during the displacement reaction preferentially nucleates at the pre-existing SiC interface and adopts the crystallography of the local grains. This is an important result, and one that was already suspected from our earlier TEM work but in this work we observe this phenomenon over a much larger region compared to the previous TEM study. Every region that was examined via EBSD showed local epitaxy across the joint line interface. The importance of this lies in understanding the strength of the joints thus formed. Early observations showed that joint shear fractures also produced fracture paths within the joined SiC pieces. Thus, local epitaxy produces a strong bond across the interface and a bond that can cause fracture to shift to the joined materials, which can be used to help design even stronger joints in the future.

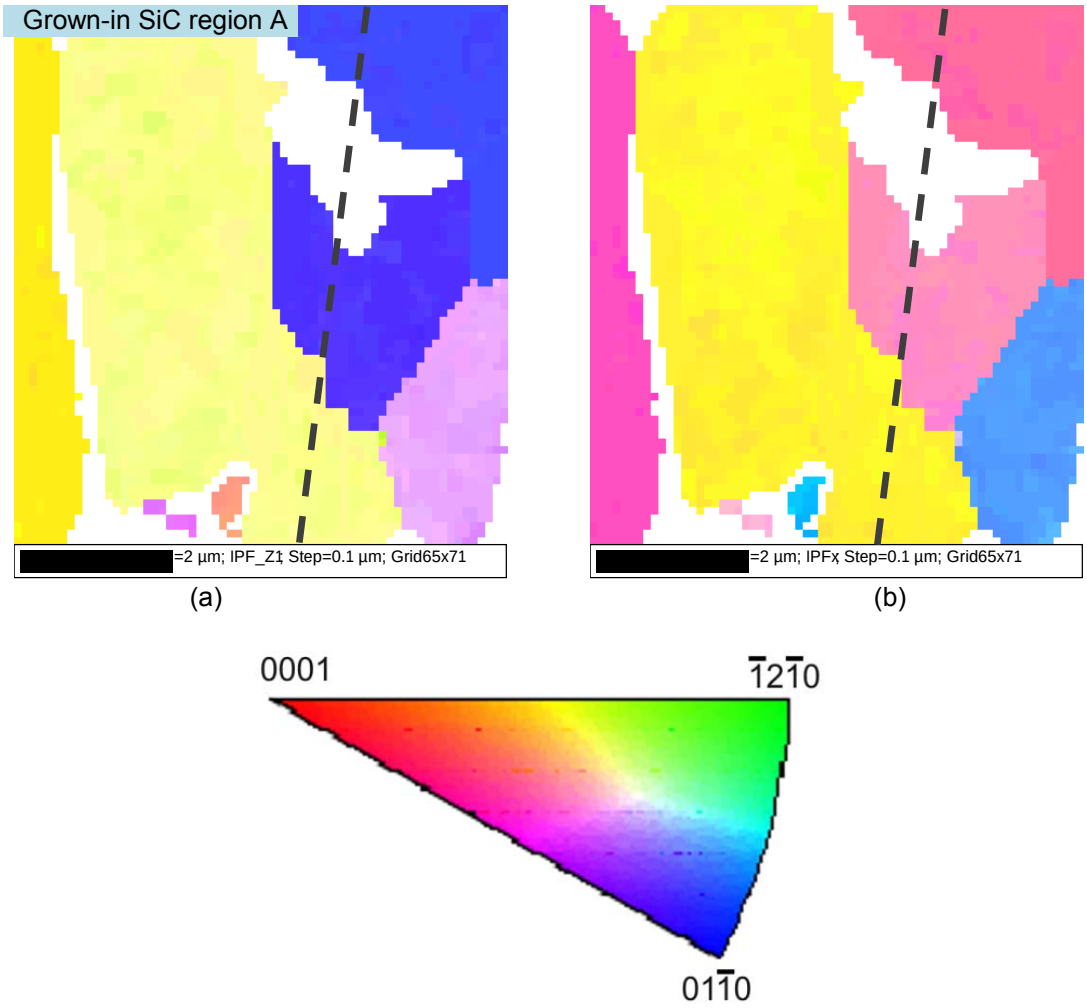

Figure 4. EBSD orientation maps showing crystallographic orientation for grown-in SiC region A shown in Fig. 3 SEM image. The location of the original SiC interface is indicated in the figure with the dashed line. The data show a continuity of crystallographic orientation, or epitaxy, across the SiC interface grains. The colors indicate the orientation relative to the standard stereographic triangle shown in Fig. 4(c) for the hexagonal SiC-6H phase. Fig. 4(a) shows the orientation map for z-axis normal to the plane of the image, while (b) shows the orientation map in the plane of the figure normal to the interface line.

CONCLUSIONS

Solid-state reaction joining was further optimized by processing tape cast TiC + Si joints in argon at 1698K and 30 to 40 MPa bonding pressure using Hexoloy SiC coupons and SiC/SiC coupons. Joints with desirable microstructures and thicknesses have been obtained. Local SiC-phase epitaxy was observed at the original joint interface indicating that SiC nucleation is facilitated by the pre-existing surface. Further work is underway to characterize the joints using transmission electron microscopy for improved phase identification and compositional mapping.

References

1. Katoh, Y., et al., Current status and critical issues for development of SiC composites for fusion applications. Journal of Nuclear Materials, 2007. 367-370 A(SPEC ISS): p. 659-671.
2. Henager, C.H.J., et al., Coatings and joining for SiC and SiC-composites for nuclear energy systems. Journal of Nuclear Materials, 2007. 367-370(1): p. 1139-43.
3. Zinkle, S.J., Advanced materials for fusion technology. Fusion Engineering and Design, 2005. 74(1-4): p. 31-40.
4. Hegeman, J.B.J., et al., Mechanical and thermal properties of SiC_f/SiC composites irradiated with neutrons at high temperatures. Fusion Engineering and Design, 2005. 75-79(SUPPL): p. 789-793.
5. Katoh, Y., et al., Progress in SiC -based ceramic composites for fusion applications. Fusion Science and Technology, 2003. 44(1): p. 155-162.
6. Jones, R.H., et al., Promise and challenges of SiC_f/SiC composites for fusion energy applications. Journal of Nuclear Materials, 2002. 307-311(2 SUPPL): p. 1057-1072.
7. Katoh, Y., et al., Property tailorability for advanced CVI silicon carbide composites for fusion. Fusion Engineering and Design, 2006. 81(8-14 PART B): p. 937-944.
8. Ferraris, M., et al., Joining of ceramic matrix composites for fusion application. Advances in Science and Technology, 2003. 33(10th International Ceramics Congress: p. 2002, Part D), 141-152.
9. Riccardi, B., et al., Low activation brazing materials and techniques for SiCf/ SiC composites. Journal of Nuclear Materials, 2002. 307-311(Pt. B): p. 1237-1241.
10. Bruce, R.L., et al., Polymer-derived SiCf/SiCm composite fabrication and microwave joining for fusion energy applications. IEEE/NPSS Symposium on Fusion Engineering, 2002: p. 1078-8891.
11. Zucchetti, M., M. Ferraris, and M. Salvo, Safety aspects of joints and coatings for plasma facing components with composite structures. Fusion Engineering and Design, 2001. 58-59: p. 939-943.
12. Raffray, A.R., et al., Design and material issues for high performance SiC_f/SiC-based fusion power cores. Fusion Engineering and Design, 2001. 55(1): p. 55-95.
13. Lewinsohn, C.A., et al., Silicon carbide based joining materials for fusion energy and other high-temperature, structural applications. Ceramic Engineering and Science Proceedings, 2001. 22(4, 25th Annual Conference on Composites, Advanced Ceramics, Materials, and Structures: B, 2001): p. 621-625.
14. Lewinsohn, C.A., et al. Joining of silicon carbide composites for fusion energy applications. 2000. Colorado Springs, CO, USA: Elsevier.
15. Colombo, P., et al., Joining of SiC/SiCf ceramic matrix composites for fusion reactor blanket applications. Journal of Nuclear Materials, 2000. 278(2): p. 127-135.
16. Riccardi, B., et al. Issues of low activation brazing of SiC_f/SiC composites by using alloys without free silicon. 2004. Kyoto, Japan: Elsevier, Amsterdam, Netherlands.
17. Katoh, Y., et al., Microstructure and mechanical properties of low-activation glass-ceramic joining and coating for SiC/SiC composites. J. Nucl. Mater., 2000. 283-287: p. 1262-6.
18. Radhakrishnan, R., et al., Synthesis of Ti_3SiC_2/SiC and $TiSi_2$/SiC composites using displacement reactions in the Ti-Si-C system. Scripta Materialia, 1996. 34(12): p. 1809.

STABILITY OF 3-D CARBON FIBER COMPOSITE TO HIGH NEUTRON FLUENCE - L. L. Snead, Y. Katoh, and K. Ozawa. (*Oak Ridge National Laboratory)*

OBJECTIVE

This work addresses the temperature and dose limitation of carbon fiber composites for nuclear applications. Additionally, the importance of relative degree of graphitization, or crystalline perfection, on the irradiation-induced changes are discussed.

SUMMARY

The dimensional stability, elastic modulus, and flexural strength of a high quality, three-dimensional balanced weave carbon fiber composite has been evaluated over a range of neutron fluence to ~32 dpa at ~ 800°C. Results indicate that while the composite exhibits continuous strengthening over this dose range, this occurs with measurable loss of mass, increased volume, and for the highest dose studied, a large reduction in elastic modulus. While the balanced weave composite was orthogonally isotropic, a significant anisotropic dimensional change occurred under irradiation. Dimensional change was dominated by fiber dimensional change and the overall shrinkage or swelling in a direction was determined by the extent to which intrinsic the fiber shrinkage was capable of restraining swelling of matrix and fiber bundles.

PROGRESS AND STATUS

Introduction

Carbon fiber composites are currently being utilized as plasma facing materials in fusion reactors and will be used in the strike plates for the ITER. Such composites are also being considered for application in core structures of high-temperature gas-cooled reactors.[1] The effects of irradiation on stability and mechanical properties have been well studied for graphite,[2,3] and in some detail for carbon fiber composites, [4-9] with their irradiation effects generally explained using a simple description of irradiation damage in the perfect graphite crystal. In the basic model, the graphite crystal is assumed to be of infinite dimension with displaced atoms preferring to come to rest between the basal planes. New interstitial planes form between these original basal planes resulting in a large dimensional change perpendicular to the basal plane (<c> axis swelling.) At low temperature irradiation,[10] (below a few hundred degrees Celcius) where vacancy mobility is limited,[10] in-plane vacancies will to a limited extent be annihilated resulting in dilation in-plane (<a> axis shrinkage.) For pyrolytic graphite this anisotropic dimensional change occurs without conserving volume. As the crystal is irradiated at temperatures where significant vacancy mobility is present (>1000K) the same anisotopic dimensional change occurs, though proceeds in a volume-conserving manner.[10] Additionally, the crystallite size (perfection) has a significant effect on the crystalline dimensional change with more perfect, larger crystals, having lower dimensional change.

This mechanism for anisotropic swelling leads to the large irradiation-induced dimensional change of pyrolitic graphite (as much as 100%,) and results in the eventual destruction of the nuclear graphite structure due to the induced internal stresses. In previous work carbon fiber composite properties such as dimensional change, strength, and thermal conductivity have been studied, and have been shown to trend in a similar manner to graphite. Specifically, both graphite and composites undergo significant increases in strength and elastic modulus while thermal conductivity is drastically reduced. However, unlike graphite, the composite dimensional change is shown to be dominated by fibers and is dependent on the composite architecture (the fiber weave), and to the selection of fiber type.[11] Of note from Burchell's original work and work to follow[1,4] is that the behavior of the composite can be well described using the theory of anisotropic dimensional change of the pyrolitic graphite (discussed above) when considering that graphite fibers are essentially very high perfection forms of graphite with graphite planes preferentially oriented parallel to their fiber axis. In this model fibers would be expected to grow in diameter and shrink axially with irradiation as the new basal planes are formed. Such behavior has been previously shown[1,4,11] and it has been speculated that though appropriate balancing of the fiber architecture the large irradiation-induced anisotropic dimensional changes of the fiber can be balanced, minimizing the overall effect on dimensional change and extending the useful lifetime of carbon fiber composite.

The irradiation effects studies to date have been limited to relatively low doses. The purpose of this paper is to explore the performance of a high-quality, balanced-weave composite to a dose considered beyond a "lifetime" dose for nuclear graphite. In particular the dimensional change under irradiation as well as its effects on strength is studied.

Experimental

The carbon fiber composite selected for this study was the Fiber Materials Incorporated FMI-222 material, a balanced weave Amoco P-120 pitch-based fiber, pitch matrix composite. The non-irradiated density of the composite is approximately 1.96 g/cm^3. Materials were irradiated in the High Flux Isotope Reactor at the Oak Ridge National Laboratory in small "rabbit" capsules sealed in a high-purity helium environment. The capsules included a SiC temperature monitor used to determine the irradiation temperature, post-irradiation. Irradiation was carried out to fast neutron fluences of 4.1, 7.3, 9.5, and 32 x 10^{25} n/m^2 (E>0.1 MeV.) The irradiation temperature of all but the highest dose capsule was ~ 800°C. At the 32 x 10^{25} n/m^2 dose level the severe swelling of the capsule distorted the sample holder which effected the gas-gap used to achieve the target temperature. This irradiation condition is therefore a combination of 800°C and (later in the irradiation) an undefined lower temperature. The geometry of the samples irradiated were bars of dimension 3.2 x 6.4 x 50.8 mm where the orthogonal axes of the bar were oriented parallel to the balanced x, y, and z tows of the composite. Elastic modulus was determined by both sonic modulus using a Grindosonic and by application of strain gages to the tensile surface of the bend bar. Four-point bend testing was carried out at room temperature with a load and support span of 20 and 40 mm.

Results and Discussion

The gross mass and dimensional change resulted in the data plotted in Figure 1, which provides data for the irradiated material, a non-irradiated set of samples, and a set of samples which were baked at 800°C in a capsule-representative environment. It is noted that within statistical uncertainty (plotted as ± standard deviation throughout) the thermal control sample set resulted in the same values as the non-irradiated (as machined) sample set. Upon irradiation a clear, increase in the envelope volume to a value of 24.8% at the 32 dpa value is achieved. This volume increase is the largest contributor towards the plotted trend for density change (figure 1), though a small loss in mass occurred. This mass loss was attributed to dislodging of matrix graphite from the surface of the composite caused by the dimensional change in the fiber tows.

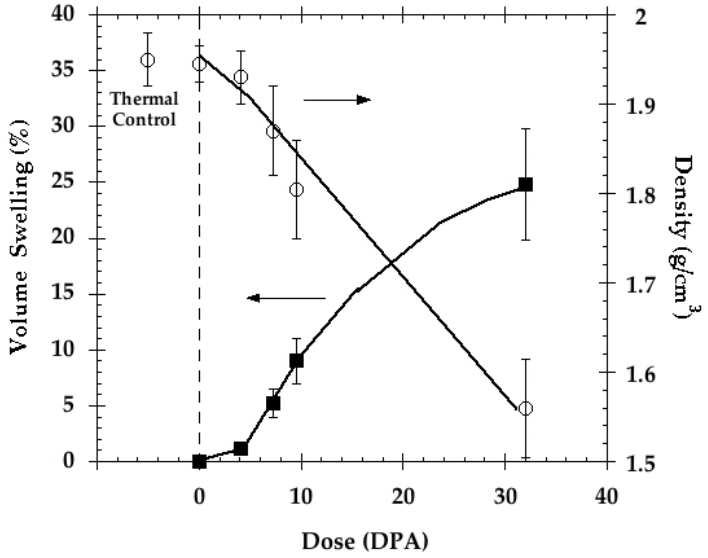

Figure 1 : Effect of irradiation on volume and density change of FMI-222 carbon fiber composite.

Discussion of volumetric change in composite materials is somewhat misleading in that the dimensional change is strongly dependent on both the architecture of the composite and the dimensions for which the change is measured.[4] This is clearly demonstrated by inspection of

Figure 2, which provides the percentage change along the bend bar axis. In this study, the composite weave was a balanced weave (same volume fraction of fibers in the x, y, and z direction) and the axis of the bend bar was aligned parallel to the axis of the fiber tows. The data of figure 2 can therefore be interpreted as the dimensional change in the longest fiber direction (Length-50.8 mm) which shows strong contraction for the entire irradiation exposure, and for the two much shorter fiber directions (Width-6.4mm, and Thickness-3.2mm) each of which exhibit expansion over the irradiation dose range studied. As mentioned in the introduction, the dimensional change behavior of fiber can be conveniently described with the classical description of the dimensional change behavior of pyrolytic graphite. However, in the case of graphite fibers, the graphene planes are oriented with their <a> axis parallel to the axis of the fibers such that the formation of inter-plane interstitial clusters will tend to cause fiber diametral (<c> axis) swelling. For the temperature of this irradiation, (800°C), significant interstitial and vacancy mobility exists such that annihilation of vacancies is expected leading to <a> contraction. For pyrolytic graphite, such contraction and expansion occurs in near volume conservation, and may be occurring in the highly crystalline fibers of this material.[10] As has been shown previously [1,4] for this material, the sample surface clearly shown evidence of the anisotopic dimensional change of the fibers, with fiber tows fattening and pulling into the free surface of the sample exposing (and liberating) the infiltrated pitch matrix. From figure 1 the contraction of the continuous fiber tow in the 50.8 mm length direction of the bend bar has had the effect of constraining any swelling that may have occurred in the matrix and dominates any aggregate effect of diametral swelling of fiber tows oriented orthogonally to the length axis. However, for the Width and Thickness direction the continuous fiber length are not able to restrain such swelling and the material swells in those directions, with the shorter fiber length (3.2 mm) having the larger swelling. The clear conclusion from this is that the swelling of such large unit cell carbon fiber composites must be viewed both in terms of the architecture, the direction through the architecture the swelling is being considered, and the thickness of the component in the direction.

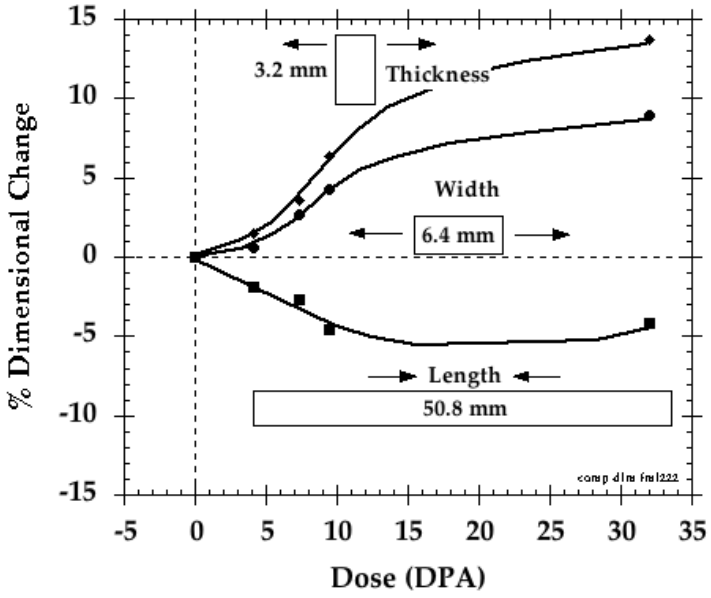

Figure 2 : Effect of Irradiation on the Dimensional Change of FMI-222 Carbon Fiber Composite.

The effects of irradiation on the mechanical properties for this material is presented in Figures 3 and 4. As seen in figure 3, the FMI-222 elastic modulus clearly shows an initial increase with irradiation with good agreement between the sonic modulus and strain gage measurement techniques. Several authors [5,8,12-14] have studied the effect of neutron irradiation on carbon fiber elastic modulus. The work of Sato [12] is the most relevant irradiation temperature to this study, reporting an increase in modulus following neutron irradiation to 1.2 x 10^{25} n/m^2, E>0.18 MeV in the temperature range of 750-810°C. Sato's irradiation, which is comparable in temperature though at about a quarter of the dose of the lowest dose point of the current study, is consistent with the findings of figure 3. He found an ~ 32 and 40% increase in elastic modulus for his composites, which is significantly higher than the interpolated data seen in figure 3. However, the larger relative increase for Sato's composite would be expected, as his PAN-based fiber composites possess much lower initial elastic modulus. The

maximum increase for the materials of this study was ~14%. In the dose range between 9.5 and 32 dpa the elastic modulus has clearly degraded for this material. However, it is not clear where the as-irradiated peak elastic modulus occurred.

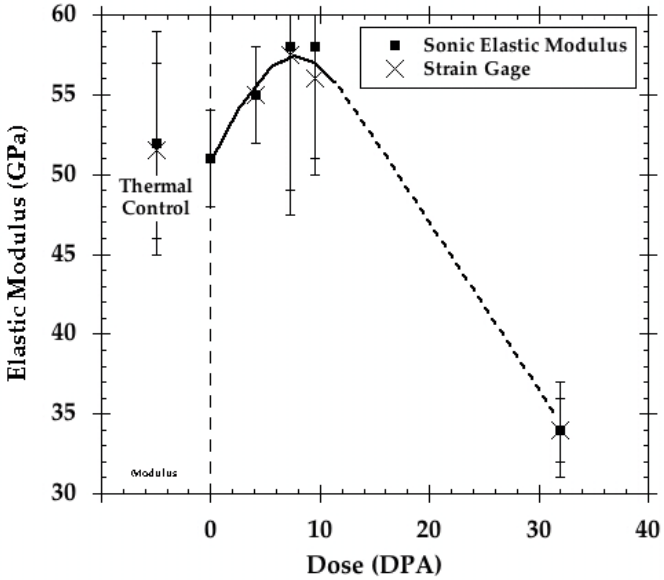

Figure 3 : Effect of Irradiation on the Elastic Modulus of FMI-222 Carbon Fiber Composite.

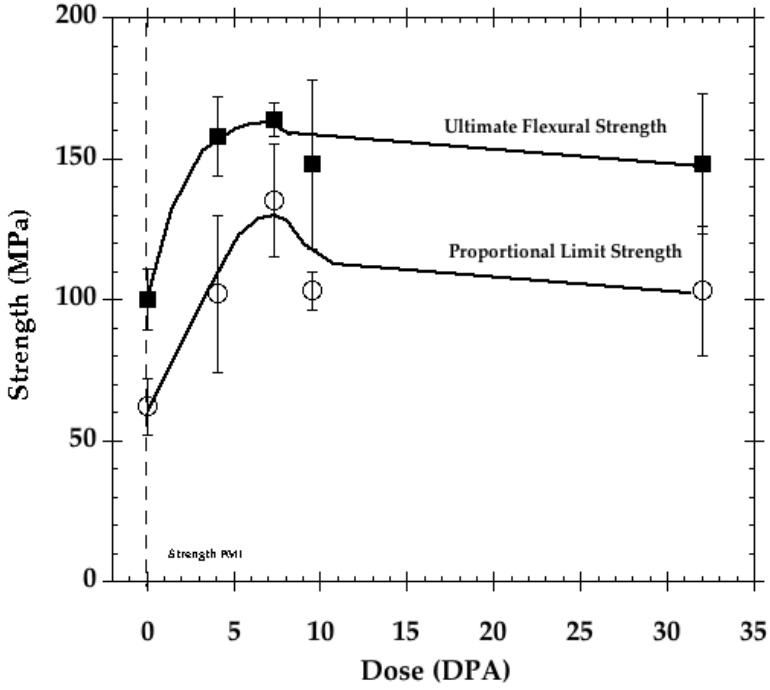

Figure 4 : Effect of Irradiation on the Strength of FMI-222 Carbon Fiber Composite.

The effect of irradiation on the mechanical properties of carbon fiber composites [5,8,12-15] has received less attention than nuclear graphite, though similar trends to graphite occur. As with graphite, CFC undergoes significantly increased strength at moderate neutron dose. For example, for identical material to the composite of this study, Burchell [15] demonstrated a 64% increase in brittle-ring strength following an intermediate irradiation dose at 600°C for the high quality, balanced weave FMI-222 composite. For identical composite, Snead et al[4] publish a nearly 100% increase in bend strength for irradiation to ~ $8x10^{25}$ n/m^2 (E>0.1 MeV.) It is noted that for nuclear graphites such as ASR-1R, TSX, and H451, irradiation in the 575-800°C temperature range results in a return to "nil swelling" and loss of mechanical properties in the dose range of 20-30 dpa (less than the dose of this study.)

Results of flexural testing is given in figure 4, which shows a significant increase in strength over the entire range of fluence studied. As seen in the figure, the 32 dpa level the composite material the FMI-222 composite has increased in ultimate bend flexural strength by approximately 50%, even though the elastic modulus has undergone significant reduction and the sample has been visibly degraded.

Conclusions

A high-quality pitch-based carbon fiber composite has been irradiated in a dose range up to 32 dpa. Resulting dimensional change is well described by the conventional description of irradiation damage in pyrolytic graphite, considering the particular morphology of the graphite fibers. For the balanced-weave composite tested volumetric change is positive over the dose range studied and quite large (24.8%) at the 32 dpa level. However, the dimensional swelling for this orthogonally isotropic composite was far from isotropic. It was seen and is speculated that for directions of long continuous fiber length (greater than 55 unit cells), the irradiation-induced fiber contraction restrains the composite in a dimensional shrinkage leading to overall shrinkage of the composite. However, when such constraint is not available (in shorter dimensions, in the case of this study ~ 3 and 6 unit cells) large expansions occur. Irradiation up to a dose of 9.5 dpa resulted in a significant increase in elastic modulus, as would be expected from previous, lower dose work on composites, and the general graphite literature. However, by the 32 dpa dose the elastic modulus showed significant degradation compared to the non-irradiated value. However, over the entire dose range of this study the bend strength of this composite increased. Such an increase occurred even though the material has undergone visible degradation, large swelling, and was well beyond the fluence from which typical nuclear graphite's would have entered into their micro-cracking and stage of severe loss of strength. Clearly the fibers, while undergoing very large dimensional changes that resulted in severe consequences on the composite matrix, including loss of mass, were able to maintain their load carrying capability.

References

[1] L. L. Snead, T. D. Burchell, Y. Katoh, J. Nucl. Mat.. (2008) 55.
[2] B. T. Kelly, Physics of Graphite; Applied Science Publishers: London, 1981.
[3] J. W. H. Simmons, Radiation Damage in Graphite; Pergamon Press, 1965; Vol. 102.
[4] L. L. Snead, T. D. Burchell, A. L. Qualls, J. Nucl. Mat.. *321*, (2003) 165.
[5] M. Eto et. al., Journal of Nuclear Materials, *212-215*, (1994) 1223.
[6] J. P. Bonal, C. H. Wu, J. Nucl. Mater., *228*, (1996) 155.
[7] V. Barabash et. al., J. Nucl. Mat., *283-287*, (2000) 138.
[8] R. E. Bullock, E. L. McKagueJr, Carbon, *1973*, (1973) 547.
[9] T. D. Burchell et. al., J. Nucl. Mat., *191-194*, (1992) 295.
[10] B. T. Kelly, J. Vac. Sci. Technol., *A 4*, (1986) 1171.
[11] T. D. Burchell. Materials Properties Data for Fusion Reactor Plasma Facing Carbon-Carbon Composites. In Physical Processes of the Interaction of Fusion Plasmas with Solids, Plasma-Materials Interactions, eds. W. O. Hofer and J. Roth; (Academic Press, 1996), 1996; pp 341.
[12] S. Sato, A. Kuramada, K. Kawamata, Fusion Engineering and Design, *13*, (1990) 159.
[13] Y. Tanabe et. al., Carbon, *1991*, (1991) 905.
[14] K. Hamada, S. Sato, A. Kohyama, J. Nucl. Mat., *212-215*, (1994) 1228.
[15] T. D. Burchell, W. P. Eatherly, J. P. Strizak. "The effect of neutron irradition on the structure and properties of carbon-carbon composite materials"; Effects of Radiation on Materials:16th International Symposium, ASTM STP 1175, 1994.

On the Fracture Toughness of Irradiated F82H: Effects of Loss of Constraint and Strain Hardening Capacity – T. Yamamoto, G.R. Odette(University of California Santa Barbara) and M.A. Sokolov (Oak Ridge National Laboratory).

OBJECTIVE

Objective of the research is to examine effects of loss of both constraint and strain hardening capacity on the fracture toughness of irradiated H82H. We have applied a constraint-loss (CL) size effect adjustment procedure to K_{Jm} for F82H-IEA heat irradiated in HFIR to≈ 6.6 dpa at ≈ 300 ºC. We c ompare the ΔT_{mo} based on the SV adjusted measured toughness to the corresponding ΔT_{co} using a physically based size adjustment procedure. We also compare the ΔT_{co} data trends to hardening model predictions. Finally we evaluate the limitations of using the small bend bars used in the High Flux Isotope Reactor (HFIR) irradiations to evaluate static ΔT_{co} for irradiated TMS with loss of strain hardening.

SUMMARY

Constraint loss adjustments, based on finite element (FE) stress analysis and local critical stress, σ^*, critical stressed volume, V*, cleavage criteria were applied to fracture toughness data from small pre-cracked bend bars of the IEA heat of F82H irradiated to 6.6 dpa at 300 ºC in the High Flux Isotope Reactor. The 100 MPa$\sqrt{m}$ master curve method reference temperature shifts were evaluated based on both the measured toughness (ΔT_{mo}) and after size-adjusting the toughness to small scale yielding conditions at reference specimen size (ΔT_o) with values of≈ 148 and 205ºC, respectively. The prediction $\Delta T_o = C_o \Delta \langle \sigma_{fl} \rangle$, where $C_o \approx 0.68$ and $\Delta \langle \sigma_{fl} \rangle$ is the change in the average flow stress over 0-10% strain is in excellent agreement with ΔT_o. The FE analyses also demonstrate an upper-bound K_{Jc} that can be measured with these small bend bars for irradiated alloys that suffer severe loss of strain hardening.

RESEARCH PROGRESS AND STATUS

Introduction

Irradiation embrittelement, as characterized by upward shifts (ΔT_o) in the cleavage fracture toughness master curve (MC)[1-5], is one of the key issues that control operation window of the 8-9Cr-1-2W normalized and tempered martensitic steels (TMS) in fusion reactor first wall application. At irradiation temperatures less than ≈ 400°C, the ΔT_o are primarily due to irradiation hardening, $\Delta\sigma_y$[1,6,7]. However, the weakening of grain boundaries by very high levels of helium may also interact synergistically with large $\Delta\sigma_y$, resulting in very large ΔT_o[1,7,8].

Assessment of irradiation-induced increases in the MC reference temperatures, ΔT_o, requires use of small specimens due to both limited space and high heating rates in available irradiation facilities. However, the fracture toughness measured using small specimens, K_{Jm}, is generally higher than those obtained from larger, conventional specimens, due to both statistical and constraint loss size effects [1,3,5,9]. Statistical effects are related to crack tip stressed volume (SV), where cleavage fracture initiates, scaling with the crack front length (B) as $K_{Jr}=[K_{Jc}(B)-K_{min}][B_r/B]^{1/4}+K_{min}$; here B_r=25.4mm is a reference length and K_{min} = 20MPa$\sqrt{m}$ is a minimum toughness [4,9]. For standard test specimen geometries, the constraint loss (CL) effect is related to the specimen ligament dimension that defines the limit of a embedded plastic region/ligament size ratio that maintains small scale yielding amplitudes of the high blunting crack tip stress fields. CL is significantly enhanced by reduced strain hardening in irradiated steels [1,10] and direct use of measured irradiated K_{Jm} can lead a highly non-conservative ΔT_m unless size effects are correctly accounted for [3,9,11]. Rathbun et al. have shown that physically based models can be used to adjust K_{Jm} data to full constraint reference conditions (plane strain, small scale yielding for B=25.4mm) K_{Jr} [3,5,9,11]. For example, application of the adjustment procedure to a large unirradiated database for F82H, K_{Jm} obtained from 13 types of specimens, resulted in a self-consistent population of K_{Jr} data well described by a single MC with a $T_o \approx$ -103 ± 3 ºC [3].

In the irradiation hardening dominated regime, $\Delta T_o \approx C_o \Delta\sigma_y$, where experimental estimates of C_o range from ≈ 0.7 °C/MPa for reactor pressure vessel (RPV) steels for low dose (< 0.1 dpa) irradiations at $T_i \approx$ 300 °C to as low as ≈ 0.33 °C/MPa for 9Cr tempered martensitic steels (TMS) for irradiations at lower temperatures (e.g., 300°C) irradiations to several dpa [1,10,12-14]. For example Odette et al. reported a $C_o \approx$ 0.58 °C/MPa for F82H irradiated between ≈ 250 to 380°C [1,13] and Sokolov has suggested even lower values [12,14]. It was also shown that the lower C_o for TMS alloys and irradiation conditions, which can be attributed to large reduction of strain hardening [1,10,13]. A model based study by Odette et al. showed that ΔT_o is controlled by a the change in the flow stress averaged over 0 to 10% plastic strain $\Delta\langle\sigma_{fl}\rangle$, that accounts for loss of strain hardening, as $\Delta T_o = 0.68\Delta\langle\sigma_{fl}\rangle$ [10]. He et al. showed theoretically as well as experimentally that the averaged flow stress can be directly related to hardness measurement [15]. As is demonstrated by Yamamoto et al. [6,16], based on the analyses of a large database on $\Delta\sigma_y$ and Chapry DBTT shift, ΔT_c, in irradiated TMS, these hardening-shift relations can be extended to include synergistic interactions with non-hardening embrittlement due to grain boundary weakening accompanying helium accumulation. It was shown that a semi-empirical hardening model for $\Delta\sigma_y(dpa,T_i,T_t)$, where T_i is the irradiation temperature and T_t is the test temperature could be combined with hardening-shift coefficients for Charpy (C_c) tests to predict $\Delta T_c = C_c\Delta\sigma_y(dpa,T_i, He)$.

In this study, we applied a CL size effect adjustment procedure to K_{Jm} for F82H-IEA heat irradiated in HFIR to ≈ 6.6 dpa at ≈ 300 ºC. The primary objectives were to:

- Compare the ΔT_{mo} based on the SV adjusted measured toughness to the corresponding ΔT_{co} using a physically based size adjustment procedure.
- Compare the ΔT_{co} data trends to hardening model predictions.
- Evaluate the limitations of using the small bend bars (see below) used in the High Flux Isotope Reactor (HFIR) irradiations to evaluate static ΔT_{co} for irradiated TMS with loss of strain hardening.

Experimental

Fracture toughness of the irradiated F82H-IEA heat was measured using a pre-cracked bend bar (PCBB) with dimensions of W=3.33, B=1.67 and L=18mm irradiated to nominally 6.6 dpa at 300ºC in the JP-26 capsule in HFIR. Details are reported by Sokolov et al. in ref [14]. Companion miniature tensile specimens, with gauge section of W=1.2, t=0.5 and L=5 mm, were also irradiated in the same capsule nominally to 7.7 dpa at 300 ºC and tested at RT. Details of the tensile test is reported in ref [17].

Constitutive model

Figure 1a shows stress strain curves for the irradiated and unirradiated F82H-IEA heat. The irradiated engineering stress-strain curve, s(e) (blue dashed curve), shows a σ_y = 953MPa and $\Delta\sigma_y$ = 402MPa. Yielding in the irradiated case is followed by immediate necking, hence, the true stress strain curve, $\sigma(\varepsilon)$, could be directly evaluated only up to≈ 0.4% plastic strain as shown by the solid blue curve. Hence, the $\sigma(\varepsilon)$ required for the crack tip stress field analysis was obtained by iterative FE simulation by modifying trail s(e) input functions until they reproduced the s(e) curves [18,19]. The green dotted (irradiated) and blue curves (unirradiated) in Figure 1b show the final iterated $\sigma(\varepsilon)$ and corresponding predicted engineering stress-strain curves, respectively. The strain hardening was assumed to be independent of temperature and the temperature dependence of σ_y determined from a master curve of thermally activated flow [20].

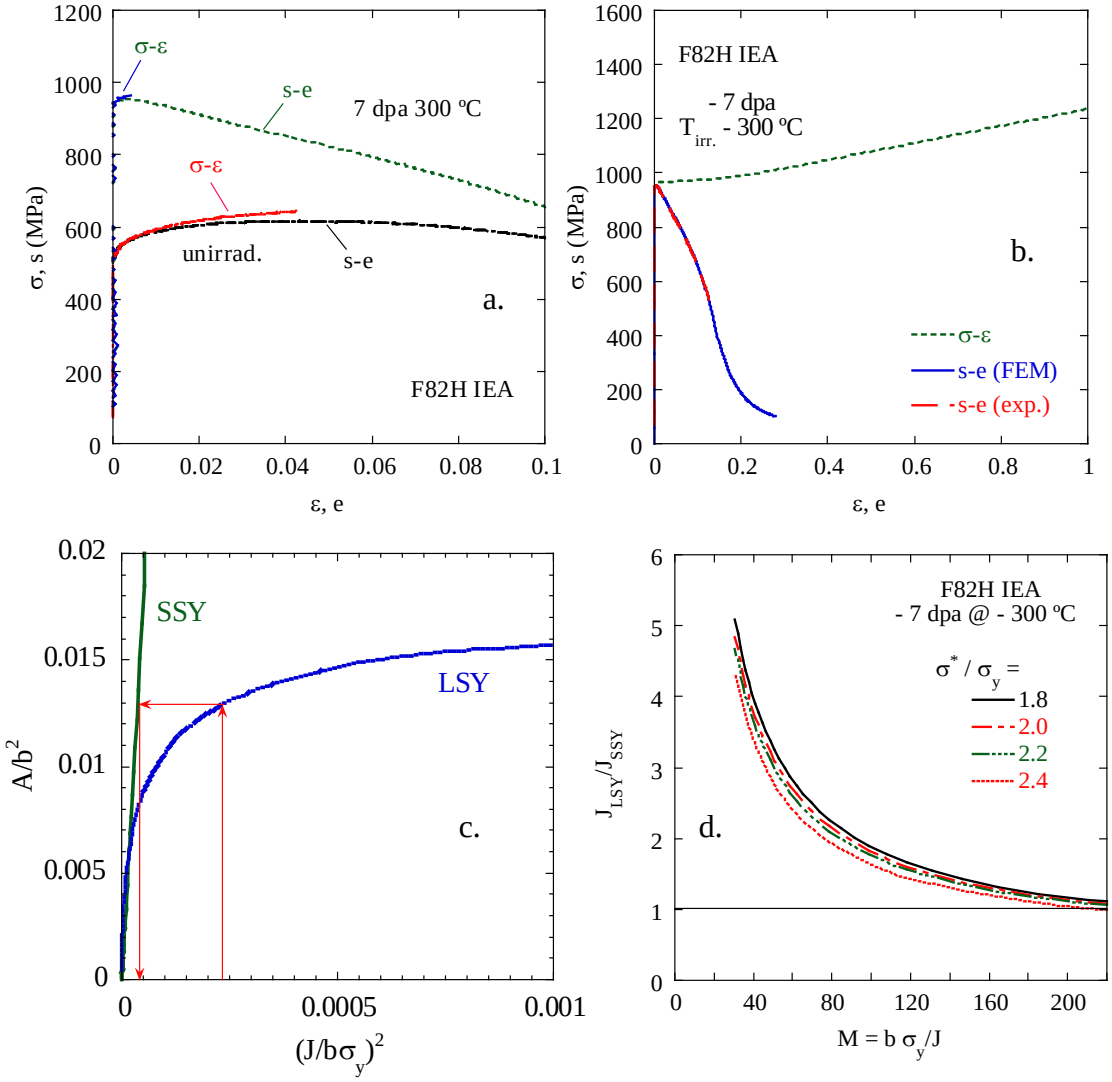

Figure 1 a) Engineering and true stress-strain curves of F82H-IEA before and after neutron irradiation to ≈ 7.7dpa at 300 ºC in HFIR; b) FEM simulated and experimental engineering stress-strain curves (s-e) with an input of constitutive model (s-e) of the irradiated F82H-IEA; c) The normalized stressed area for σ^*/σ_y = 2.0 as a function of $J/b\sigma_y$ for both SSY and LSY conditions showing constraint loss (CL) at higher loading in LSY. Red arrows illustrate the CL adjustment procedure; d) the CL adjustment factor (J_{LSY}/J_{SSY}) as a function of constraint parameter M (= $b\sigma_y/J_{LSY}$) for various σ^*/σ_y ratios.

Size effect adjustment based on FE

Cleavage fracture initiates in the high stress region near the tip of a blunting crack [1,9]. The crack tip fields can be described by isostress contours that reach peak values of 3 to 5 times σ_y, depending on the alloy strain-hardening rate [1,9,22]. Under plane strain, small-scale yielding (SSY) conditions for specimens with a/W≠ 0.5, the spatial dimensions of the stress field scale with the crack tip opening displacement, $\delta \approx J/2\sigma_y$ (or $K_J^2/2\sigma_y E$), where J, K_J, E are J-integral, plastic elastic loading and elastic modulus, respectively[1,9,22]. However, if the deformation level, hence the d, that is required to produce cleavage is not very small compared to the characteristic dimension of the specimen, typically taken as the uncracked ligament length, b = W - a, then the crack tip stress fields fall below small scale yielding values. The reduction of the stress fields at higher $J/b\sigma_y=2\delta/b$ is known as constraint loss (CL) [1,9,22].

Finite element (FE) simulations were performed to obtain the average stressed areas (A) along the crack front as a function of normalized stress σ_{22}/σ_y perpendicular to the crack plane and $J/b\sigma_y$ for the $\sigma(\varepsilon)$ derived previously. Three-dimensional (3D) large scale yielding (LSY) FE models were used to simulate the actual specimen geometry and a 2D plain strain model was used to calculate the fields for small scale yielding (SSY)[1,3,9].

Figure 1c shows normalized A/b^2 versus $[J/b\sigma_y]$ under both SSY and LSY conditions at -40 ºC. for σ^*/σ_y = 2.0. Here it is assumed that σ^* = 2100MPa is unaffected by irradiation and that the calibration value derived from the unirradiated $K_{Jc}(T)$ curve can be used in all cases [3]. Deviation from the linear SSY relation indicates that CL begins at $(J/b\sigma_y)^2 \approx 3x10^{-5}$ (or $d/b \approx 0.005$) and becomes significant at $(J/b\sigma_y)^2 \approx 5x10^{-5}$ (or $\delta/b \approx 0.01$). These low deformation are exaggerated by the low σ^*/σ_y ratio (≈ 2.0) at the test temperature and the low strain hardening in irradiated TMS. The red arrows in Figure 1c illustrate a procedure to adjust a toughness value to remove the CL effect. The $(J_{LSY}/b\sigma_y)^2$ value at cleavage for LSY condition is converted to an SSY $(J_{SSY}/b\sigma_y)^2$ for the same A/b^2. The J_{LSY}/J_{SSY} adjustment as a function of $M = b\sigma_y/J_{LSY}$ for various σ^*/σ_y ratios is shown in Figure 1d. The CL begins at M < 200 and is massive at M = 30 which is the very non-conservative constraint loss limit recommended in ASTM E1921 MC method.

Statistical stressed volume (SV) size adjustment relates to the variations in the probability of initiating weakest link cleavage as a function of the total volume (V) of material under high stress. Since for SSY conditions, A scales with J^2 or K_J^4, and $V^*=BA^*$, simple theory suggests that K_{Jc} scales as $\approx B^{-1/4}$ [1,8]. However, other mechanistic considerations and empirical observations show that this $B^{-1/4}$-scaling is modified by a minimum toughness, K_{min}, as $K_{Jr}(B_r)=[K_{Jc}(B)-K_{min}][B_r/B]^{1/4}+K_{min}$ [1,5,8]. The ASTM MC standard E1921, specifies a $K_{min} \approx 20$ MPa$\sqrt{m}$ and a reference thickness B_r=25.4mm [4]. More detailed description on the CL and SSV size effects adjustment procedures can be found in the literature [1,9,11].

Results and Discussion

Figure 2a shows toughness data of the irradiated PCBB specimens adjusted to a reference B_r = 25.4mm, with (unfilled red squares) and without (blue diamonds) CL-adjustment. Multi-temperature MC analyses [2,4] yields corresponding reference temperatures of T_{coi} = 102 ºC (red lines) and T_{mo} = 39 ºC (blue lines). Note the thick lines are for the median toughness and the thin lines represent the 5% to 95% bounds. The unirradiated MC with $T_{co} \approx$ -103ºC results in shifts of 205 and 247 ºC, with and without CL-adjustment, respectively.

Figure 2b shows ΔT_o as a function of $\Delta\sigma_y$ literature data for irradiations at a similar temperature using relatively large specimens or with CL-adjustments applied [5,13,23,24]. The $\Delta T_o/\Delta\sigma_y$ ratio of 0.51 °C/MPa found in this study falls slightly below the overall fitted trend of $\approx$ 0.56 °C/ MPa. Odette et al. showed that the micromechanical cleavage fracture model used in this study also predicts a universal relation between ΔT_o and the change in the average flow stress $<\sigma_{fl}>$ between 0 and 10% plastic strain [10] that accounts for the strain hardening loss in highly irradiated steels. Figure 2c shows the predicted $\Delta T_o(\Delta<\sigma_{fl}>)$ relation for various combinations of yield and strain hardening contributions to the overall flow stress, representing the competing effects of irradiation. The $\Delta T_o/\Delta<\sigma_{fl}>$ of 0.68 found in this study is a remarkable agreement with the model.

We can also estimate ΔT_o based on the hardening-shift relation $\Delta T_o = C_o\Delta\sigma_y(dpa,T_i)$, where the $\Delta\sigma_y(dpa,T_i)$ was derived from our analysis of the larger TMS database [6]. For T_i = 300 °C, using the $\sigma_y(dpa,T_i)$ model and the C_o = 0.56 °C/MPa for room temperature tensile tests from the fit shown in Figure 2b, yields the relation; $\Delta T_o=286[1- \exp(-dpa/7.7)]^{1/2}$. As shown in Figure 2d, the hardening-shift model $\Delta T_o(dpa)$ predictions are in excellent agreement with experimental data for $T_i \approx$ 300 ºC.

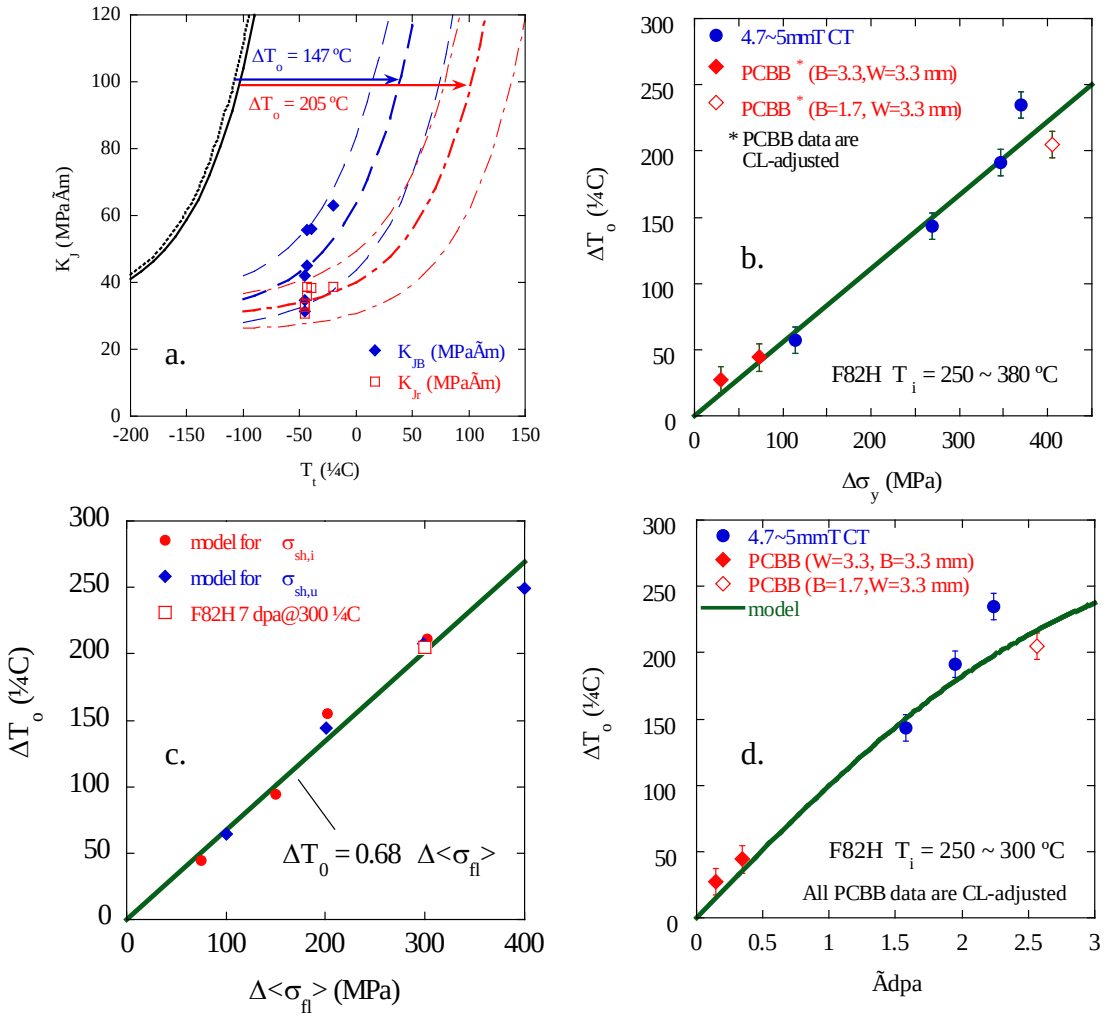

Figure 2 a) 1T-conveted toughness data with MCs before (K_{JB}) and after (K_{Jr}) constraint loss adjustment; b) ΔT_o versus $\Delta\sigma_y$ relations in CL-adjusted PCBB or CT specimens of F82H-IEA irradiated at 250 to 380 ºC to various doses; c) ΔT_o versus $\Delta\langle\sigma_{fl}\rangle$ (change in flow stress) relations of the irradiated F82H compared with theoretical study by Odette et al.[10]. d) ΔT_o in relatively high constraint specimens of F82H irradiated at ≈ 300ºC with irradiation hardening based model prediction.

Figure 3a shows the magnitude of the CL-adjustment, K_{Jm}- K_{Jc}, applied for the 7dpa irradiated toughness data versus K_{Jm} in red diamonds along with corresponding results for unirradiated and low dose irradiated specimens in black open square and blue circles, respectively, as previously reported [5]. The adjustments follow a similar trend. The 7dpa data adjustments are only slightly larger than the average trend for the previous cases, shown in solid green line. Indeed larger differences might be expected in view of the lower strain hardening, smaller σ^*/σ_y ratio as well as the thinner specimen. Note, the adjustment would have been much more in the 7dpa case if a higher toughness had been measured as would occur higher test temperature. Note the proportionality between K_{Jm} and the constraint adjustment means that any larger scatter in the measured toughness is highly compressed in CL-adjusted toughness.

The reason for this behavior and important implications are illustrated in Figure 3b showing the variation in the normalized stress area for σ^*/σ_y= 2 as a function of $(J/b\sigma_y)^2$ in both the 7 dpa and 0.12 dpa irradiated specimens. In the latter case, the curve approaches a constant slope, which means that as the measured K_{Jm} increases it is adjusted by an almost equal amount back to only a slightly higher K_{Jc}. This is

to some extent an artifact of the procedure and means that actual variations in K_{Jc}, which could be measured in larger specimens, cannot be detected in small specimens beyond a $J/b\sigma_y$ deformation limit. The limited toughness measurement capacity is even more severe for 7dpa specimen where the stress area reaches saturation level at $(J/b\sigma_y)^2 \approx 0.001$ that corresponds to $K_{Jm} \approx 110$ MPa$\sqrt{m}$ for this specimen size and geometry. The saturation is largely due to the large strain hardening loss in the more highly irradiated condition. Adjusted 1T-toughness would never be more than $\approx$ 40 MPa$\sqrt{m}$ in the 7 dpa irradiation case, or the specimen will more likely experience ductile tearing or plastic collapse as alternatives to mode cleavage. In fact some tests showed data clearly separated into two extreme cases – ones showing very low toughness and the others with no cleavage [25,26]. Such testing limit of small size specimens must be recognized, especially for materials with low strain hardening capacity.

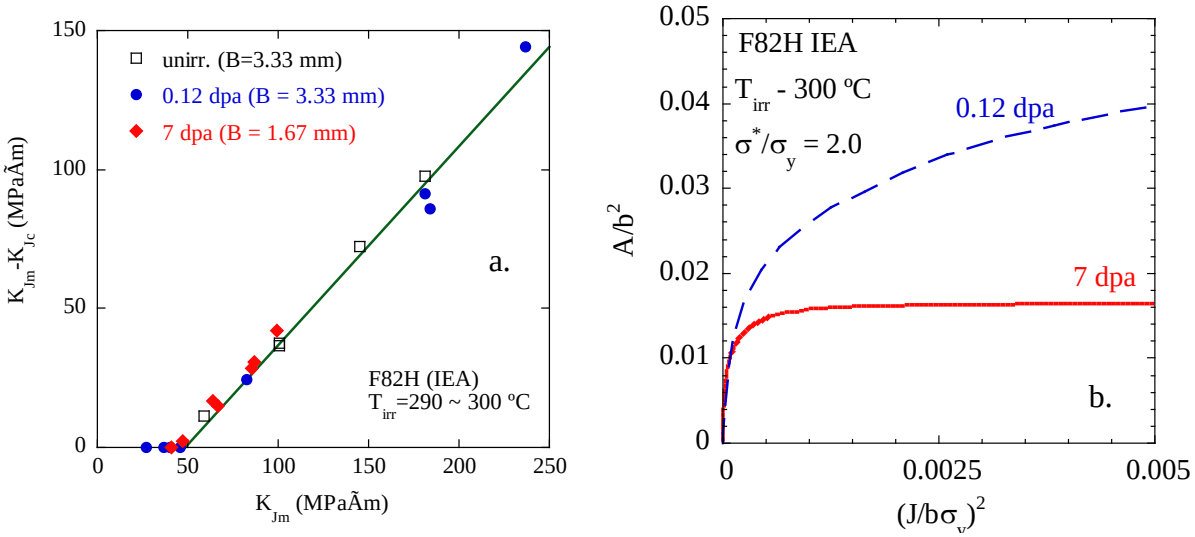

Figure 3 a) magnitude of the constraint loss adjustment as a function of measured toughness and b) normalized stressed area versus normalized loading relations in F82H irradiated to 0.12 and 7 dpa at $\approx$ 300 ºC.

Conclusions

A combined constraint loss and statistical size adjustment procedure was applied to fracture toughness data for small pre-cracked bend bar specimens (W = 3.33, B = 1.67 and L = 18 mm) for the IEA heat of F82H irradiated to $\approx$ 7 dpa at $\approx$ 300ºC in HFIR. The cleavage transition MC reference temperature shifts, based on the measured toughness, $K_{Jm}(T)$, data (ΔT_m) as well as reference temperature shifts (ΔT_o) found after size-adjusting the $K_{Jm}(T)$ data yielded $\Delta T_{m/o} \approx$ 148 and 205 ºC, respectively. The $C_o = \Delta T_o/\Delta\sigma_y$ = 0.51 is in good agreement with but falls slightly below corresponding data in the literature. A more universal measure of shifts related to irradiation hardening is based on the low stress change and gives the $C_o = \Delta T_o/\Delta\langle\sigma_{fl}\rangle$ = 0.68 in excellent agreement with model predictions. The FE analyses also showed that crack tip stressed area saturates at much lower deformation level in the F82H IEA after 7 dpa irradiation, primarily due to loss of strain hardening. These results demonstrate that there are upper limits on K_{Jc} values that can be measured with small specimens that are further decreases in highly irradiated steels that suffer severe loss of strain hardening capacity.

Acknowledgements:

Experimental data used in this study were obtained under the collaboration with Oak Ridge National Laboratory, Pacific Northwest National Laboratory and Japan Atomic Energy Agency. The authors are grateful to Drs. Steve Zinkle, Roger Stoller, Shiro Jitsukawa, Hiroyasu Tanigawa and other researchers involved in the US-JAEA collaboration. The research performed at University of California, Santa Barbara was supported by the US Department of Energy, Office of Fusion Science Grant #DE-FG03-94ER54275 and US Department of Energy, NERI Grant #DE-FG07-05ID14663.

References

[1] G. R. Odette, T. Yamamoto, H.J. Rathbun, M.Y. He, M.L. Hribernik, J.W. Rensman, *J. Nucl. Mater.* **323** (2003) 313.

[2] K. Wallin, A. Laukkanen, S. Tahtinen, *Small Specimen Test Techniques 4*, ASTM STP 1418 (2002) 33.

[3] G. R. Odette, T. Yamamoto, H. Kishimoto, M. Sokolov, P. Spätig, W. J. Yang, J. -W. Rensman and G. E. Lucas, *J. Nucl. Mater.* **329-333** (2004) 1243

[4] ASTM E 1921-09, "Standard Test Method for Determination of Reference Temperature, To, for Ferritic Steels in the Transition Range," ASTM, 2009.

[5] T. Yamamoto, G.R. Odette, D. Gragg, H. Kurishita, H. Matsui, W.J. Yang, M. Narui, M. Yamazaki, *J. Nucl. Mater.* **367-370** (2007) 593.

[6] T. Yamamoto, G. R. Odette, H. Kishimoto, J-W. Rensman, P. Miao, *J. Nucl. Mate*r. **356** (2006) 27,

[7] R. Kasada, T. Morimura, A. Hasegawa, A. Kimura, *J. Nucl. Mater.* 299 (2001) 83.

[8] Y. Dai, Z. Tong, L. Peng, G.R. Odette, T. Yamamoto, *this conference.*

[9] H.J. Rathbun, G.R. Odette, M.Y. He, T. Yamamoto, *Eng. Fracture Mechanics*, **73** (2006) 2723.

[10] G.R. Odette, M.Y. He, T. Yamamoto, *J. Nucl. Mater.* **367-370** (2007) 561.

[11] H.J. Rathbun, G.R. Odette, T. Yamamoto, M.Y. He, G.E. Lucas, *Eng. Fracture Mechanics*, **73** (2006) 134.

[12] M. A. Sokolov and R. K. Nanstad, *Effects of Irradiation on Materials-18th International Symposium,* ASTM STP 1325 (1999) 167.

[13] G. R. Odette, H. J. Rathbun, J. W. Rensman and F. P. van den Broek, *J, Nucl. Mater.* **307-311** (2002) 1624.

[14] M.A. Sokolov, G.R. Odette, T. Yamamoto, H. Tanigawa, H. Okubo, this conference.

[15] M.Y. He, G.R. Odette, T. Yamamoto, D. Klingensmith, *J. Nucl. Mater.* **367-370** (2007) 556.

[16] T. Yamamoto, Y. Dai, G.R. Odette, M. Salston, P. Miao, *Trans. American Nuclear Society,* 98 (2008) 1111.

[17] T. Hirose, H. Okubo, H. Tanigawa, M. Ando, M.A. Sokolov, R.E. Stoller, this conference.

[18] G.R. Odette, M.Y. He, E.G. Donahue, G.E. Lucas, ASTM STP 1418 (2002) 221.

[19] G.R. Odette, M. He, D. Gragg, D. Klingensmith, G.E. Lucas, *J. Nucl. Mater.*, **307-311** (2002) 1643

[20] M.L. Hribernik, G.R. Odette, T. Yamamoto, to be published.

[21] G. R. Odette, J. Nucl. Mater., **212-215** (1994) 45.

[22] T.L. Anderson, *Fracture Mechanics: Fundamentals and Applications,* Third Ed., CRC Press, Boca Raton, Florida, 2005.

[23] P. Spatig, "Small-scale fracture mechanics – modeling of brittle to ductile transition behaviors using appropriate theories. Formation of rules for transferability to standards and fusion components," TTW2-TTMS-005b, CPPI, Switzerland (2005)

[24] M.A. Sokolov, R.L. Klueh, G.R. Odette, K. Shiba and H. Tanigawa, ASTM STP 1447 (2004) 408

[25] P. Spatig, G. R. Odette, G. E. Lucas, *J. Nuc. Mater.* **275** (1999) 324

[26] J. W. Rensman, personal communication.

He Transport and Fate of Tempered Martensitic Steels: Summary of Recent TEM Observations – D. J. Edwards, R. J. Kurtz (Pacific Northwest National Laboratory, Richland, WA 99336, USA), G. R. Odette and T. Yamamoto (University of California, Santa Barbara, CA 93106-5070, USA)

OBJECTIVE

The work discusses the recent investigation of in-situ He-implanted tempered martensitic steels irradiated in HFIR using transmission electron microscopy.

SUMMARY

As an extension of prior work [1-4], we summarize recent observations made on a He-implanted tempered martensitic steel (TMS), F82H mod 3, irradiated in the HFIR, in both as-tempered (AT) and cold-worked (CW) conditions. A novel implantation technique was used to uniformly inject He into 3-mm diameter TEM discs to depths ranging from ≈ 5-8 μm. The He is generated by two-step transmutation reactions in Ni contained in a NiAl coating layer adjacent to paired 3 mm TEM discs. NiAl layers from 1 to 4 μm thick produced He/dpa ratios between 5 and 40 appm/dpa. The irradiations were at temperatures of 300, 400 and 500°C from 3.9 to 9 dpa and 90 to 380 appm He. Electron transparent samples were prepared by a cross-sectional thinning technique that allowed investigating microstructural evolution over a range of implantation depths. Irradiation of the AT alloy to 9 dpa at 500°C and 380 appm He resulted in relatively large, faceted cavities, that are likely voids, along with a much higher density of smaller He bubbles. The cavities were most often aligned in pearl necklace like strings, presumably due to their formation on pre-existing dislocations. A finer distribution of cavities was also present on precipitate interfaces, lath and grain boundaries. Nine dpa irradiations that produced 190 appm He resulted in a somewhat more random distribution and lower density of smaller matrix cavities; but lower He levels had a less noticeable effect on bubbles in the lath and precipitate boundaries. Corresponding irradiations of the CW F82H produced a larger number of smaller cavities. Irradiation of the AT alloy to 3.9 dpa and 90 ppm He at 400°C produced a similar cavity population to that observed at 500°C at 190 appm He, while the corresponding cavities at 500°C are slightly larger and more numerous at 380 appm He. The cavity strings were less obvious for the 400°C irradiations, and the bubble distribution appeared to be more random. No cavities were observed in the case of the 300°C irradiations. Overall the cavity number densities compare favorably with those previously reported [4], but details, including size distributions, are still under investigation. Dislocation structures were complex and varied greatly as a function of irradiation dose and temperature, and will be more thoroughly characterized in the next phase of the work.

PROGRESS AND STATUS

Introduction

Understanding the effects of He accumulation during neutron irradiation is a key challenge to developing materials for fusion energy. For example, He bubbles in the grain interiors and He on grain boundaries enhance void swelling and fast fracture, respectively. The key to understanding the effects of He, is a corresponding understanding and models of its transport and fate, including interactions with displacement damage, and as mediated by both metallurgical (starting composition, dislocation, grain and precipitate structures) and irradiation (dpa and dpa rate, He/dpa ratio, temperature) variables.

A novel *in situ* implantation technique was used to uniformly inject He into 3-mm diameter TEM discs to a depth of about 5-8 μm. The He is generated by two-step transmutation reactions in Ni contained in a NiAl coating layer adjacent to paired 3 mm TEM discs. The He/dpa ratios are determined by the thickness of the Ni-Al layer. The *in situ* injection technique has been applied to a large matrix of structural steels and model alloys in the JP26-29 experiments in HFIR. Details of this coating process and irradiations have been described in detail in earlier publications [2-5]. Here we focus on *in situ* implantation studies of a TMS alloy F82H mod 3 in both AT and CW conditions, at various temperatures, dpa and He levels.

Experimental Procedure

The F82H alloy irradiated in this study is a high-Ta variant called F82H-mod3 [4] produced by modifying the F82H-IEA alloy, with 7.5 %Cr, 2 %W, 0.2 %V, 0.1 %C, 0.1 %Si, 0.02 %Ta and 60 ppm N. The N and Ti were reduced to 14 ppm and 0.001%, respectively, in mod3 and the Ta was increased to 0.1%. The AT condition involved austenitization at 1040°C for 30 minutes followed by normalization (air-cooling) and tempering at 750°C for 1.5 hours. The CW condition was achieved by cold rolling AT coupons to a 20% thickness reduction. A large number of 3-mm TEM discs were punched and coated with a thin Ni-Al intermetallic layer by electron beam deposition at the UCSB Materials Processing Laboratory. Nominal coating thicknesses were 1, 2 and 4 μm, which yields He/dpa ratios of 5, 20 and 40 in the HFIR PTP position at 9 dpa. The discs in this study were irradiated in HFIR JP26 experiment at 300, 400°C to 3.9 dpa and at 500°C to 9 dpa. A summary of the irradiation matrix is shown in Table 1.

Table 1. Irradiation Matrix for F82H mod3 for both AT and CW conditions. The shaded conditions have not been examined.

Nominal Ni-Al Thickness	300°C, 3.9 dpa	400°C, 3.9 dpa	500°C, 9 dpa
	Total He (appm)	Total He (appm)	Total He (appm)
0	0	0	0
1	20	20	95
2	45	45	190
4	90	90	380

Cross-sectional TEM specimens were prepared by mounting the implanted disc between two pieces of a split Mo rod. The rod was then sectioned into thin wafers, composed of a sandwich of Mo-F82H-Mo. The wafers were then mounted on a stainless steel washer for support, dimpled and ion milled to electron transparency in a Gatan Precision Ion Polishing Instrument at 5 keV with 6° tilt in the dual beam mode. The milling started in the middle of the F82H and gradually expanded until perforation was achieved at the vicinity of the Ni-Al interface. This process yielded a continuous range of thinned material over distances that can be referenced to the Ni-Al layer. To remove as much of the ion damage as possible, a final 20 minute ion polish was carried out at 1.9 keV and 4° tilt.

The cross-sectional TEM specimens were characterized using a JEOL 2010F at PNNL. The instrument was operated at 200 keV and all images were recorded digitally using a Gatan ORIUS CCD camera. Various techniques were used to image the cavity and dislocation microstructures. Through focal sequence images were used to study the bubbles and void microstructures in the lath interiors and at interfaces. Images taken both within and outside the uniform He deposition region were carefully examined in order to better understand surface and Ar ion milling artifacts. Dislocations were imaged using **g(**011) reflections, and thickness estimates were obtained using convergent beam diffraction.

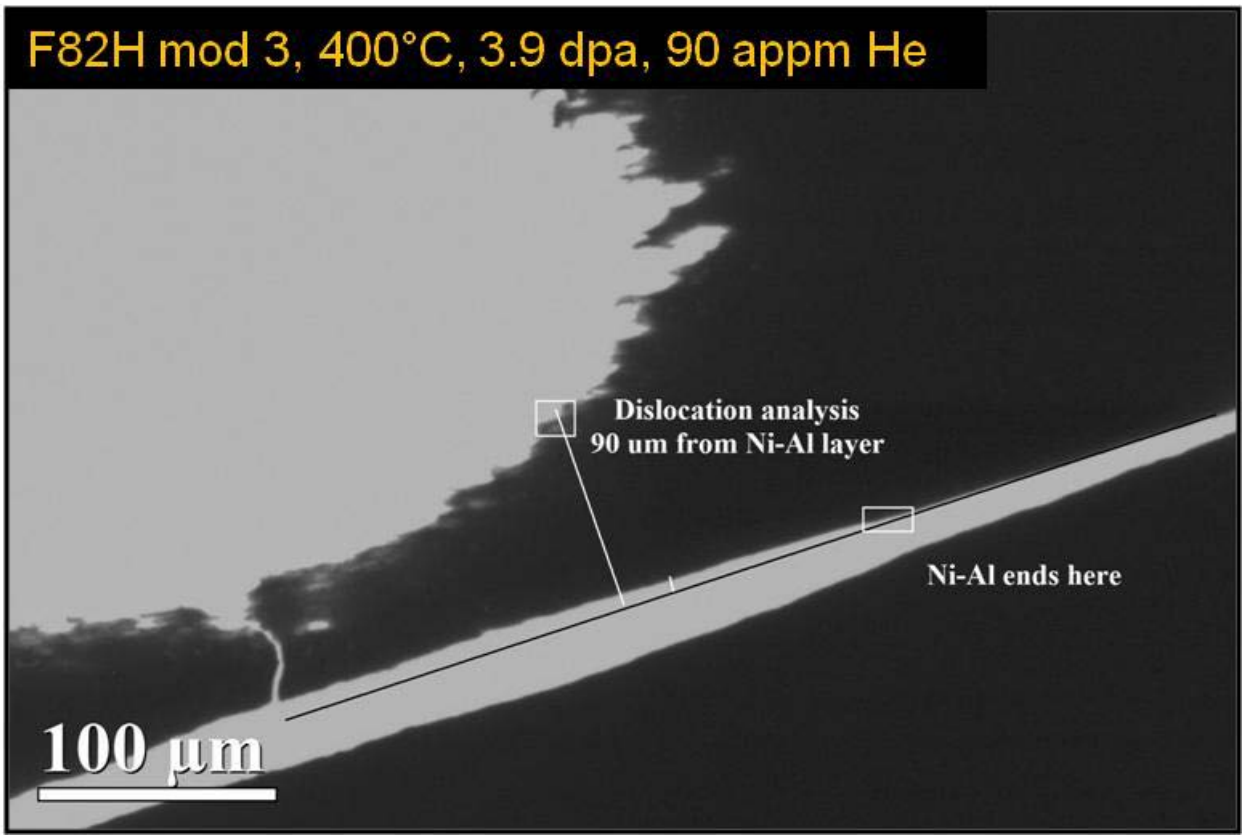

Figure 1. A low magnification image of a cross-section sample after final ion polishing.

A low magnification example of a thinned sample after final ion polishing is shown in Figure 1, highlighting the location of the Ni-Al interface. Individual samples thinned a bit differently, but overall it was possible to reliably characterize the microstructure both within and outside the uniform He deposition layer.

Results and Discussion

The average size and number density of the cavities for the two alloy and various irradiation conditions are summarized in Table 2. In this report we use the term cavities in a generic sense to refer to both He-filled cavities and faceted voids. By definition voids are larger, and in this case faced features, while bubbles are smaller and below the critical size and He content to growing voids. The presence of bubbles and void is often manifested in a bimodal cavity size distribution, although the precise transition between the two forms at intermediate sizes may be difficult to distinguish We first describe results for irradiations at 500°C to 9 dpa. Examples of strings of bubbles and voids found in two regions are shown in Figure 2 for the AT alloy containing 380 appm He. These results suggest a strong cavity association with dislocations. However, tilt experiments indicated that this association did not persist since dislocations were no longer present in the vicinity of the cavity stringers. Presumably, the He bubbles nucleated on pre-existing dislocations, but under further irradiation the dislocations climbed away, perhaps before the formation of voids. Note that the observation of strings of cavities was reported in our earlier work; however, at the time it wasn't clear if the original dislocations were still present. The comparison in Figure 3 shows a distribution of smaller, less numerous and more randomly distributed cavities in the AT alloy containing a lower concentration of 190 appm He. Cold working increases the density and decreases the size of the visible cavities, and appears to suppress the formation of larger voids.

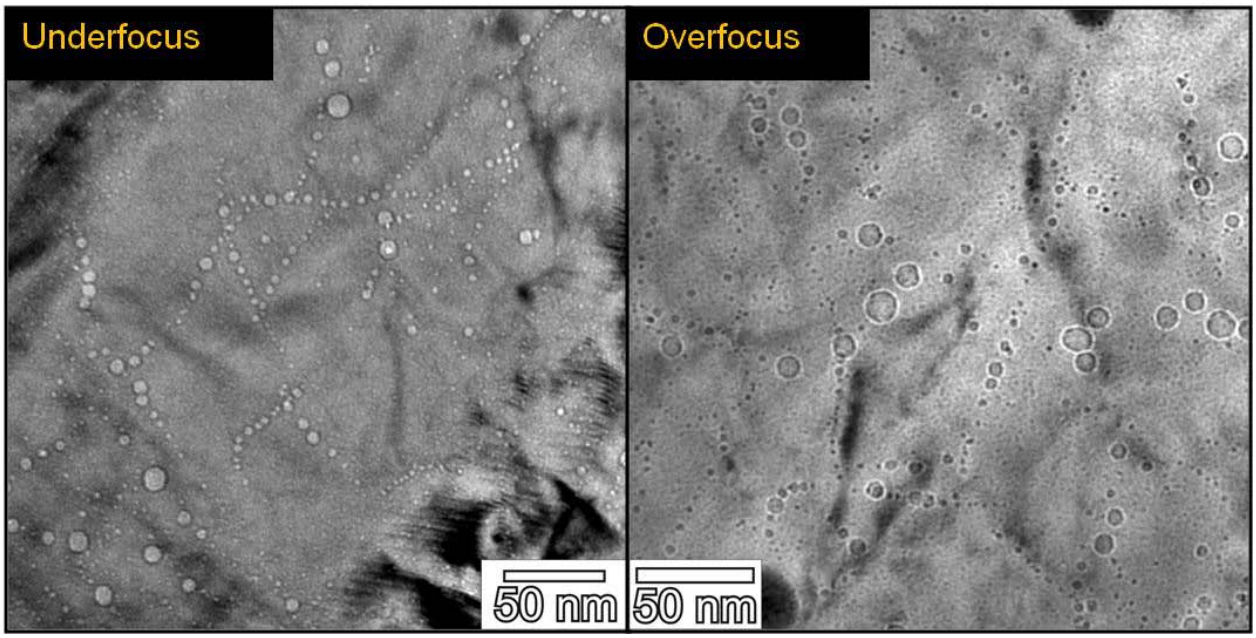

Figure 2. Examples of the bubbles and voids formed during irradiation at 500°C in the AT F82H mod3. The images were taken in different regions, one in the underfocussed (-1280 nm) condition and the other in the overfocussed (+1280 nm) condition. Most cavities appear to have formed on pre-existing dislocations that are no longer present, perhaps due to climb during irradiation.

As shown in Figure 3, bubbles were also observed on lath boundaries and carbide interfaces in both the AT and the CW conditions at both 190 and 380 appm He. Virtually all lath boundaries appeared to have a high density of small bubbles, while the corresponding bubble association with carbides was more sporadic. The numbers and sizes of the interface bubbles have not yet been quantified.

In the case of irradiation at 400°C to 3.9 dpa and 90 appm He, cavities were clearly observed only in the AT condition. Smaller features that may be bubbles were seen in both the AT and CW condition, but they could not reliably be distinguished from ion polishing and surface artifacts. Examples of the cavities in the AT alloy are shown in Figure 4 in regions with different thickness. The cavity distribution appears to be more random in this case, with less obvious association with either dislocations or interfaces. These results are not surprising, since lower temperature alone would be expected to result in smaller more homogeneously nucleated bubbles. Thus these observations are consistent with a population of sub-visible bubbles that require higher dpa and He levels to grow to the size range where the can be clearly observed in TEM. TEM did not identify any cavities that could be distinguished with confidence from the surface and ion polishing artifacts for the 300°C irradiations. Comparisons of cavity size distributions for the various irradiation and alloy conditions are shown in Figure 5.

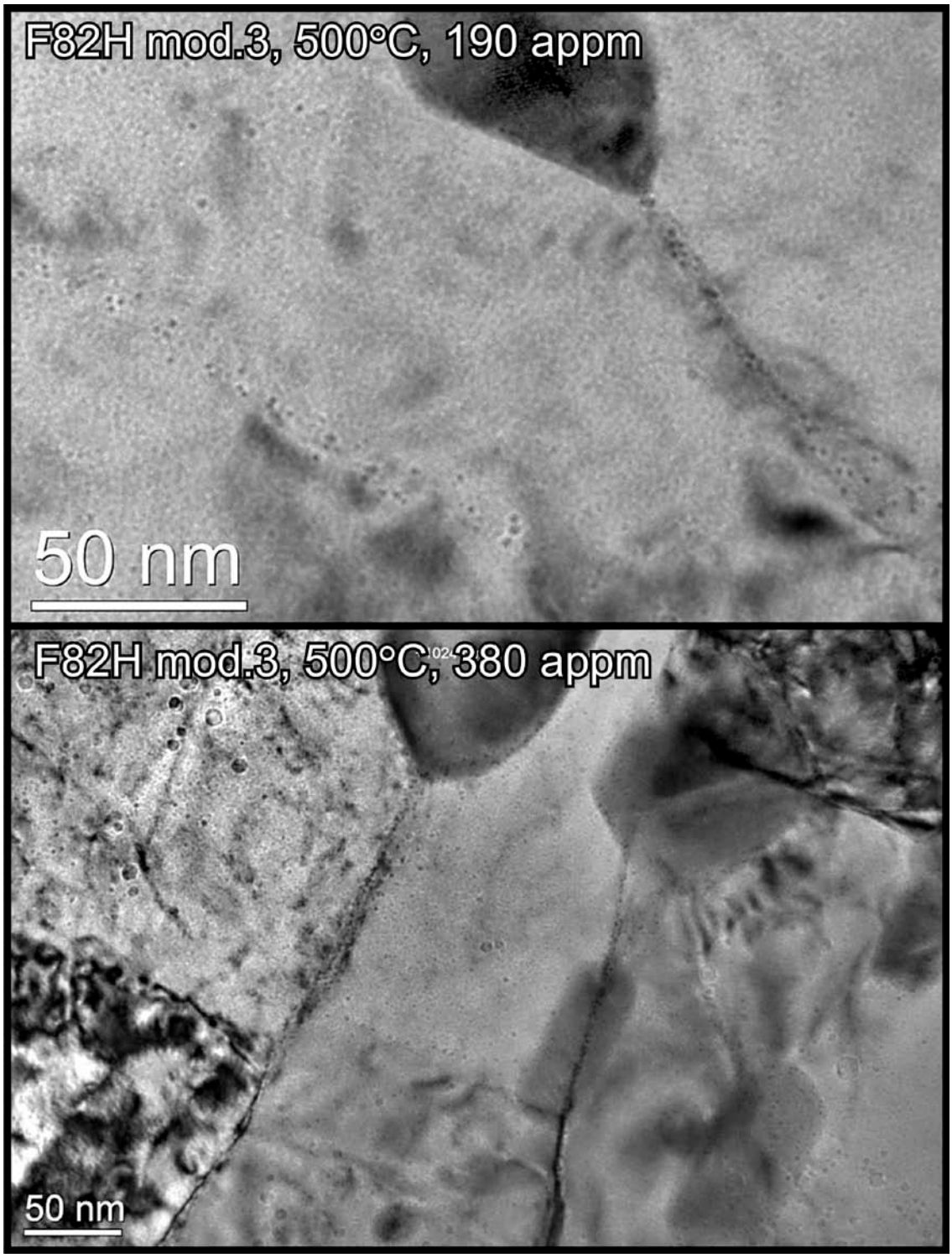

Figure 3. TEM bright field images showing He bubbles on lath boundaries and carbide interfaces in the AT F82H mod3 alloy irradiated at 500°C to the indicated He levels. Small He bubbles decorate virtually every lath boundary, whereas bubbles are somewhat more sporadically distributed on the carbide interfaces. Both images were taken in an overfocussed condition.

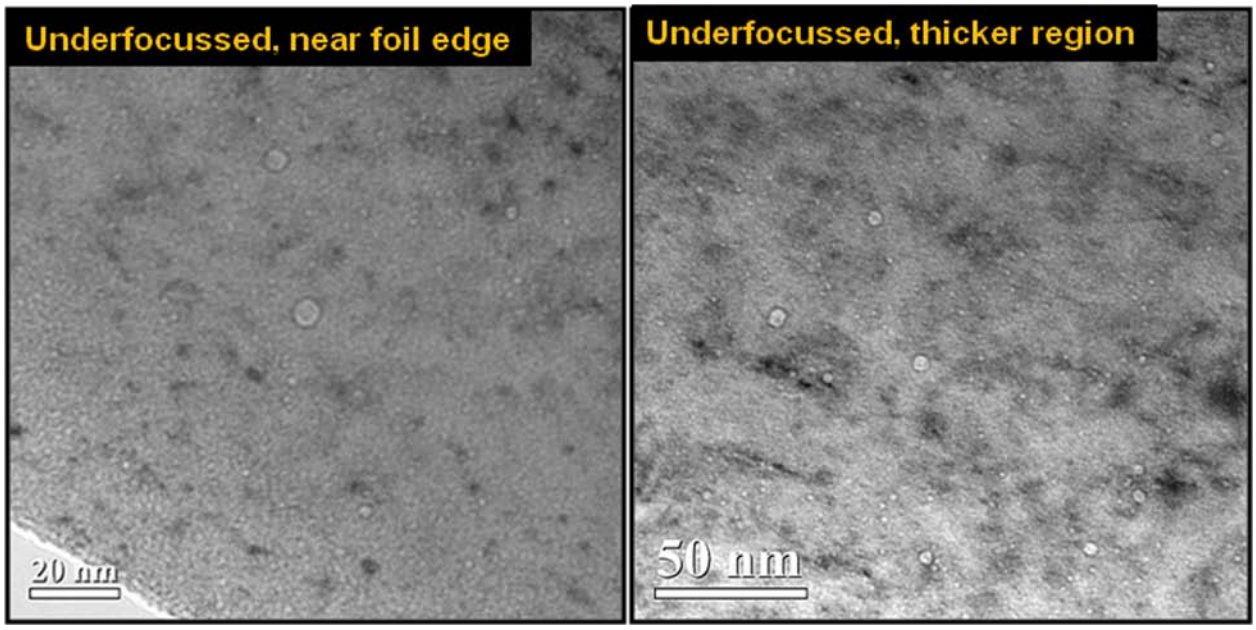

Figure 4. Small He bubbles and larger voids are visible in the AT F82H samples irradiated to 3.9 dpa at 400°C. The bubbles are randomly distributed in the lath interiors, with much less association with lath boundaries, carbide interfaces or dislocations compared to that observed at 500°C.

Table 2. The average diameter and number density of the cavities.

	As-Tempered			As-Tempered & 20% Cold Worked	
	400°C 90 appm	500°C 190 appm	500°C 380 appm	500°C 190 appm	500°C 380 appm
Avg. Size with Std Deviation (nm)	2.6 ±1.3	2.4 ±1.5	3.4 ±1.6	1.4 ±0.3	1.9 ±0.7
Density (m^{-3})	5.7×10^{22}	5.2×10^{22}	7.9×10^{22}	8.1×10^{22}	1.1×10^{23}

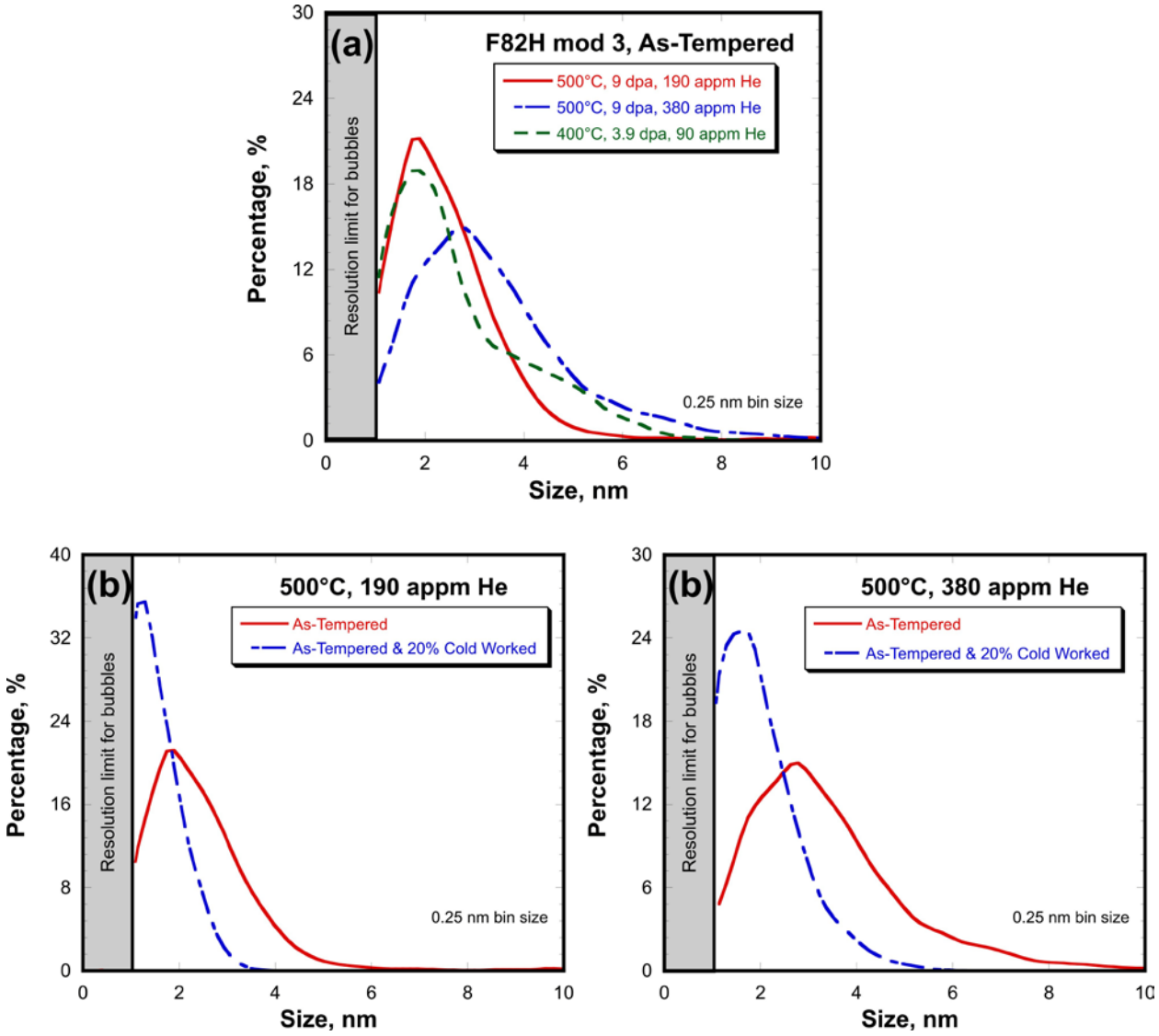

Figure 5. Size distributions are shown comparing the cavity distributions in F82H mod3 alloy irradiated at (a) 400°C and 500°C and (b) irradiated at 500°C for two different He levels in both the AT and CW conditions. ***Note:*** *The cavity size distributions and number densities are being reexamined. A practical resolution limit is about 1 nm. While bubbles smaller than 1 nm can be seen, it is difficult to accurately measure their size. Furthermore, there exists the possibility of bubbles being present that are too small to separate from the artifacts in the foil.*

Examples of the dislocation structure at all three irradiation temperatures are shown in Figure 6. Preliminary characterization of the alloys irradiated at 500°C revealed a moderate density of line dislocations accompanied with a low density of large loops in both the AT and CW conditions. A rough estimate taken from bright field images near a **g**(011) vector indicates a dislocation density of≈ 0.8 x 10^{15} m^{-2} in both alloy conditions. Given the surprising result that the dislocation densities are similar between the AT condition and AT & CW condition, these preliminary observations need further elaboration and confirmation, including determining the nature of the line dislocations. At 400°C, relatively large dislocation loops were the dominant irradiation induced feature. In the AT condition the loops had an average size of ≈13 nm with a number density of ≈10^{21} m^{-3}. In the CW condition the loop size was slightly larger at ≈ 20 nm with a lower density of ≈ 0.6 x 10^{21} m^{-3}. Again, these numbers will be refined and the nature of the loops determined in ongoing work. The dislocation structure at 300°C in the AT condition was composed of a uniform density of line segments. In the CW condition, the dislocation structure was dominated by a tangled network of line dislocations introduced by the cold working prior to irradiation. Small dislocation loops in the range of 1-5 nm could be seen, but their density has yet to be determined. Notably, the dislocation structures were qualitatively similar in the in both the He-implanted and unimplanted regions.

Summary

Irradiation at 500°C to 9 dpa at 380 appm He? led to a large population of bubbles and smaller number of voids. Most of the cavities were associated with pre-existing dislocations in both the AT and CW conditions. In the AT condition containing 380 appm He, the dislocations appear to have climbed away from the stringers of voids and bubbles that formed on the dislocations at earlier stages in the irradiation. Some evidence of residual void/bubble-dislocation association was found for the 500°C irradiations that produced 190 appm He. Cold working led to a larger number of smaller cavities and suppressed the formation of larger voids. Smaller bubbles were also observed on lath boundaries and to a lesser extent carbide interfaces in all four alloy-irradiation conditions at 500°C.

Irradiation of the AT alloy at 400°C to 3.9 dpa and 90 appm He resulted in a similar number density and average size of cavities compared to those observed the 500°C irradiation that produced 190 appm He. The cavities also didn't appear to be as strongly associated with dislocations at the lower He level and temperature. Bubbles in the CW condition irradiated at 400°C could not be distinguished from possible artifacts, so measurements exist for this condition. Similarly, bubbles that could be clearly distinguished from foil artifacts were not observed in the case of the 300°C irradiation, in either the AT or CW conditions.

Preliminary characterization of the dislocation structure yielded a complex picture of varying densities of line dislocations, dislocation loops and line segments that vary depending on the irradiation temperature and dose as well as the AT versus CW condition. However, these preliminary observations suggest that He has little qualitative effect on dislocation structures.

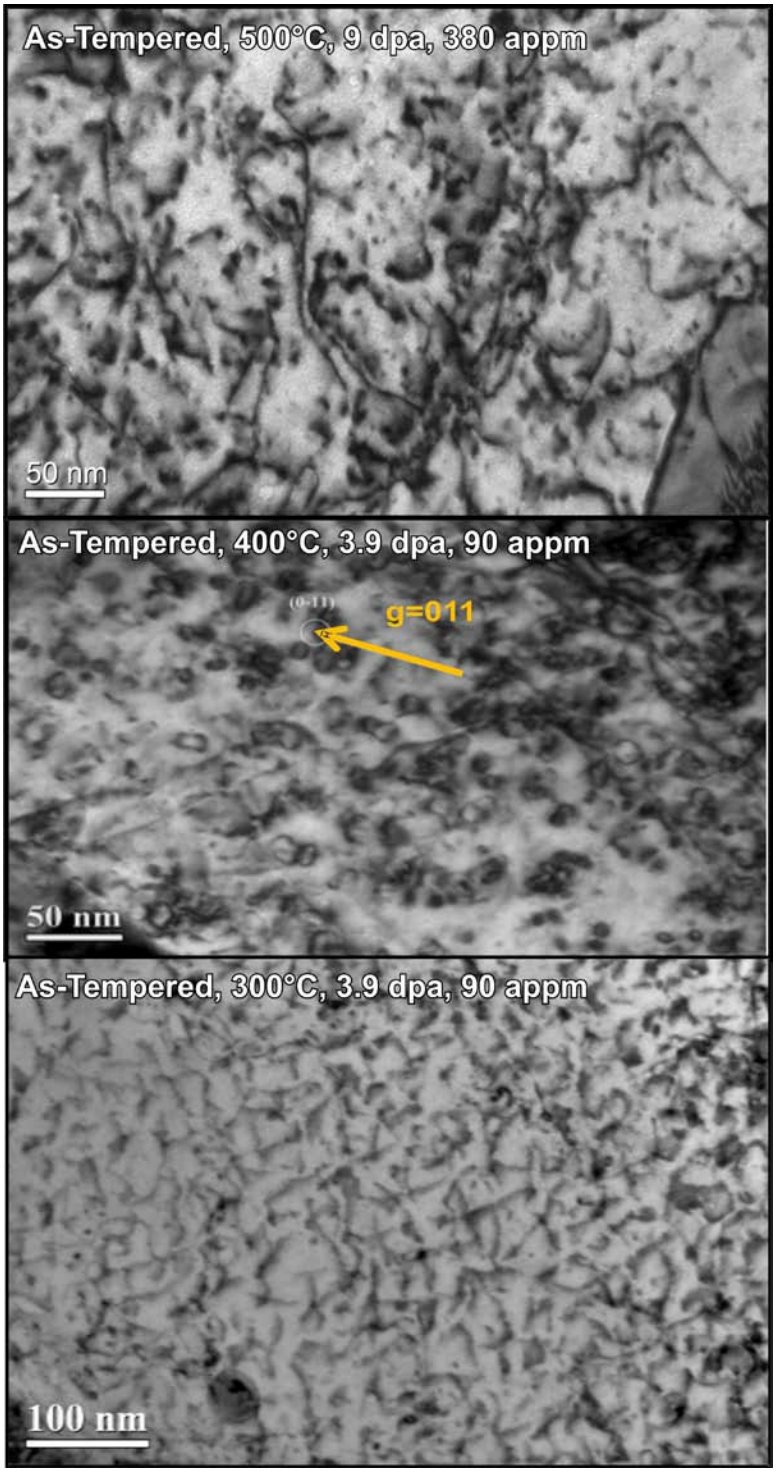

Figure 6. Dislocation structures in the AT condition after irradiation at 300, 400 and 500°C. Variations in the irradiation temperature and dose lead to significant differences in line versus dislocation loop populations. The nature of these dislocation structures will be determined in subsequent work.

References

1. G.R. Odette, P. Miao, T. Yamamoto, D.J. Edwards, R.J. Kurtz, Fusion Materials Semiannual Report 1/1 to 6/30/2008 DOE/ER313/44 (2008) p. 41.
2. T. Yamamoto, G. R. Odette, P. Miao, D. T. Hoelzer, J. Bentley, N. Hashimoto, H. Tanigawa, R. J. Kurtz, *J. Nucl. Mater.* **367-370** (2007) 399.
3. R.J. Kurtz, G.R. Odette, T. Yamamoto, D.S. Gelles, P. Miao, B.M. Oliver, *J. Nucl. Mater.* **367-370** (2007) 417.
4. T. Yamamoto, G.R. Odette, P. Miao, D.J. Edwards, R.J. Kurtz, *J. Nucl. Mater.* **386–388** (2009) 338–341
5. T. Yamamoto, G. R. Odette, L. R. Greenwood, *Fusion Materials Semiannual Report 1/1 to 6/30/2005* DOE/ER-313/38 (2005) 95.

Characterization of Y Distributions and Nano-feature Formation In As Atomized, Milled, Milled and Annealed and Milled and Consolidated 14YWT Powders

N. J. Cunningham, Y. Wu, G. R. Odette and T. Yamamoto (University of California Santa Barbara)

SUMMARY

We report here on work supported by the DOE Office of Nuclear Energy that is complementary to our OFES work on nano-structured ferritic alloys (NFA) for fusion applications. Three variants of Fe14Cr3W0.4Ti0.2Y rapidly solidified powders were gas atomized by Crucible Research (CR) in Ar, Ar/O and He atmospheres. This work is part of an collaborative effort between CR, LANL, ORNL, UCSB, UC Berkeley and South Dakota School of Mines to develop larger heats of NFA using best practice processing routes. One objective was to determine if rapid solidification could introduce a uniform distribution of Y prior to mechanically alloying (MA), which is the standard method for mixing Y in NFA powders. The Y distribution in the powders was characterized by TEM, EPMA, APT and SANS in as atomized, ball milled and milled and annealed conditions. It was found that pre-alloying Y during gas atomization does not produce a uniform Y distribution. However, sufficient ball milling improves the homogeneity of the Y distribution. A bimodal grain size distribution was observed in the milled and annealed powders for all gas atomization atmospheres, and Y-Ti-O precipitates are present in both the large and small grains in sizes and quantities comparable to other NFA.

Introduction and Background

Nano-structured ferritic alloys (NFA) have high tensile and creep strength permitting operation up to 800°C, manifest remarkable resistance to radiation damage and can manage a high concentration of He [1]. These outstanding properties derive from an ultrahigh density of Ti-Y-O enriched nano-features (NF) that provide dispersion strengthening, help stabilize dislocation and fine grain structures, reduce excess concentrations of displacement defects and trap He in fine bubbles [1].

NFA are typically processed by MA rapidly solidified powders with Y_2O_3. The Y and O dissolve in the Fe matrix, subsequently precipitating with Ti during hot consolidation. However, the distribution of NF is often non-uniform, due to a corresponding non-uniform distribution of Y. Previous research suggested that the larger grains have a low density of NF [2].

Pre-alloying rapidly solidified powders with Y during gas atomization could, in principle, produce a more uniform dispersion of this element. If successful, this approach could significantly reduce, or even eliminate, ball milling times. Our specific objectives were to evaluate similarities and differences in three powder variants by characterizing the Y distribution in the as-atomized powders, following SPEX milling for 10 h and after annealing that mimics HIP consolidation temperature-time histories. The CR powders in the milled and annealed condition were also compared to conventional MA milled and annealed NFA powders and MA957.

Material and Methods

Three rapidly solidified powder variants with nominal composition (wt%) Fe-14Cr-3W-0.4Ti-0.2Y were acquired from CR. The variants involved gas atomization in different atmospheres - Ar, Ar/O, and He. The Ar atmosphere is standard. The Ar/O mixture was used to introduce a specified concentration of≈ 0.15 wt% O. The higher thermal conductivity He atmosphere was intended to explore the effect of higher powder cooling rates on the Y distribution. Small charges of each powder variant were severely deformed in a SPEX shaker mill under the following conditions: 5:1 ball mass to charge ratio, 10h mill time, 100g ball mass and 8 mm ball diameters. A portion of the milled powder was then encapsulated, along with a Nb O getter foil, in a quartz tube and annealed at 1100°C for 3h in an inert He atmosphere with ramp rates of 15°C/min. Annealing is much more convenient and efficient than actual consolidation and previous research showed the NF formation is primarily dependent on temperature and time and not on consolidation [3].

A Cameca SX-50 electron probe micro-analyzer (EPMA) fitted with 5 wavelength spectrometers and a PGT X-ray energy dispersive detector was used to determine the Y content and distribution in the as-atomized powders, MA and MA and annealed powders. Fe, Cr, Ti, W, and O were also measured. The powder samples were mounted in a conductive polymer and polished on an Allied MultiPrep™ with a final polishing step using 0.05 μm colloidal silica. Three to five measurements, spaced≈ 5 μm apart, were made on each particle with a total of 15 to 45 data points taken on 5 to 9 particles.

SANS measurements were performed at the NIST Center for Neutron Research (NCNR) facility in Gaithersburg, MD [4]. All measurements used a neutron wavelength of 5Å and a sample to detector distance of 1.547 m. Each powder sample was contained in a sealed, 1100 series aluminum holder with 7.4 mm diameter by 2 mm deep pocket with aluminum window thicknesses of 0.25 mm. The detector was offset in the horizontal direction to increase the q-range. The samples were placed inside a strong magnetic field of around 1.7 T to separate the magnetic scattering from the nuclear scattering. A minimum of 5 million detector counts was acquired for each sample run. The scattering cross sections for each sample were then found after subtracting background and empty container scattering and normalizing for each sample mass and measured transmission relative to a water standard. To allow quantitative analysis, scattering from a control specimen without Y-Ti-O NF was also measured and subtracted from the sample scattering. The control was a Fe14Cr3W0.3Ti rapidly solidified powder that was also SPEX milled for 10 h and annealed at 1100ºC for 3 h. Further details on the SANS analysis are given in Ref. [5].

TEM measurements were performed on an FEI Tecnai G2 Sphera Microscope. Following a procedure by Harris [6], M-Bond 610 epoxy was mixed with each powder sample, and after partially curing, the powders were punched into 3mm disks, dimple ground, and then dual ion beam polished using a Gatan 691 ion polishing system, first at 5 kV and incrementally stepped down to 2 kV. Using bright field imaging and energy dispersive x-ray spectroscopy (EDS), the grain size was observed and the composition of the large precipitates was measured.

Atom probe tomography (ATP) measurements were performed using an Imago 3000X HR Laser LEAP. The atom probe samples were micro-machined by an annular milling technique, described by Miller [7], from the Ar atomized milled and annealed sample, using an FEI Helios 600 dual beam FIB in conjunction with an Omniprobe Autoprobe 200 manipulator. The FIB SEM was also used to image the grain structures of the powders. The SEM also allowed selecting atom probe lift out samples from both the large and small grain regions. The atom probe was run in the laser mode with run parameters of 0.15 nJ laser pulse energy, 0.5-2% evaporation rate, 33.5 K temperature and a pulse frequency of 200kHz.

Results

EPMA analysis showed that pre-alloying Y during gas atomization does not produce a uniform Y distribution and that MA is necessary to improve homogeneity. The average wt% Y and one standard deviation from all analysis points was found to be 0.214±0.170, 0.215±0.474, and 0.154±0.089 for the as-received Ar, Ar/O, and He atomized powders, respectively. After MA, the EPMA analysis shows much improved average and standard deviation values for Y of 0.206±0.027, 0.250±0.048, 0.196±0.035 for Ar, Ar/O, and He, respectively.

TEM and EDS showed the presence of large elongated and spherical Y rich features between 20 nm and 100 nm in all of the atomized powder variants. An example image of the He atomized powder is shown in Figure 1. Variations in size, morphology, and composition of the Y-rich precipitates were observed. Likely candidate phases include intermetallic Y_2Fe_{17} and complex yttrium oxides, as suggested by the EDS spectra shown in Figure 1.

SANS measurements showed almost no scattering in the high q-range associated with NF in the as-atomized powders compared to the control specimen. Only a small amount of additional scattering was present in the milled powders. In contrast, similar NF scattering was observed in all the powder variants after annealing, as shown in Figure 2a. Here the scattering cross section 45° to the magnetic axis is shown for the 3 powder variants in the milled and annealed condition, along with the Y-free milled and annealed control. Note the 45° curve represents the sum of the nuclear plus half the magnetic scattering. The large bulge in the scattering below $q \approx 2.5$ nm^{-1} is due to scattering of nm-scale features. Fits to the Ar atomized data showed a precipitate radius, volume fraction and number density of 1.5 nm, 1.47%, and 9.9 $X10^{23}/m^3$, which are comparable to other NFA materials such as MA957 [3]. This is shown in Figure 2b comparing the Ar atomized, milled and annealed powder with scattering curves for commercial vendor MA957 and previous data for powders that had been milled with Y_2O_3.

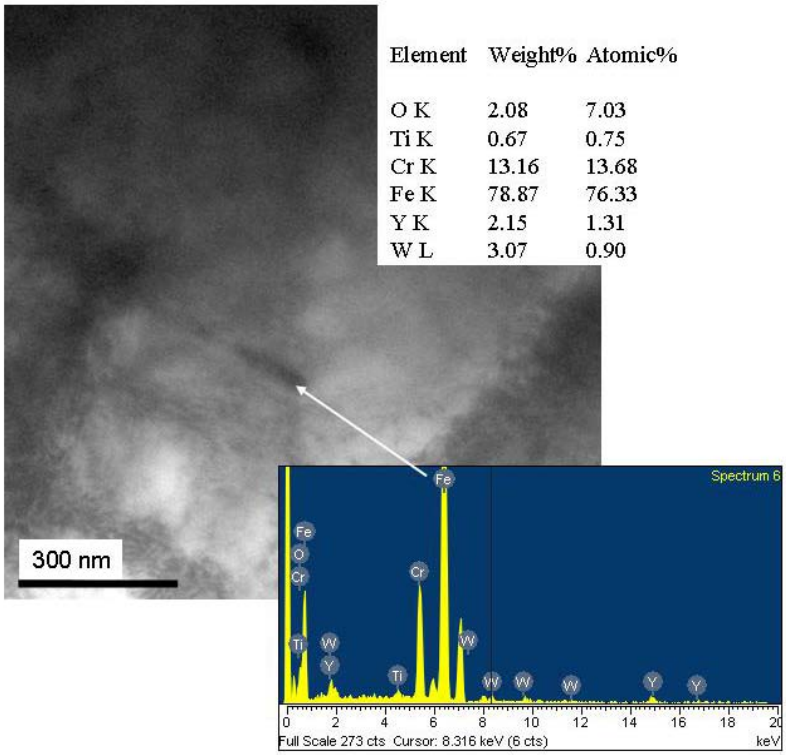

Fig. 1 Elongated Y-enriched feature in an as-received He atomized powder.

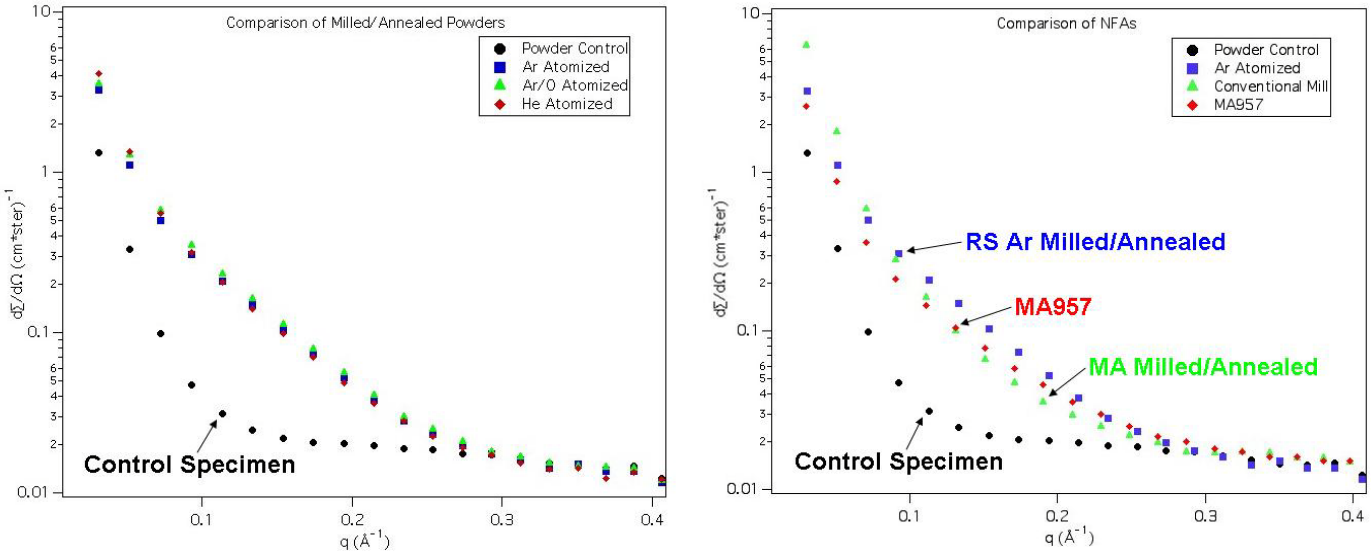

Fig. 2 a) Comparison of absolute scattering between Ar, Ar/O, and He atomized milled/annealed powders; b) Comparison of Ar atomized milled/annealed powder with MA957 and conventional MA milled/annealed powder.

SEM showed a bimodal grain size distribution in all three variants of the milled and annealed powders. Previous research suggested that the larger grains have a very low density of NF [including Hoelzer]. However, shown in Figure 3, APT found NF in both small and large grains in the Ar atomized milled and annealed powders. Eiselt et

al. recently reported a similar observation [8, 9]. The solute contents of the NF were similar, with average Y/Ti/O ratios of 30/30/40 for the small grains and 26/33/41 for the large grains. The number density of the precipitates was found to be 3.3 $X10^{23}/m^3$ and 7.5 $X10^{23}/m^3$ for small and large grains, respectively. These results compare well with TEM and SANS measurements of other NFA.

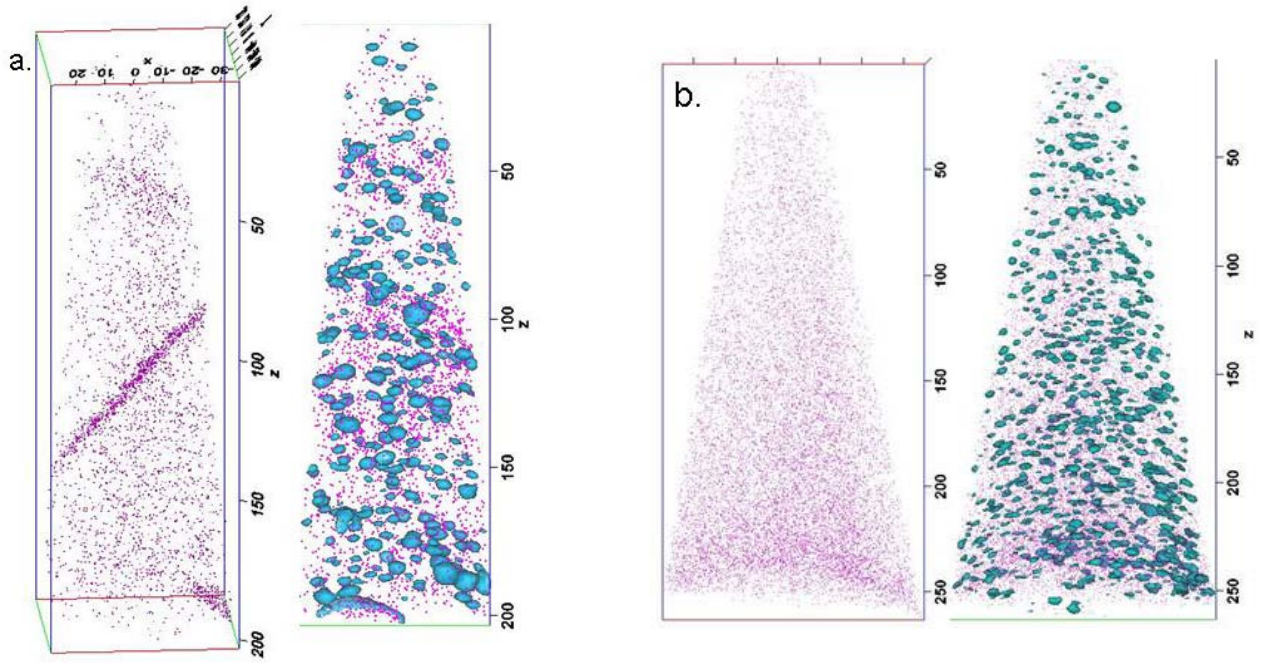

Fig. 3 (a) Phosphorus segregation and NFs in small grains in the Ar atomized milled/annealed sample and (b) NFs unexpectedly present in large grain.

Summary

The Y distribution in three variants of Fe14Cr3W0.3Ti0.2Y rapidly solidified powders was characterized at UCSB by TEM, EPMA, APT and SANS in the as atomized, MA, and MA/annealed conditions. Rapid solidification in all three atmospheres of Ar, Ar/O, and He produce large Y-enriched features and non-uniform Y distributions on a μm scale. While there are some apparent differences in their size, morphology and composition, TEM and EDS show Y rich particles between 0.02 and 0.1 μm in all three of the powder variants. However, SPEX ball milling for 10 h produces a uniform distribution of Y. The Y clusters along with O and Ti during annealing at 1100°C produce a high density of NF. There is a bimodal grain size distribution in all of the milled and annealed powders. Notably, Y-Ti-O precipitates are present in both the large and small grains. The size, number density, volume fraction and composition of the NF compare favorably to those found in other NFA, such as MA957.

Future Research

A large heat of Ar atomized 0.2Y powders will be prepared by CR. After systematic characterization and small batch processing studies are completed, the powders will be milled and consolidated by a best practice processing route.

References

1. G.R. Odette, M.J. Alinger, and B.D. Wirth, Annual Review of Materials Research, Vol. 38, (2008).
2. P. Miao, G.R. Odette, T. Yamamoto, M.J. Alinger, D.T. Hoelzer, and D. Gragg, J. of Nucl. Mater., 367–370 (2007) 208–212.
3. M. J. Alinger, On the Formation and Stability of Nanometer Scale Precipitates in Ferritic Alloys during Processing and High Temperature Service, Thesis (PhD), University of California Santa Barbara (2004).
4. C.J. Glinka, J.G. Barker, B. Hammouda, S. Krueger, J.J. Moyer, and W.J. Orts, J. Appl. Cryst., 31, (1998), 430-445.

5. M.J. Alinger, G.R. Odette, and D.T. Hoelzer, Acta Mater, 57 (2009), 392-406.
6. A.M. Harris, G.B. Schaffer, and N.W. Page, J. Mater. Science Letters, 12, (1993), 160-161.
7. M.K. Miller, Atom Probe Tomography: analysis at the atomic level, Kluwer Academic/Plenum, New York, (2000).
8. C.C. Eiselt, M. Klimenkov, R. Lindau, A. Möslang, H.R.Z. Sandim, A.F. Padilha, and D. Raabe, J. Nucl. Mater., 385 (2009) 231-235.
9. C.C. Eiselt, M. Klimenkov, R. Lindau, and A. Möslang, J. Nucl. Mater., 386-388 (2009) 525-528.

Helium Transport, Fate and Management in Nanostructured Ferritic Alloys: In Situ Helium Implanter Studies – G. R. Odette, P. Miao, T. Yamamoto (University of California Santa Barbara, Santa Barbara), D. J. Edwards, R. J. Kurtz (Pacific Northwest National Laboratory) and H. Tanigawa (Japan Atomic Energy Agency)

OBJECTIVE

Objective of the study to understand transport and fate of transmutation helium using thin Ni-bearing implanter layers to inject high-energy a-particles into an adjacent sample simultaneously undergoing neutron induced displacement damage. We summarize here the results of microstructural studies on a 14Cr-NFA, MA957, following HFIR irradiations at 500°C to 9 dpa and 380 appm, with a focus on TEM characterization of cavities formation and the association of these cavities with NF and other interfaces.

SUMMARY

High helium levels produced in fusion neutron spectra may lead to severe increases in the brittle fast fracture temperature, enhanced void swelling and degradation of creep rupture properties at lower, intermediate and higher irradiation temperatures, respectively. Thus it is important to develop structural alloys with stable microstructures that can manage helium based on understanding of its transport, fate and consequences. We report on the initial results of a study of helium f in a nanostructured ferritic alloy (NFA), MA957, that is dispersion strengthened by an ultra-high density of nm-scale Y-Ti-O nanofeatures (NF). An in situ helium implanter technique uniformly deposited ≈ 380 appm helium to ≈ 6 μm in MA957 irradiated in the High Flux Isotope Reactor (HFIR) to 9 dpa at 500°C. Through focus transmission electron microscopy (TEM) showed that helium is in extremely fine bubbles that often appear to coincide with bright field features taken as NF.

PROGRESS AND STATUS

Introduction

Predicting and mitigating the effects of a combination of large levels of transmutant helium and displacement damage (dpa) produced by high energy neutrons on the dimensional stability and mechanical properties of structural materials is one of the key challenges to developing of fusion energy. Fundamental questions about helium-dpa synergisms include: a) what are the basic interacting mechanisms controlling helium and defect transport, fate and consequences, and how are they influenced by the microstructural and irradiation (dpa rate, He/dpa ratio, temperature and applied stress) variables; and, b) how can the detrimental effects of high He-dpa synergisms be mitigated and managed by proper microstructural design? We have proposed that NFA containing an ultra-high density of NF that pin dislocations, resulting in remarkably high creep strength, could mitigate radiation damage by trapping helium in fine bubbles, while permitting operation at temperatures above the displacement damage accumulation regime [1].

We have shown that in-situ He implantation in mixed spectrum fission reactor irradiations provides a very attractive approach to assessing the effects of helium-dpa synergisms [2-7]. The basic idea is to use thin Ni (or B or Li)-bearing implanter layers to inject high-energy a-particles into an adjacent sample simultaneously undergoing neutron induced displacement damage. In this case, irradiations in the HFIR uniformly implanted 4.8 MeV a-particles (helium) to a depth of 5 to 8 mm at controlled helium/dpa ratios from ≈ 5 to 40 appm/dpa. The helium -implanted region is suitable for extensive microstructural characterization by TEM (and, potentially, a variety of other techniques) and is sufficiently thick to permit low load microhardness or nanohardness measurements. We summarize here the results of microstructural studies on a 14Cr NFA, MA957, following HFIR irradiations at 500°C to 9 dpa and 380 appm. These results focus on TEM characterization of the transport and fate of helium in forming cavities (helium bubbles), and the association of these cavities with NF and other interfaces. These observations

are briefly compared to the corresponding results for an 8Cr normalized and tempered martensitic steel (TMS), F82H, reported elsewhere [7].

Experimental Procedures

The Fe-14Cr, 0.9Ti, 0.3Mo and 0.5Y_2O_3 (wt.%) INCO MA957, examined in this study, was supplied by A. Alamo (CEA) in the form of a 9 mm thick, 65 mm outer diameter thick-walled tubing. The tube was fabricated by center drilling an as-extruded bar followed by hot extrusion to form the tube. Further details of the processing history of the French MA957 tube are not available. However, the micro and nanostructures of the French MA957 broadly resemble that found in a US heat of MA957 in the 1150°C as-extruded condition. Small angle neutron scattering (SANS) measurements show the French MA957 contains ≈ $7x10^{23}/m^3$ NF with an average diameter of ≈ 2.6 nm and volume fraction of 0.7% [8].

Three mm diameter, 0.2 mm thick TEM discs were irradiated in the HFIR JP26 experiment at 300, 400 and 500°C to produce a range of dpa and He/dpa for a large matrix of alloys, including the French MA957 studied here. A thin NiAl intermetallic layer was electron beam co-deposited at UCSB on discs that were paired with adjacent uncoated discs. Target coating thicknesses of 1, 2 and 4 μm produced nominal He/dpa ratios of 5, 20, and 40 at 9 dpa.

An electron transparent TEM specimen was prepared by focused ion beam micromachining (FIBed). The initial FIBed specimen contained substantial amounts of surface contamination, including features that could be easily confused with NF or bubbles [5]. Thus the specimen was re-FIBed and subsequently plasma cleaned prior to re-examination at the Pacific Northwest National Laboratory (PNNL) on a 200 keV JEOL 2010F TEM in transmission with digitally recorded images. A flash polishing techniques was also developed involving ≈ 5 second electro-polishing in 2% perchloric/2-butoxyethanol solution to further clean-up the specimen surfaces; however, flash polishing was not found to be necessary in this study. The TEM characterization focused on the NF and helium bubbles. The NF were imaged under both bright field and weak beam dark field conditions. The NF observed in TEM were found to be broadly comparable to those found in the SANS studies as well as with other TEM studies at UCSB [8]. The cavities were primarily characterized by the through-focus sequence technique. They appear as white regions surrounded by a dark ring in the under-focused condition (-512 to -1024 nm), as dark regions surrounded by white rings in the over-focused condition (+512 to +1024 nm); the cavities are largely invisible in the focused condition. Local foil thicknesses were measured by convergent beam electron diffraction (CBED).

Given the very small size of the cavities, special efforts applied to the image analysis of the micrographs. The features observed in the three sets of images processed by Photoshop for the through focus sequence were individually identified by overlay comparisons. Cavities were identified as those features that clearly showed a bright-dark contrast in the under-over focus conditions. The NF were identified as those features appearing under in-focus conditions. Cavities are found in both the matrix and in probable association with the NF and larger precipitates. Of course, it is not possible to ensure the absence of some artifacts in these observations, particularly since the cavities are so small. Thus some features that are not cavities may be counted as such, while other cavities may remain invisible. The results unambiguously show the absence of larger cavities, such as those observed in TMS (see below) [7], and this conclusion is further supported by the fact that cavities are generally not observed in the un-implanted regions of the irradiated French MA957. Thus the results described below represent a best estimates of the cavity population in the helium implanted French MA957.

Experimental Results

Figure 1 shows a typical through-focus sequence image for the implanted region at -1024 nm underfocus (a), +512 overfocus (b) and in-focus (c) imaging conditions. The imaging sequence showed a high degree of association between over-focused, darkly imaging features and under-focused, brightly imaging features (again note, the features that did not image in both cases were not counted as cavities). There is

also a high, but slightly smaller, association between the cavities and particles that show contrast for the in-focus condition, which are assumed to be NF. The micrographs also show that cavity-NF combinations appear to be fairly frequently associated with dislocation line segments. Figure 1d illustrates the general absence of cavities in the un-implanted region. Figure 2 shows the cavity size distribution in the helium implanted MA957 compared to that observed in TMS F82H-mod.3 [7]. The size distribution is much narrower in the MA957, with a maximum cavity diameter of less than 2.5 nm and an average diameter of 1.3 nm. In contrast, the largest cavity diameters exceed 10 nm in F82H, with an average value of 2.8 nm. The corresponding number densities are $4.3x10^{23}/m^3$ and $5x10^{22}/m^3$ for MA957 and F82H, respectively. Figure 3 shows another -1024 under-focused image of an implanted region containing larger particles and a boundary. Examples of the decoration of particles with associated cavities are shown in the inserts. The boundary appears to be relatively cavity free, and there does not seem to be a large nearby NF-cavity denuded zone. Figure 4 shows blow up views of through focus sequence images of cavities attached to larger particles.

Discussion

While we have referred to cavities in the previous discussion, it seems likely that these features are actually near-equilibrium helium bubbles with a gas pressure $P_g \approx 3Z(P_g)mkT/4\pi r_b^3 \approx 2g/r_b$ [10], where g is the surface energy, r_b is the bubble radius, m is the number of helium atoms in the bubble and $Z(P_g)$ is the compressibility factor (> 1) for high pressure helium [10]. Assuming equal partitioning of all the 380 appm helium to $4.3x10^{23}$ bubbles/m^3 (≈ 70 helium atoms/bubble) and g =2 J/m^2 gives $r_b \approx$ 1.3 nm at 500°C, in remarkable agreement with the measured average cavity size. Thus we conclude that helium in the implanted MA957 is primarily stored in near-equilibrium bubbles at a capillary pressure of $2g/r_b \approx$ 2670 MPa. A higher helium content of 2000 appm helium partitioned to the same number of bubbles (≈ 370 helium atoms/bubble) increases r_b to 2.2 nm. Note, once established helium bubbles act as very deep traps for helium. Thus the helium stored in matrix bubbles is prevented from reaching and thereby embrittling grain boundaries.

Such microstructures are also highly resistant to void swelling. Voids are cavities with $P_g <$ to << $2g/r_b$ that unstably grow by accumulating an excess flux of vacancies over self-interstitial atoms (SIA) flowing to them, due to a bias of dislocation sinks for the SIA [1,11-13]. For a specified sink microstructure and irradiation condition, cavities grow as stable bubbles up to a critical helium content, m*, where they convert to unstably growing voids, leading to bimodal cavity size distributions [10-13]. Thus the incubation dose, dpa_i, prior to the onset of rapid void swelling is governed by the requirement that a significant population of bubbles reach the ≥m m* condition. A corollary is that the incubation dose, dpa $_i$, decreases with the number of bubbles.

However, helium bubbles also act as neutral sinks for annihilating and equal number of vacancies and SIA. The corresponding sink strength is $Z_b \approx 4\pi r_b N_b$, or ≈ $7x10^{15}/m^2$ for $4.3x10^{23}/m^3$, 1.3 nm bubbles, is much higher that typical of other sinks, including SIA biased dislocations (typically $Z_d < 1x10^{15}/m^2$). Such high neutral sink strength results in a low radiation induced vacancy flow excess, $D_vX_v - D_iX_i$, where D is the diffusion coefficient and X the atomic fraction of vacancies (v) and SIA (i), respectively. The effective vacancy super-saturation is defined as $f = [D_vX_v - D_iX_i + D_{sd}]/D_{sd}$, where D_{sd} is the self-diffusion coefficient. If f is low (≈ 1), which is the case for large Z_d, then m*, which is proportional to≈ $1/[1-f]^2$, is so large that voids do not nucleate [1,10-13]; and even if they did vacancies would accumulate at a slow rate due to the dominance of neutral bubble sink vacancy-SIA recombination centers [1,10-13]. A corollary is that the flow and accumulation of SIA would also be reduced, presumably resulting in lower rates of loop evolution and other related processes such as irradiation creep, enhanced diffusion and induced solute segregation. Further discussion of the elements of radiation damage resistance can be found in Reference [1].

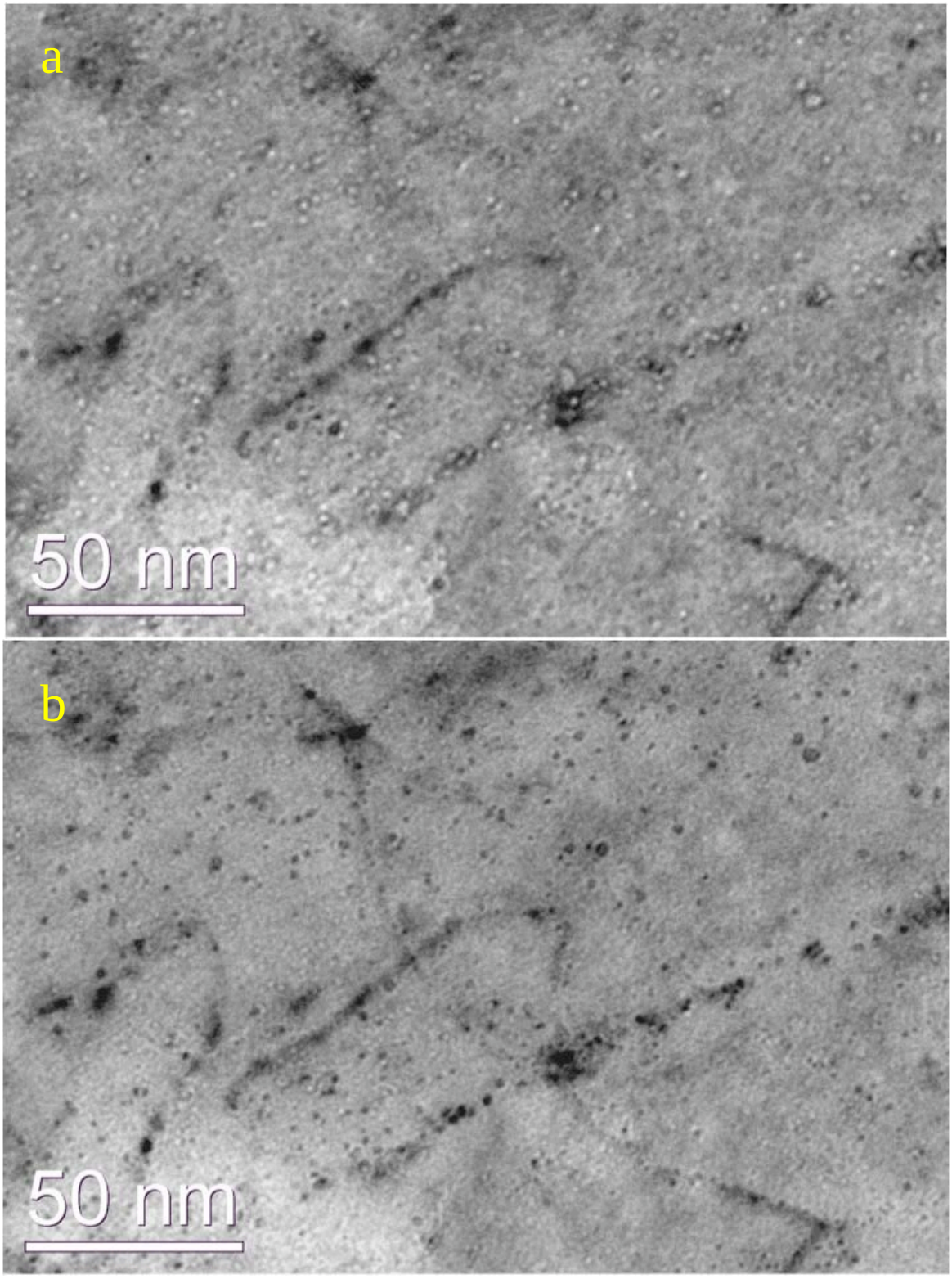

Figure 1 TEM bright field images: a) -1048 under-focus; b) +524 over-focus.

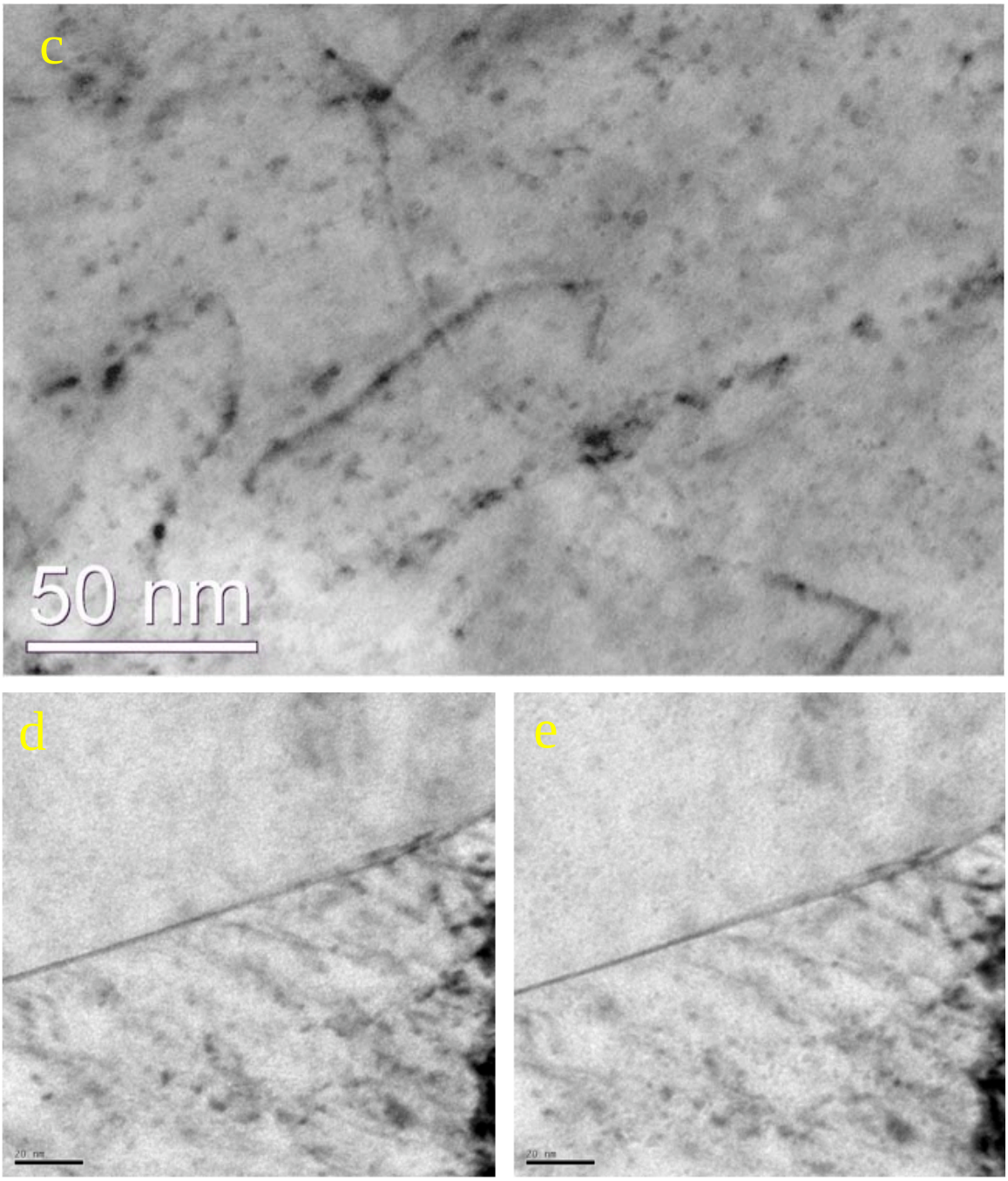

Figure 1 (cont.) c) in-focus BF images of particles assumed to be NF; d) ±524 nm over/under-focus images of on un-implanted region

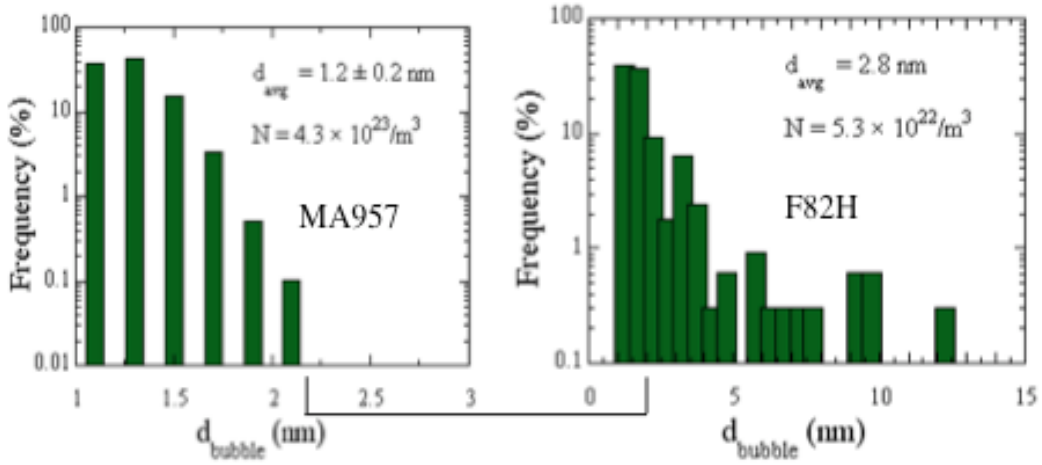

Figure 2 The cavity size distribution in helium imp[lanted MA957 compared to that observed in TMS F82H.

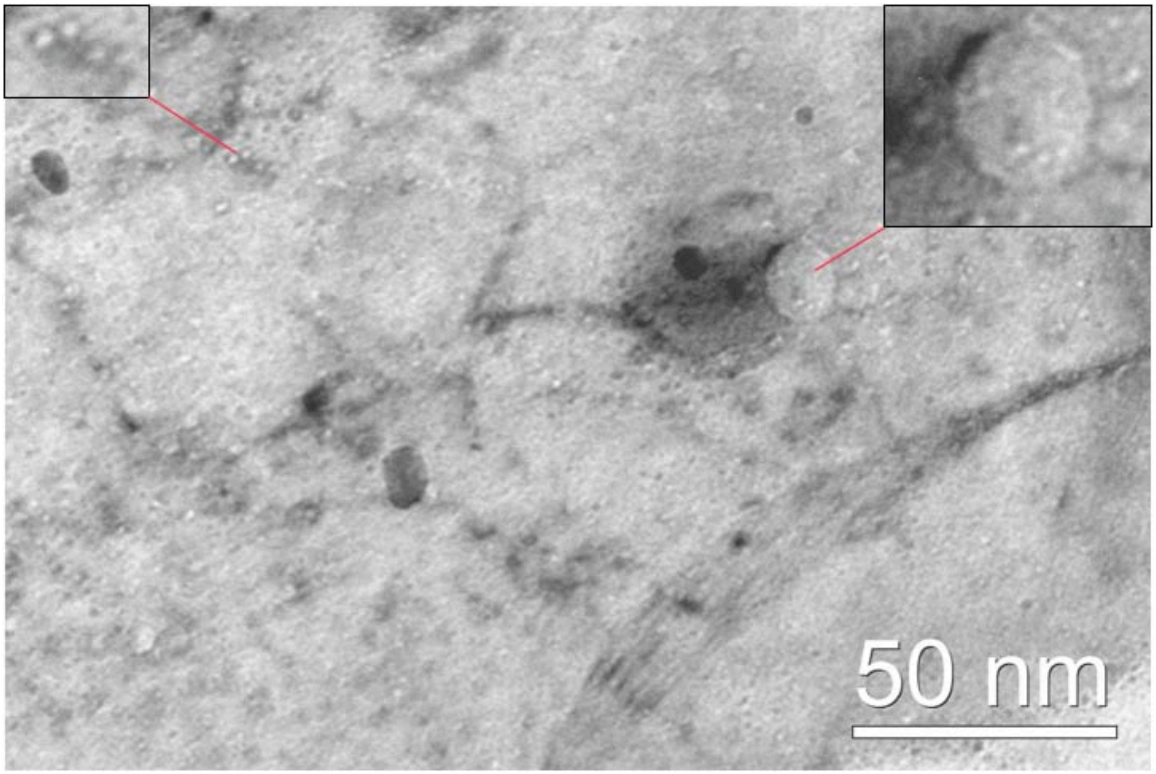

Figure 3 TEM bright field -1048 under-focus images showing matrix particles and a boundary. The insert blow-ups show cavities on larger particles.

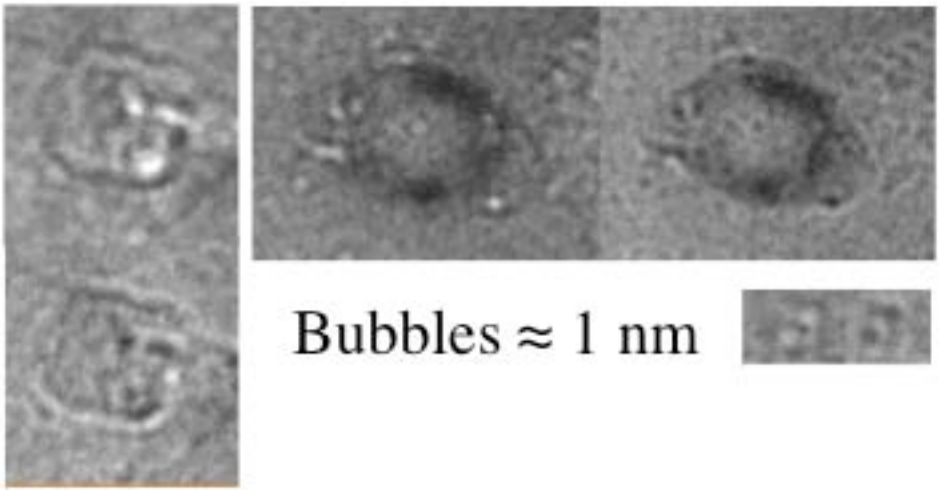

Figure 4. Through focus series images showing cavities on larger particles.

Concluding Remarks

An in-situ injection technique was used to study the transport and fate of helium in NFA MA957 irradiated in HFIR to 9 dpa at 500°C at a nominal helium/dpa ratio of 40 appm/dpa. A very high density of nm - scale bubbles was observed. The bubbles were preferentially associated with dislocations, and NF and precipitate interfaces. However, grain boundaries appeared to be relatively bubble free. These initial results barely scratch the surface of what can be learned about the transport, fate and consequences of helium using the in situ injection technique. Thus in addition to further characterization studies of the alloys and irradiation conditions described in this and previous publications, a major future effort will be directed at characterizing the large matrix of other alloys and irradiation conditions from the JP26 and JP27 experiments, that contained a total of ≈ 360 He injected TEM discs.

Future Research

Post irradiation examination of the large matrix of in situ implanted alloys is continuing as part of UCSB collaborations with PNNL, LANL and ORNL. Notably, specimens are now available fro the JP27 experiment with much higher levels of He up to 1400 appm at 22 dpa at 500°C

Acknowledgements

This research was supported by the U. S. Department of Energy, Office of Fusion Energy Sciences, under contracts DE-FG03-94ER54275 (UCSB) and DE-AC06-76RLO1830 (PNNL). The authors also acknowledge the significant contributions of R. Stoller and D. Hoelzer as well as their Oak Ridge National Laboratory colleagues in contribution a large amount of time and effort to the HFIR irradiations and providing the specimens for examination.

References

[1] G. R. Odette, M. J. Alinger, B. D. Wirth, *Annual Review of Materials Research* 38, 471 (2008).
[2] G.R. Odette, *J. Nucl. Mat.* 141 (1986) 101
[3] L.K. Mansur and W.A. Coghlan, Effects of Irradiation on Materials-14, ASTM STP 1046, 315 (1989).
[4] T. Yamamoto, G. R. Odette, L. R. Greenwood, *Fusion Materials Semiannual Report 1/1 to 6/30/2005* DOE/ER-313/38, 95 (2005).

[5] T. Yamamoto, G. R. Odette, P. Miao, D. T. Hoelzer, J. Bentley, N. Hashimoto, H. Tanigawa, R. J. Kurtz, *J. Nucl. Mater.* 367-370, 399 (2007).
[6] R.J. Kurtz, G.R. Odette, T. Yamamoto, D.S. Gelles, P. Miao, B.M. Oliver, *J. Nucl. Mater.* 367-370, 417 (2007).
[7] T. Yamamoto, G.R. Odette, P. Miao, D.J. Edwards, R.J. Kurtz, *J Nuc Mater*. 386-388, 338 (2009).
[8] M. J. Alinger, G. R. Odette, and D. T. Hoelzer, Acta Mater. 57, 392 (2009).
[9] P. Miao, G. R. Odette, T. Yamamoto, M. J. Alinger and D. Klingensmith, *J Nuc Mater 377*, 59 (2008)
[10] R. E. Stoller and G. R. Odette, *J. Nucl. Mater.* 131, 118 (1985).
[11] G.R. Odette, "On Mechanisms Controlling Swelling in Ferritic Alloy and Martensitic Alloys", *J. Nucl. Mat*. 154, 921 (1988).
[12] G.R. Odette, P.J. Mazaisz and J.A. Spitznagel, *J. Nucl. Mat*. 103, 1239 (1981).
[13] G.R. Odette, "Modeling Microstructural Evolution in Fusion Reactor Environment", *J. Nucl. Mat*. 133, 127 (1985).

COMPATIBILITY OF MATERIALS EXPOSED TO ISOTHERMAL Pb-Li – B. A. Pint and K. A. Unocic (Oak Ridge National Laboratory, USA)

OBJECTIVE

One proposed U.S. test blanket module (TBM) for ITER uses ferritic-martensitic alloys with both eutectic Pb-Li and He coolants at ~475°C. In order for this blanket concept to operate at higher temperatures (~700°C) for a DEMO-type reactor, several Pb-Li compatibility issues need to be addressed. Some of the issues being currently investigated are the use of corrosion resistant alloys and coatings, the transformation of alumina exposed to PbLi and the effect of impurities on dissolution of these materials.

SUMMARY

The specimens from a recent set of capsule experiments are being characterized. The experiments examined the effect of Fe and Ni impurities on the 700°C dissolution of type 316 stainless steel (316SS) and Fe-9Cr-2W (T92) in Pb-Li. The addition of 1000 ppma Fe or Ni did not appear to significantly change the amount of dissolution or the surface morphology. Also, a series of capsule exposures at 600°C examined possible dissimilar material reactions between Fe and SiC. Based on surface analysis of the capsules, no Fe or Si was transferred. Future characterization will focus on C transfer. A new series of experiments planned for 500-700°C will clarify any dissimilar material interaction in this system.

PROGRESS AND STATUS

Introduction

A current focus of the U.S.fusion energy materials program is to address issues associated with the dual coolant Pb-Li (DCLL) blanket concept[1] for a test blanket module (TBM) for ITER and enhanced concepts for a DEMO-type fusion reactor. A DCLL blanket has both He and eutectic Pb-Li coolants and uses ferritic steel as the structural material with a SiC/SiC composite flow channel insert (FCI). Thus, recent U.S. compatibility research has examined compatibility issues with Pb-Li.[2-7] Compared to Li,[8] a wider range of materials can be compatible with Pb-Li because of the low activity of Li.[9] In particular, SiC readily dissolves in Li, but not Pb-17Li.[3,4,10] However, because of higher Ni and Fe solubilities, Pb-Li readily dissolves many conventional alloys above 500°C. This is not a concern for a DCLL TBM operating at <500°C, however, a DCLL blanket for a commercial reactor would be more attractive with a higher maximum operating temperature, perhaps >600°C if oxide dispersion strengthened (ODS) ferritic steels[11] were used. Even at 550°C, a recent study of Eurofer 97 (Fe-Cr-W) showed a very high dissolution rate in flowing Pb-Li.[12] Therefore, preliminary Pb-Li compatibility capsule experiments are being conducted at 500°-700°C in order to investigate several concepts before flowing Pb-Li compatibility tests are conducted. Recent capsule experiments have investigated (1) the effectiveness of Al-rich coatings to inhibit dissolution, (2) the effect of Fe and Ni impurities on the amount of dissolution and (3) potential dissimilar material effects between Fe and SiC. Characterization of the first set of coated specimens was presented in the previous report.[13] The initial characterization results from the second set of capsules that addressed the second and third topics is reported here.

Experimental Procedure

Static capsule tests were performed using Mo, carbon steel or SiC inner capsules and type 304 stainless steel outer capsules to protect the inner capsule from oxidation. Because the SiC capsule could not be welded shut, an additional Mo capsule was used in that case. For the steel and Mo capsules, 1 mm diameter Mo wire was used to hold the specimens. For the SiC capsule, a SiC spacer held the specimen at the bottom of the capsule. The specimens were ~1.5 mm thick and 4-5 cm^2 in surface area with a 600

Table 1. Chemical composition using inductively coupled plasma and combustion analysis of the starting Pb and commercial Pb-Li ingots (in ppma except for Li in atomic%).

	Li	Fe	Cr	Ni	Mn	Si	Al	Mo	C	O	N	S
Pb	n.d.	<4	<4	<4	<4	<40	<8	<2	<170	1270	<40	<50
PbLi (UCLA)	14.3%	<30	<70	<30	<30	<120	<60	<40	750	4820	180	<50
PbLi (Atlantic)	19.8%	21	<3	<3	<3	18	<6	<2	2510	4730	<12	<100
PbLi (Atlantic)	21.0%	165	<3	<3	<3	17	<6	<2	2760	14460	<12	<100

grit surface finish. The Fe specimen was unalloyed and the SiC specimen was high-purity from Rohm & Haas and made by chemical vapor deposition. The Mo and Fe capsules were loaded with 125 g of commercial purity Pb-Li in an argon-filled glove box. The Pb-Li used in these experiments was from a different batch (from Atlantic Metals) than the previous batch (received from UCLA) and the chemistry from two different locations is shown in Table I. There was a distinctly higher Li content in the new batch of Pb-Li. Additions of Fe or Ni powder were made during loading. The capsules were welded shut in a glove box to prevent the uptake of impurities during exposure. After exposure, residual Pb-Li on the specimen surface was removed by soaking in a 1:1:1 mixture of acetic acid, hydrogen peroxide and ethanol for up to 72 h. Post-test specimen surfaces were examined using x-ray diffraction (XRD) and secondary electron microscopy (SEM) equipped with energy dispersive x-ray (EDX) analysis. Specimen and capsule surfaces were examined by x-ray photoelectron spectroscopy (XPS). After surface characterization, the specimens were metallographically sectioned and polished and examined by light microscopy.

Results and Discussion

Table 2 summarizes the mass change data from the second capsule series as reported previously.[13] Prior runs using a different batch of Pb-Li are included for comparison. Additions of Fe and Ni were made to simulate Pb-Li contaminated by Fe or Ni from dissolution. The behavior of T92 was examined because in the reported 550°C loop data,[12] the loop is partially made of stainless steel and therefore the Pb-Li in the loop should contain some Ni. However, capsule experiments use nominally uncontaminated Pb-Li. Even a monometallic martensitic steel loop would become saturated with Fe and Cr during operation. The results also are plotted in Figure 1a. Unfortunately, the baseline Pb-Li exposures for T92 and 316SS without a Fe or Ni addition at 700°C (Table 2) was conducted with a different Pb-Li source (Table 1). The

Table 2. Mass change of specimens in second series after 1000h exposures in Pb-Li

Specimen	Capsule	Temperature	Addition	Mass Change (mg/cm^2)
*316SS	Mo	700°C	none (UCLA)	- 5.06
316SS	Mo	700°C	1000ppma Fe	-11.89
316SS	Mo	700°C	1000ppma Ni	- 9.60
*T92	Mo	700°C	Pb-Li (UCLA)	- 3.47
T92	Mo	700°C	1000ppma Fe	- 6.02
T92	Mo	700°C	1000ppma Ni	- 6.41
CVD SiC	Fe	600°C	none (Atlantic)	- 0.04
Fe	SiC	600°C	none (Atlantic)	- 0.18
Fe	Mo	600°C	none (Atlantic)	- 0.47

* Prior work with different Pb-Li chemistry

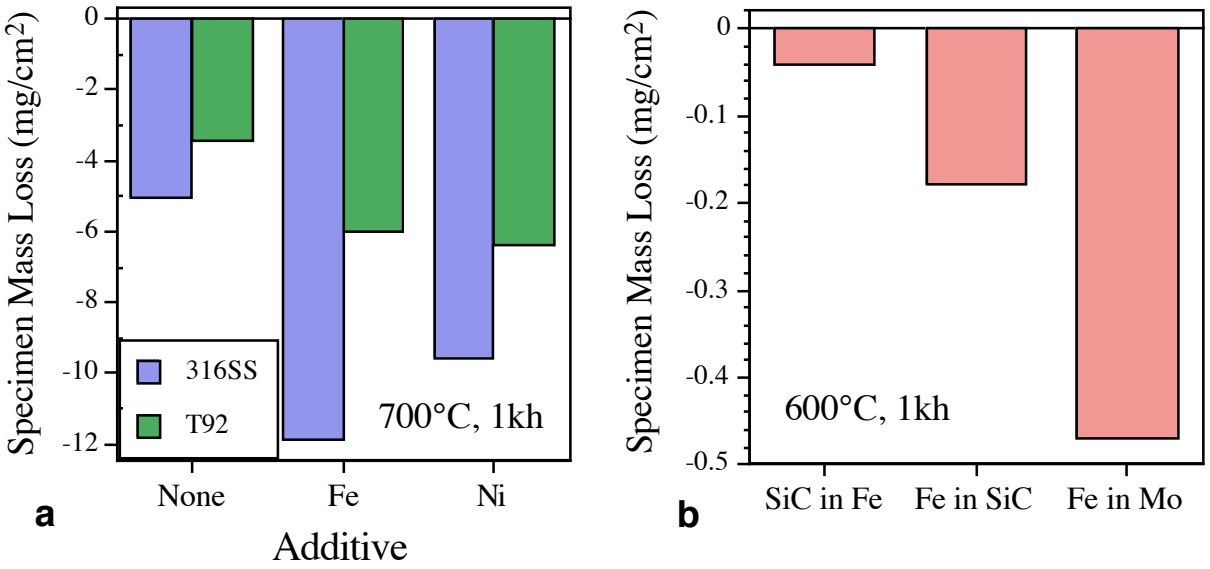

Figure 1. Mass loss results from the second series of capsule experiments.(a) the effect of Fe and Ni additions on the mass lass after 1kh at 700°C and (b) the dissimilar material effect between SiC and Fe after 1kh at 600°C.

difference in Pb-Li chemistry appears to have significantly affected the mass loss and a reliable comparison is not possible with the current data set. Generally, the dissolution was higher for 316SS compared to T92, as expected. Compared to the Fe addition, the Ni addition slightly reduced the mass loss for 316SS, which is expected since Ni is selectively removed from 316SS. By increasing Ni in the Pb-Li, the liquid is closer to saturation which should decrease the amount of dissolution. In contrast, the Ni addition had little effect on the mass loss for T92.

Figure 2 shows examples of the surface morphologies of 316SS and T92 after exposure to Pb-Li. On the 316SS surface, remnants of a Mo-rich phase in the steel could be observed, Figure 2a. No difference in surface morphology was noted between the Fe and Ni additions. Figure 2b shows the morphology of the T92 specimen exposed with additional Fe in the Pb-Li. Some areas were observed to have relatively little dissolution, which is likely due to the inhibiting affect of the native oxide on the specimens.[12] The T92 specimen exposed with a Ni addition had a similar surface morphology. Figures 3 and 4 show cross-sections of the T92 and 316SS specimens, respectively. Again, little difference was noted between the Fe and Ni additions. In Figure 4, the Ni-depleted ferritic surface layer can be observed and is similar in depth in both specimens. The ferritic layer also was detected by XRD. The amount of depletion in each case will be quantified using electron microprobe analysis (EPMA).

Figure 1b summarizes the dissimilar material experiments conducted at 600°C. The 0.04mg/cm^2 mass loss for SiC was higher than observed at 1000°-1200°C using SiC capsules.[3,4] A small amount of residual Li and C contamination was found on the SiC specimen surface by XPS but otherwise no significant degradation was apparent after exposure. The difference in mass loss compared to prior work at higher temperatures could be due to the higher Li content in this experiment, Table 1.

For the Fe specimens, the mass loss was lower in the SiC capsule compared to the Mo capsule. A potential C transfer could have occurred between the SiC capsule wall and the Fe specimen. No transfer would be expected in the Mo capsule, where only Fe dissolution is expected. A similar transfer could have occurred between the SiC specimen and the mild steel capsule wall in the first experiment resulting in a

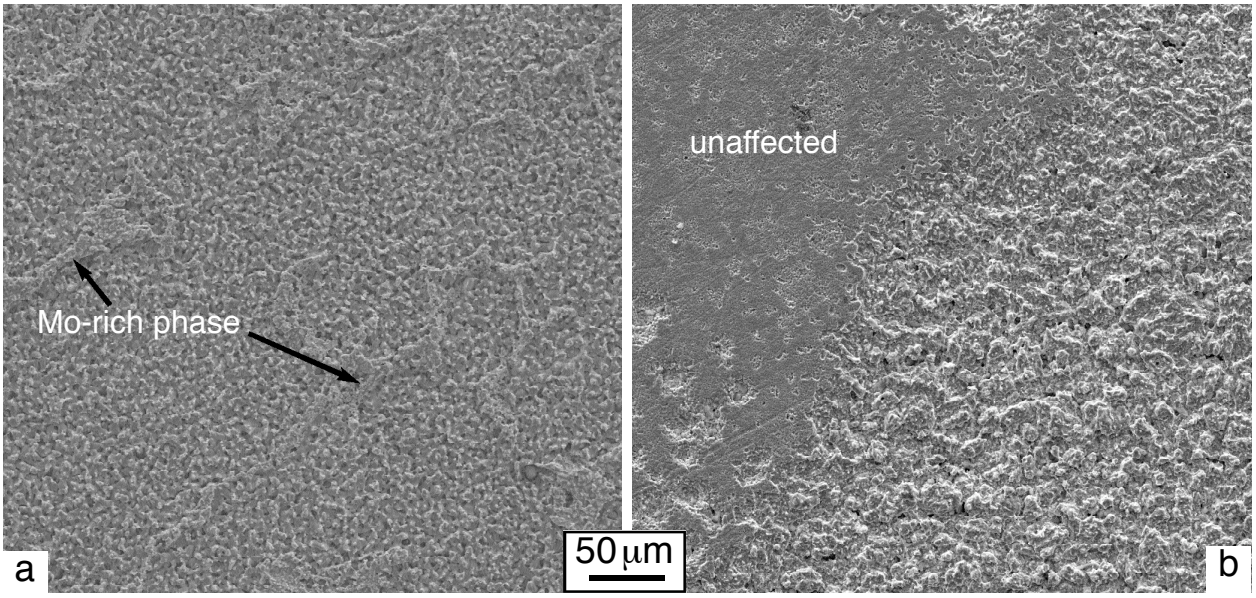

Figure 2. SEM plan view images of the surface of specimens after exposure to Pb-Li at 700°C for 1,000h (a) 316SS with 1000 ppma Ni addition and (b) T92 with 1000 ppma Fe addition.

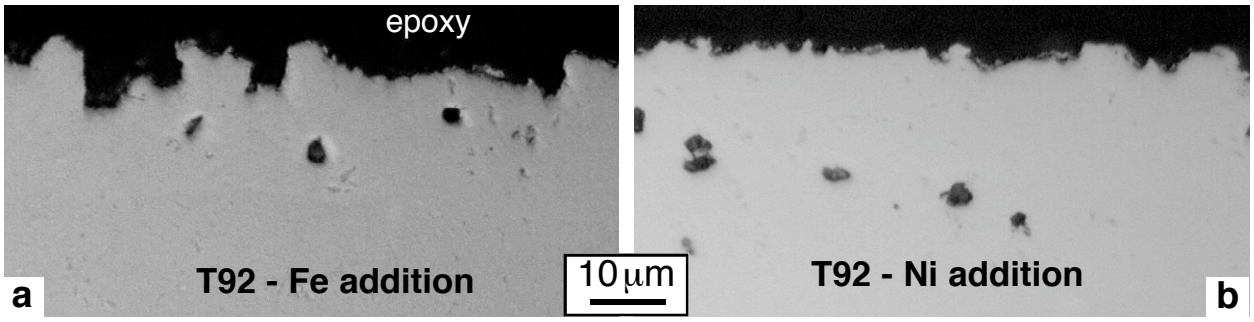

Figure 3. Light microscopy of polished cross-section of T92 after 1000h at 700°C (a) Pb-Li with 1000ppma Fe addition and (b) Pb-Li with 1000ppma Ni addition.

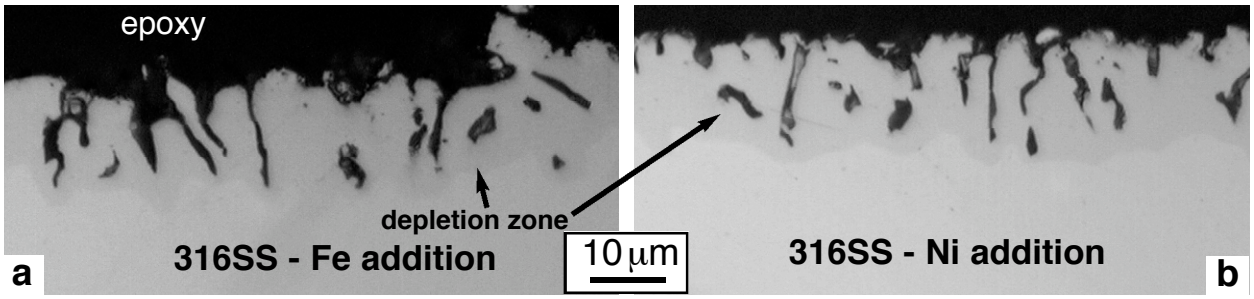

Figure 4. Light microscopy of polished cross-section of type 316 stainless steel after 1000h at 700°C (a) Pb-Li with 1000ppma Fe addition and (b) Pb-Li with 1000ppma Ni addition.

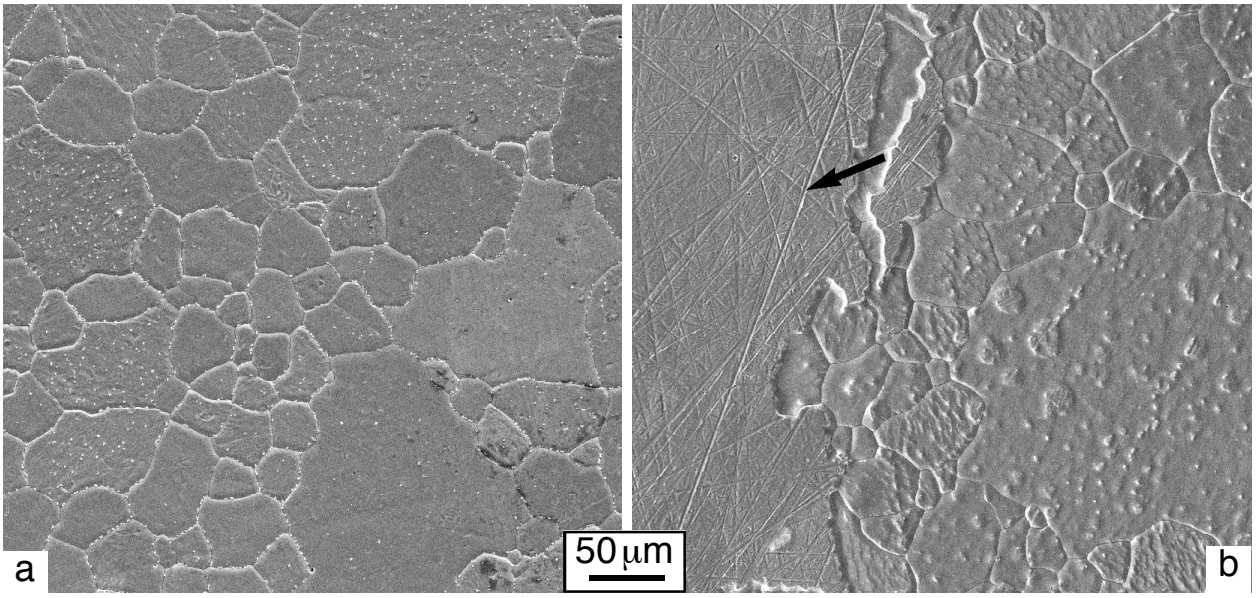

Figure 5. SEM plan view images of the surface of Fe specimens after exposure to Pb-Li at 600°C for 1,000h (a) SiC capsule and (b) Mo capsule.

mass loss. Figure 5 shows the surface of the Fe specimens in each experiment. The grain boundaries in the specimen are highlighted because they were selectively attacked, creating a groove (Fig. 6a) with faceting (arrow in Fig. 6a) seen at high temperature. The small bright particles seen in Figure 5 and 6a

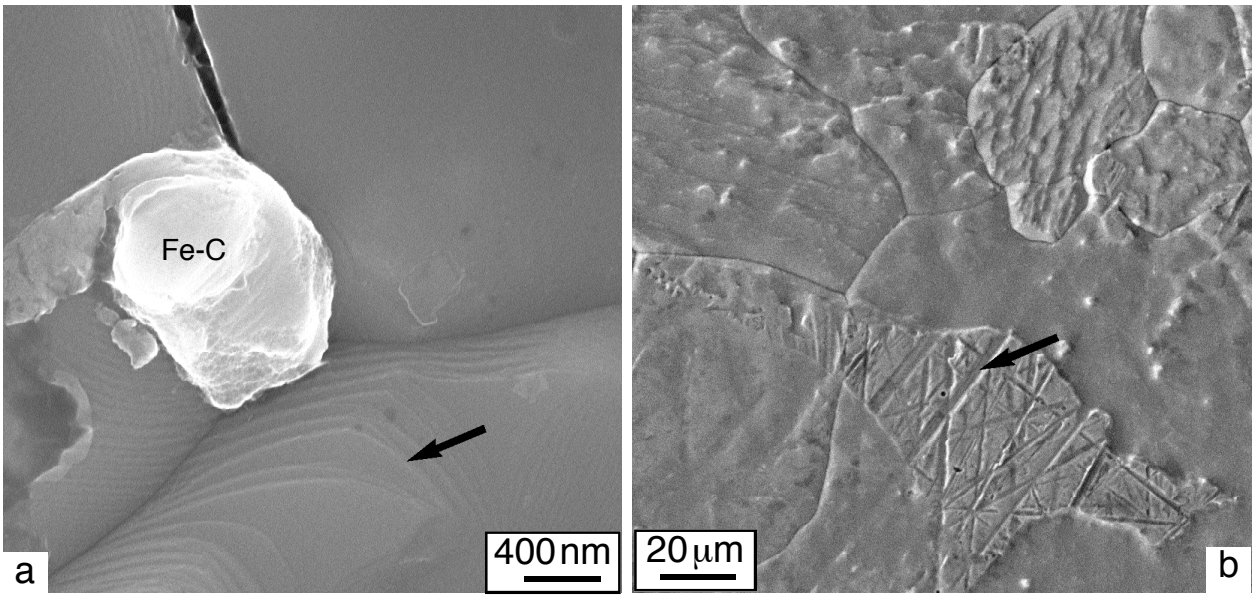

Figure 6. SEM plan view images of the surface of Fe specimens after exposure to Pb-Li at 600°C for 1,000h (a) SiC capsule, showing Fe-C particle and faceting at a triple point and (b) Mo capsule, where the arrow marks a grain with unusual features, also seen in Figure 5b at lower magnification.

had a C peak using EDX analysis. However, they could not be conclusively identified and were found for both types of capsule. For the specimen exposed in the Mo capsule, some grains appear to have scratches on them. However, at higher magnification, there may be some orientation related phase formation, arrows in Figures 5b and 6b. Cross-section of these specimens showed little difference with no obvious phase formation (e.g. carbides) or degradation. More surface characterization is needed for these specimens to further understand these surface features.

The steel and SiC capsules also were examined by XPS after exposure. There was no indication of Fe deposition on the SiC capsule or Si deposition on the mild steel capsule. Therefore, if mass transfer is occurring in this system, C is the primary element of interest and further characterization will focus on determining any difference in C content in the Fe specimens.

Based on the results of these dissimilar material experiments, a more complete test matrix will be conducted at 500°-700°C with Fe and SiC specimens and SiC and mild steel capsules. The results from these capsule experiments should more conclusively determine if any mass transfer is occurring in this system and the effect of temperature on the mass transfer.

References

[1] M. Abdou, D. Sze, C. Wong, M. Sawan, A. Ying, N. B. Morley and S. Malang, Fus. Sci. Tech., 47 (2005) 475.
[2] B. A. Pint J. L. Moser and P. F. Tortorelli, Fus. Eng. Des. 81 (2006) 901.
[3] B. A. Pint, J. L. Moser and P. F. Tortorelli, J. Nucl. Mater. 367-370 (2007) 1150.
[4] B. A. Pint, Fus. Sci. Tech. 52 (2007) 829.
[5] B. A. Pint and K. L. More, J. Nucl. Mater. 376 (2008) 108.
[6] B. A. Pint, Mater. Sci. Forum, 595-598 (2008) 549.
[7] B. A. Pint, submitted to J. Nucl. Mater. (2009).
[8] J. E. Battles, Intern. Mater. Rev. 34 (1989) 1.
[9] P. Hubberstey, J. Nucl. Mater. 247 (1997) 208.
[10] T. Yoneoka, S. Tanaka and T. Terai, Mater. Trans. 42 (2001) 1019.
[11] S. Ukai and M. Fujiwara, J. Nucl. Mater. 307 (2002) 749.
[12] J. Konys, W. Krauss, J. Novotny, H. Steiner, Z. Voss and O. Wedemeyer, J. Nucl. Mater. 386-88 (2009) 678.
[13] B. A. Pint, DOE/ER-0313/46 (2009) 28.

MODELLING THERMODYNAMICS OF ALLOYS FOR FUSION APPLICATION

P. Erhart, M. Serrano de Caro, B. Sadigh (Lawrence Livermore National Laboratory),
S.G. S. Srivilliputhur (UNT), J. Hetherly (UNT), and A. Stukowski (Germany)

SUMMARY

This report is the final of a series started in 2005, when I became the PI of this project. All along these years, this research has followed a path towards a quantitatively accurate atomic scale description of metallic alloys. The progress in the description of Fe alloys in its bcc phase has been important. Our work, together with those of several other groups in the world, has achieved a certain degree of success.

However, the atomic scale description for ferromagnetic alloys has reached a barrier that seems quite difficult to overcame, that of the finite temperature behavior of the magnetic excitations: Our work, as well as all other models for the atomic scale interactions in ferritic alloys, is valid for temperatures well below the Curie temperature (~ 1000 K). Going beyond these temperatures, a necessary objective for nuclear applications at 500 C and above requires a new approach to the problem. This new approach is being worked out right no by a few groups around the world and hopefully will provide new ways to describe these alloys.

Within the restriction just mentioned, i. e. a description valid for T < 1000 K, our work has made significant progress in the last year, by producing results in the developments of both tools and algorithms.

- We implemented the formalism of the composition dependent embedded atom model for ternary alloys (CD-EAM) into Lammps, a freely distributed code for molecular dynamics. We also implemented a 'variance constrained' Metropolis Monte Carlo, MMC, algorithm into Lammps, also for ternary alloys. This work has been the result of a fruitful collaboration with a Ph D student of Prof. K. Albe from Darmstadt, Germany, A. Stukowsky.
- We developed a modified version of the CD-EAM, that we call 'one site' CD-EAM that significantly improves the performance of a MMC algorithm without affecting the accuracy of the interatomic potential. This has been the result of P. Erhart's work.
- We developed a ternary FeCr-He potential based on data obtained from Prof. K. Nordlund's group in Finland. We validate this potential against *ab initio* data on He in FeCr obtained from within a collaboration with Chu Chun Fu at CEA-Saclay, France. This is the result of A. Caro's work.
- We started simulation of He bubbles in FeCr alloys, determining the pressure versus size relation for the 1He/vacancy ratio and the mechanisms of bubble growth at varying density. This has been the result of the collaboration with M. Caro, L. Zepeda-Ruiz and a student of Prof. Srinivasan from UNT, J. Hetherly.

It is important to mention that these tools are free for distribution. Some of them are already part of the Lammps official download package, some others are at the Stukowski web page and the last one, the parallel variance constrained Metropolis Monte Carlo within Lammps is soon being release after submission of the corresponding paper (under B. Sadigh's responsibility).

PROGRESS

In the period covered by this report, we evaluated some properties of He bubbles in ferritic alloys. These results are the subject of a publication that will be ready before my departure from LLNL, at the end of February 2010.

Advances in the improved understanding of the energetics of Fe-Cr alloys have provided the basis for the development of accurate interatomic potential models, which enable large scale simulations of the microstructural evolution. Two approaches were developed, known as the two band model \cite{OlsWalDom05} and the composition dependent model, \cite{CarCroCar05} which both address the complex shape of the heat of formation curve at 0 K as determined from first-principles calculations.

Development of the ternary FeCrHe potential

In a recent paper we proposed a simple scheme to construct composition dependent interatomic potentials for multicomponent systems that can reproduce the heat of mixing of every binary in the system over the entire compositional range [see publications below]. The methodology, a formal extension of our previous composition-dependent interatomic potentials model published in 2005, provides a systematic approach to modeling arbitrarily complex multicomponent alloys.

The case of FeCrHe is a particularly simple ternary because the addition of a chemically inert element such as He to the binary FeCr can be done with interactions based on pair potentials alone, reducing the complexity of the composition dependence to the FeCr binary alone.

A ternary potential is constructed from the potentials for the three pure element Fe, Cr, He, plus the elements needed for the description of the three binaries Fr-Cr, Fe-He, Cr-He.

He has been studied for a long time and the present state of the art for the classical potential description of its energetics and thermodynamics is highly accurate. We have taken the He-He potential derived by Beck with the cut off and short-range behavior adapted by Morishita, the Fe-Fe potential derived by Ackland in 2004 and the Cr potential derived by Terentyev in 2009.

For the Fe-He and Cr-He cross potentials we used the recent results by Juslin and Terentyev. The Fe-Cr potential is a new derivation similar to the original CDM but here based on state-of–the-art pure element potentials (Fe from Ackland 2004, instead of Mendelev 2003, and Cr from Terentyev in 2009. The mixed interaction has been constructed to reproduce the mixing enthalpy curve obtained from first-principles calculations by Olsson in 2004.

He EOS

We start analyzing results for pure He in the (ρ, T) region of interest of Fe alloys for nuclear applications, i. e. for densities around 1 He/vacancy and temperatures 300 < T < 800 K. This value is the result of the fact that He as created by nuclear transmutations sits initially at interstitial sites in the Fe matrix, and converts into a substitutional impurity as soon as it encounters a vacancy. This reaction is energetically highly favorable. It has been proven that He-V complexes have a tendency to coalesce into larger clusters that further evolve by capturing/emitting additional He atoms, vacancies, and interstitials, thus evolving from ρ = 1 to nearby values.

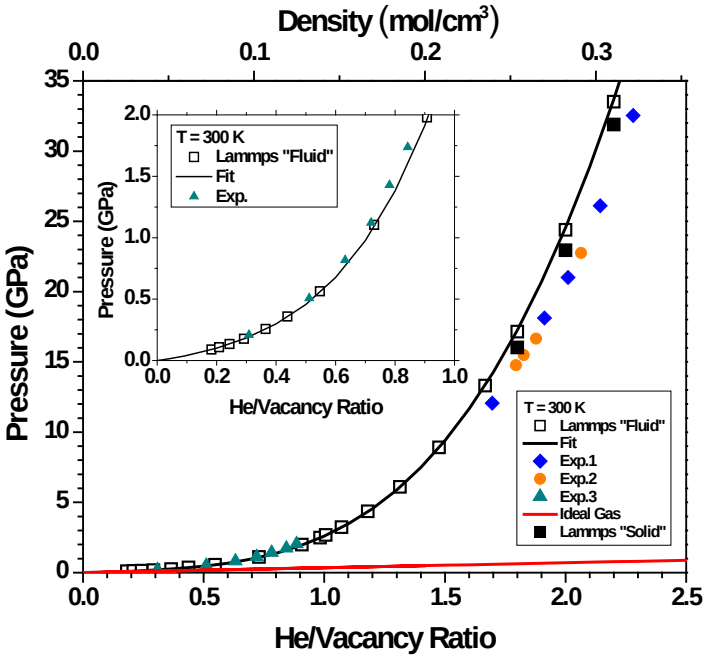

Figure 1: Pressure - density relation at 300 K as obtained by MD in the region of interest for nuclear materials studies. Inset shows the low density region magnified. Branching at around r = 1.7 reflects the solid-fluid transition. Red line is the pressure of an ideal gas (kinetic contribution alone). Lammps fluid refers to simulations done increasing pressure, where finite size effects delays solidification. Lammps solid is the result of solidification with the presence of defects (see Figure 2).

At densities and temperatures in this range He has solid–liquid phase transition. Figure 1 shows the results for MD simulations for the P-ρ relation at T = 300 K. Starting at low densities (ρ < 1) the agreement with experimental results from is excellent, see inset in Fig.1. As density approaches 1.7 He/vacancy we observe a branching corresponding to the two phases fluid and solid, as measured experimentally and by MD simulations. We mention here that the fluid phase is retained in the simulation in regions where equilibrium indicates a solid phase, as a result of finite size effects. We come back to this point later, when discussing Fig. 2.

The discrepancy between the MD simulations for the solid phase (indicated by solid squares as Lammps “solid’ in the figure, and the experimental results is due to the rapid solidification and finite size effects in the simulation that freeze a highly defective solid. The red line corresponds to the pressure of an ideal gas at similar densities (kinetic contribution alone), showing that most of the pressure in He at these densities comes from the finite size of the He atoms and their He-He repulsion.

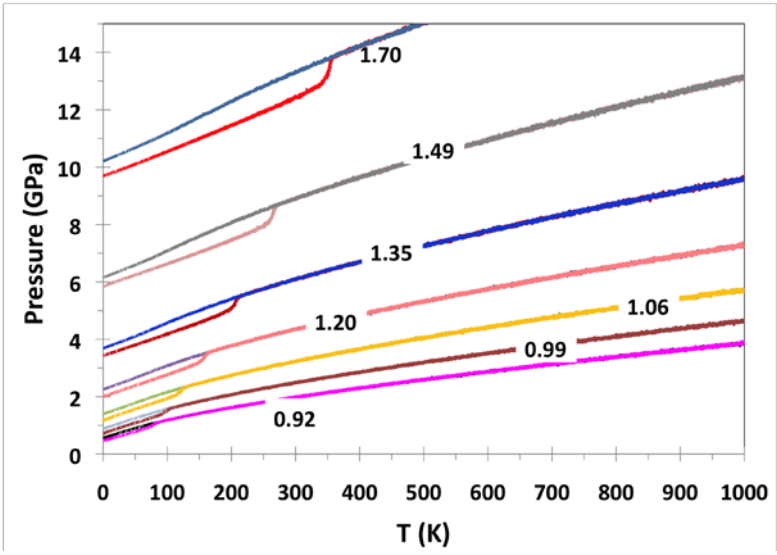

Figure 2: Pressure – Temperature relation for different densities for He. Curves are labeled by density, in units of He/Vacancy. Simulations start at 0K with an fcc solid phase, rise T up to 1000 K and then decrease T to 0K. Branching reflects the solid-fluid transition. Significant hysteresis is due to finite size effects.

A first observation from this figure is that at densities around and above 1 He/V the pressures are above 1 GPa, which is the order of magnitude of the strength of a metal, suggesting that these densities will probably induce plastic deformation of the matrix. A second observation is that at the T-ρ of interest, He presents a solid-fluid phase transition.

Figure 2 shows P-T relationship at different densities. The solid-fluid transition is clearly visible, although it is not at the thermodynamic equilibrium transition temperature due to finite size effects. Upon quenching, a defective solid forms in all cases.

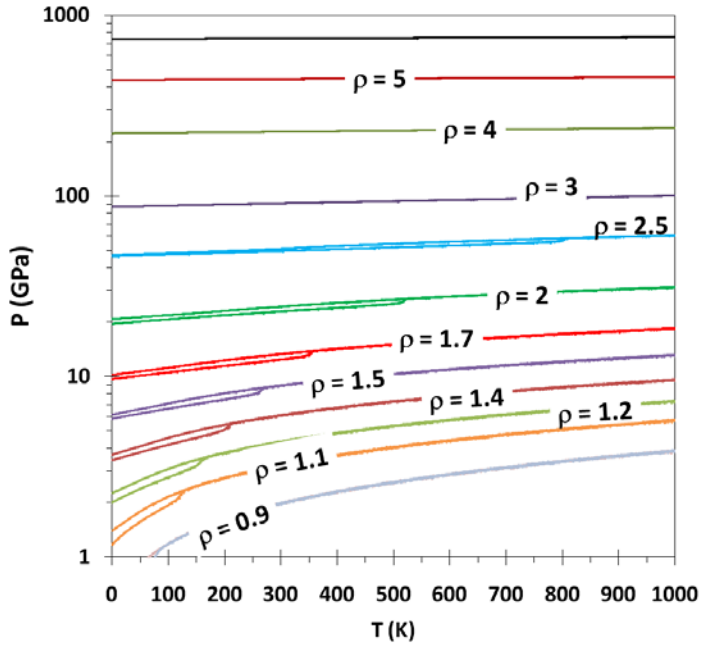

Figure 3: P-T relation at high densities for the fluid phase of He.

At densities higher than 1, the main contribution to the pressure comes from the He-He repulsion, being only slightly dependent on T. Figure 3 shows that regime for densities up to 6 He/V and pressure in the hundreds of GPa

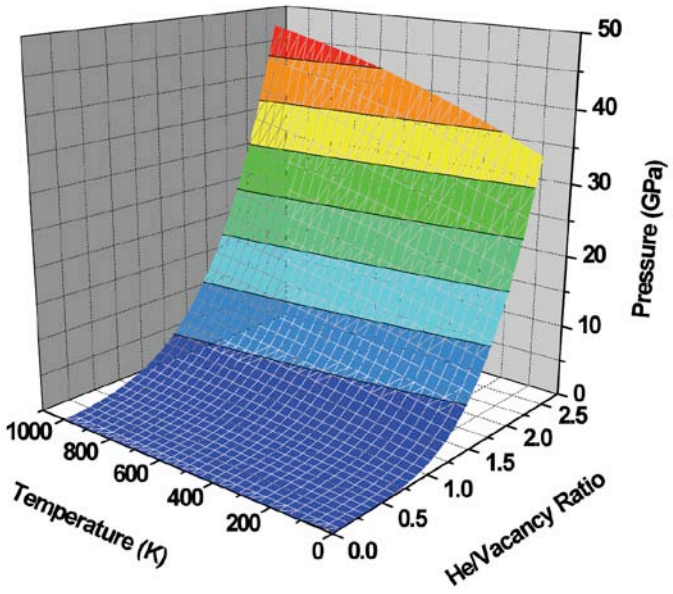

Figure 4: Equation of State for the fluid phase of He.

Figure 4 shows the equation of state, EOS, for the fluid phase of He obtained from a fit to the ensemble of data presented in Figures 2 and 3. The surface P(ρ,T) is described by,

$$P(\rho,T) = a_0(\rho) + a_1(\rho) * T + a_2(\rho) * T^2$$

$$a_0(\rho) = -5.98E\text{-}01 * \rho^5 + 3.29E+00 * \rho^4 - 1.76E+00 * \rho^3 + 3.76E\text{-}01 * \rho^2 - 1.10E\text{-}02 * \rho$$

$$a_1(\rho) = 1.02E\text{-}03 * \rho^5 - 4.24E\text{-}03 * \rho^4 + 4.66E\text{-}03 * \rho^3 + 2.19E\text{-}03 * \rho^2 + 1.07E\text{-}03 * \rho$$

$$a_2(\rho) = -6.49E\text{-}07 * \rho^5 + 2.39E\text{-}06 * \rho^4 - 2.09E\text{-}06 * \rho^3 - 9.56E\text{-}07 * \rho^2 + 1.20E\text{-}07 * \rho$$

This expression will be used to estimate the density inside He bubbles in FeCr.

He bubbles in FeCr

Experiments and simulations show that solid He exists in three different stable crystallographic structures, namely hcp, fcc, and bcc depending on temperature and pressure. When embedded in a matrix, the behavior of He bubbles will reflect the influence of the surroundings, most probably transforming from a fluid at low density to an amorphous solid.

A full EOS of He bubbles in metals P(ρ, R, T, μ_{He}) with R the radius of the bubble and μ_{He} the He chemical potential is still missing. In what follows we explore some aspects of this problem, namely the P-ρ relation for bubbles.

We use two computational techniques for these studies. One is a Metropolis Monte Carlo in the semi grand canonical ensample that allows us to randomly swap the chemical identity of an atom between Fe, Cr or He, according to user-determined chemical potentials for each species. The Metropolis algorithm controls acceptance or rejection of the swap. The displacement component of the ensemble is accomplished by molecular dynamics. Alternating MC and MD the system evolves towards equilibrium via nucleation and growth of He bubble and eventually α' precipitates.

Figure 5 shows several He bubbles, form very small to a 7 nm one, containing several thousand He atoms. Pressures measures on He and matrix atoms are in a range of several GPa, being larger for the smaller clusters. The lower figure shows the interesting fact that α' precipitates (in green) do not attract He bubbles (in blue).

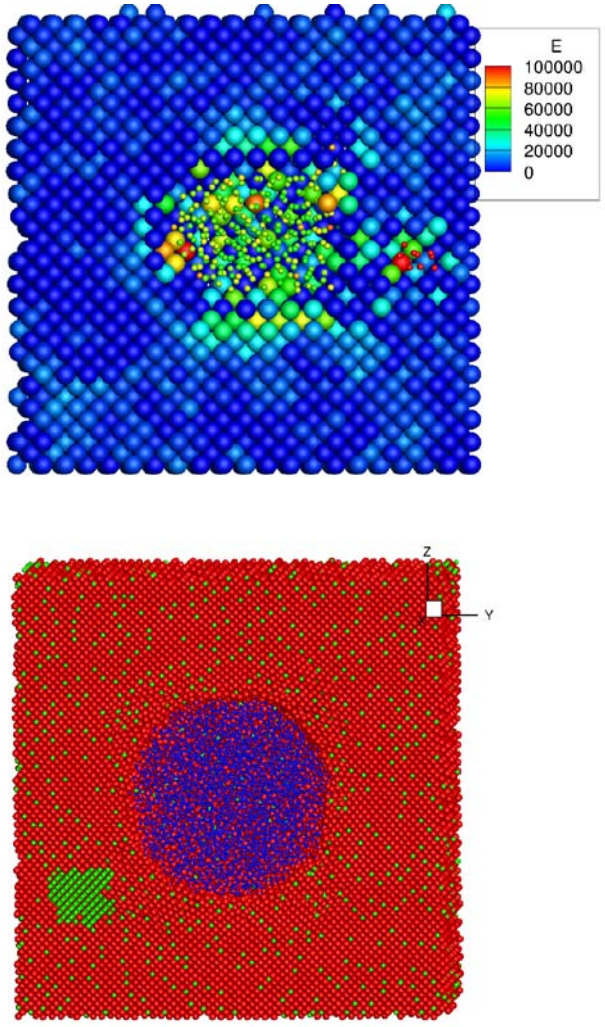

Figure 5: (upper figure) Two small He bubbles at density = 1 He/V showing the pressure range, from 10 GPa for He atoms in a small (~ 0.5nm) bubble to about 5 GPa in a medium (~ 2nm) bubble.(lower figure) A 7 nm He bubble in a 15% FeCr alloy showing that Cr rich α' phase (shown in green) does not make contact with the He bubble (blue). Suggesting that precipitation of α' is not providing sites for heterogeneous he precipitation.

Mobility of the He interstitial

The mobility of a He interstitial atom has been studied with MD in FeCr for composition between 0 and 15 at% Cr, in random solid solutions and in short range ordered solutions. SRO has been established using a Metropolis Monte Carlo code. The details of the simulations are the following: time-step of 0.1 fsec, thermalization of the samples for 10 psec, total run time of 0.2 nsec; sample size is 2000 atoms. The diffusion coefficient is obtained from the < r(t), r(o) > correlation function and the Eisntein formula. An Arhenious plot provides the activation energy, as shown in Figure 6.

As it can be seen form Figure 6, the mobility of He interstitials is only slightly dependent on Cr composition and on the degree of order of the alloys, showing a slight increase of the activation barrier a the Cr content increases. The dispersion of the data is significant and the thermal noise precludes a determination of the interstitial type, namely octahedral or tetrahedral. These results are in qualitative agreement with those reported by Terentev et al. in 2009 using the same potential for Fe-He but a different one for Fe-Cr.

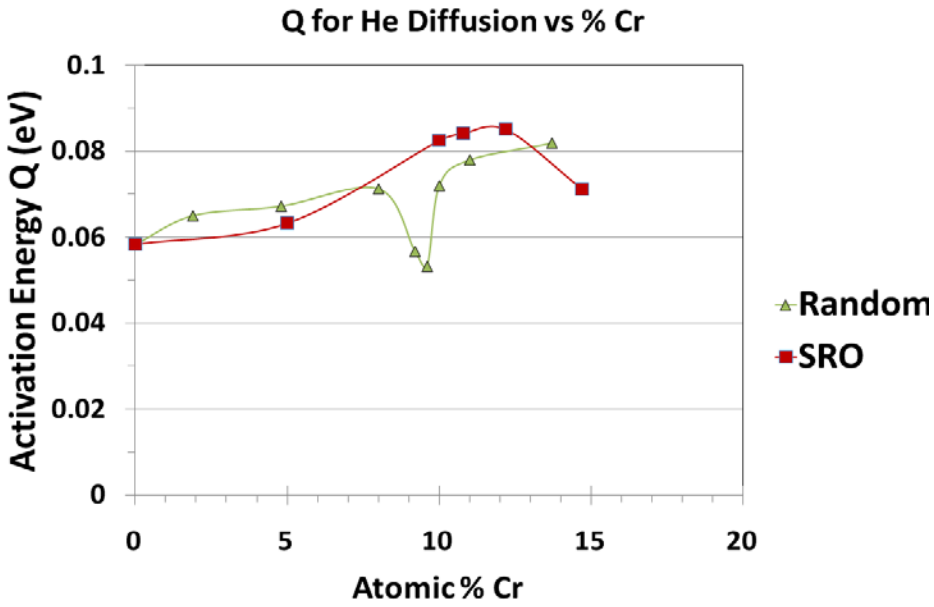

Figure 6: Arrhenious plot of the activation energy for interstitial He diffusion in FeCr alloys in the random solid solution and in the short range ordered solution.

These data is an important input for kinetic Monte Carlo approaches.

Finally, an important results obtained form this work is shown in Figure 7. As a He bubble grows in a Fe sample at 800 K from having 1 atom up to 450 atoms in an initial 27 V cavity, the pressure builds up and induces distortions on the matrix atoms surrounding the bubble. This pressure reaches a peak of about 15GPa, corresponding to a density of about 2 He/V and then starts decreasing reaching a plateau at about 10GPa. During this processes, the matrix yields to accommodate the increasing volume of the bubble and this yielding seems to be accomplished by the emission of <111> interstitial dislocation loops of a dimension comparable with the bubble.

These emissions are not reflected on the pressure vs density curve, which evolves smoothly as the size increases. This simulation suggests that the emission of single interstitials or He interstitials sis not occurring.

To conclude, the present state of this work allows us to define the future direction of work, related to the particular way the bubbles grow via incorporation of He both as interstitial and substitutional, and by the absorption of vacancies. Some of these processes can be studied by direct MD or Metropolis MC, but others, such as the rate of absorption of substitutional He, have to be studied using kinetic MC using off-lattice calculations to incorporate the stress field of around the bubble.

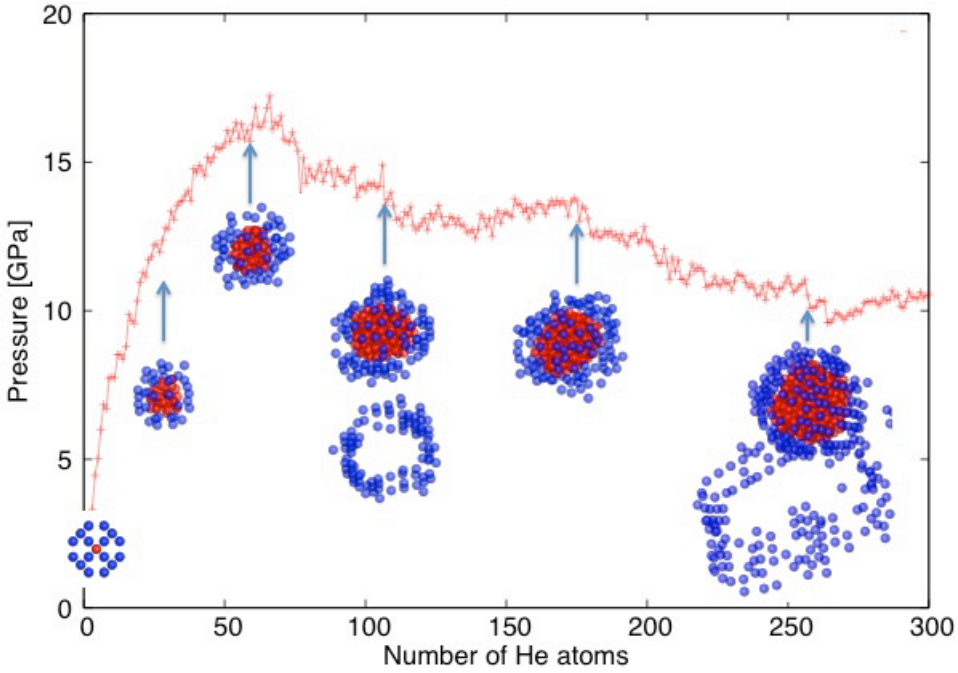

Figure 7: Pressure inside a He bubble as a function of the number of He atoms inside it. Red are He atoms and blue are non-bcc Fe atoms. It can be observed that the bubble grows by emmision of interstitial dislocation loops occurring along the growth path with no particular signature left on the pressure of the bubble.

Publications

Multiscale modelling of radiation damage and phase transformations: The challenge of FeCr alloys
Author(s): Malerba L, Caro A, Wallenius J
Conference Information: Symposium on Microstructural Processes in Irradiated Materials held at the 2007 TMS Annual Meeting, FEB 25-MAR 01, 2007 Orlando, FL
Source: JOURNAL OF NUCLEAR MATERIALS Volume: 382 Issue: 2-3 Pages: 112-125 Published: DEC 1 2008

The influence of short range order on the thermodynamics of Fe-Cr alloys
Author(s): Bonny G, Erhart P, Caro A, et al.
Source: MODELLING AND SIMULATION IN MATERIALS SCIENCE AND ENGINEERING Volume: 17 Issue: 2 Article Number: 025006
Published: MAR 2009

Numerical prediction of thermodynamic properties of iron-chromium alloys using semi-empirical cohesive models: The state of the art
Author(s): Bonny G, Pasianot RC, Malerba L, Caro A. et al.
Conference Information: 3rd Symposium on Nuclear Materials held at the EMRS 2008 Spring Meeting, MAY 26-30, 2008 Strasbourg, FRANCE

Source: JOURNAL OF NUCLEAR MATERIALS Volume: 385 Issue: 2 Pages: 268-277 Published: MAR 31 2009

Efficient implementation of the concentration-dependent embedded atom method for molecular-dynamics and Monte-Carlo simulations
Author(s): Stukowski A, Sadigh B, Erhart P, Caro A. et al.
Source: MODELLING AND SIMULATION IN MATERIALS SCIENCE AND ENGINEERING Volume: 17 Issue: 7 Article Number: 075005
Published: OCT 2009

Composition-dependent interatomic potentials: A systematic approach to modelling multicomponent alloys
Author(s): Sadigh B, Erhart P, Stukowski A, Caro A. et al.
Source: PHILOSOPHICAL MAGAZINE Volume: 89 Issue: 34-36 Pages: 3371-3391 Published: 2009

B. Sadigh, P. Erhart, A. Caro et al., “Heterogeneous nucleation in alloys using MCCask, a parallel Monte Carlo code in the transmutation ensemble with displacements”, in preparation.

A NEW Fe-He INTERATOMIC POTENTIAL BASED ON *Ab Initio* CALCULATIONS IN α-Fe – F. Gao, H. L. Heinisch, R. J. Kurtz (Pacific Northwest National Laboratory)

OBJECTIVE

The objective of this research is to develop multiscale models describing the transport and fate of He and its effect on microstructural evolution in ferritic steels irradiated in a fusion environment. Previous molecular dynamics investigations of He bubble formation and He-vacancy clustering were performed using a Fe-He pair potential developed by Wilson and Johnson, but the relative stability of octahedral and tetrahedral interstitial He atoms is inconsistent with that determined by *ab initio* methods and, more importantly, the binding energies of He atoms to He-vacancy and interstitial He clusters are much higher than those determined from *ab initio* calculations. Consequently, a new Fe-He potential has been developed to better reproduce the *ab initio* results.

SUMMARY

A new interatomic potential for the Fe-He interaction has been developed by fitting to results obtained from *ab initio* calculations. Based on electronic hybridization between Fe d-electrons and He s-electrons, an s-band model, along with a repulsive pair potential**,** has been proposed to describe the Fe-He interaction. The atomic configurations and formation energies of single He defects and small interstitial He clusters are considered in the fitting process. The binding properties and relative stabilities of the He-vacancy and interstitial He clusters are studied, and the results are compared with available *ab initio* calculations as well as with those obtained from previous Fe-He potentials. The present Fe-He potential overcomes the disadvantages that appear in previous Fe-He potentials, and it will be applied to simulate the interactions of He with Fe in various microstructural features in large-scale molecular dynamics simulations.

PROGRESS AND STATUS

Introduction

Understanding the interactions of a helium impurity with metal atoms is of fundamental importance within a fusion reactor environment, where the first wall will be exposed to a high flux of helium generated under irradiation by (n,α) transmutation reactions [1]. The accumulation of helium atoms in materials can result in the formation of helium bubbles, which can lead to void swelling and produces high temperature intergranular embrittlement, surface roughening and blistering [2]. These phenomena can significantly degrade the mechanical properties of materials. A detailed study of how He interacts with various microstructures is needed to develop a multi-scale model for prediction of long-time material behavior in the high helium environment of a fusion reactor. At the atomic-level molecular statics, molecular dynamics and the dimer method of potential surface mapping have been used to understand helium behavior in alpha-iron, such as the fate of He atoms in the vicinity of dislocations [3], the migration of He interstitials and He-vacancy clusters [4], and He effects on the primary damage state and subsequent defect evolution [5,6]. However, the results obtained from these simulations are found to depend on the empirical potentials used in the Fe-He system.

In early molecular statics and dynamics simulations most studies of He behavior in Fe employed the repulsive Fe-He potential of Johnson and Wilson [7], which predicts the most stable He interstitial position to be in the octahedral configuration, in contrast to the recent *ab initio* calculations [8] that demonstrated that the tetrahedral interstitial position is the most stable configuration. Furthermore, when using the Johnson and Wilson potential the binding energies of a He atom to both He_xV and He_x clusters (x=1 to 10) are much higher than those determined from *ab initio* calculations. In recent years new empirical Fe-He potentials have been developed. Seletskaia et al. [9] argued that, along with a repulsive pair-potential form, a three-body interaction term is needed to produce a more stable tetrahedral He interstitial relative to the octahedral configuration. Detailed calculations with this potential indicate that a singularity exists in

the force when the angle between a He atom and an Fe atom is 0° or 180°, which may cause the octahedral He interstitial to be unstable. However, the binding energies of He clusters calculated using this new potential are in good agreement with those obtained from *ab initio* calculations. On the other hand, Juslin and Nordlund (JN) have demonstrated that an Fe-He pair potential is sufficient to describe the relative stabilities of single He interstitials [10], since He is a noble gas atom. However, the binding energies of small He clusters calculated using the JN potential are too small relative to the *ab initio* calculations, and also, the potential has a force discontinuity at a distance of 0.12 nm.

We report here on the development of a new Fe-He potential that is based on an "s-band model." Using the Ackland et al. potential [11] for the Fe-Fe interactions, the atomic configurations and formation energies of single He defects and small interstitial He clusters are considered in the fitting process. The binding properties and relative stabilities of the He-vacancy and interstitial He clusters are studied, and the results are compared with available *ab initio* calculations, as well as with those obtained from previous Fe-He potentials.

Fitting Interatomic Potential

Ab initio calculations

It may be difficult to directly determine from experiments the detailed configurations and relative stabilities of He atoms in materials at the scale needed for understanding He behavior. Thus, obtaining this information for our purposes largely depends on *ab initio* calculations in the framework of density functional theory (DFT). The atomic configurations, formation energies and binding properties of He defects and He-V clusters in metals have been studied by different groups [9,12,13], using either VASP or SIESTA codes. In general, all the calculations demonstrate that the He tetrahedral is the most stable interstitial in Fe. The formation energies of He defects and small clusters are listed in Table 1. In the fitting process, the formation energy of a He_nV_m cluster is defined as following:

$$E_f(He_nV_m) = E_{tot}(He_nV_m) - [nE_{He}^c + (N-m)E_{Fe}^c], \quad (1)$$

where N is the total number of Fe atoms in a perfect crystal, and E_{He}^c and E_{Fe}^c are the cohesive energies of a perfect fcc He crystal and a perfect bcc Fe crystal, respectively. The binding energy of a He to the He_nV_m cluster can then be calculated by

$$E_b(He) = E_f(He) + E_f(He_nV_m) - E_f(He_{n+1}V_m), \quad (2)$$

where $E_f(He)$ is the formation energy of a single He interstitial in Fe.

Table 1. Formation energies of He defects in Fe calculated from *ab initio* methods, along with those obtained by different potentials for comparison. All the values are in eV.

Defect	VASP[a](ORNL)	SIESTA[b] (Fu)	ORNL[a](pot)	Juslin[c] (pot)	Present
He sub	3.84 – 4.08	4.22	3.75	4.10	3.71
He tetra	4.37	4.39	4.26	4.39	4.42
He oct	4.60	4.58	4.57	4.51	4.47
He-He-V	6.61		6.46		6.79
He-He-He-V	9.28		9.37		9.88
He-He	8.79		8.24		8.54

[a]Reference [9]
[b]Reference [12]
[c]Reference [10]

More recently, the binding properties of He defects and host atoms have been characterized using the total electronic density of states and charge densities of Fe atoms due to a He interstitial [13]. Fig. 1 shows the changes of the charge densities produced by the He octahedral and tetrahedral defects in Fe. It is of interest to find that the He interstitial and its nearest neighbor Fe atoms are all polarized due to the interactions between them with and without spin polarization, which arises from electronic hybridization between Fe d- and He s-electrons. It should be noted that the bonding interaction due to electronic hybridization is weak since He has a closed-shell electronic structure. However, this demonstrates that the electron density is dependent on the local environment in a Fe-He system.

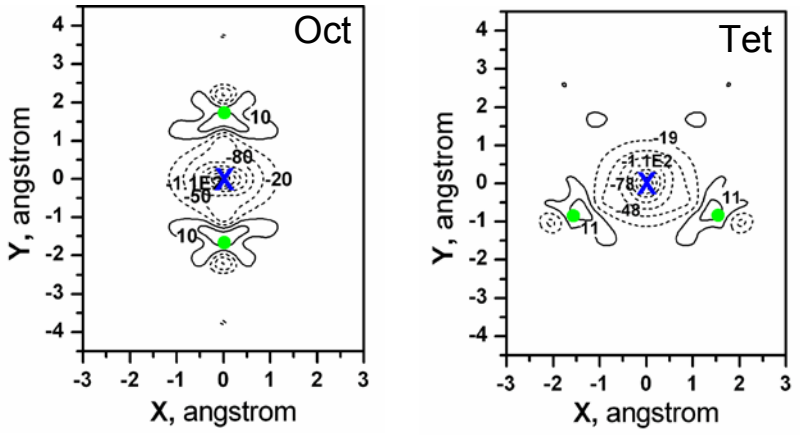

Fig 1. Changes in the charge densities of Fe atoms due to the presence of a He interstitial in octahedral and tetrahedral locations, where the structures are fully relaxed. The lines represent contours of equivalent charge density (*10^3) with the same separation of 0.03e/Å^3, where the solid lines indicate an increase in charge density and dashed lines represent charge depletion. The cross indicates the position of He and filled green circles specify the positions of its nearest-neighbor Fe atoms.

Fitting Methodology

The pair interaction and the many-body functional for Fe were taken from the work of Ackland et al. [10], while the pair potential developed by Aziz et al. [14] that describes He properties in vacuum was used for the He-He interaction in Fe. Similar to the many-body potential formalism, the potential for the Fe-He interaction consists of a pair potential and an embedding function, and then the total energy of an Fe-He system can be written as

$$U = \sum_{i=1}^{N-1} \sum_{j=i+1}^{N} V(r_{ij}) + \sum_i F_d(\rho_d^i) + \sum_i F_s(\rho_s^i), \tag{3}$$

where the first term represents a purely repulsive potential and the second and third terms are the many-body terms that provide the contribution due to electron density, as discussed before.

$$V(r) = \sum_{k=1}^{8} a_k (r_k - r)^3 H(r_k - r), \tag{4}$$

$$F_k(\rho_k) = b_1^k \sqrt{\rho_k} + b_2^k \rho_k^2 + b_3^k \rho_k^4, \tag{5}$$

where k indicates the s- or d-band model. These functions are the same as those for the Fe-Fe interaction, and are relatively easy to compute. For the mixed-pair electron density, we have employed the 1s-type and 4d-type Slater functions for He and Fe [15], respectively, but without considering the directional bonding of 4d electrons in Fe:

$$\chi^{1s} = N_{1s}\, exp(-\xi r)\,, \tag{6}$$

$$\chi^{4d} = N_{1d} r^3\, exp(-\xi r)\,. \tag{7}$$

The electron density for one Fe-He pair is the product of eqs. (6) and (7);

$$\phi_s^{FeHe} = N_s r^3\, exp(-2\xi_s r)\,, \tag{8}$$

where ξ_s is an average ξ from single ξ approximations of the 4d and 1s Hartree-Fock Fe and He orbitals, with a natural cutoff distance at 4.1 Å. N_s is equal to N_{1s} times N_{1d}, and it is chosen to be 20.0, so that the s-electron density at the first nearest-neighbor distance is equal to 0.01%. This demonstrates that the contribution to the total energy from s-electrons is very small, which is consistent with *ab initio* observations. The total electron density of an atom calculated from s-band model is given by

$$\rho_s = \sum \phi_s^{FeHe}(r) \tag{9}$$

The potential parameters are fitted using a least-squares fitting procedure with the objective function, U, defined as

$$U = \sum w_i [\, f_i(\lambda) - F_i \,]^2\,, \tag{10}$$

which determines the goodness of fit of each individual set. The calculated properties f_i depend on N parameters λ. The smaller the value of U, the closer is $f_i(\lambda)$ to the reference values F_i. The weight of each data item i in the fit, denoted w_i, determines how well the final fit will reproduce each property. Also, the atomic configurations of He defects and clusters are spontaneously relaxed using classical molecular static relaxation in a 432-atom cell during the fitting. I n the present fitting, the defect formation energies of relaxed substitutional, octahedral, and tetrahedral He interstitials and some small He-V and He-He clusters are used, and these values calculated using SIESTA and VASP are listed in Table 1.

Results

Interatomic Potential

The parameters of the pair potential and the many-body interaction are given in Table 2, while the pair potential and density function of Fe-He interaction are presented in Figs. 2 (a) and (b), respectively, along with those of Fe-Fe and He-He interactions for comparison. It can be seen that the contribution of s-electrons to many-body interaction is much smaller than that from d-electrons of Fe atoms.

Table 2. Parameters for pair potential and many-body interaction given by Eqs. (4) and (5).

Pair Potential		**s-band Model**
a_k(eV/Å^3)	**r_k(Å)**	**b_k^s (eV)**
a_1= 35.094090416476	r_1=1.35	b_1= 0.205594333601
a_2= -45.327101078621	r_2=1.50	b_2= 0.726210815237
a_3= 552.620374840293	r_3=1.65	b_3= 3.390462179478
a_4= 162.211114487242	r_4=1.80	N_s= 20.0 (Å^{-3})
a_5= -1.705295512930	r_5=2.00	ξ_s= 2.8936295071479 Å^{-1}
a_6= 0.105401602643	r_6=2.50	r_{cut}=4.1 Å
a_7= 0.072769270707	r_7=3.50	
a_8= 0.037744606924	r_8=3.90	

Formation and Binding Properties of He Defects

The results of the fitting procedure for single He defects and small He clusters are given in Table 1, together with those calculated by other empirical potentials for comparison. In general, the potential reproduces the formation energies of He defects reasonably well, and the tetrahedral He interstitial is the most stable configuration in all the iron matrices. The most stable configuration of a He_2-V cluster is found to be a <100> dumbbell, with a formation energy of 6.79 eV and a separation distance of 1.6 Å, in excellent agreement with the values calculated by *ab initio* methods. The new potential somewhat overestimates the formation energy of a He_3V cluster, but the binding energy of a He di-interstitial is determined to be 0.31 eV, in good agreement with 0.28 eV calculated by the three-body Fe-He potential, and slightly smaller than the value of 0.48 eV obtained using SIESTA.

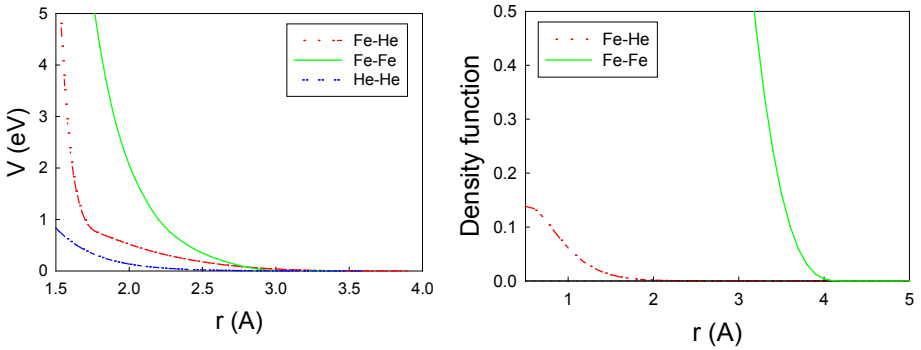

Fig. 2. (a) The repulsive pair potentials for Fe-He, Fe-Fe [11] and He-He [14] interactions, and (b) the density functions for Fe-He and Fe-Fe interactions.

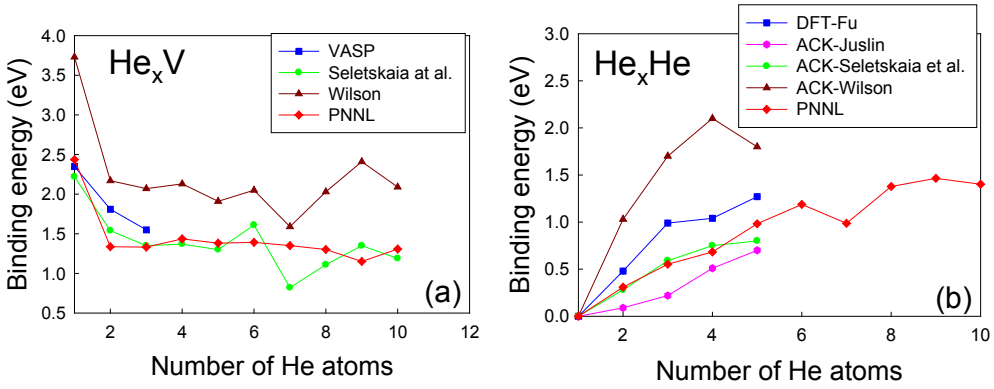

Fig. 3. (a) Binding energy of an additional He atom to a He-V cluster, and (b) binding energy of an additional He atom to a He-He cluster.

The newly developed Fe-He potential has been employed to study the properties of He-V and He-He clusters, and their binding energies as a function of cluster size when a He atom is added to He-V or He-He cluster. A cubic computational cell of $10a_0x10a_0x10a_0$ units (a_0 – bcc iron lattice constant) was used, and periodic boundary conditions were applied in all directions. The atomic configurations were relaxed using a molecular statics approach at 0 K, with a constant volume condition. The results for a He atom binding to a He-V cluster and a He-He cluster are presented in Figs. 3 (a) and (b), respectively. The binding energies calculated from first principles, and the previous Fe-He potentials are imposed for comparison. The binding energies calculated with the current Fe-He potential are slightly smaller than those obtained from first principles, but they are generally in good agreement with those calculated from Seletskaia's Fe-He potential. Wilson's potential systematically overestimates the binding of a He atom to both the He-V cluster and the He-He cluster.

The binding energy of an additional He atom to the He-V cluster initially decreases and then remains almost a constant value of about 1.3 eV. In the calculations by Seleskaia et al., there exists a local maximum when a total of six He atoms are involved in a He-V cluster that forms a He compact octahedron with a vacancy at the center, whereas a sudden decrease in the binding energy occurs for a He-V cluster with seven He atoms. In the latter case, the local dilatations produced by the cluster are strong enough to begin displacing iron atoms at the periphery of the cluster, which is responsible for this decrease. In the present study, the dilatations around a He-V cluster have been observed to occur when a cluster contains He atoms larger than four, and they increase with increasing cluster size. However, a compact He octahedron is also observed in the present simulations for a cluster containing six He atoms, which is in consistent with the previous investigations.

The binding energy of an additional He atom to a He cluster generally increases with increasing cluster size, as shown in Fig. 3(b), and it approaches a value of about 1.4 eV when the total number of He atoms is larger than eight. The binding energies calculated with the new potential agree with *ab initio* calculations within 0.25 eV, and they are in excellent agreement with those for small He clusters calculated by Seletskaia at al. It should be noted that the binding energies of small He clusters determined using Juslin and Nordlund's Fe-He potential is very small (~0.1 eV), which suggests that the small He clusters can easily dissociate, even at low temperatures. This may account for the significant differences between the results using the present potential and Juslin and Nordlund's potential. It has been observed that significant matrix distortions occur for large He clusters for the present simulations, leading to large displacements of the neighboring Fe atoms. This may suggest that interstitial Fe clusters can be directly generated through a so-called loop punching mechanism, which needs to be further investigated using molecular dynamics simulations.

CONCLUSIONS

Based on *ab initio* studies, we have proposed an s-band model to develop a new interatomic potential for the Fe-He interaction using a relaxation-fitting approach, using a least-squares fitting technique. The atomic configurations and formation energies of single He defects and small interstitial He clusters are considered in the fitting process. Calculations using the new potential demonstrate that both tetrahedral and octahedral interstitials are stable, but tetrahedral He forms the most stable configuration. The binding properties and relative stabilities of He-vacancy and interstitial He clusters are studied, and compared with available *ab initio* calculations as well as with results obtained from previous Fe-He potentials. The results are in reasonable agreement with both the *ab initio* and previous potential calculations. The present Fe-He potential represents an important improvement over currently available potentials because it overcomes the disadvantages existing in previous Fe-He potentials, and it can be easily applied to study the interactions of He with Fe in various microstructural features in large-scale molecular dynamics simulations.

References

[1] S.J. Zinkle, Phys. Plas.12, 058101 (2005).
[2] Y. Katoh, M. Ando, and A. Kohyama, J. Nucl. Mater. 323, 251 (2003).
[3] H.L. Heinisch, F. Gao, R.J. Kurtz and E.A. Le, J. Nucl. Mater., in press.
[4] F. Gao, H.L. Heinisch and R.J. Kurtz, J. Nucl. Mater. 386-288, 390 (2009).
[5] L. Yang, X. T. Zu, H. Y. Xiao, F. Gao, H. L. Heinisch, R. J. Kurtz and K. Z. Liu, Appl. Phys. Lett. 88, 091915 (2006).
[6] G. Lucas and R. Schaeublin, J. Phys.: Condens. Mater. 20, 415206 (2008).
[7] W. D. Wilson and R. D. Johnson, Proceedings Interatomic Potentials and Simulation of Lattice Defects, Plenum, New York (1972) 375.
[8] T. Seletskaia, Y. Osetsky, R.E. Stoller, G.M. Stocks, Phys. Rev. Lett. 94, 046403 (2005).
[9] T. Seletskaia, Yu. N. Osetsky, R. E. Stoller, and G. M. Stocks, J. Nucl. Mater. 367-370, 355 (2007).
[10] N. Juslin and K. Nordlund, J. Nucl. Mater. 382, 143 (2009).

[11] G. J. Ackland, M. I. Mendelev, D. J. Srolovitz, S. Han and A. V. Barashev, J. Phys.: Condens. Mater. 16, 52629 (2004).
[12] C. C. Fu and F. Willaime, J. Nucl. Mater. 367-370, 244 (2007).
[13] X. T. Zu, L. Yang, F. Gao, S. M. Peng, H. L. Heinisch, X. G. Long and R. J. Kurtz, Phys. Rev. B80, 0541041 (2009).
[14] R. A. Aziz, A. R. Janzen and M. R. Moldover, Phys. Rev. Let. 74, 1586 (1995).
[15] E. Clementi and C. Rostti, Atomic data and nuclear data tables 14, 177 (1974).

ATOMISTIC STUDIES OF PROPERTIES OF HELIUM IN BCC IRON -

David Stewart, Yuri Osetskiy, and Roger Stoller (Oak Ridge National Laboratory)

OBJECTIVE

The objective of this work is to use molecular dynamics techniques to increase understanding of the behavior of transmutation-produced helium in reduced-activation ferritic/martensitic steels that are candidate materials for fusion reactors. As there is no suitable iron-carbon-helium interatomic potential, simulations are performed using helium in pure iron.

SUMMARY

Helium created by transmutations plays an important role in the response of reduced-activation ferritic/martensitic (RAFM) steels to neutron radiation damage. We have performed extensive atomistic simulations using the ORNL 3-body Fe–He interatomic potential combined with three interatomic potentials for the iron matrix. Interstitial helium is very mobile and coalesces to form interstitial clusters, with some mobility of small clusters. When an interstitial He cluster reaches sufficient size, it punches out an Fe interstitial, creating an immobile helium–vacancy cluster. If more helium atoms join it, more Fe interstitials can be created, and the He–V defect is a nascent bubble. These mechanisms are investigated in simulations that examine the nucleation of He defects. Mobile interstitial He clusters and helium bubbles 1 to 6 nm diameter are also simulated separately. Results are compared based on temperature and interatomic potentials used.

PROGRESS AND STATUS

1. Introduction

Reduced activation ferritic/martensitic steels are a candidate material for use in fusion reactors [1]. The presence of transmutation-created helium plays an important role in the microstructural evolution of these steels under neutron irradiation. Kinetic models demonstrate that the growth, migration and coalescence behavior of helium defects is very sensitive to the properties of individual He interstitials and helium–vacancy clusters [2].

In a recent paper [3], we presented a detailed comparison of the behavior of He in Fe as described by the ORNL three-body potential [4–6] with that predicted by two pair potentials found in literature [7,8]. Here, we extend that work in three ways. Firstly, we simulate helium clustering over a substantially longer physical time frame. Secondly, we investigate the diffusion behavior of interstitial helium clusters as described by the different potentials. Thirdly, we simulate helium bubbles of diameter up to 6nm with different helium-to-vacancy (He/V) content over a wide temperature range.

2. Simulation Method

The NVE molecular dynamics simulation methods used in this paper are described in detail in [3]. Three different types of simulations were used here to investigate different phenomena.

Nucleation, growth and coalescence of interstitial He clusters and subsequent formation of helium–vacancy clusters and Fe interstitials were simulated by annealing a system containing a certain population of single interstitial He atoms initially homogenously distributed in BCC iron matrix. Here we describe results for 125 helium atoms in a BCC crystal containing 59,582 Fe atoms, which corresponds to the mean He concentration of 2089 appm. Annealing at several temperatures in the range from 200 to 1200K was simulated for times up to 12_ns. The Ackland Fe potential [9] was used in combination with the ORNL Fe–He potential.

Diffusion of helium interstitial clusters was modeled in a 10×10×10 box containing 2000 Fe matrix atoms. Interstitial defects of 1 to 6 helium atoms were simulated over the temperature range 250 to 1000K. Diffusion coefficients of He interstitial defects were estimated using the technique described earlier [3, 10].

A relatively long simulation time, up to 30ns, has allowed us to estimate the diffusion coefficients with a high accuracy. Typically the standard error is so small that the error bar is hidden behind the symbol on the corresponding graphs. Three potentials for the Fe matrix [9,11,12] and three Fe–He potentials [4–8] were used in this study.

The He–V defects nucleated in the coalescence simulation described above are nascent bubbles. We investigated the properties of larger bubbles, from 1 to 6nm, in larger simulated crystals, up to 432,000 Fe atoms. First a void of the corresponding size was created and then a certain number of He atoms was homogenously distributed inside. The system was then annealed for over 1ns to obtain an equilibrium state. Voids from 1 to 6 nm contain from 59 to 9577 vacancies and we simulated He-to-vacancy ratios: He/V = 0 to 0.6 in the temperature range from 100 to 900K. During this simulation we monitored the He distribution inside the bubble, the effective bubble size (radius), the He pressure inside bubbles and the total pressure in the simulated system. In these simulations we used the Ackland iron [9], the ORNL He–Fe [4–6], and the Aziz [13] helium potentials.

3. Results

3.1. Coalescence

In this study we investigated the fate of single interstitial He atoms subjected to annealing at different temperatures. The set of phenomena observed includes diffusion of He atoms and interactions in which interstitial He clusters are formed. Being small, these clusters are also mobile and can coalesce forming larger clusters. Depending on the temperature these larger clusters can change their structure from interstitial He clusters to He–vacancy clusters pressing out iron interstitial atoms. The resulting He-vacancy cluster is immobile. Further interaction with mobile interstitial He clusters leads to the formation of additional vacancy–SIA pairs, increasing the size of immobile He–vacancy clusters (growth) and the number of iron SIAs in the system.

Figure 1 shows the number of Frenkel pairs created as a function of time at different temperatures. At 200K, the helium slowly and inexorably coalesced until it formed interstitial clusters too big to be mobile. Due to the slow diffusion and the inability of even a di-helium pair to dissociate, a high density of clusters formed, each containing only 2 to 8 He atoms. After 12.9ns a cluster of size 10 formed, which created a Frenkel pair within 20ps.

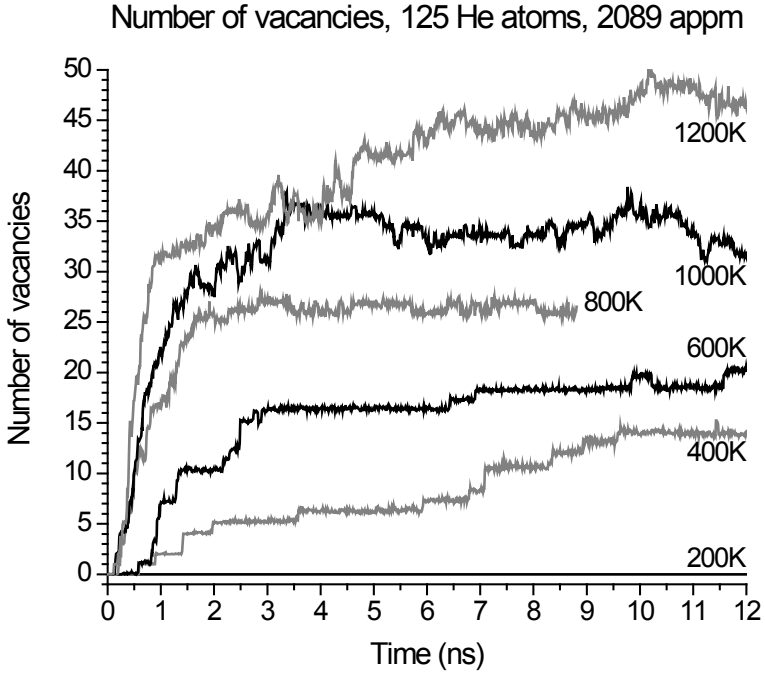

Figure 1. Vacancy production due to the formation of He–V defects for different temperature simulations.

At 400K, the helium was more able to form large clusters, and started creating Frenkel pairs when they reached 9 or more He atoms. One pair was created by a size 7 cluster. 15 Frenkel pairs were created gradually over the entire simulation. All SIAs except one remained trapped by the He–V defect that had created them.

At 600K, the number of He atoms in a cluster required to create a Frenkel pair ranged from 7 to 11. In one case a cluster of 5 created a Frenkel pair, but it recombined 0.7ns later. Defect creation proceeded more rapidly at this temperature, and most (16 of 19) Frenkel pairs were created in the first 3ns. Most SIAs remained pinned to the He–V defect that had created them.

At 800K, coalescence proceeded even faster. Frenkel pair creation, which happened in clusters of 6 or more heliums, saturated at about 25 after 2ns. After 3ns, all helium atoms were part of a He–V defect. The ejected SIAs escaped from the three single vacancy He–V defects and were captured by larger (up to 6 vacancy) ones.

At 1000K, coalescence proceeded faster still. Frenkel pair creation, which happened in clusters of 6 or more heliums, reached 30 in the first 2ns and then slowly increased further. After 3ns, all helium atoms were part of a He–V defect. Some ejected SIAs escaped from the smallest (2 vacancy) He–V defects and were captured by the larger (up to 8 vacancy) ones.
At 1200K, about 30 Frenkel pairs were created in the first nanosecond and about 15 more in the rest of the simulation. At 2.25ns, all helium atoms were part of a He–V defect, but later some helium atoms escaped from the single vacancy He–V defects and were captured by other defects. Ejected SIAs escaped from the 1 and 2 vacancy He–V defects and were captured by the larger (up to 9 vacancy) ones.

3.2. Cluster Diffusion

The study described above demonstrated the formation of mobile interstitial He clusters and we therefore investigated the mobility such clusters in this work. Depending on the number of He interstitials in the cluster and the ambient temperature three different types of behavior were observed:

- The interstitial cluster remained intact and moved as a whole. This was observed for smaller clusters at lower temperatures. In this case we could measure mobility via estimation of their diffusion coefficient.
- The interstitial cluster broke up/dissociated into smaller clusters and/or He interstitial atoms, which diffused away from each other.
- The interstitial cluster created a Frenkel pair, resulting in an SIA and an immobile helium–vacancy defect.

The second and third types of behavior were favored for larger clusters and at higher temperatures.

The cluster diffusion rate is considered to be the diffusion rate of the centre of mass of the He atoms. An Arrhenius plot of the rates is shown in Fig. 2. When a cluster remains intact, the diffusion rate is calculated using the entire simulation, and shown as a solid symbol in Fig. 2. In the cases when a cluster dissociates or ejects an SIA after a certain length of time, the diffusion coefficient is calculated from the simulation up to that point, and is shown as an empty symbol in Fig. 2.

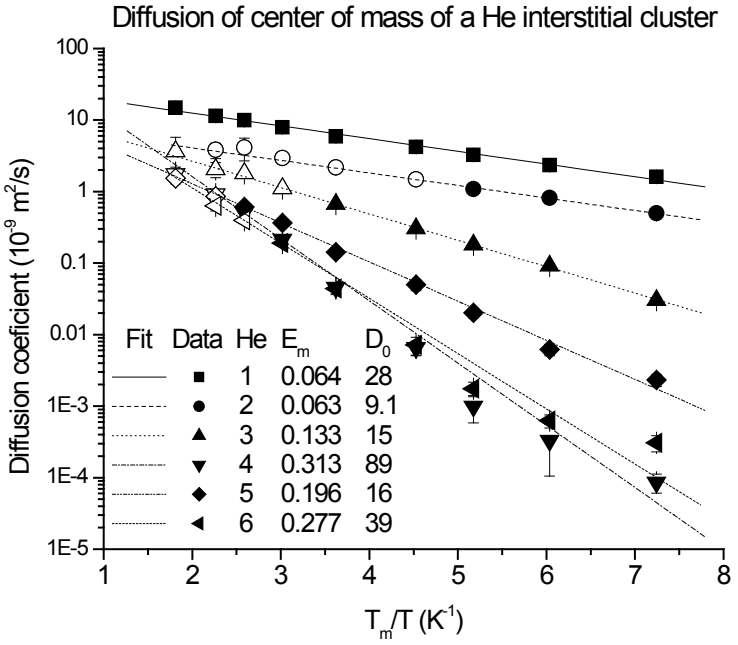

Figure 2. Arrhenius plot for diffusion of helium interstitial clusters using Ackland97 and ORNL potentials. Open symbols present treatment of He interstitial clusters diffusion before either their dissociation or formation of He–vacancy clusters and emitting iron SIAs.

Arrhenius fits to the data were done for several different combinations of matrix and He–Fe potentials, and the resulting energy barriers are plotted in Fig. 3.

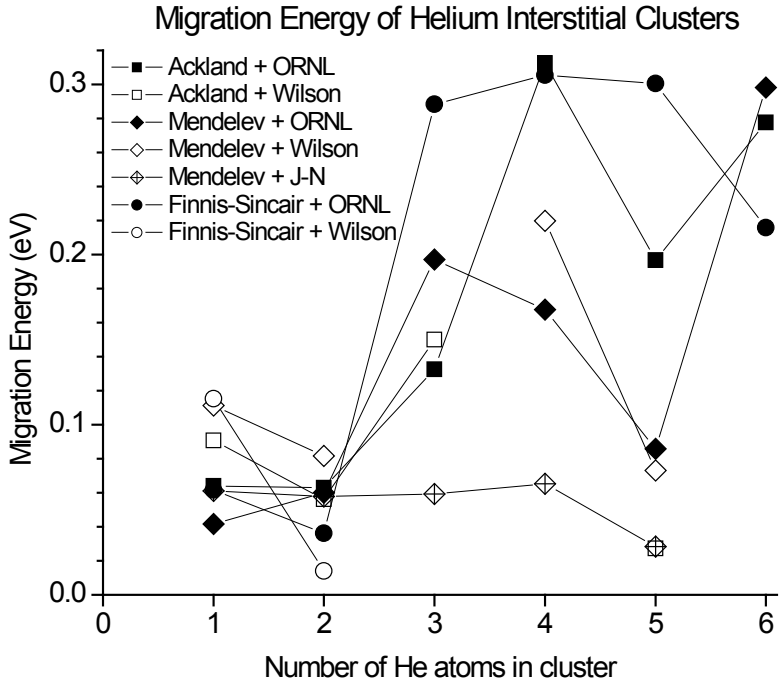

Figure 3. Cluster migration energies calculated using different interatomic potentials.

The test matrix for this measurement was 3 He–Fe potentials times 3 Fe matrix potentials times 6 He

interstitial cluster sizes times 9 different temperatures. The Juslin–Nordlund He–Fe potential [8] with Ackland [9] or Finnis–Sinclair [11] predicts that all clusters will dissociate into individual interstitial helium atoms, so there are no cluster diffusion rates for these combinations. The Mendelev matrix [12] with the Juslin–Nordlund potential showed consistently low barriers compared to the other combinations.

The Ackland matrix potential with the ORNL He–Fe potential [4–6] showed almost identical barriers of about 0.06eV for a single He and the He_2 pair. He_3 had the next lowest barrier followed by He_5. He_4 and He_6 had the highest barriers of about 0.3eV.

The Mendelev matrix with the ORNL He–Fe potential showed different behavior. The barrier for a single He was only 0.04eV and for He_2 remained at 0.06eV. The next lowest was He_5 with a barrier of only 0.09eV. He_3 and He_4 showed very similar diffusion rates and barriers of about 0.18eV. The highest barrier was He_6 with 0.3eV.

With the Finnis–Sinclair matrix and the ORNL He–Fe potential, the He_2 cluster had a lower barrier than a single He. Clusters of size 3, 4 and 5 showed very similar diffusion rates and barriers of about 0.3eV, while He_6 had a barrier closer to 0.2eV.

The Ackland matrix potential with the Wilson He–Fe potential [7] also showed the He_2 cluster with a lower barrier than a single He. Surprisingly, the He_5 cluster had an even lower barrier of only 0.03eV, based on simulations below 400K. At 400K and higher, it ejects an SIA too quickly to calculate a diffusion rate. The He_3 cluster shows very strange behavior, repeatedly ejecting an SIA and recombining with it. This suggests that the two states have similar energy. The ability of the SIA to recombine may be somewhat an artifact of the simulation, since it has periodic boundary conditions and a small size. The He_4 cluster remained intact for a long time, especially at low temperatures, but would eject an SIA rather than move. At all temperatures, the He_6 cluster ejected an SIA too quickly to calculate a diffusion rate.

The Mendelev matrix potential with the Wilson He–Fe potential again shows decreasing barriers from the single He to the He_2 cluster to the He_5 cluster. The He_4 cluster showed very slow diffusion—the barrier was 0.2eV, but it had an extremely low pre-exponential factor. The He_5 cluster showed a 2-process behavior: fast diffusion along a ⟨111⟩ direction with occasional direction changes. This suggests that there are 2 energy barriers, one for the ⟨111⟩ movement and one for the rotation. However the analysis procedure used in this work looks at the movement as a whole and generates a single (effective) diffusion coefficient. Above about 400K, He_4 and He_5 ejected an SIA too quickly the gather diffusion data. At all temperatures, the He_3 and He_6 clusters immediately ejected an SIA.

3.3 Helium bubbles

Figure 4 (visualized using the PyMol software [14]) shows a cross-section of a 4nm (2741 vacancies) bubble with He/V = 0.5. It was discovered that the helium atoms stand off a small distance from the surface iron atoms, leading to the gap visible in Figure 4. The gap was large enough that in these simulations the He atoms rarely come close enough to an iron atom to invoke the 3-body component of the ORNL Fe–He potential (range 2.2Å), so their interactions are effectively described by the pair part of the potential.

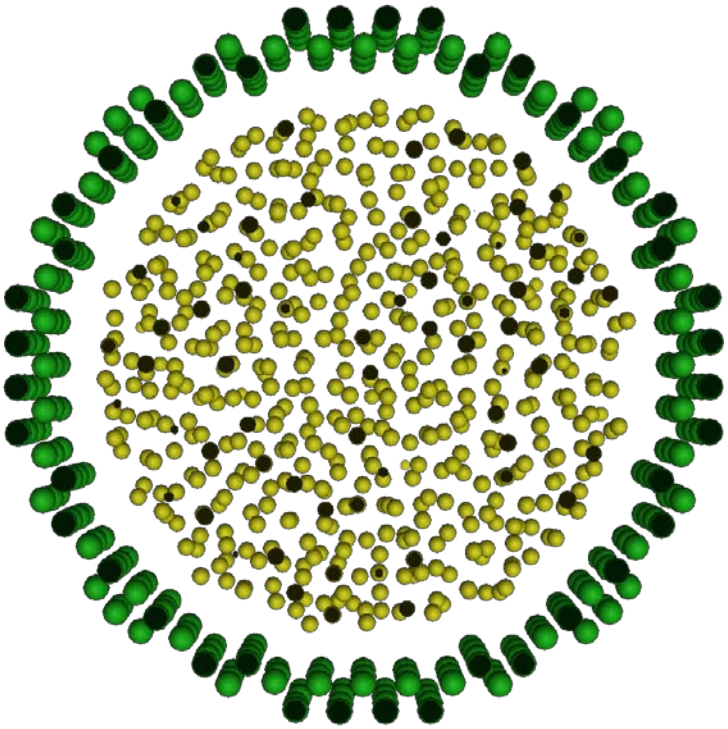

Figure 4. Cross-section from a simulation of a 4nm 0.5He/V bubble at 100K, green spheres are iron are and yellow spheres are helium atoms. Atoms cut by the cross-section plane are shown partly black.

Figure 5 shows the radial density function of an equilibrium 2nm bubble with a He/V = 0.49 at 300K. The red circles show the iron atoms that make up the surface of the bubble, while the blue squares represent the density of helium atoms in the space, averaged over a 1ns simulation. The helium density oscillates enough to suggest a shell structure to the arrangement of atoms, but not enough to suggest solid helium. This agrees with [15] prediction that the helium in the bubble would not be solid. The dotted line in the figure, an approximation to a uniform distribution, shows that the actual helium density (1.04) is just over double the nominal density (0.49). The helium occupies a sphere of radius 7.7Å (just under half the volume of the void), and the radial gap is approximately 2.2Å.

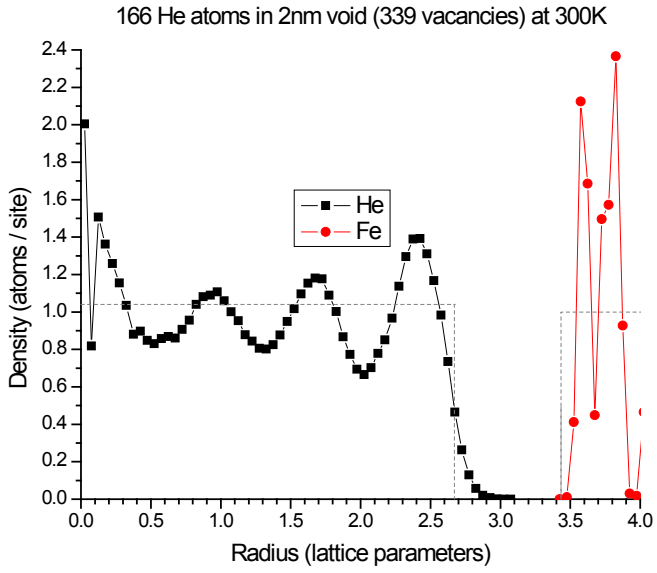

Figure 5. Radial distribution function of a 2nm equilibrium bubble at 300K.

In a void, the surface matrix atoms relax inwards slightly, reducing the volume of the void. At higher temperatures, they move in more due to the thermal expansion of the iron. Adding helium to the void pushes the atoms outwards, increasing the volume again. The more helium added, the further the bubble expands. There is a point where the forces balance and the bubble is neither expanded nor contracted; the surface atoms are at the same place as they would be in a perfect lattice. We use this point as our condition for equilibrium. The equilibrium He/V ratio is temperature and size dependant. In general, the equilibrium He/V ratio is lower for higher temperatures and larger bubbles.

Figure 6 shows the dilation of a 2nm diameter bubble as a function of He/V ratio for different temperatures. The equilibrium ratio for each temperature can be determined by where it crosses the horizontal zero line. At 2nm, the curves for the different temperatures are close together and the equilibrium He/V ratios lie in the range 0.4–0.55; for larger bubbles, the curves spread out more (not shown).

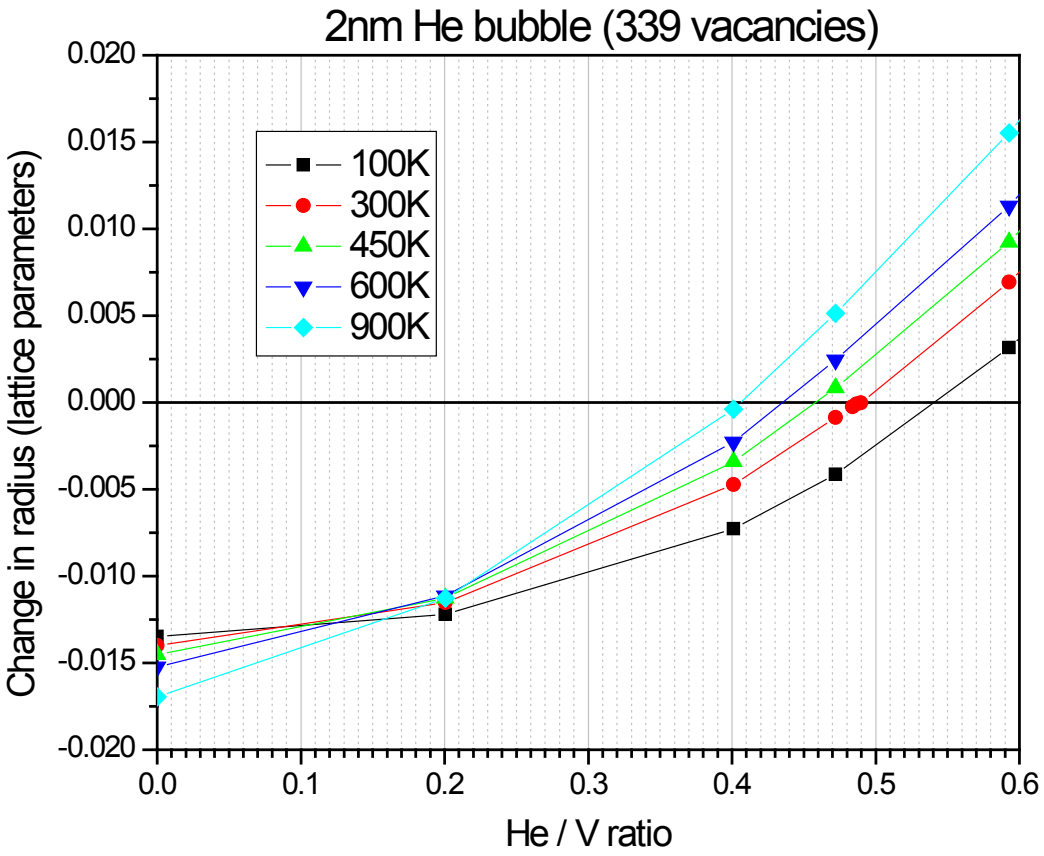

Figure 6. Dilation of 2nm bubbles as a function of He/V ratio at different temperatures.

Figure 7 shows the dilation of different sized bubbles as a function of He/V ratio at 300K. The He/V ratio at equilibrium initially decreases as the bubble size increases, but the incremental change is reduced for smaller bubbles. There is little change in the equilibrium ratio between a 2 and 1.5 nm bubble, and the ratio increases for smaller sizes as shown by the curve for the 1nm bubble. Since the equilibrium pressure (which increases as ratio increases) is expected to follow a $2\gamma/r$ relationship (where γ is the surface energy and r is the bubble radius), the reduction in ratio with increasing size for the 2, 4 and 6nm bubbles is expected. The bubble volume is defined by the position of the surface iron atoms, but the volume actually occupied by helium is defined by the He atom positions, and is substantially smaller. The smaller the bubble gets, the greater fraction of the bubble volume is in the He-free gap and the less is occupied by helium. In the 1nm bubbles the helium occupies less than 30% of the volume, which leads to the reduction in the equilibrium ratio.

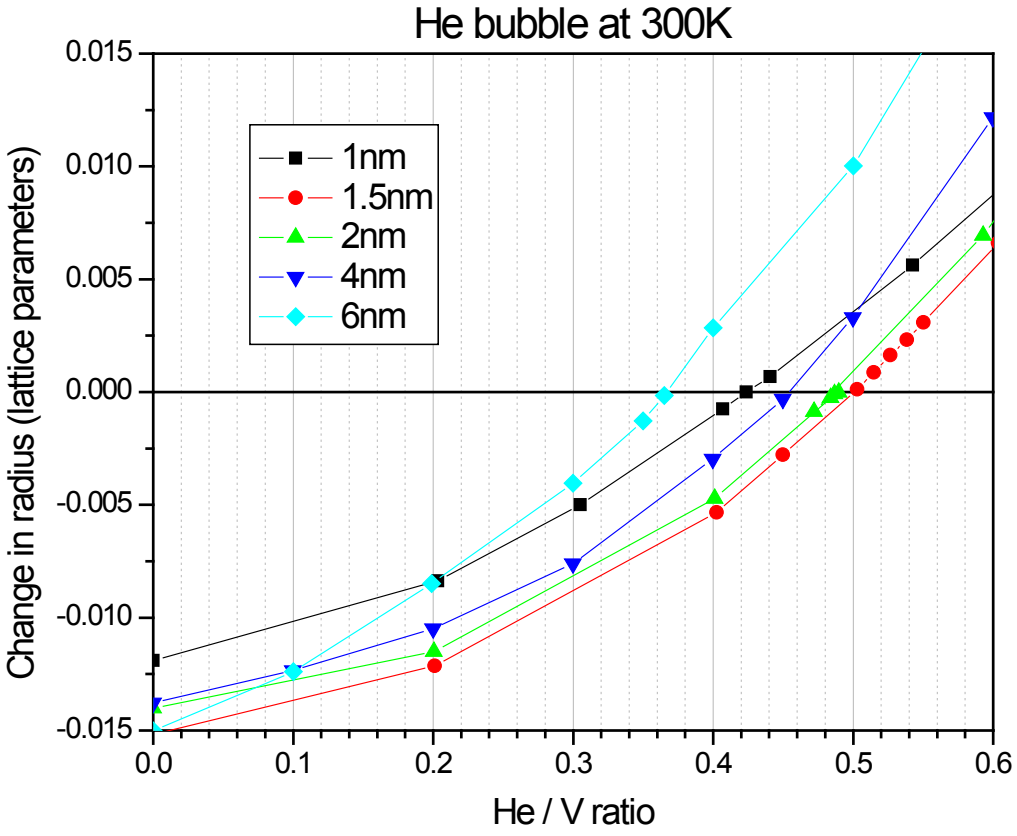

Figure .7 Dilation of different size bubbles as a function of He/V ratio at 300K.

4. Discussion and Conclusions

4.1. Coalescence

Simulations investigating the nucleation of nascent helium bubbles from interstitial helium atoms were carried out using the Ackland iron and ORNL He–Fe potentials. He interstitial cluster growth, coalescence and Frenkel pair creation were almost negligible at 200K but prevalent at all higher temperatures. The temperature affected not just the rate but also the nature of the defect creation process.

The higher the temperature, the faster He atoms and clusters diffuse, which makes coalescence occur faster. This is balanced by higher temperatures leading to small clusters being broken up, delaying the creation of larger, stable clusters. The result is that that the cluster size distribution is temperature dependant: higher temperatures lead to fewer but larger clusters. Higher temperatures also increase the number of Frenkel pairs likely to be emitted from a larger He–V cluster.

4.2 Cluster Diffusion

Diffusion rates for clusters of 1 to 6 interstitial helium atoms were calculated for several combinations of potentials. Three combinations, Ackland + ORNL, Finnis–Sinclair + ORNL and Mendelev + Juslin–Nordlund reproduced the DFT result [16] of 0.06 eV for the migration of a single He interstitial. In general, larger clusters were found to diffuse slower, however there were significant differences between the potentials. He_2 clusters tended to have a similar or lower energy barrier than single interstitial helium atoms but still diffuse slower due to a lower pre-exponential factor. The ORNL and Wilson potentials show significantly higher barriers for He_3 and larger. The J–N potential shows barriers of about 0.06eV for

clusters of 1 to 4 interstitials, with the pre-exponential factor decreasing with increasing cluster size. He_5 was found to have a (usually substantially) lower migration barrier than He_4 with all combinations of potentials used. A possible explanation is that the tetrahedral arrangement of He_4 is much more stable due to its high symmetry that matches the symmetry of the Fe matrix. He_5 configurations are far less symmetrical and, in some potentials, allow for rapid 1D diffusion.

4.3 Bubbles

1, 1.5, 2, 4 and 6nm diameter bubbles have been simulated. In a void, the surface matrix atoms relax inwards; the addition of helium atoms pushes them back outwards. The balance point (i.e. zero total dilation) defines an equilibrium condition.

The equilibrium He/V ratio is size dependent, with a maximum when the bubble diameter is close to 1.5nm. Larger bubbles have a smaller ratio because the pressure is lower, while smaller bubbles have a smaller ratio because the space available for helium decreases rapidly due to the increasing fraction of the volume accounted for by the He-free gap. The equilibrium He/V ratio also decreases as temperature increases, so bubbles formed under high temperature irradiation may be out of equilibrium during room temperature experiments.

This paper provides a brief review of the general phenomena and mechanisms observed in extensive simulations of He atom behavior inside an Fe matrix. More detailed descriptions of the mechanisms observed and their quantification will be presented in separate publications.

Acknowledgement

Research sponsored by the Office of Fusion Energy Sciences (DMS) and the Division of Materials Sciences and Engineering (YNO, RES), U.S. Department of Energy, under contract DE-AC05-00OR22725 with UT-Battelle, LLC.

References

[1] S. J. Zinkle, Physics of Plamas, 12 (2005) p. 058101.
[2] S. I. Golubov, R. E. Stoller, S. J. Zinkle, and A. M. Ovcharenko, J. Nucl. Mater. 361 (2007) p. 149.
[3] D. M. Stewart, Y. N. Osetsky, R. E. Stoller, S. I. Golubov, T. Seletskaia1, P. J. Kamenski, accepted for publication in Philos. Mag. (2009).
[4] T. Seletskaia, Y. N. Osetsky, R. E. Stoller, and G. M. Stocks, J. Nucl. Mater. 351 (2006) p. 109
[5] T. Seletskaia, Y. N. Osetsky, R. E. Stoller, and G. M. Stocks, J. Nucl. Mater.367 (2007) p. 355.
[6] R. E. Stoller, S. I. Golubov, P. J. Kamenski, T. Seletskaia, and Yu. N. Osetsky, "Implementation of A New Fe–He Three-body Interatomic Potential for Molecular Dynamics Simulations," accepted for publication in Philos. Mag. (2009).
[7] W. Wilson and R. Johnson, Rare Gases in Metals, Interatomic Potentials and Simulation of Lattice Defects, Battelle Institute Materials Science Colloquia, 1972, 375–390 (1972).
[8] N. Juslin and K. Nordlund, J. Nucl. Mater. 382 (2008) p. 143.
[9] G. J. Ackland, D. J. Bacon, A. F. Calder, and T. Harry, Philos. Mag. A 75 (1997) p. 713.
[10] Yu. N. Osetsky, Defect and Diffusion Forum 188–190 (2001) p. 71.
[11] M. W. Finnis and J. E. Sinclair, Philos. Mag. A 50 (1984) p. 45.
[12] M. I. Mendelev, S. Han, D. J. Srolovitz, G. J. Ackland, D. Y. Sun, and M. Asta, Philos. Mag. 83 (2003) p. 3977.
[13] R. Aziz, A. Janzen, and M. Moldover, Phys. Rev. Lett. 74 (1995), pp. 1586–1589.
[14] W. L. DeLano, “The PyMol molecular graphic system,” DeLano Scientific LLC, San Carlos, Ca, USA. http://www.pymol.org.
[15] S. M. H. Haghighat, G. Lucas and R. Schäublin, Europhysics Letters 85 (2009) p, 60008
[16] C.C. Fu and F. Willaime, Phys. Rev. B 72 (2005) p. 064117.

MULTIPOLAR ELASTIC REPRESENTATION OF DEFECT FIELDS IN METALS-

D. Seif (University of California, Los Angeles), N.M. Ghoniem (University of California, Los Angeles)

OBJECTIVE:

The objective of this study is to develop a hybrid atomistic-continuum method to obtain an elastic representation of radiation-induced defects in α-Fe. This will make available calculations of elastic interaction energies between defects in various strain environments within the framework of continuum elasticity theory.

SUMMARY

In this study, a hybrid method has been developed to couple the results of molecular statics calculations with classical isotropic elasticity theory to extract a continuum representation of various defects through the use of force multipoles. These calculations have provided a means to account for the changes in defect energetics due to local strain environment effects. In uniform strain environments, the use of the elastic dipole tensor is sufficient to calculate the interaction energy. However we find the use of higher order multipole tensors necessary to represent many defects and their interactions in environments with strain gradients, such as the vicinity of grain boundaries or other extended defects. In addition, isotropic elastic Green's functions are found to provide material response very consistent with atomistic simulations when these higher order terms are implemented. We have made calculations of interactions between defects including Fe and He point defects, Fe self-interstitial clusters, He-vacancy clusters, and extended defects in α-iron.

PROGRESS AND STATUS

Introduction

Internal structural components which operate in the nuclear fusion environment are subject to significant damage doses stemming from the onslaught of 14 MeV neutrons produced in the D-T cycle. The internal production of point defects such as self-interstitial atoms (SIA) and vacancies from elastic interactions, and helium from (n,α)-reactions lead to severe material degradation over time, including swelling [1] and low-temperature embrittlement [2]. The prediction of damage evolution and component lifetime is highly dependent upon accurate models of point defect production and interactions within the material. The development of truly predictive long-timescale simulation techniques has been quite scarce in recent history due to the trade-offs between computational efficiency and rigorous physical treatments. While an accurate physical model of damage accumulation and evolution requires a comprehensive understanding of point defect energetics and interactions, there has been an absence in many studies [3,4,5], of the consideration of local strain environment effects on defect migration properties and stability. The goal of this work is to combine atomistic simulation with elasticity theory to implement the method of force multipoles to represent defects, and use continuum elasticity calculations to quantify interactions between these defects and with various strain fields. These interactions can be made available to future KMC simulations to account for strain-biased diffusion, and give a physically-based description of the accumulation and evolution of damage in irradiated metals.

Force Multipole Representation of Defects

The insertion of a point defect into a perfect crystalline lattice creates a displacement field around the defect on surrounding atoms. This displacement field is typically modeled using one of multiple approaches. Eshelby [9] developed a very simple and elegant way to approach the problem within the confines of elasticity theory. He treated the point defect as a center of dilatation, modeled as a spherical inclusion within an elastic isotropic medium, whose strength may be determined from experiment. This model is only suited, however, to describe defects of high symmetry acting in materials with very low anisotropy. Another method, proposed by Kanzaki [6], involves representing the defect as an array of

forces located on neighboring atoms. Generally called the method of 'Kanzaki forces', this method has been successfully implemented in the past, for example, to give the atomic displacements around vacancies in Cu and Al [7]. However, this approach suffers from a few inherent limitations. Among them, the formulation requires the spatial extent of these forces to be as restricted as possible, typically to first nearest neighbor atoms. For this reason, the elastic response of the material must be modeled with complex 'lattice' Green's functions that have no closed form expression [8], to account for the complex displacements inherent in a defected crystalline lattice. In addition, each point force will introduce a singularity, and additional effort will be required in the computations.

For our application, we have found the method of 'force-multipoles' to be most beneficial. In this method, the defect is represented as a multipolar expansion of forces acting at the center of the defect. As in the Kanzaki approach, the addition of a point defect in a perfect crystal can be alternatively represented as a configuration of point forces acting on all affected, neighboring atoms. Consider a defect at the origin surrounded by N atoms (v) with separation vectors $\mathbf{l}^{\nu}$. Following the formulations of Siems [10] and Teodosiu [11], the displacement field caused by a defect at the origin can expressed as

$$u_m(\mathbf{x}) = \sum_{\nu=1}^{N} G_{ms}(\mathbf{x}-\mathbf{l}^{\nu})P_s^{\nu}, \tag{1}$$

where $\mathbf{G}(\mathbf{x})$ is the elastic Green's tensor function of the material and $\mathbf{P}^{\nu}$ are the point forces acting on initial lattice atom locations $\mathbf{l}^{\nu}$. We note here that repeated indices imply summation. Expanding $\mathbf{G}(\mathbf{x}-\mathbf{l}^{\nu})$ in a Taylor's series about $\mathbf{x}$ gives

$$G_{ms}(\mathbf{x}-\mathbf{l}^{\nu}) = \sum_{k=0}^{\infty} \frac{(-1)^k}{k!} G_{ms,q_1\ldots q_k}(\mathbf{x})\mathbf{l}^{\nu}_{q_1}\ldots\mathbf{l}^{\nu}_{q_k} = G_{ms}(\mathbf{x}) - G_{ms,n}(\mathbf{x})\mathbf{l}^{\nu}_n + \frac{1}{2!}G_{ms,nq}(\mathbf{x})\mathbf{l}^{\nu}_n\mathbf{l}^{\nu}_q - \ldots.. \tag{2}$$

Plugging this Green's function expansion back into (1), the displacement field can be rewritten as

$$u_m(\mathbf{x}) = \sum_{k=0}^{\infty} \frac{(-1)^k}{k!} G_{ms,q_1\ldots q_k}(\mathbf{x})\mathbf{P}^{(k)}_{q_1\ldots q_k n} = G_{ms}(\mathbf{x})\mathbf{P}^{(0)}_s - G_{ms,n}(\mathbf{x})\mathbf{P}^{(1)}_{ns} + G_{ms,nq}(\mathbf{x})\mathbf{P}^{(2)}_{nqs} - \ldots, \tag{3}$$

where

$$\mathbf{P}^{(k)}_{q_1\ldots q_k s} = \sum_{\nu=1}^{N} l^{\nu}_{q_1}\ldots l^{\nu}_{q_k}\mathbf{P}^{\nu}_s, \qquad k = 1, 2, \ldots.., \infty \tag{4}$$

are called the multipole moments of k^{th} order. It is important to note that the k=0 moment represents a sum of the applied force vectors over all atoms, which equals zero for equilibrium conditions to be satisfied. The k = 1, 2 and 3 moments are called the dipole, quadrupole, and octopole moments and can be expressed as

$$\begin{aligned}
\mathbf{P}^{(1)} &= \sum_{\nu=1}^{N} \mathbf{l}^{\nu}\mathbf{P}^{\nu} & P^{(1)}_{ns} &= \sum_{\nu=1}^{N} l^{\nu}_n P^{\nu}_s \\
\mathbf{P}^{(2)} &= \sum_{\nu=1}^{N} \mathbf{l}^{\nu}\mathbf{l}^{\nu}\mathbf{P}^{\nu} & P^{(2)}_{nqs} &= \sum_{\nu=1}^{N} l^{\nu}_n l^{\nu}_q P^{\nu}_s \\
\mathbf{P}^{(3)} &= \sum_{\nu=1}^{N} \mathbf{l}^{\nu}\mathbf{l}^{\nu}\mathbf{l}^{\nu}\mathbf{P}^{\nu} & P^{(3)}_{nqrs} &= \sum_{\nu=1}^{N} l^{\nu}_n l^{\nu}_q l^{\nu}_r P^{\nu}_s
\end{aligned} \tag{5}$$

The displacement equation (3) states that the elastic response of a defected material requires knowledge of the Green's function of the material and the values of the multipole moments of the defect. We point

out that this differs greatly from the Kanzaki approach in that all forces and higher order moments occur at the center of the defect, and not on lattice sites. To lowest order, the defect can be represented by the dipole tensor as is usually the case for defects of high symmetry (vacancies, interstitials, etc).

Solution Methodology

We have recently developed a hybrid method to compute the values for the multipolar moments of lattice defects using molecular statics (MS) calculations and continuum elasticity theory. Thus far, our focus has been on radiation induced defects in the bcc alpha-iron lattice. These defects include self-interstitial atoms (SIA), SIA clusters, helium point defects, and helium-vacancy clusters. Our method first requires an atomistic simulation of the defect in the host lattice to acquire the displacement field around the defect. For our molecular statics calculations we have chosen interatomic potentials well suited for simulation of these types of defects. For Fe-Fe, Fe-He, and He-He interactions we have chosen the well known Ackland [12], Juslin-Nordlund [13], and Lennard-Jones [14] interatomic potentials, respectively. In our atomistic calculations the defect was introduced in the center of the simulation box and a static relaxation (0 K) was implemented via conjugate gradient minimization to allow relaxation of the atoms. The lattice parameter used was 2.866 Angstroms. The supercell was a cube with an edge length of 18 lattice parameters (~52 Angstroms) and periodic boundary conditions were applied on all sides. This cell size was found to be large enough to contain the full extent of the lattice distortions produced, with the total number of host Fe atoms being 11664. After performing the MS calculations, the next step is to use the atomic displacement information to obtain a multipolar representation of the defect. Taking another look at equation (3), we can alternatively view this equation as a matrix-vector multiplication of the form

$$\{u\} = [G]\{P\}. \tag{6}$$

In this light, {u} is a 3N by 1 column vector containing the MS displacement vector components of N chosen neighboring atoms and can be expressed as $\{u\} = \{\{u_1, u_2, u_3\}_1 \{u_1, u_2, u_3\}_2 .... \{u_1, u_2, u_3\}_N\}^T$. The column vector {P} represents the values of the chosen multipolar moments used to describe the defect. It has size $N^{(k)}$ by 1, where $N^{(k)}$ equals the total number of multipolar values chosen to be solved for. For example, if the dipole moment is sufficient to represent the defect, then $N^{(k)} = 9$. This vector can be expressed as $\{P\} = \{\{P_{11}, P_{12}, ...P_{33}\}^{(1)} ... \{P_{1...1}, P_{1...2}, ...P_{3...3}\}^{(k)}\}^T$. The matrix [G] represents the corresponding elastic Green's function derivatives evaluated at the desired field point. This matrix has size 3N by $N^{(k)}$. We have found that the use of the isotropic elastic Green's function provides adequate response of the material as compared to our MS calculations. This response function is well known and provides a tractable closed-form solution simplifying the necessary calculations. It can be expressed as

$$G_{ms}(\vec{x}) = \frac{1}{8\pi\mu(\lambda + 2\mu)} \left[(\lambda + 3\mu) \frac{\delta_{ms}}{r} + (\lambda + \mu) \frac{x_m x_s}{r^3} \right], \tag{7}$$

where the Lamé's constants λ and μ define the material, and r = $\sqrt{x_i x_i}$. The multipole (k) value also implies the order of derivative of the Green's function necessary for the calculations. We note these derivatives fall off as $O(r^{-(k+1)})$. While the displacement field contributions decay rapidly for k>1, and the dipole moment dominates at longer distances, we have typically found the inclusion of up to the octopole tensor, to be necessary to accurately match the lattice displacements near the defect. With the values of {u} and [G] known from MS calculations and elasticity theory, respectively, equation (6) can be posed as a least squares optimization problem which can then be solved to obtain the multipole moment values {P}. This step has a significant benefit since displacements beyond the first few shells may also be used to extract information about the defect.

The lifetime and fate of point defects operating in radiation damaged environments are governed by the many elastic interactions they may have with any number of other defects within the host material. These interactions affect the stability and migration tendencies of defects and have been a topic of great concern within the nuclear materials community for some time. Thus, it is of most importance to have a detailed, quantitative understanding of these interactions. Consider again a point defect at **x** modeled as

a configuration of point forces $\mathbf{P}^{\nu}$ acting on neighboring atoms ν, this time placed within an existing displacement field **u**. It is clear that the resulting interaction energy can be expressed as

$$E_{int} = -\sum_{\nu=1}^{N} \mathbf{P}^{\nu} \cdot \mathbf{u}(\mathbf{x} + \mathbf{l}^{\nu}). \tag{8}$$

Now expanding $\mathbf{u}(\mathbf{x}+\mathbf{l}^{\nu})$ in a Taylor's series about **x** we have

$$u_m(\mathbf{x} + \mathbf{l}^{\nu}) = u_m(\mathbf{x}) + u_{m,i}(\mathbf{x}) l_i^{\nu} + \frac{1}{2!} u_{m,ij}(\mathbf{x}) l_i^{\nu} l_j^{\nu} + \frac{1}{3!} u_{m,ijk}(\mathbf{x}) l_i^{\nu} l_j^{\nu} l_k^{\nu} + \ldots \tag{9}$$

Introducing this expression back into (8), allows the interaction energy to be expressed in terms of the multipolar moments as

$$E_{int} = -\sum_{n=1}^{\infty} \frac{1}{n!} u_{m,q_1 \ldots q_n}(\mathbf{x}) \mathbf{P}^{(n)}_{q_1 \ldots q_n m} = -\mathbf{P}^{(1)}_{im} u_{m,i}(\mathbf{x}) - \frac{1}{2!} \mathbf{P}^{(2)}_{ijm} u_{m,ij}(\mathbf{x}) - \frac{1}{3!} \mathbf{P}^{(3)}_{ijkm} u_{m,ijk}(\mathbf{x}) - \ldots \tag{10}$$

Applications

The focus of our research has been primarily on radiation induced defects in the bcc α-iron lattice. In this section we will highlight some representative results obtained for a small selection of defects that have been modeled.

I. Fe SIA <110> dumbbell

Self interstitial atoms (SIA) are generated in significant quantities in fission, and to a larger extent, fusion reactors. They are produced in the wake of displacement cascades caused by incoming fluxes of high energy neutrons. Studies of the energetics and mechanisms of migration for these point defects have been a topic of interest for many years. Single SIAs in α-iron take the form of a split dumbbell configuration. In the past, experimental studies [15], as well as ab-initio calculations [16,17], have concluded the ground state configuration to be the <110> dumbbell. In our MS calculations, we have found the formation energy to be 3.35 eV, which is in agreement with values reported previously by Terentyev, *et al* [18], but lower than those predicted by DFT. Implementing our hybrid method for multipolar representation of this defect, we have calculated the multipolar moments up to the octopole tensor ($\mathbf{P}^{(3)}$). Calculated values for the dipole tensor are given in table 1. In figure 1 we have plotted the displacements versus distance from the defect center. The plots on the left and right show the radial and Cartesian components, of the displacements, respectively. The circles in these plots are those obtained from MS calculations, while the points represent the calculated displacements using the multipolar representation via equation (3).

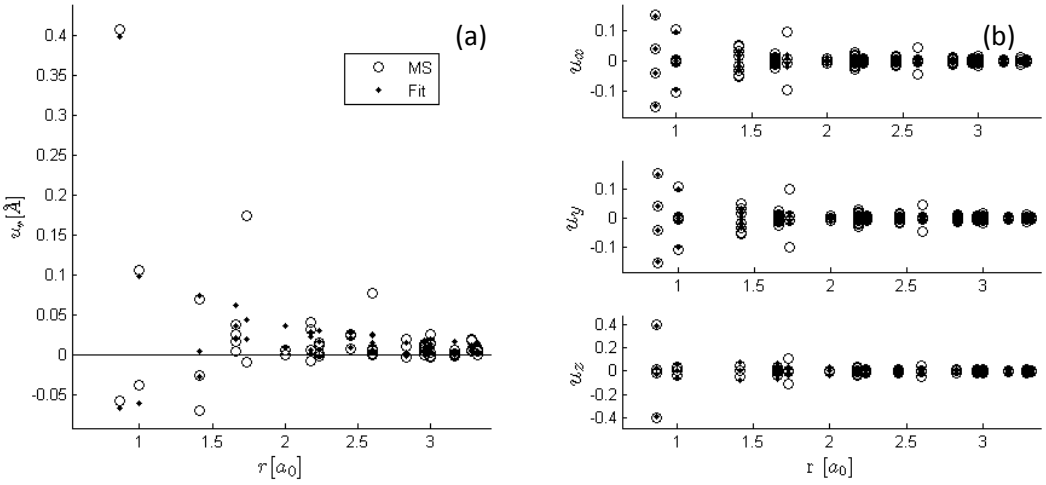

Figure 1. Displacement vs. radial distance plots for [110] Fe SIA. (a) radial (b) Cartesian components.

We see very good agreement in the displacements predicted by the multipolar representation. First, it is important to note the complexity of the lattice response to this defect. In the first shell alone we see the very large expansion of the four atoms lying on the (110) plane with a contraction of the remaining four atoms. This immediately suggests any attempt to model this defect as an inclusion or center of dilatation would be in vain. In fact we have found that without the inclusion of the octopole moment, the dipole tensor alone struggles to replicate these phenomena. The largest contribution to elastic energy is contained within the first few shells around the defect, and we see very good agreement in this vicinity. To obtain an overall quantity to compare the accuracy of this new multipolar representation of the defect compared to the MS calculations, we have chosen to compare the predicted formation energy of both representations. To do this, we apply the multipole displacements to a perfect bcc Fe lattice and hold these new positions fixed. Next we evaluate the energy of this system using the Fe interatomic potential. This allows direct comparison of the formation energies. We find the multipolar representation to give a formation energy of 4.02 eV giving a percent difference of roughly 20% with the MS value. This over-prediction stems from the inherent inability of continuum elasticity to account for the intricate atomic interactions that occur within the discrete atomic lattice. We also note this percent difference lies within the variation of several Fe interatomic potentials [23].

We have recently studied the effect of deformation on the formation energy of SIAs in α-iron [19]. This problem is important in severe radiation conditions where the lattice undergoes deformations under applied loads. Ab-initio calculations were made for various strain loadings of volumetric and uniaxial type. These calculations were then compared to results from obtained using MS calculations with the above mentioned interatomic potential, and also with the multipolar representation of the defect using continuum elasticity (CE) formulations. The formation energy of a defect in a strained environment can be computed as

$$E^f = E_0^f + E_{int} \tag{11}$$

where E_0^f represents the equilibrium formation energy of the defect and E_{int} is the elastic interaction of the defect with the strain field. As a reference, we have taken E_0^f to be that calculated by MS. In a homogeneous strain field, we see from equation (10) the interaction term can be computed as

$$E_{int} = -P_{ij}^{(1)}\varepsilon_{ij} \,. \tag{12}$$

This equation implies that under constant strain, only the dipole moment contributes to the interaction energy. In the case of defect interactions with varying strain fields (dislocations, grain boundaries, other point defects), this will not be the case, and the higher order moments will contribute to the interactions. Results for formation energies of the [110] SIA under both strain modes can be found in figure 2. For volumetric strains, the applied strain tensor can be expressed as $\varepsilon_{ij}=\varepsilon_v/3\ \delta_{ij}$, and for uniaxial strains the only nonzero component was ε_{33}.

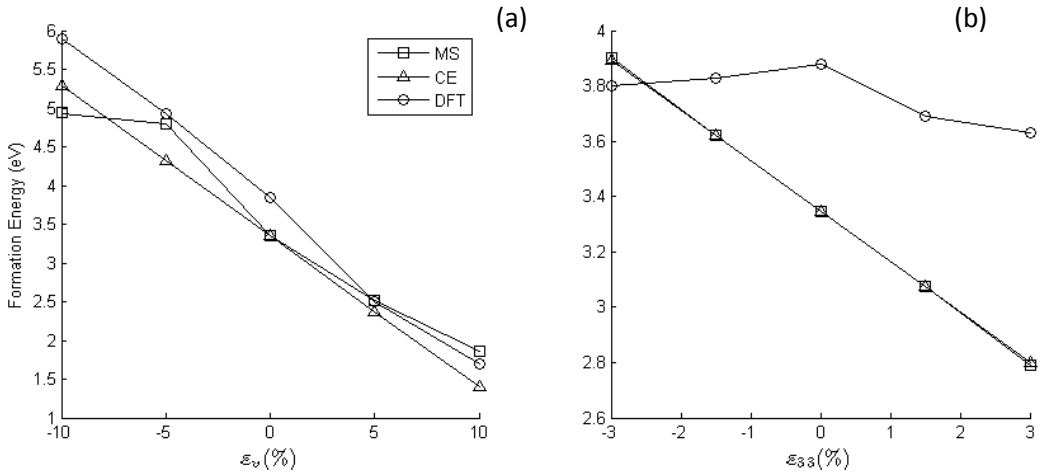

Figure 2. Formation energy vs. applied external strain for [110] Fe SIA. (a) Volumetric (b) Uniaxial.

In the volumetric strain studies we found very good agreement in the energetic trends. The linear behavior of energetic favorability of defect formation under lattice expansion is predicted by the continuum approach and verified by the MS and ab initio calculations. The discrepancies in the values can be attributed to several causes. Above all, the formation energy of a defect will contain contributions of both elastic and electronic interaction with the host lattice. The MS calculations do not account for these electronic interactions though they do contain information about the lattice. The continuum elasticity solutions contain neither energetic contributions from the lattice structure nor the electronic interactions and thus predict lower formation energies compared to the ab-initio calculations. Under uniaxial strain we see near identical prediction of the formation energy in the MS and continuum calculations. However the predicted trends in both defects are not observed in the ab-initio results. This suggests highly influential electronic reconfigurations are at play in uniaxial deformations.

II. Helium point defects

Extrinsic radiation induced defects are well known to contribute to the mechanisms of damage accumulation and evolution in irradiated materials. Substantial quantities of helium atoms are generated within the α-iron lattice by (n,α) transmutation reactions. Helium is highly insoluble in iron and thus interstitials rapidly migrate with an energy barrier less than 20% than that of Fe interstitials [20]. We have undergone calculations of the multipole moments for helium in both octahedral and substitutional configurations. The results for these calculations are found in table 1. Figure 3 (a) shows the radial displacement versus distance for the octahedral interstitial.

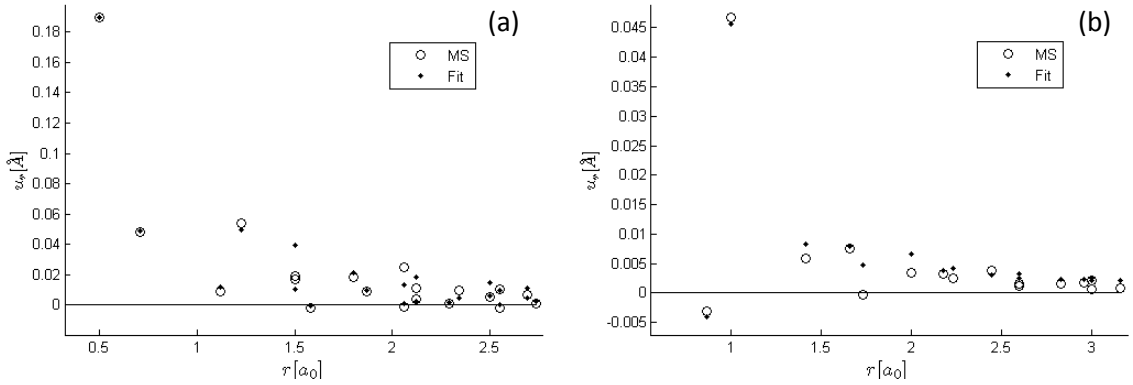

Figure 3. Radial displacement vs. distance plots for helium point defects in α-Fe. (a) Octahedral (b) Substitutional.

We see excellent agreement in the first four atomic shells, with an over-prediction in the slightly anisotropic fifth shell, but good decay agreement in the shells that follow. We found it necessary to implement the octopole moment in order to get good matching for the displacements in the third and fourth shell. Comparing the formation energies between MS and the multipole representation, we found the percent difference to be only 0.89% between the continuum value (4.49 eV) and the MS value (4.45 eV).

The displacement field generated by the substitutional helium is somewhat more complex (see figure 3 (b)). In our MS calculations we find a 0.307 pm radial contraction of the 8 nearest neighbors, contrasted by a 4.67 pm expansion of the 6 second nearest neighbors. This behavior is not well suited for classical elasticity and we find the use of the octopole tensor as the only way to account for the discontinuity. Our calculations give a percent difference of 33% and 2.3% in the radial displacements of the first two shells, respectively, and we find the octopole tensor to assume only six non-zero components. We note the large percent difference in the first shell is due to the very small contraction, and does not influence the defect energy to the extent the second shell does.

Table 1. Computed dipole tensor values (in eV) for selected defects in α-Fe. (*P_{12}/P_{21} given for HeV cluster)

	P_{11}	P_{22}	P_{33}	P_{12}	P_{23}	P_{13}
Octahedral Helium	5.37	5.37	8.73	0.00	0.00	0.00
Substitutional Helium	3.51	3.51	3.51	0.00	0.00	0.00
[110] Fe SIA Dumbbell	20.02	20.02	18.22	-9.107	0.00	0.00
He12V4 Cluster	64.65	71.91	72.84	0.606/-0.095*	0.00	0.00

III. Helium vacancy clusters

The rapid diffusion of helium within the host lattice is halted as these solute atoms meet their fate at system sinks such as dislocations, grain boundaries, and vacancy voids. Helium has long been known to stabilize voids against their otherwise collapse by vacancy emission [21], and lead to swelling in the material. The stability and migration energetics of helium-vacancy clusters (He_nV_m) have been studied in the past using atomistic simulations [20,21]. We have found our hybrid multipole method to accurately mimic the displacements seen in MS calculations of these defects. We describe here the results of our calculations for a $He_{12}V_4$ cluster. This defect was found to produce a highly anisotropic displacement field in the lattice and illustrates the point that when the higher order multipolar moments are included, then isotropic elastic Green's functions are capable of predicting these non-uniformities. The defect was created by adding 12 atoms into 4 vacancies in a random fashion. Then dynamics were run at 100 K for 1 ns allowing the cluster reach a more energetically favorable configuration. Lastly the defect and lattice were allowed to relax at 0 K. We do not suggest here that this particular final configuration is the ground state of the defect. Figure 4 shows the displacement field of the defect. 14 nonzero components

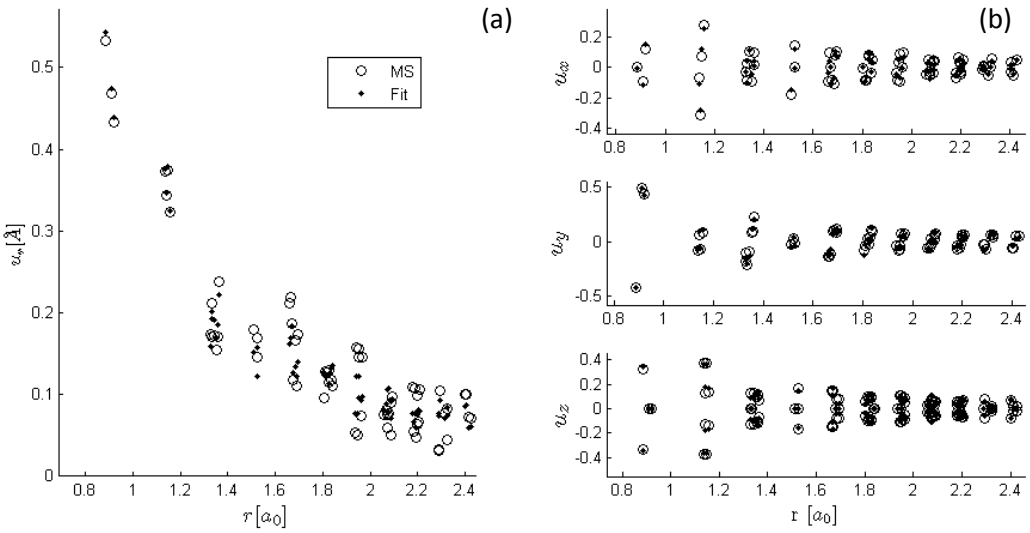

Figure 4. Displacement vs. radial distance plots for a $He_{12}V_4$ cluster in α-Fe. (a) radial (b) Cartesian components.

We chose to define the center of the defect to be the center of mass of the helium atoms within the cluster in the final configuration which explains the minor radial variations in the shell distances. We note the very close agreement in the atomic displacements within about 1.7 lattice parameters of the defect center. In this region the discrete lattice effects will be maximum, however we see isotropic elasticity is capable of reproducing this foreign nature. Furthermore, the fitting scheme was generated using the MS displacements of 40 neighboring atoms which includes all atoms within this region. The elasticity-predicted decay beyond this point is seen to match well with the MS calculations. We note the asymmetry of the dipole tensor for this defect as seen in table 1. It is found that $P_{12} \neq P_{21}$ which suggests the defect is not without moment.

Elastic Interactions of Defects

With the multipolar values known for various defects, equation (10) may be implemented to calculate interaction energy fields between defects. Plotted in figure 5 are the interaction energy contours of (a) an octahedral helium interstitial and (b) an Fe [110] SIA atom, with a $He_{12}V_4$ cluster residing at the center.

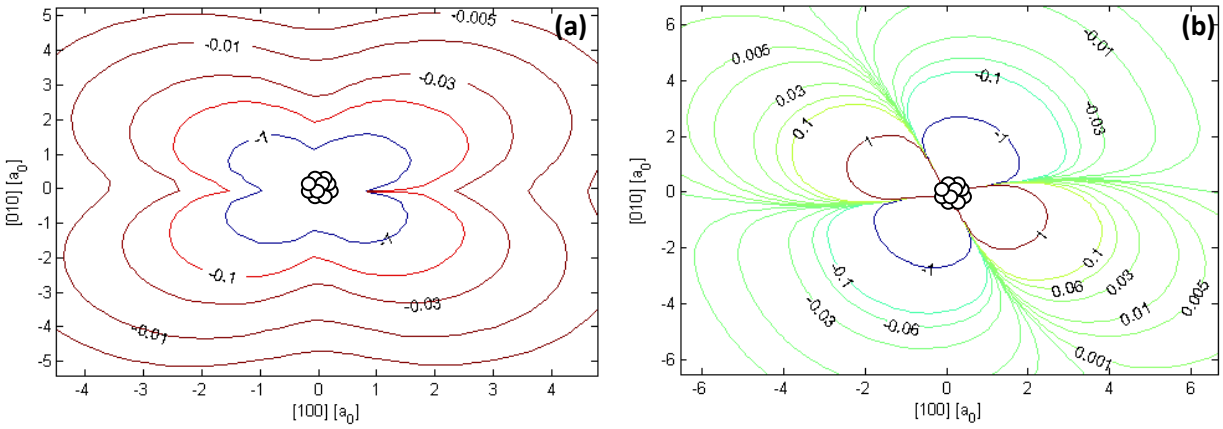

Figure 5. Iso-interaction energy contours (in eV) of (a) He octahedral (b) [110] Fe SIA dumbbell, with $He_{12}V_4$ cluster at the origin in α-Fe.

The interaction energy contours in (a) show attraction between the defects at all positions on the (100) plane. This elastic attraction which leads to cluster growth is well known to exist between interstitial helium atoms and HeV clusters, and is confirmed by our elasticity calculations. The iron SIA on the other hand shows four distinct regions around the HeV cluster. Two regions that indicate a repulsive interaction, and two that show attraction. We propose that for a sufficiently strong repulsive interaction near the cluster, one of two phenomena may occur. The SIA will either rotate its orientation to a more energetically favorable configuration, or migrate to one of the attractive regions. Its choice will obviously depend on the energy barriers involved in those processes. In these plots we note that not all positions will be available to the point defects due to the presence of the host lattice, however we find the trends and energy scales very useful.

We have also conducted calculations between extended- and point defects. Using the edge dislocation model given in Hirth and Lothe [22] for an infinite isotropic elastic solid, we have obtained interaction energy contours for the multipolar defects. These calculations are meant only to be approximations, especially near the dislocation core where the singularity causes divergence in the energy. Plotted in figure 6 are the interaction energy contours of (a) an octahedral helium interstitial and (b) an Fe [110] SIA atom, with an $a_0/2[111]\{110\}$ edge dislocation in iron.

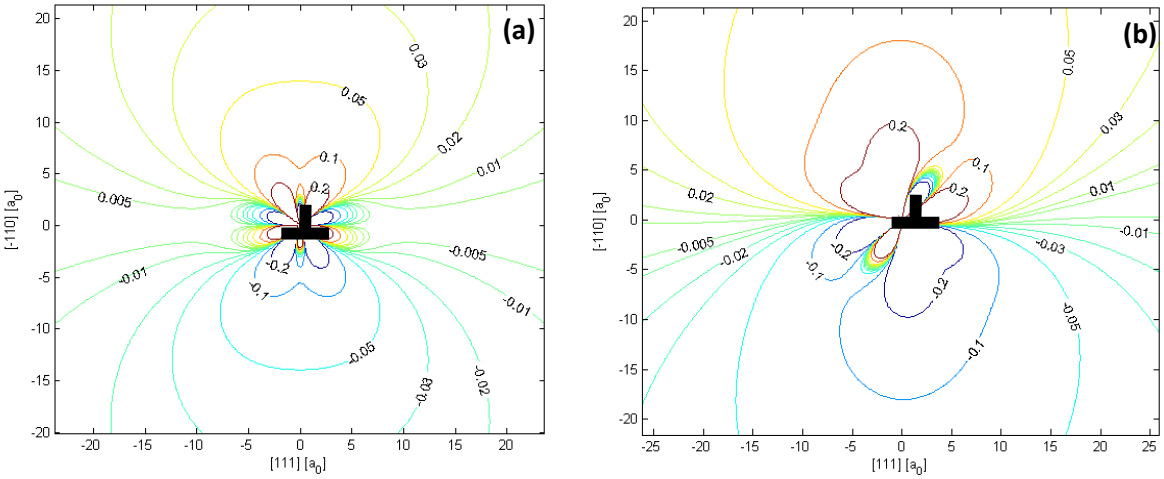

Figure 6. Iso-interaction energy contours (in eV) of (a) He octahedral (b) [110] Fe SIA dumbbell, with an $a_0/2[111]\{110\}$ edge dislocation in α-Fe.

In both plots of figure 6 we see the tendency for the interstitials to be drawn to the dislocation core while on the tensile side of the dislocation (repulsion is seen on the compressive side). We also see some higher order effects in the contours of both cases within roughly 5 a_0 of the dislocation. These effects fade with distance as the dipole tensor term in equation (10) dominates the interaction. The strength and extent of interaction of the Fe interstitial with the dislocation is found to be roughly 2.5 times greater than that of the helium interstitial.

Conclusion

In this study, a hybrid method has been developed to couple the results of molecular statics calculations with classical isotropic elasticity theory to extract a continuum representation of various defects through the use of force multipoles. These calculations have provided a means to account for the changes in defect energetics due to local strain environment effects. The isotropic elastic Green's function is found to provide material response very consistent with atomistic simulations when higher order moments describing the defect are implemented. We have found the use of the octopole tensor in many cases is necessary, and is able to capture anisotropies in the displacement field as well as discrete lattice irregularities, both of which are foreign phenomena within isotropic elasticity theory.

We have also performed calculations of the interaction energies between multipolar defects and intrinsic extended defects in iron. Our solutions have thus far provided approximations for the energetics and general trends in the affinity of defects to show attraction or repulsion to other defects. We are currently developing hybrid methods to model dislocations and grain boundaries, to use in these calculations for increased accuracy. The method we describe and its outcomes will allow for more accurate models of defect diffusion and interaction within the radiation damage environment, where long- and short-range elastic interactions govern the accumulation and evolution of defects in the material.

References

[1] L.K. Mansur, Journal of Nuclear Materials 216 (1994), 97.
[2] B.N. Singh, H. Trinkaus, A.J.E. Foreman, Journal of Nuclear Materials 249 (1997), 103.
[3] C. Domain, C.S. Becquart, L. Malerba, Journal of Nuclear Materials 335 (2004), 121.
[4] K. Morishita, R. Sugano, Nuclear Instruments and Methods in Physics Research B 255 (2007), 52.
[5] B.D. Wirth, E.M. Bringa, Physica Scripta 108 (2004), 80.
[6] H. Kanzaki, Journal of Physics and Chemistry of Solids 2 (1957), 24.
[7] R. Bullough and J. Hardy , Philosophical Magazine 17 (1968), 833.
[8] C.S. Hartley and R. Bullough, Journal of Applied Physics 48 (1977), 4557.
[9] J.D. Eshelby, Journal of Applied Physics 25 (1954), 255.
[10] R. Siems, Physica Status Solidi, 30 (1968), 645.
[11] C. Teodosiu, Springer, Berlin, Heidelberg, New York, (1982).
[12] G.J. Ackland, M.I. Mendelev, D.J. Srolovitz, S. Han, and A.V. Barashev, Journal of Physics: Condensed Matter 16 (2004), S2629.
[13] N. Juslin and K. Nordlund, Journal of Nuclear Materials 382 (2008), 143.
[14] J.E. Lennard-Jones, Proceedings of the Royal Society A 106 (1924), 463.
[15] P. Ehrhart, K.H. Robrock, and H.R. Schober, Elsevier-Amsterdam (1986), 63.
[16] C. Domain and C.S. Becquart, Physical Review B 65 (2002), 024103.
[17] C.C. Fu, F. Willaime, and P. Ordejon, Physical Review Letters 92 (2004), 175503.
[18] D.A. Terentyev, L. Malerba, and M. Hou, Physical Review B 75 (2007), 104108.
[19] Z.Z. Chen, N. Kioussis, N.M. Ghoniem, and D. Seif, (submitted for publication).
[20] M.J. Caturla, C.J. Ortiz, C.C. Fu, Comptes Rendus Physique 9 (2008), 401.
[21] K. Morishita, R. Sugano, B.D. Wirth, T. Diaz de la Rubia, Nuclear Instruments and Methods in Physics Research B 202 (2003), 76.
[22] J.P. Hirth and J. Lothe, John Wiley & Sons, (1982).
[23] B.J. Lee and M.I. Baskes, Physical Review B 62 (2000), 8564.

HFIR Irradiation Experiments – F. W. Wiffen, Oak Ridge National Laboratory

The current status of Fusion Materials Program irradiation experiments in the HFIR reactor is tabulated.

Table - Summary of Recent, Current and Planned Fusion Materials Program Experiments in the High Flux Isotope Reactor (HFIR)

Experiment Designation	Primary Materials	Specimen Types*	Irradiation Temperature (°C)	Max Exposure (dpa)	Number of Reactor Cycles	Irradiation Period (month/year)
Beryllium reflector (RB) irradiation positions						
RB-15J	F82H	T, F, FT	300, 400	6	10	6/08 – 12/09
Target zone capsules						
JP-25	F82H	T, FT	300, 500	20	10	2/99 - 1/10
JP-26	F82H	T, FT	300,400,500	9	50	
JP-27	F82H	T, FT	300, 400	21	13	12/03 - 1/08
JP-28	F82H	T, FT	300,400,500	80-?	50	1/05 – 6/13
JP-29	F82H	T, FT	300,400,500	80	50	1/05 - 6/13
Target zone rabbit capsules						
F8A-1	F82H	T, FT	300	50	28	2/09 – 6/13
F8A-2	“	“	“	“	“	“
F8B-1	“	“	“	“	“	“
F8B-2	“	“	“	“	“	“
Target zone rabbit capsules						
JCR-1	SiC/SiC	Bend bars	800	30	15	10/04 – 1/09
JCR-2	“	“	“	“	“	“
JCR-3	“	“	“	“	“	“
JCR-4	“	“	“	“	“	“
JCR-5	“	“	“	>50	>25	10/04 - ??
JCR-6	“	“	“	“	“	“
JCR-7	“	“	“	“	“	“
JCR-8	“	“	“	“	“	“
JCR-9	“	“	500	30	15	10/04 – 1/09
JCR-10	“	“	“	“	“	“
JCR-11	“	“	“	“	“	“
JCR-12	“	“	“	“	“	“

*T = Tensile, F = Fatigue, FT = Fracture Toughness. Most experiments also contain TEM disks and other specimens and monitors occupying a small portion of the available volume.